



# LUND UNIVERSITY

## Search for Dark Matter in events with missing transverse momentum and a Higgs boson decaying into bottom quarks with the ATLAS detector

Skorda, Eleni

2022

[Link to publication](#)

*Citation for published version (APA):*

Skorda, E. (2022). *Search for Dark Matter in events with missing transverse momentum and a Higgs boson decaying into bottom quarks with the ATLAS detector*. Lund University.

*Total number of authors:*

1

### General rights

Unless other specific re-use rights are stated the following general rights apply:

Copyright and moral rights for the publications made accessible in the public portal are retained by the authors and/or other copyright owners and it is a condition of accessing publications that users recognise and abide by the legal requirements associated with these rights.

- Users may download and print one copy of any publication from the public portal for the purpose of private study or research.
- You may not further distribute the material or use it for any profit-making activity or commercial gain
- You may freely distribute the URL identifying the publication in the public portal

Read more about Creative commons licenses: <https://creativecommons.org/licenses/>

### Take down policy

If you believe that this document breaches copyright please contact us providing details, and we will remove access to the work immediately and investigate your claim.

LUND UNIVERSITY

PO Box 117  
221 00 Lund  
+46 46-222 00 00

# Search for Dark Matter in events with missing transverse momentum and a Higgs boson decaying into bottom quarks with the ATLAS detector

ELENI SKORDA

DEPARTMENT OF PHYSICS | FACULTY OF SCIENCE | LUND UNIVERSITY





Search for Dark Matter in events with missing transverse momentum and a Higgs boson decaying into bottom quarks with the ATLAS detector



# Search for Dark Matter in events with missing transverse momentum and a Higgs boson decaying into bottom quarks with the ATLAS detector

by Eleni Skorda



**LUND**  
UNIVERSITY

Thesis for the degree of Doctor of Philosophy  
Thesis advisors: Associate Prof. Ruth Pöttgen  
Faculty opponent: Prof. Greg Landsberg

To be presented, with the permission of the Faculty of Science of Lund University, for public criticism in Rydberg lecture hall (Rydbergsalen) at the Department of Physics on Sunday, the 4th of November 2022 at 13:00.

Organization <b>LUND UNIVERSITY</b> Department of Physics Box 118 SE-221 00 LUND Sweden		Document name <b>DOCTORAL DISSERTATION</b>	
		Date of disputation 2022-11-04	
		Sponsoring organization	
Author(s) Eleni Skorda			
Title and subtitle Search for Dark Matter in events with missing transverse momentum and a Higgs boson decaying into bottom quarks with the ATLAS detector			
Abstract Many astrophysical observations indicate the existence Dark Matter, which is not predicted by the Standard Model (SM) of particle physics. Many theories beyond the Standard Model (BSM) predict new heavy particles called WIMPs (Weakly Interacting Massive Particles). One way to search for WIMP dark matter is through its pair-production in collider experiments. A possible signature, in this case, is the associated production of a WIMP pair with a Higgs-boson decaying to a pair of b-quarks. The WIMPs leave the detector without interacting, leading to events with a large amount of missing transverse momentum and two highly-energetic b-jets due to the decay of the Higgs-boson. The search presented in this thesis uses such events based on data from proton-proton collisions recorded with the ATLAS detector from 2015 to 2018 at $\sqrt{s} = 13$ TeV. A profile likelihood fit is performed to extract a possible signal. No significant excess above the SM predictions is observed, and the results are interpreted in terms of the $Z'$ -2HDM and $2HDM+a$ benchmark models. In addition, model-independent limits are set on the cross-section for new physics at 95% confidence level (CL). The thesis also presents a reinterpretation of the results in terms of the Dark-Higgs model. All physics analyses rely on the reconstruction of physics objects and the high-precision measurements of their energy and momentum. The outermost part of the ATLAS Inner Detector, Transition Radiation Tracker (TRT), contributes significantly to the momentum measurement of the charged particles by extending the length of the measured trajectories. This thesis describes studies of the drift-time calibration of the TRT. These studies examine the dependence of the calibration parameters on the transverse momentum of reconstructed tracks and pile-up using simulated events. Furthermore, the effect of additional drift-time corrections in straw tubes filled with Argon-based gas mixture is studied.			
Key words ATLAS, LHC, Beyond the Standard Model, Dark Matter, Higgs-boson, bottom quarks, missing transverse momentum, Recast, Transition Radiation Tracker			
Classification system and/or index terms (if any)			
Supplementary bibliographical information		Language English	
ISSN and key title		ISBN 978-91-8039-415-4 (print) 978-91-8039-416-1 (pdf)	
Recipient's notes		Number of pages 284	Price
		Security classification	

I, the undersigned, being the copyright owner of the abstract of the above-mentioned dissertation, hereby grant to all reference sources the permission to publish and disseminate the abstract of the above-mentioned dissertation.

Signature 

Date 2022-09-21

# Search for Dark Matter in events with missing transverse momentum and a Higgs boson decaying into bottom quarks with the ATLAS detector

by Eleni Skorda



**LUND**  
UNIVERSITY

**Cover illustration front:** Modified picture from : **The Matter of the Bullet Cluster** Image Credit: X-ray: NASA/CXC/CfA/ M. Markevitch et al.; ).  
The graphic illustrations on top the figure were added by the author of this thesis.

© Eleni Skorda 2022

Faculty of Science, Department of Physics

ISBN: 978-91-8039-415-4 (print)

ISBN: 978-91-8039-416-1 (pdf)

ISSN: <ISSN number>

Printed in Sweden by Media-Tryck, Lund University, Lund 2022



*To my grandmother Anna*



# Contents

List of publications . . . . .	iv
Acknowledgements . . . . .	v
Popular summary in English . . . . .	vii
<b>1 Introduction</b>	<b>1</b>
<b>2 The Standard Model of particle physics</b>	<b>5</b>
2.1 Standard Model in a nutshell: particles and interactions . . . . .	5
2.2 Symmetries in the Standard Model . . . . .	8
2.3 Quantum Electrodynamics . . . . .	9
2.4 Quantum Chromodynamics . . . . .	11
2.5 The Electroweak theory . . . . .	13
2.6 Symmetry breaking and the Higgs mechanism . . . . .	15
2.7 Open questions in the Standard Model . . . . .	18
<b>3 Dark Matter</b>	<b>21</b>
3.1 Key elements of cosmology . . . . .	21
3.2 Evidence of Dark Matter . . . . .	26
3.3 Candidates for Dark Matter . . . . .	30
3.4 WIMP searches . . . . .	31
3.5 Simplified models for the $E_T^{\text{miss}} + H(b\bar{b})$ search for Dark Matter .	36
<b>4 Proton-proton collisions</b>	<b>43</b>
4.1 Description of a $pp$ collision . . . . .	43
4.2 Before the collision: from protons to partons . . . . .	44
4.3 The hard scatter . . . . .	48
4.4 From partons to hadrons . . . . .	51
4.5 Event generators . . . . .	52
<b>5 The Large Hadron Collider</b>	<b>55</b>
5.1 Accelerator complex . . . . .	55
5.2 The LHC experiments . . . . .	56
5.3 Luminosity . . . . .	57
5.4 Performance overview . . . . .	58

<b>6</b>	<b>The ATLAS Experiment</b>	<b>61</b>
6.1	Detector Overview . . . . .	61
6.2	Inner detector . . . . .	63
6.3	Calorimeter System . . . . .	65
6.4	Muon Spectrometer . . . . .	68
6.5	Forward Detectors . . . . .	70
6.6	Triggering and Data Acquisition . . . . .	71
6.7	Data taking and processing . . . . .	72
6.8	Reconstruction of detector objects . . . . .	73
6.9	Event simulation chain in ATLAS . . . . .	86
<b>7</b>	<b>Calibration of the Transition Radiation Tracker</b>	<b>89</b>
7.1	Detector design . . . . .	90
7.2	Signal description . . . . .	93
7.3	Calibration figures of merit . . . . .	95
7.4	Calibration procedure . . . . .	99
7.5	Validation of the calibration constants . . . . .	101
7.6	Calibration using simulated events with $LT = 100$ eV for straw tubes filled with Ar-based mixture . . . . .	103
7.7	Dependence on the $p_T$ of the reconstructed tracks . . . . .	105
7.8	Results for simulated events with $\langle\mu\rangle \in (20, 30)$ . . . . .	108
7.9	Study of the pile-up dependence of the time offset values . . . . .	111
<b>8</b>	<b>Analysis strategy</b>	<b>117</b>
8.1	Signal Characteristics . . . . .	118
8.2	Background Contributions . . . . .	121
8.3	Statistical Analysis . . . . .	123
<b>9</b>	<b>Data and simulated events</b>	<b>129</b>
9.1	Data . . . . .	129
9.2	Simulated events . . . . .	133
<b>10</b>	<b>Object Definition and event selection</b>	<b>139</b>
10.1	Physics Objects definition . . . . .	139
10.2	Event Selection . . . . .	148
10.3	Validation of the particle-level definitions of the event selection requirements . . . . .	161
<b>11</b>	<b>Systematic uncertainties, fit setup, and pre-fit data to MC comparisons</b>	<b>173</b>
11.1	Systematic uncertainties . . . . .	173
11.2	Fit Setup . . . . .	179
11.3	Data and MC comparison . . . . .	183

<b>12 Results and interpretation</b>	<b>191</b>
12.1 Background-only fit . . . . .	191
12.2 Nuisance parameter impact . . . . .	204
12.3 Interpretations . . . . .	205
<b>13 Reinterpretation of the MonoH(bb) analysis with RECAST</b>	<b>211</b>
13.1 RECAST . . . . .	212
13.2 Analysis Preservation using containerised workflows . . . . .	212
13.3 Analysis reinterpretation . . . . .	215
<b>14 Conclusion</b>	<b>221</b>
<b>15 References</b>	<b>223</b>
<b>A TRT auxiliary material</b>	<b>243</b>
A.1 r-t relations for the calibration with LT=100 eV and new signal shaping . . . . .	243
A.2 Position and time residuals for Xe-based straw tubes using simu- lated samples without pile-up . . . . .	244
A.3 Position and time residuals for Ar-based straw tubes with ToT correction only . . . . .	245
A.4 Position and time residuals for Ar-based straw tubes with ToT and HT corrections . . . . .	245
<b>B Comparison plots between reconstructed and truth variables</b>	<b>249</b>
B.1 Signal region . . . . .	249
B.2 One-muon CR . . . . .	249
B.3 Two-lepton CR . . . . .	249
<b>C Comparison of Standard Model predictions to data</b>	<b>259</b>
C.1 Signal region pre-fit distributions . . . . .	259
C.2 Selected pre-fit distributions in the one-muon control region . . . . .	261
C.3 Selected prefit distributions in the two-lepton signal region . . . . .	262
<b>D Mono-H analysis results-auxiliary material</b>	<b>267</b>

# List of publications

Some of the original work presented in this thesis lead to the results reported in the following publications:

- I **Search for Dark Matter produced in association with a Standard Model Higgs boson decaying to b-quarks using the full Run 2 collision data with the ATLAS detector**  
ATLAS Collaboration  
ATLAS-CONF-2021-006. Moriond 2021 Note  
This publication will be superseded by II
  
- II **Search for Dark Matter produced in association with a Standard Model Higgs boson decaying to b-quarks using the full Run 2 collision data with the ATLAS detector**  
ATLAS Collaboration  
Paper Submitted to JHEP

## Acknowledgements

Doing a PhD was one of the most interesting, exciting, happy and at the same time challenging experiences of my life. I want, on this page, to express my thanks to all the people who were part of this unique journey and supported me, especially during the tough times.

First and foremost, I want to thank my thesis supervisor, Ruth Pöttgen, for her constant support, guidance and infinite patience. You were always there for me, always available to answer questions, share your knowledge and enthusiasm about science, offer valuable advice and let me explore my interests and ideas. I especially want to thank you for taking the time to carefully review this manuscript and provide valuable feedback. You are the best supervisor I could have asked for!

I would also like to thank my co-supervisor, Torsten Åkesson for always finding the time to offer advice, and Johan Rathsman, for all his advice and the valuable feedback on the theory chapters of this thesis. Special thanks go to my unofficial co-supervisor for the last two years, Else Lytken, for taking the time to discuss things, offer valuable advice and for reviewing the TRT chapter. Also I would like to thank Peter Christiansen, who reviewed the thesis and offer valuable feedback.

I want to thank all the incredible people from the TRT group, especially Fred Lieuring and Philippe Calfayan for the many hours of explaining things to me, answering questions and their support. I also want to thank Peter Hansen and Anatoly Romaniuk for their valuable feedback in the TRT meetings and for sharing their vast knowledge of the detector. I would also like to express my gratitude to my TRT colleague and, most importantly, friend Christophe Roland: the time we spent working together was, without a doubt, one of the happiest, thank you for proofreading almost all the chapters of this thesis, for playing board games online during the Covid pandemic, and for all the support during last-minute panics.

For the main part of this thesis, I had the chance to work with many excellent scientists within the JDM and Exotics group. A special thanks goes to James Frost and Patrick Rieck, for their advice and feedback in meetings, and to Dan Guest and Spyros Argyropoulos, for coordinating the analysis and keeping everything running smoothly. Many thanks also go to Andrea , Anindya and Jay from the  $E_T^{\text{miss}} + H(b\bar{b})$  analysis group for the many hours of discussions and debugging, we shared. I hope I will have the chance to work with you in the future. I want to thank Lukas Heinrich for his help and support with the RECAST framework. Also, I would like to thank all the people from the

REANA platform for their support.

Going to Sweden from Greece was a huge step for me. However, adapting to a new country was easy because of all the people I met in the particle physics division. I would like to thank Bozena Wlosinska for making the transition smooth, helping with all the paperwork and always with so much kindness and patience. I can not imagine the division without you. Special thanks also go to Florido Paganelli, for solving all the IT problems, and setting up our work computers. Also I want to thank both Florido and Amanda, for all the fun times we shared outside work, I am going to miss you both.

One person I had the chance to meet in Lund, during my PhD years is Melissa Franklin. During her stay in Lund, Melissa had a unique impact in our lives. I want to thank you for the blackboard discussions, for pushing us to do better, and for your advice.

The first years of my PhD life are those with some of the happiest memories, full of trips, exciting conversations, fikas, and afterworks, and for that, I have to thank my incredible everyone in Lund, the senior members, post-docs, and my fellow PhD students. I want to thank all the people in the ATLAS office: Katja, Trine, Eric and Eva for always providing a supporting shoulder, for all the fun times in the office, in trips, and afterwork, and for organising the best Christmas parties, Caterina, for being a great listener, and Nathan for bringing positive vibes to the office. An equally cool and fun place was the ALICE office: Jonatan, Vytautas, Adrian, Oliver and Omar, thank you for all the fun times we had during and after work. Finally, a special thanks go to our post-docs: Geoffrey, Will, and Jannik, for all the fun times we shared while working and playing board games. I also want to thank Marius (from theory) for all the nice walks and intriguing conversations during and running cool DND campaigns.

I would also like to express my gratitude to my friends from Greece: Stella, Giorgos, Michalis, Anna, Panos, Maria, Dora and Nikos. Guys, thank you for always being there for me, making me part of your family, always providing support and encouragement, for staying up with me when I was working late, for always cheering me up, and making sure I arrived safely home after every trip. Thank you for showing me the fun, creative and exciting aspects life away from work. You are the most kind, understanding, caring and amazing people I met, and I am the luckiest person to have you in my life.

Finally, I want to express my deepest gratitude to my mother, for her unconditional love and endless support, for always believing in me, inspiring me, pushing me to do my best, and for teaching me to never give up.

## Popular summary in English

Particle physics studies the fundamental particles from which the world around us is built and the laws that bind them together. Developed in the second half of the 20th century, the Standard Model (SM) of particle physics describes the fundamental building blocks that constitute the matter and the interactions between them. Since its formulation, a vast amount of experimental data has confirmed the SM predictions. The most recent triumph of the theory was the discovery of the Higgs-boson at the Large Hadron Collider in 2012, which completed the particle inventory of the SM. Despite its great success, the SM does not provide an explanation for several phenomena, one of which is another great discovery of the 20th century, the Dark Matter.

Many cosmological observations, showed that the SM accounts only for approximately 20% of the matter in the universe, while the rest is a non-luminous form of matter, called *Dark Matter*. Even though the existence of Dark Matter is known for ninety years, its particle nature remains an open question. At the same time, many theories beyond the Standard Model predict as candidates for Dark Matter new heavy particles that have very weak interactions (if any) with the regular matter, called WIMPs (Weakly Interacting Massive Particles). There is a variety of experiments searching for WIMPs, including collider experiments.

In principle, if WIMPs exist, then we should be able to produce them by colliding particle beams in the laboratory. Since WIMPs are supposed to have large masses, based on the famous Einstein's  $E = mc^2$ , we need to accelerate the particles in the laboratory to high enough energies.

The largest accelerator built so far is the Large Hadron collider. Inside its rings, two high-energy proton beams are accelerated to a speed very close to the speed of light before they are made to collide in four points, where detectors are built to capture the products of the collisions.

One of these detectors is the ATLAS, a general-purpose detector designed to surround almost completely the collision point, to catch the products of the collisions in almost all possible directions.

However WIMPs, due to their elusive nature will go through the detector unnoticed. The only way to “feel” their presence is by using energy-momentum conservation, when they are produced with something that the detector can capture. If the energy-momentum conservation is not valid for the products of the collision then we suspect that something passed through the detector unnoticed. One thing we can capture (from its decay products) is the Higgs boson. The

search presented in this work is looking for such events where DM is produced together with a Higgs-boson. It is quite exciting to think that the particle that was the last missing piece of the Standard Model puzzle is now helping us to look for physics beyond the theory that predicted it.

# Chapter 1

## Introduction

“ *‘The Answer to the Great Question... Of Life, the Universe and Everything... Is... Forty-two’, said Deep Thought, with infinite majesty and calm.*”  
— The Hitchhiker’s Guide to the Galaxy, Douglas Adams

To place the beginning of particle physics, as we currently understand it at a specific point in history is difficult, as the notion that Nature is built from indivisible particles, dates back to almost 2500 years ago to the Greek philosophers. However, it was the discovery of electrons in 1897 by Thomson, which changed the picture of atoms from indivisible, to a soup of positive charges in which discreet negative charges are embedded, and ignited the idea of underlying structure. Ever since, a plethora of experimental evidence and theoretical predictions led to the current theory of particle physics, the *Standard Model*.

The Standard Model (SM) describes the interactions between the elementary particles that constitute the matter, the *fermions*, and the force-carrying particles, the *gauge bosons*. There are three generations of fermions within the SM, each of which comprises of a charged and a neutral lepton and two quarks. Quarks are never observed individually, instead they exist in bound states. Besides the matter-particles, there are also the force-carriers, that mediate the three forces described by the SM, the strong the weak and the electromagnetic. The fourth known force, gravity, has not been successfully included in the SM, despite many attempts. Finally, the mechanism that explains how the fundamental particles acquire mass predicts the existence of a scalar boson, the Higgs-boson.

Despite successfully describing almost all experimental observations to date with remarkable precision, the SM does not provide an explanation for several phenomena, one of which is the existence of the *Dark Matter* (DM), a non luminous,

gravitationally interacting form of mass that according to astrophysical observations, makes up of roughly 80% of the matter content of the universe.

One of the first to postulate the existence of a non-luminous form of matter was the Dutch astronomer Jan Oort 1932 [1], who measured the velocity of stars near the galactic plane by studying their Doppler shifts, and found that they were moving much faster than expected. In fact, their speed would have been enough to allow them to escape from their orbits. He thus hypothesised that more galactic mass had to be present to keep the stars in orbit. A year later, Fritz Zwicky [2] used the virial theorem to infer the dynamical mass of the Coma cluster system and found it two orders of magnitude larger than what he estimated using the cluster's luminosity. To explain this result, the majority of the Coma cluster's mass should be non-luminous. Many astrophysical observations since provided evidence for the existence of DM, among others, the shapes of rotation curves from galaxies.

Despite the plethora of astrophysical evidence for its existence, the particle nature of DM remains an open question. At the same time, many theories beyond the Standard Model predict new particles that could be candidates for Dark Matter. In particular, many models predict new heavy particles, with masses that range from few GeV to several TeV, that interact only weakly with the regular matter, called Weakly Interacting Massive Particles (WIMPs). There is a variety of experiments searching for WIMPs, including collider experiments.

The key to improving our understanding of Nature at a fundamental level have been, for many decades, particle accelerators and colliders. To study the elementary particles and their interactions, we need to probe deeper into structure i.e. go to smaller and smaller scales and increasingly higher energies. Since the kinetic energy of colliding particles determines the mass scale of the particles produced in a collision, particle accelerators that can reach exceedingly high energies are crucial to allow access to new heavy states. The most powerful accelerator built to date is the Large Hadron Collider (LHC) at CERN. It is designed to accelerate proton beams to centre-of-mass-energies up to 14 TeV and bring them to collision in four points delivering instantaneous luminosities of more than  $10^{34} \text{ cm}^{-2}\text{s}^{-1}$ . The design luminosity and energies are necessary for the discovery of new physics.

A typical signature for DM searches at particle colliders is events with imbalanced transverse momentum due to the DM particles escaping the detector without leaving any signal. Events with a Higgs-boson and high missing transverse momentum are very interesting because they can provide insight into the interaction with DM. This thesis presents a search for DM in such events, using data recorded by the ATLAS experiment at the LHC from 2015 to 2018.

An analysis preservation effort has gained momentum in the recent years at CERN and more specifically within the ATLAS collaboration. This effort, aims to make the analysis easily accessible by people outside the original collaborations, and to provide frameworks and platforms for reinterpretations. The thesis also presents the preservation of the  $E_T^{\text{miss}} + H(b\bar{b})$  analysis, as well as an interpretation study.

All physics analysis rely on an efficiently operated detector that delivers high-quality data. Equally important is the correct reconstruction of the various physics objects, for which calibrations are necessary. This thesis also presents studies related to the performance of the calibration of the Transition Radiation Tracker (TRT), which significantly contributes to the momentum measurements of the charged particles trajectories in the ATLAS detector.

## Thesis Outline

The thesis starts by introducing the theoretical foundation necessary for the explanation of the search presented in this thesis: Chapter 2 provides a summary of the Standard Model and the currently open questions, Chapter 3 gives an overview of the experimental evidence for the existence of Dark matter, the particle candidates for DM, the main search strategies for WIMP DM, and the simplified benchmark models used to interpret the analysis results. Chapter 4 presents the basic concepts of proton-proton collisions and their simulations. The next two chapters introduce the experimental tools and concepts used in the analysis: Chapter 5 provides information on the LHC and Chapter 6 on the ATLAS experiment. Chapter 7 presents studies on the drift time calibration of the ATLAS Transition Radiation Tracker. The remaining chapters present the  $E_T^{\text{miss}} + H(b\bar{b})$  search for WIMP Dark Matter. Chapter 8 outlines the general analysis strategy, and Chapter 9 compiles information on the data and simulated event samples. Chapter 10 defines the physics objects used in the analysis and summarises the event selection. Chapter 11 describes the systematic uncertainties in the fit inputs for the statistical analysis, the fit setup, and contains comparisons between data and the Standard Model predictions before the fit in all the analysis regions. Chapter 12 presents and discusses the results of the statistical analysis, and their interpretation. Chapter 13 presents the implementation of the analysis in the RECAST framework and a reinterpretation of the analysis results using an alternative signal model. Finally, Chapter 14 concludes the thesis.

## Author's contributions

The results presented in this thesis have been possible due to the efforts of all the members of the ATLAS collaboration, and were produced in small groups. My personal contributions are listed below:

- **Chapter 7** : This chapter presents my work on the drift-time calibration of the Transition Radiation Tracker (TRT). My work aimed to improve the calibration using simulated events and test the dependence of the calibration parameters on the transverse momentum of reconstructed tracks and the pile-up. I also implemented additional corrections for the estimated drift time for the Argon-filled straws. Finally, I was involved in calibration studies for Run-3. This work is documented in Sections 7.4-7.8. It should be noted here that the numbers presented in the first and third row of Table 7.7 were produced by Christophe Roland, after adapting the code written by the author of this thesis, to run the full-Argon scenario. The studies presented in this chapter had an impact to many ATLAS analyses, since it is the foundation for using the data from this detector.
- **Chapters 8-12** : These chapters present my work as one of the five main analysers that searched for Dark Matter produced together with a Higgs boson that decays to a pair of b-quarks. I made significant contributions to the software development and maintenance that selected the physics objects, and applied the full event selection. My main contribution was to prepare all the necessary inputs used for the estimation of the theoretical uncertainties on the acceptance for background and signal models. To estimate these uncertainties, the full analysis event selection had to be reimplemented to be applied to Monte Carlo simulated events at a level before the detector simulation step, and be carefully validated. I contributed to the development of the statistical analysis framework, mostly on the implementation of the theoretical uncertainties in the fit. I have run the full analysis chain and provided important cross-checks.
- **Chapter 13** : I was responsible for the preservation of the  $E_T^{miss} + \text{Higgs}(bb)$  analysis. This included preparing the public likelihood and the majority of the publication results for the hepdata repository, and implementing the full analysis chain in the RECAST framework. This chapter presents my implementation of the analysis in the RECAST framework. It also contains a study I performed using my implementation of the analysis, in which I reinterpreted the analysis results using a model that predicts the associated production of DM and a hypothetical dark Higgs boson that decays to b-quarks. This work is documented in Sec. 13.2 and 13.3.

## Chapter 2

# The Standard Model of particle physics

This chapter provides an overview of the current theory of particle physics, the *Standard Model* (SM), based on references [3–8]. The first section of this chapter, 2.1, is a survey of the particle inventory of the Standard Model. Section 2.2 introduces the key elements of the mathematical framework of Quantum Field Theory (QFT), which is used to formulate the theories of the fundamental interactions described by the SM. The following sections, 2.3-2.5, will use the notion of *gauge symmetries* to present how each of the fundamental interactions is modelled in the theory. Section 2.6 briefly describes how the different particles obtain masses through the idea of *spontaneous symmetry breaking* and focuses on the role of the Higgs boson in the theory. Finally, Section 2.7 provides a short overview of the several shortcomings of the SM theory.

### 2.1 Standard Model in a nutshell: particles and interactions

The Standard Model describes the interactions between the elementary particles that constitute the matter, the *fermions*, and the force-carrying particles, the *gauge bosons*. In general, bosons are particles with integer spin that follow the Bose-Einstein statistics. The fermions, on the contrary, have half-integer spin, follow the Fermi-Dirac statistics and obey the exclusion principle of Pauli. In the SM interactions between fermions are described via the exchange of spin-1 gauge bosons.

Each interaction is associated with one or more gauge boson mediators. Even though there are four known forces, the SM includes only three: the electromagnetic, the weak and the strong. Including the fourth fundamental force, the gravitational, into the theoretical framework of the SM is still an open challenge. Gravity, however, can be considered negligible at the energy scale of the collider experiments.

The mediator of the electromagnetic interactions is the massless and electrically neutral *photon* ( $\gamma$ ), which couples to electric charge. The range of electromagnetic interactions is infinite because the photon has no mass. The strong interaction is mediated by eight *gluons* ( $g$ ), which are massless and electrically neutral. They carry, however, the corresponding charge for strong interactions. This charge is called *colour* and has three types: *red*, *green* and *blue*. Because gluons carry colour charge, they can couple to each other. The self-interaction of gluons limits the range of the strong force. The bosons responsible for the weak interaction are the electrically charged  $W^\pm$  and the neutral  $Z$ -boson, which couple to the 3-component of the weak isospin. These bosons are massive ( $m_{W^\pm} \approx 80.4 \text{ GeV}$  and  $m_Z \approx 91.2 \text{ GeV}$ ) [9]. Table 2.1 contains a summary of the interactions described by the SM.

Interaction	Gauge boson	Mass	Charge	Range (m)
Electromagnetic	$\gamma$	0	electrical	$\infty$
Strong	$g$	0	colour	$10^{-15}$
Weak	$Z$	91.2 GeV	weak isospin	$10^{-18}$
	$W^\pm$	80.4 GeV	weak isospin	$10^{-18}$

**Table 2.1:** Summary of the three fundamental interactions described by the SM the corresponding mediators, charges and range

There are two types of fermions, the *leptons* and the *quarks*. There are six leptons, in total, grouped into three families, also known as *generations*, as illustrated in Figure 2.1. Each generation consists of one (negatively) electrically charged lepton and a corresponding electrically neutral particle, the *neutrino*. The neutrino carries only weak charge. The charged leptons for each of the three families are the *electron* ( $e$ ), the *muon* ( $\mu$ ) and the *tau-lepton* ( $\tau$ ). There are, also, three types of neutrinos and each inherits the name of the charged lepton of the family. Figure 2.1 shows for each lepton its spin, charge and mass. We see that the mass of the charged leptons increases significantly in each generation: the electron is the lightest of the charged leptons and has a mass of approximately 511 keV, the muon has mass of 105 MeV, while the heaviest is the  $\tau$ -lepton with mass of 1.8 GeV [9]. For each lepton there is an anti-particle with the same mass and opposite values of all charges.

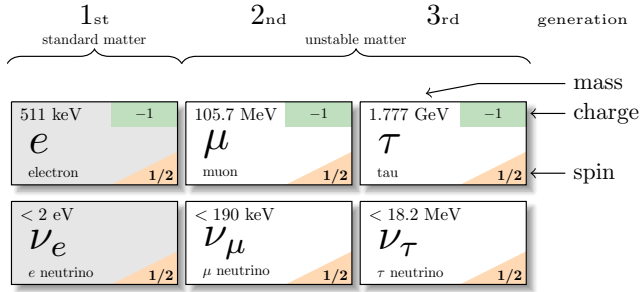


**Figure 2.1:** Summary of the Standard Model leptons. In the figure the generations are indicated on the top. Modified picture from [10]

The other type of matter particles, the quarks, come into six *flavours*, namely the *up*, *down*, *charm*, *strange*, *top* and *bottom* which are grouped into three generations, as illustrated in Figure 2.2.

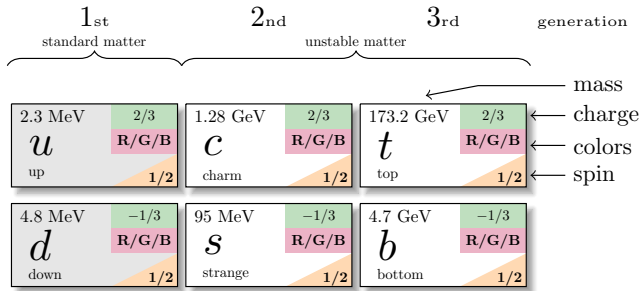


**Figure 2.2:** Summary of the quarks in SM. In the figure the generations are indicated on the top. Modified picture from [10]

In each family, there are two components one “*up*” and one “*down*”. The names refer to the 3-component of the weak isospin, which is  $+1/2$  for “*up*”-type quarks and  $-1/2$  for “*down*”-type. Furthermore, each “*up*” component has electric charge equal to  $2/3 |e|$ , while each “*down*”-type quark has  $-1/3 |e|$ , and all quarks carry colour charge. The theory requires for each quark an anti-quark to exist with the same mass but opposite values of all charges. Similar to the lepton families, the mass of the quarks increases significantly in each generation. The quarks of the first generation have masses of the order of a few MeV, the second generation of  $\sim 1$  GeV, while the third generation contains the two heaviest quarks: the bottom with a mass of 4.7 GeV and the top with a

mass of 173.2 GeV.

Quarks have never been individually observed by experiments. Instead, they are found only in bound colourless states collectively known as *hadrons*. Hadrons can be combinations of either three quarks, in which case are known as *baryons*, or of a quark and an anti-quark, called *mesons*. Protons ( $p$ ) and neutrons ( $n$ ), the ingredients of the atomic nuclei, are baryons: the proton is a combination of two up quarks and one down ( $uud$ ), while the neutron has two down quarks and one up ( $ddu$ ). Therefore, it seems that all the ordinary matter is made from fermions from the first generation. At the same time, the fermions from the second and third generations are unstable and decay to lighter particles.

The following section provides an overview of the key elements of the theoretical framework used to describe the dynamics of particle interactions.

## 2.2 Symmetries in the Standard Model

The Standard Model is a quantum field theory (QFT), a theory in which all the particles are treated as quanta of fields. The underlying idea of field quantization is similar to the classical quantum mechanics: the fields are promoted to operator valued functions of space-time,  $\phi(x)$ . For the mathematical description of field dynamics, the Lagrangian formalism is used both in classical mechanics and in QFT.

A very important quantity in Lagrangian mechanics is the so-called *action*. The action is the space-time integral of the Lagrangian density<sup>1</sup>  $\mathcal{L}$  :

$$S = \int \mathcal{L}(\phi, \partial_\mu \phi) d^4x. \quad (2.1)$$

To derive the equations of motion of a generic field,  $\phi$ , we use the variational principle of Lagrangian mechanics, which states that the solution,  $\phi(x)$ , is a stationary point of the action. By setting  $\frac{\delta S}{\delta \phi} = 0$  we derive the equations of motion

$$\partial_\mu \frac{\partial \mathcal{L}}{\partial (\partial_\mu \phi)} - \frac{\partial \mathcal{L}}{\partial \phi} = 0, \quad (2.2)$$

where  $\partial_\mu = \left( \frac{\partial}{\partial t}, \frac{\partial}{\partial x}, \frac{\partial}{\partial y}, \frac{\partial}{\partial z} \right)$ .

---

<sup>1</sup> $L = \int \mathcal{L} d^3x$ , where  $L$  is the Lagrangian

There is a class of theories, known as *gauge theories*, based on the requirement of the Lagrangian to be invariant under a group of gauge transformations. The gauge transformations define symmetries, which, according to Noether's theorem, lead to physical conservation laws. The Standard Model is a gauge theory based on a specific group of symmetry transformations:  $SU(3)_C \times SU(2)_L \times U(1)_Y$ . The first term,  $SU(3)_C$ , is the symmetry group that describes the strong interactions ( $C$  denotes colour), while the term  $SU(2)_L \times U(1)_Y$  is the combined symmetry that describes the weak and the electromagnetic interactions together (the labels will be discussed in 2.5). Besides the gauge symmetries, which are continuous, there are three important discrete symmetries for particle physics, namely the *parity* ( $P$ ), *charge conjugation* ( $C$ ) and *time reversal* ( $T$ ). The parity operator inverts the spatial coordinates through the origin. The charge conjugation operator switches particles to antiparticles and vice versa. These symmetries are important because all the local Lorentz-invariant gauge field theories are invariant under the combined operation  $CPT$  (in any order), according to the *CPT theorem*. The following sections will review, briefly, the underlying gauge theory of each interaction separately, starting with *Quantum Electrodynamics* (QED), the (gauge) field theory of electromagnetism.

## 2.3 Quantum Electrodynamics

The theory of Quantum Electrodynamics (QED) was the first gauge theory to be developed and formed the basis for the development of the rest of the theories in the SM framework. The starting point for this presentation is the Lagrangian density of a free fermion field,  $\psi$ , with mass  $m$ ,

$$\mathcal{L} = \bar{\psi} (i\gamma^\mu \partial_\mu - m) \psi, \quad (2.3)$$

where  $\gamma^\mu$  are the Dirac matrices ( $\{\gamma^\mu, \gamma^\nu\} = 2g^{\mu\nu}$ ),  $g^{\mu\nu}$  is the metric tensor of four dimensional space-time and  $\bar{\psi} = \psi^\dagger \gamma^0$  is the conjugate of the fermion field.

The corresponding equation of motion, using 2.2, is the well-known *Dirac equation*

$$(i\gamma^\mu \partial_\mu - m) \psi(x) = 0. \quad (2.4)$$

The equation of motion is invariant under global phase transformations of the type  $\psi(x) \rightarrow \psi' = e^{iqg} \psi(x)$ , where  $q$  is the charge and  $g$  some real number. In the following we will demonstrate how the coupling to the electromagnetic field occurs once gauge invariance is required under *local* gauge transformations for the equation of motion 2.4.

Performing a local gauge transformation,  $\psi(x) \rightarrow \psi' = e^{iqg(x)}\psi(x)$ , in which the phase factor depends on the space-time position, leads to

$$\begin{aligned} (i\gamma^\mu \partial_\mu - m) e^{iqg(x)}\psi(x) &= e^{iqg(x)} (i\gamma^\mu \partial_\mu \psi(x) - m\psi(x)) - \gamma^\mu q e^{iqg(x)} (\partial_\mu g(x))\psi(x) \\ &= -q\gamma^\mu (\partial_\mu g(x)) e^{iqg(x)}\psi(x) = -q\gamma^\mu (\partial_\mu g(x))\psi'. \end{aligned}$$

The result does not satisfy 2.4 and to conserve the symmetry locally, one has to introduce the electromagnetic field which transforms as follows

$$A_\mu(x) \rightarrow A'_\mu(x) = A_\mu(x) - \partial_\mu g(x),$$

and replace the derivative  $\partial_\mu$  in the Lagrangian, 2.3 with the covariant derivative  $D_\mu$ :

$$D_\mu = \partial_\mu - iqA_\mu. \quad (2.5)$$

After introducing the interaction term between  $\psi$  and the vector field  $A_\mu$  and the kinetic term of the free vector field, which is expressed by  $F_{\mu\nu} = \partial_\mu A_\nu - \partial_\nu A_\mu$ , the Lagrangian for QED reads

$$\mathcal{L}_{QED} = \bar{\psi} [i\gamma^\mu (\partial_\mu - iqA_\mu) - m] \psi - \frac{1}{4} F_{\mu\nu} F^{\mu\nu}. \quad (2.6)$$

The mass term of the field  $A_\mu$  is not allowed in 2.6, due to the gauge transformation invariance, which means the corresponding gauge boson must be massless. This is consistent with the experimental observations of massless photons in Nature.

The local gauge transformations of QED form the unitary symmetry group  $U(1)$ , which is represented by one-dimensional unitary complex matrices. This symmetry group has one *generator*<sup>2</sup>, which is associated with the vector boson field. When the generators of a group commute, the group is characterised as *abelian*, thereby  $U(1)$  is an abelian group.

The process described in this section can be generalised to gauge theories based on *non-abelian groups*. Without repeating the steps presented here, the following section will overview the non-abelian gauge theory based on  $SU(3)$  symmetry group, which is the underlying theory of the strong interactions.

---

<sup>2</sup>Each symmetry group has one or more elements called *generators*. The repeated action of the group generators can give every element of the group.

## 2.4 Quantum Chromodynamics

The gauge theory that describes the strong interactions, the *Quantum Chromodynamics* (QCD), is based on the SU(3) symmetry group. The SU(3) is non-abelian and has eight generators<sup>3</sup>, which correspond to eight massless gauge boson fields, the gluons. The group generators are represented by the so-called Gell-Mann matrices,  $\lambda_\rho$  with  $\rho = 1, \dots, 8$ , which follow the commutation rule

$$[\lambda_a, \lambda_b] = i2f_{abc}\lambda^c,$$

where  $f_{abc}$  are the structure constants of SU(3). For the Lagrangian of a free quark field,  $q$ , to be invariant under the local gauge transformation, the gauge fields  $G_\mu^\rho$  must be introduced. The covariant derivative is

$$D_\mu = \partial_\mu - ig_s \frac{\lambda_\rho}{2} G_\mu^\rho. \quad (2.7)$$

The coupling  $g_s$  is related to the strong coupling and is written as  $\alpha_s = \frac{g_s^2}{4\pi}$ . The QCD Lagrangian, after using 2.7 reads

$$\mathcal{L}_{QCD} = \sum_q \bar{q} (i\gamma^\mu D_\mu - m) q - \frac{1}{4} G_\rho^{\mu\nu} G_{\mu\nu}^\rho, \quad (2.8)$$

where  $\bar{q}$  is the conjugate of the quark field  $q$ . The first term of 2.8 describes the interaction between gluon and quark fields, and the summation index runs over all possible quark flavors, while  $G_{\mu\nu}^\rho$  is the gluon field tensor,

$$G_{\mu\nu}^\rho = \partial_\mu G_\nu^\rho - \partial_\nu G_\mu^\rho - g_s f^{\rho bc} G_\mu^b G_\nu^c. \quad (2.9)$$

The last term of 2.9 describes the self interaction of gluon fields, which occur because gluons carry colour charge. The gluon self coupling gives rise to the special properties of the strong interaction.

Due to gluon self-coupling, quantum fluctuations create, in the close vicinity of a quark field, virtual gluon pairs, besides the virtual quark anti-quark pairs. Opposite colour charges attract, and as a result, the virtual  $q\bar{q}$  pairs align themselves in a way that they “screen” the original charge. On the contrary, the gluon pairs have an “anti-screening” effect, which dominates at short distances, leading to a weaker coupling, in which case quarks are quasi-free particles. This property is known as *asymptotic freedom*. As the distance increases, the coupling constant becomes larger, leading to the *confinement* of quarks within hadrons.

---

<sup>3</sup>The number of the generators of SU( $N$ ) symmetry groups is equal to the dimension of the group, i.e.  $N^2 - 1$

The dependence of the coupling constant on the energy is referred to as “running” of the coupling constant. At some scale  $\Lambda$ , for which  $\alpha_s$  is assumed to be known, the coupling constant is expressed (in leading order), as a function of the momentum transfer  $Q$ , via the relation

$$\alpha_s(Q) = \frac{12\pi}{(33 - 2n_f) \log \frac{Q^2}{\Lambda^2}}, \quad (2.10)$$

where  $n_f$  is the number of the quark flavours available at the scale  $Q$ . From 2.10 follows that the value of coupling constant for  $n_f \leq 16$  and large momentum transfer ( $Q \gg \Lambda$ ) is close to zero, in which case the quarks are asymptotically free. Figure 2.3 illustrates the running of the coupling constant showing a summary of measurements in various scales of momentum transfer ( $Q$  is in a range between 2 GeV up to almost 2000 GeV). A usual scale to give the value of  $\alpha_s$  is the mass of the  $Z$ -boson. The value of  $\alpha_s(M_Z^2)$  reported in Fig. 2.3 is estimated by a fit of independent measurements listed in the figure.

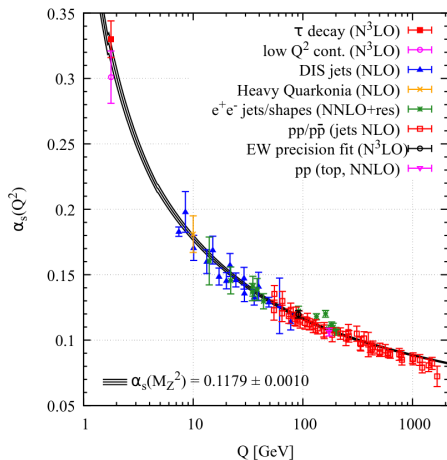


**Figure 2.3:** A summary of measurements of the strong coupling constant,  $\alpha_s$ , as a function of the energy scale  $Q$ . [11]

The value of the coupling constant is important for the calculation of cross-sections. To obtain solutions when interaction terms are introduced in the Lagrangian, it is necessary to use perturbation theory: If the interaction term is small, it is considered a perturbation of the free field case, and the solution can be written as a power series in the coupling. In both the theories discussed so far, the interaction term in the Lagrangian contains the coupling constant, and to apply perturbation theory, its value must be sufficiently small. However, from Eq.2.10 we see that  $\alpha_s$  increases for low values of  $Q$  and when  $Q$  is lower

than few MeV, the coupling constant becomes larger than one. In this case we can no longer use perturbation theory. For QCD, the perturbation theory can only be used in the regime of high energies where quarks are asymptotically free. Chapter 4, which will discuss the outcome of proton-proton collisions, will come back to the topic of perturbative and non-perturbative regimes of QCD. Before that, the review of the SM gauge theories will continue in the next section with the presentation of the gauge theory that describes the weak and electromagnetic interaction combined.

## 2.5 The Electroweak theory

Before their unified description by the *Electroweak theory* (EWK), the weak and electromagnetic interactions were considered separate. Initially only charged interactions were known from the experimental observations of particle decays. Besides changing the charge of the involved leptons and quarks by  $\pm 1$ , which hints at two charged mediators ( $W^\pm$ ), the charged interactions were also known to allow the transition between different quark flavors and violate parity: they involves only the *left-handed* component of the fermion field.

The right- and left-handed components occur by decomposing the fermion field using the chiral projection operators  $P_R = \frac{1}{2}(1 + \gamma^5)$  and  $P_L = \frac{1}{2}(1 - \gamma^5)$  respectively, as follows

$$\psi = (P_R + P_L)\psi = \underbrace{\frac{1}{2}(1 + \gamma^5)\psi}_{\psi_R} + \underbrace{\frac{1}{2}(1 - \gamma^5)\psi}_{\psi_L}.$$

Additionally, the strength of the coupling is found to be the same for all fermions. On the contrary, the neutral weak interaction that does not change the charge of the participating particles, couples to both left- and right-handed fermions, and the coupling strength depends on the charge of the fermions.

The gauge transformation for the weak charged interaction form the  $SU(2)_L$  symmetry group and are written as

$$\psi_L(x) \rightarrow \psi'_L(x) = e^{iga(x)\cdot\vec{\tau}}\psi_L(x), \quad (2.11)$$

where  $\vec{\tau}$  are the generators of the group, represented by the *Pauli matrices*,  $\vec{\tau} = \frac{1}{2}\vec{\sigma}$ , and  $g$  is the weak coupling. Another quantum number the *weak isospin*,  $I$ , needs to be introduced. All left-handed fermion fields are arranged into doublets of  $I = 1/2$  as follows

$$\begin{pmatrix} \nu_e \\ e^- \end{pmatrix}_L \quad \begin{pmatrix} \nu_\mu \\ \mu^- \end{pmatrix}_L \quad \begin{pmatrix} \nu_\tau \\ \tau^- \end{pmatrix}_L \quad \begin{pmatrix} u \\ d' \end{pmatrix}_L \quad \begin{pmatrix} c \\ s' \end{pmatrix}_L \quad \begin{pmatrix} t \\ b' \end{pmatrix}_L.$$

The upper member of each doublet has the third component of weak isospin,  $I_3$ , equal to  $+1/2$ , while the bottom member has  $I_3 = -1/2$ . The right-handed quarks and charged leptons form singlets with  $I = I_3 = 0$  that do not couple to the charged gauge bosons. It should be mentioned, here, that there are no experimental observations of right-handed neutrinos.

The weak interactions describe transitions within the doublets, and for quarks there are also transitions between generations. To explain these transitions the mass eigenstates,  $d, s, b$ , of the down-type quarks must not be the same as the weak eigenstates, marked as  $d', s', b'$ . The relation between them is given by the Cabibbo-Kobayasi-Maskawa (CKM) matrix[12, 13]

$$\begin{pmatrix} d' \\ s' \\ b' \end{pmatrix} = \begin{pmatrix} V_{ud} & V_{us} & V_{ub} \\ V_{cd} & V_{cs} & V_{cb} \\ V_{td} & V_{ts} & V_{tb} \end{pmatrix} \begin{pmatrix} d \\ s \\ b \end{pmatrix}.$$

The diagonal elements of the matrix correspond to transitions within the same generation and their absolute are very close to one.

The electromagnetic and weak interaction were unified in a single theory by Glashow, Salam and Weinberg [14, 15]. The gauge theory is based on the  $SU(2)_L \times U(1)_Y$  symmetry. The development of the theory follows the same steps as before: the Lagrangian is required to be invariant under a specific group of gauge transformations, leading to the introduction of gauge fields and the formulation of the covariant derivatives.

In the unified picture the *weak hypercharge*,  $Y$ , is introduced and is defined by the Gell-Mann-Nishijima relation [16, 17] as the linear combination of  $I_3$  and the electric charge,  $Q$ ,

$$Y = 2(I_3 + Q). \quad (2.12)$$

The invariance introduces three fields,  $W_\mu^i$ , for the  $SU(2)_L$ , the weak isospin group and one,  $B_\mu$ , for the hyper-charge group  $U(1)_Y$ . The corresponding field tensors are given as

$$W_{\mu\nu}^i = \partial_\mu W_\nu^i - \partial_\nu W_\mu^i - g\varepsilon_{ijk} W_\mu^j W_\nu^k$$

$$B_{\mu\nu} = \partial_\mu B_\nu - \partial_\nu B_\mu$$

The covariant derivative is formulated as

$$D_\mu = \partial_\mu + ig\vec{\tau} \cdot \vec{W}_\mu + i\frac{g'}{2}YB_\mu, \quad (2.13)$$

where  $g$  and  $g'$  are the coupling constants of  $SU(2)_L$  and  $U(1)_Y$  respectively. Writing the covariant derivative separately for left-handed fermion doublet and right-handed singlet states, the electroweak Lagrangian reads :

$$\begin{aligned} \mathcal{L}_{EWK} = & \sum_f \bar{\psi}_L^f \gamma^\mu \left[ i\partial_\mu + g\vec{\tau} \cdot \vec{W}_\mu + \frac{g'}{2} Y B_\mu \right] \psi_L^f + \sum_f \bar{\psi}_R^f \gamma^\mu \left[ i\partial_\mu + \frac{g'}{2} Y B_\mu \right] \psi_R^f + \\ & - \frac{1}{4} \vec{W}_{\mu\nu} \cdot \vec{W}^{\mu\nu} - \frac{1}{4} B_{\mu\nu} \cdot B^{\mu\nu}, \end{aligned}$$

where the index  $f$  in the sum runs for all fermions. The gauge invariance does not allow any mass terms for the gauge bosons. The short range of the interaction indicates massive bosons, and measurements showed masses for  $Z$  and  $W^\pm$  of the order of 100 GeV. The mechanism that gives masses to the gauge bosons is based on the notion of *spontaneous symmetry breaking* and will be discussed in the next section, completing the overview of the EWK interaction and the Standard Model.

## 2.6 Symmetry breaking and the Higgs mechanism

The Brout-Englert-Higgs Mechanism spontaneously breaks the  $SU(2)_L \times U(1)_Y$  symmetry to  $U(1)_{EM}$  and this way gives masses to the gauge bosons (and the fermions). This is accomplished by introducing two complex scalar fields  $\phi^0$  and  $\phi^+$  placed in an isospin doublet:

$$\phi = \begin{pmatrix} \phi^+ \\ \phi^0 \end{pmatrix} = \frac{1}{\sqrt{2}} \begin{pmatrix} \phi_1 + i\phi_2 \\ \phi_3 + i\phi_4 \end{pmatrix}.$$

The indices in the fields  $\phi^+$  and  $\phi^0$  indicate the electric charge, calculated from 2.12 replacing  $Y = 1$  and the corresponding  $I_3$  for each component of the doublet. The Lagrangian for this field reads:

$$\mathcal{L}_{\text{Higgs}} = (D^\mu \phi)^\dagger D_\mu \phi - V(\phi^\dagger \phi), \quad (2.14)$$

where  $D^\mu$  is the covariant derivative 2.13 and the potential  $V(\phi^\dagger \phi)$  is expressed as

$$V(\phi^\dagger \phi) = \mu^2 \phi^\dagger \phi + \lambda \left( \bar{\phi}^\dagger \phi \right)^2, \quad \lambda, \mu \in \mathbb{R}. \quad (2.15)$$

The choice of the parameters  $\mu^2$  and  $\lambda$  determines the shape of the potential. For the potential to have a finite minimum,  $\lambda$  must be positive, however, there

is no restriction for  $\mu^2$ , which can be either positive or negative. Positive values for  $\mu^2$  lead to a shape with a single minimum at  $\phi = 0$ . Choosing, instead  $\mu^2 < 0$ , leads to a local maximum for  $\phi = 0$  and an infinite set of degenerate minima that satisfy the relation  $\phi^\dagger\phi = \mu^2/2\lambda$ , and correspond to a circle around the origin.

By specifying the ground state the symmetry is spontaneously broken. The ground state for  $\phi^+ = 0$  can be written as

$$\langle\phi\rangle = \frac{1}{\sqrt{2}} \begin{pmatrix} 0 \\ v \end{pmatrix}, \quad v = \frac{2\mu}{\sqrt{\lambda}}.$$

The scalar field can be written as a small excitation of this ground state:

$$\phi(x) = \frac{1}{\sqrt{2}} \begin{pmatrix} 0 \\ v + h(x) \end{pmatrix}. \quad (2.16)$$

Replacing this expression of the scalar field in the potential 2.15 and subsequently in the Lagrangian 2.14 will lead to a Lagrangian that describes a massive scalar field and the massive gauge bosons. The mass terms result from the  $(D^\mu\phi)^\dagger D_\mu\phi$  term of the Lagrangian, and for the scalar field, identified as the Higgs boson, the mass is given by

$$m_H = \sqrt{2v^2\lambda}.$$

The observed vector boson fields  $A_\mu$ ,  $W_\mu^\pm$  and  $Z_\mu$  can be expressed in terms of  $W_\mu^i$  and  $B_\mu$  as follows:

$$A_\mu = W_\mu^3 \sin\theta_W + B_\mu \cos\theta_W,$$

$$Z_\mu = W_\mu^3 \cos\theta_W - B_\mu \sin\theta_W,$$

$$W_\mu^\pm = \frac{1}{\sqrt{2}} (W_\mu^1 \mp W_\mu^2),$$

where  $\theta_W$  is the Weinberg angle and is defined as:

$$\sin\theta_W = \frac{g'}{\sqrt{g^2 + g'^2}}.$$

The mass terms of the gauge bosons result from the Lagrangian, as well, and are

$$m_A = 0, \quad m_W = \frac{1}{2}vg, \quad m_Z = \frac{1}{2}v\sqrt{g^2 + g'^2}.$$

Finally, the electric charge,  $e$ , is connected with the coupling constants via the relation:

$$e = g \sin \theta_W = g' \cos \theta_W.$$

The spontaneous breaking of the symmetry also gives rise to the masses of fermions via their couplings to the Higgs scalar field, called *Yukawa couplings* which result by adding in the Lagrangian the terms

$$\mathcal{L} = -g_f (\bar{\psi}_L \phi \psi_R + \bar{\psi}_R \bar{\phi} \psi_L), \quad (2.17)$$

where  $\psi_L$  is the left-handed doublet and  $\psi_R$  is the right-handed singlet. Using 2.16 in the relation above, a mass term of the form  $-m\bar{\psi}\psi$  occurs when the coupling  $g_f$  is equal to  $\sqrt{2}m_f/v$ . Expanding the Lagrangian in this way, generates the masses only for the lower members of the isospin doublets. To generate the mass for the up-type quarks, instead of substituting 2.16 to 2.17, we use  $-i\sigma_2\phi^*$ . The mass terms of the gauge bosons and the fermions are proportional to the coupling of the respective particle to the Higgs field. Massive particles are expected to couple stronger to the Higgs and vice versa. The Higgs boson is observed experimentally indirectly by looking at its decay products. The probability for a particle to decay through a specific process is given by the so-called *branching ratio* (BR), which is the ratio of the decay width of a specific mode over the total decay width. For the Higgs boson, the expected branching ratios for various decay channels are shown in Figure 2.4 as a function of its mass.

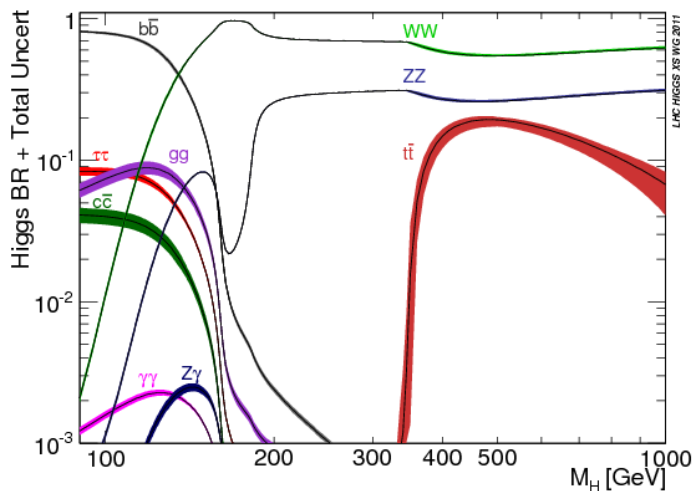


**Figure 2.4:** Branching ratios for the Higgs decay modes as a function of the boson mass [18]

The Higgs boson was discovered in 2012 by the ATLAS [19] and CMS [20] collaborations and the mass was found to be approximately 125 GeV. The main

decay channels used for the discovery were  $H \rightarrow ZZ$  and  $H \rightarrow \gamma\gamma$ . Despite their lower BR for  $m_H \approx 125 \text{ GeV}$ , these two channels produce relatively clean experimental signatures. In contrast, the decay channel  $H \rightarrow b\bar{b}$ , which has the highest BR, was observed for the first time in 2018 [21, 22] at the LHC. The main challenge was the large abundance of quarks produced from other processes -as will be discussed in Chapter 4- at hadron colliders.

This section concluded the overview of the Standard Model. The next, and final, section of this chapter contains a short overview of the currently open questions in the theory.

## 2.7 Open questions in the Standard Model

The Standard Model successfully describes the experimental observations and has been thoroughly tested and verified in the last decades with high precision measurements from various experiments. Despite its success, the theory has several limitations and does not explain several phenomena. The following paragraphs briefly review some of them.

As already discussed, the SM does not include gravity. The gravitational force can be neglected for scales up to the electroweak ( $O(100 \text{ GeV})$ ). At the Planck scale of approximately  $10^{19} \text{ GeV}$ , however, the strength of gravitational interaction is comparable to the other forces. It is unknown why there is a vast difference between the electroweak and the Planck scale. This problem is known as *the hierarchy problem*. An additional challenge is known as the *fine tuning*: for the Higgs mass to be approximately  $125 \text{ GeV}$  its bare mass must be of the order of the Planck mass to cancel out the quantum corrections.

Another open item is related to the number of light generations. Even though the existence of three light generations is experimentally confirmed, there is no explanation in the theory. Similarly, it is unknown why there is such a large discrepancy between the fermion masses. Also, within the SM, neutrinos are treated as massless, but neutrino oscillation experiments have confirmed non-vanishing values for the masses. The current upper limit is  $m_\nu < 1.1 \text{ eV}$  [23].

The origin of matter-antimatter asymmetry also has not a sufficient explanation in the SM. In the early days of the Universe, it is believed that matter and anti-matter were created on the same amount, however, today the Universe consists of mostly matter. The explanation of this evolution requires the violation of the  $CP$  combined symmetry. The SM accounts for only a small part of the required  $CP$ -violation.

Finally, astrophysical and cosmological observations indicate that about 5% of

the energy-mass content in the Universe is made of SM particles. Approximately 27% is a non-luminous matter of unknown origin called *dark matter*. The remaining almost 68% is the so-called *dark energy*, which is assumed to be a flow of energy that counteracts the gravitational pull, leading to the accelerated expansion of the universe observed today.

Explaining such phenomena requires the existence of yet undiscovered physics, commonly known as *new physics* or *physics beyond the Standard Model* (BSM). There are several classes of extensions to the Standard Model that provide answers to several of the listed open questions above. A theory, for example, that provides explanation to several of the open items listed above is known as *supersymmetry* (SUSY). This theory is an extension to the SM which introduces a new type of symmetry between fermions and bosons, and thereby doubles the particle content of the SM by assigning a super-partner to each particle. All fermions in the SM have boson super-partners which are collectively called *sfermions*. Likewise, the term *gauginos* is used to summarise the (fermion) super-partners of SM bosons. Gauginos mix to electrically neutral mass eigenstates, the *neutralinos*, and electrically charged states, the *charginos*. The next chapter will discuss the topic of possible dark matter candidates that are provided by a class of extensions to the SM with an extended the Higgs sector.



# Chapter 3

## Dark Matter

This chapter starts with a brief introduction to cosmology, in Section 3.1, which aims to present key concepts needed in this work. The following section, 3.2, overviews some of the astrophysical and cosmological observations that are explained with the existence of Dark Matter. The next section, 3.3, briefly presents some of the particle candidates for Dark Matter, and Section 3.4 summarises the main detection strategies for weakly interacting massive particles. The content of Section 3.1 is based on Ref. [24], while the text of section 3.3 is inspired by Ref. [25].

### 3.1 Key elements of cosmology

The current consensus in cosmology is that the history of the cosmos started with a “bang”, the *Big Bang*. According to this cosmological scenario all the known universe came into existence roughly 14 billion years ago, and at that time it was in a state of extremely high energy and pressure. To describe the evolution from that highly compressed state to the present date the cosmologists use the so-called *standard cosmological model*  $\Lambda$ CDM.

There are three main ingredients, for this model: the *Einstein equations* of general relativity, which relate the matter and energy content of the Universe to its geometry, the metric, describing the structure of spacetime, and the *equation of state* that specifies the physical properties of the matter and energy content.

It is possible to derive the Einstein equation almost from first principles with only few assumptions. The equation reads

$$R_{\mu\nu} - \frac{1}{2}g_{\mu\nu}R = -\frac{8\pi G_N}{c^4}T_{\mu\nu} + \Lambda g_{\mu\nu}, \quad (3.1)$$

where  $R_{\mu\nu}$  is the Ricci tensor and  $R = g_{\mu\nu}R^{\mu\nu}$  is the Ricci scalar,  $g_{\mu\nu}$  is the metric tensor,  $G_N$  is Newton's constant,  $T_{\mu\nu}$  is the energy-momentum tensor, and  $\Lambda$  is the so-called *cosmological constant*. The cosmological constant, in the Einstein equation represents a “vacuum energy” associated with space-time, creating in the absence of matter a gravitational field.

To solve Eq. 3.1 it is necessary to define the Universe's symmetry. The assumption of a homogeneous and isotropic Universe greatly simplifies the solutions, and is justified by many observations. These properties imply a specific form of metric, the line element of which is expressed as

$$ds^2 = -c dt^2 + a(t)^2 \left( \frac{dr^2}{1 - kr^2} + r^2 d\Omega^2 \right),$$

where  $a(t)$  is the so-called *scale factor*,  $k$  is a constant that describes the spatial curvature, and can take the values  $-1$ ,  $0$ , or  $+1$ . The value  $k = 0$  corresponds to Euclidean space. Solving the Einstein equation with this metric (and  $k = 0$ ), the  $\mu\nu = 00$  component is the Friedmann equation [26]

$$\left( \frac{\dot{a}}{a} \right)^2 + \frac{k}{a^2} = \frac{8\pi G_N}{3} \rho_{tot}, \quad (3.2)$$

where  $\rho_{tot}$  is the total average energy density of the universe, and includes  $\Lambda$ , as well as, the matter and radiation contributions. The first term of the left-hand side of the Friedmann equation is the so-called *Hubble parameter*

$$H(t) = \frac{\dot{a}(t)}{a(t)}.$$

The present value of the Hubble parameter is known as the *Hubble constant* and according to a recent measurement from Planck Collaboration, its value is  $H_0 = 67.4 \pm 0.5 \text{ km s}^{-1} \text{ Mpc}^{-1}$  [27]. As the Universe expands, the wavelength of the light emitted from distant galaxies is lengthened as it travels, leading to a cosmological redshift in the observed light. The redshift parameter  $z$  is defined by

$$1 + z \equiv \frac{\lambda_o}{\lambda_e}, \quad (3.3)$$

where  $\lambda_e$  is the emitted wavelength and  $\lambda_o$  is the observed wavelength. For the scale factor the relation to the red shift is shown [28] to be

$$1 + z = \frac{a(t_o)}{a(t_e)}, \quad (3.4)$$

where  $t_e$  and  $t_o$  are, respectively, the time of emission and observation. From Eq. 3.2, another quantity can be defined: the energy density of a flat Universe ( $k = 0$ ), called the *critical density*,  $\rho_c$ ,

$$\rho_c \equiv \frac{3H^2}{8\pi G_N}. \quad (3.5)$$

As a convention the abundance,  $\Omega_i$ , of a species,  $i$ , in the Universe is expressed in units of the critical density as

$$\Omega_i = \frac{\rho_i}{\rho_c}. \quad (3.6)$$

By defining

$$\Omega = \sum \Omega_i, \quad (3.7)$$

the Friedmann equation can be written as

$$\Omega - 1 = \frac{k}{H^2 a^2}. \quad (3.8)$$

From Eq. 3.8 follows that the value  $k$  takes determines whether  $\Omega$  is below, above or equal to one. The Universe is called *flat*, for  $\Omega = 1$ , *closed* for  $\Omega < 1$ , and *open* for  $\Omega > 1$ . The abundance of particle species evolves differently with time. The quantity  $\Omega_k = -\frac{k}{H^2 a^2}$  is defined at present time from Eq. 3.8 ( $\Omega + \Omega_k = 1$ ). Its value at an earlier time (using Eq. 3.4) is equal to  $\Omega_k(1+z)^2$ . The density,  $\Omega_M$ , of the matter content is diluted with the changing volume as the Universe expands, and scales as  $(1+z)^3$ . For radiation, it scales as  $(1+z)^4$ . For a general component with equation of state  $p_X = a_X \rho_X$ , the density scales as  $(1+z)^{3(1+a_X)}$ . Putting everything together leads to the following expression for the expansion rate as a function of the redshift

$$\frac{H^2(z)}{H_0^2} = \left[ \Omega_X(1+z)^{3(1+\alpha_X)} + \Omega_K(1+z)^2 + \Omega_M(1+z)^3 + \Omega_R(1+z)^4 \right]. \quad (3.9)$$

This equation is important because it allows us to extrapolate back in time, by measuring the abundance of each form of density in the present, approaching the Big Bang. The following paragraph contains a brief history of the Universe.

At a temperature of  $\sim 10^{16}$  GeV, also known as the Planck epoch, the Universe starts to be described by the Standard Model and the gauge symmetry  $SU(3)_C \times SU(2)_L \times U(1)_Y$ . The temperature of  $\sim 10^2$  GeV marks the era by the end of which the SM gauge symmetry breaks down to  $SU(3)_C \times U(1)_Q$ . Then, at  $T \sim 10^2 - 10^3$  GeV follows the so-called Dark Matter *freeze-out*, which is the period when the potential weakly interactive massive candidates for Dark

Matter *decoupled* from SM particles. For  $T \sim 0.3 \text{ GeV}$  the so called *QCD phase transition* takes place, in which quarks and gluons are confined into hadrons. The neutrino freeze-out occurs at  $T \sim 1 \text{ MeV}$ . The first light elements are formed at  $T \sim 100 \text{ keV}$  by the fusion of protons and neutrons in a procedure known as *Big Bang nucleosynthesis* (BBN). BBN puts some of the strongest constraints on the Big Bang theory, and its predictions agree remarkably well with the observed abundances. At  $T \sim 1 \text{ eV}$  the matter density becomes equal to the radiation density leading to structure formation. The *cosmic microwave background* (CMB) radiation, is produced by photon freeze-out at  $T \sim 0.4 \text{ eV}$ . Currently, the temperature of the Universe is roughly  $10^{-4} \text{ eV}$ ,

Before discussing the experimental evidence for the existence of Dark Matter, we need to define an important quantity that will be used often in the rest of this chapter, the *relic density*.

## Relic density

In the early Universe, when a particle species is in a state of thermal equilibrium, its creation and annihilation rates are in balance. This state is maintained as long as these reactions proceed more rapidly than the expansion rate of the Universe. As the temperature drops, the number density decreases because the available energy is not enough for particle production, while the annihilation continues. When the annihilation becomes much slower than the cosmic expansion rate, the comoving<sup>1</sup> number density of the particle species becomes stable, and the particle species *decouples*. This process is also known as the *freeze-out*, while the temperature at which it takes place is called *freeze-out temperature*. The density abundance of a thermal relic is known as the *relic density*. The following paragraphs are going to discuss an expression for the relic density, for non-relativistic particles, because the  $\Lambda$ CDM model, is based on the assumption of cold, non-relativistic, Dark Matter.

For non-relativistic particles, the relic density can be derived from the Boltzmann equation, which describes the evolution of the number density  $n_x$ , from the initial state of thermal equilibrium,

$$\frac{dn_x}{dt} = -\langle\sigma v\rangle (n_x^2 - n_x^{eq2}) - 3Hn_x, \quad (3.10)$$

where  $H$  is the Hubble parameter,  $n_x^{eq}$  is the particle number density at the equilibrium,  $\sigma$  is the annihilation cross section,  $v$  is the relative velocity of the annihilating particles and the angle brackets denote thermal average.

---

<sup>1</sup>moving relative to the expansion of the Universe

To derive the expression for the relic density the Boltzmann equation is solved in two regimes, long before and long after the freeze-out, and the expression of the relic density is obtained by requiring the two solutions to match. The expression for the relic density can approximately be written as

$$\Omega_X h^2 \approx \frac{3 \times 10^{-27} \text{ cm}^3 \text{ s}^{-1}}{\langle \sigma v \rangle}, \quad (3.11)$$

where  $h = H_0/100 \text{ km s}^{-1} \text{ Mpc}^{-1}$  is the scaled Hubble constant. This equation shows that the annihilation cross section at the time of freeze-out of a particle species determines its relic density. In fact, these two quantities are inversely proportional. Figure 3.1 shows the comoving number density as a function of the parameter  $x = m/T$ , where  $m$  is the mass of the particles and  $T$  the temperature. The density drops until the freeze-out is reached, and then, remains constant.

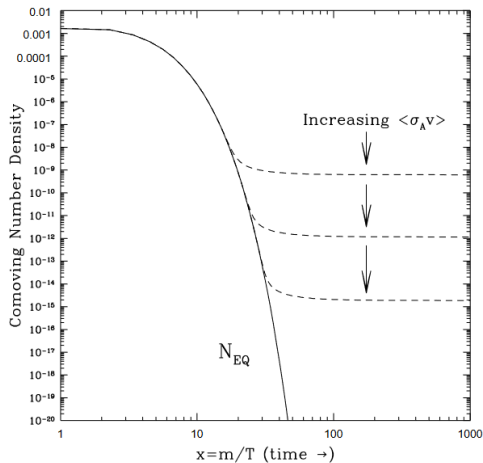


**Figure 3.1:** Evolution of the comoving number density and freeze-out as a function of the mass over the temperature. Figure from Ref.[28]

For lower values of the annihilation rate the freeze-out is reached sooner and the relic abundance is higher. The approximate result of Eq. 3.11 holds only under a series of simplifications and assumptions, which are discussed in greater detail in References [29, 24], together with more complex scenarios that can significantly change this expression.

## 3.2 Evidence of Dark Matter

This section reviews only some of the various cosmological observations, which span a wide range of scales and offer compelling evidence for the existence of Dark Matter.

One evidence for the existence of Dark Matter comes from studying the velocity distribution of stars orbiting the galaxy. Using Newtonian dynamics the orbital velocity of the stars can be written as a function of their distance from the galactic centre,

$$u(r) = \frac{G_N M(r)}{r}, \quad M(r) = 4\pi \int \rho(r) r^2 dr \quad (3.12)$$

where  $G_N$  is the gravitational constant, and  $\rho(r)$  the mass density profile. Based on Eq. 3.12, the velocities should decrease as  $\propto 1/\sqrt{r}$ , at distances larger than the galaxy's visible disk radius. However, experimental observations, such as the one shown in Figure 3.2 for galaxy NGC 6503 [30], rarely display this (expected) behaviour. Instead, the data distribution is flat at large distances, even much larger than the radius of the visible disk. To describe the data points accurately, besides the disk and gas profiles, we need to consider an additional source of mass, in the form of a halo of non-luminous matter with mass  $M(r) \propto r$ , and density profile  $\rho(r) \propto 1/r^2$ .

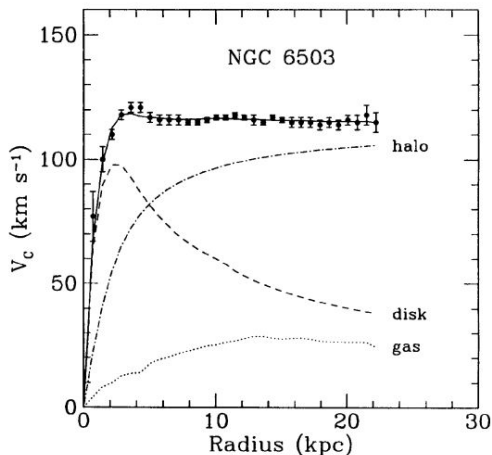


**Figure 3.2:** Rotation Curve of Galaxy NGC 6503. The measured data points are presented along with the contributions from disk, gas and the Dark Matter halo, which need to be added to describe the data. Figure taken from [30]

Other indications for Dark Matter come from *gravitational lensing*. In this phenomenon, the light emitted from a luminous object is deflected by spacetime

distortions, created from a huge amount of mass between the source and the observer. By measuring the distortions in the observed images, the masses of astronomical objects, like galaxy clusters, can be inferred. The main advantage of this method is that it does not require any knowledge of the dynamical state or composition of the interfering mass structures.

The observation of the galaxy cluster 1E 0657-558, commonly referred to as the “bullet cluster”, provides one of the most spectacular pieces of evidence for Dark Matter. Figure 3.3a shows an optical image of the cluster, while Figure 3.3b is an X-ray image of the hot gas in the cluster. The cluster was created from the collision of two large clusters of galaxies. During the collision, the galaxies separated into two sub-clusters, as the probability of individual galaxies to collide is small. On the other hand, the two clouds of X-ray emitting hot gas from each of the clusters interact, and as they pass through each other are slowed down by a drag force similar to air resistance. As a result the hot gas clouds spatially decouple from the galaxies. The green contours that are superimposed in both pictures of Fig. 3.3 correspond to the mass density distribution of the cluster reconstructed from weak gravitational lensing. The contours clearly show a shift with respect to the dominant component of visible mass, which is the X-ray emitting hot gas. The separation between the gas and the regions of high mass density suggests the presence of an additional non-luminous and collision-less source of matter.

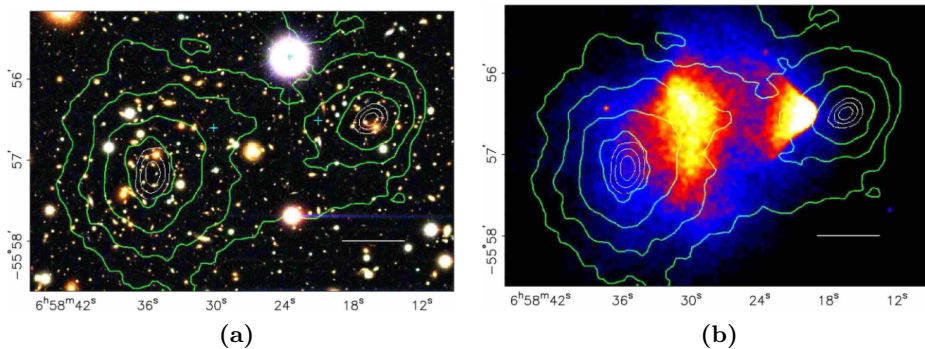


**Figure 3.3:** Optical (left) and X-ray(right) images of the galaxy cluster 1E0657-558, or Bullet Cluster, obtained with the Magellan telescopes (Las Campanas observatory, Chile) and Chandra satellite respectively. In both images the overlaid green contours map out the gravitational potential obtained from gravitational lensing and show the offsets between the distribution of baryons and that of the reconstructed gravitational field. Figures taken from Ref. [31]

The experimental observations presented above, despite providing evidence for

the existence of Dark Matter, do not offer a way to estimate the total amount of DM. The relic abundance of DM, and other cosmological parameters, can be extracted from the analysis of the Cosmic Microwave Background (CMB) spectrum. As mentioned earlier in Sec. 3.1, CMB was produced by photon freeze-out. After the photons decoupled, they travelled freely through spacetime leaving a snapshot of the Universe, when it was approximately 380000 years old. At the present day, these photons reached microwave frequencies, and CMB appears as black body radiation with a temperature of  $\sim 2.7255$  K [32]. The most recent CMB sky map from the Planck satellite is shown in Figure 3.4. The spectrum is overall isotropic except for tiny temperature fluctuations of

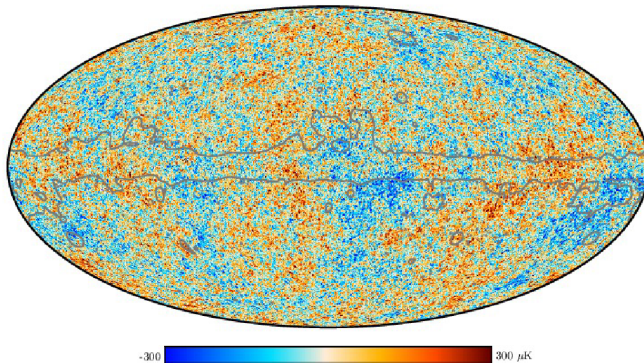


**Figure 3.4:** Cosmic microwave background (CMB) as observed by Planck. The grey lines map out a region masked in the analysis because it lies mostly around the Galactic plane, where there are sizeable residuals from foreground emission. Figure taken from Ref. [33]

the order of  $10^{-5}$  K. These fluctuations are used to constrain the cosmological parameters. They are parametrised as the expansion of spherical harmonics,

$$\frac{\delta T}{T}(\theta, \varphi) = \sum_{l=2}^{\infty} \sum_{m=-l}^l a_{lm} Y_{lm}(\theta, \varphi),$$

where  $a_{lm}$  are the multipole coefficients. The parameter constraints are obtained by fitting an N-dimensional model (where N is the number of parameters) to the spectrum and extracting the best-fit values. Figure 3.5 shows the most recent measurement, again by the Planck Collaboration [34], of the power spectrum of the temperature fluctuations as a function of the *multipole moment*,  $l$ , which is related to the angular scale,  $\phi \sim \pi/l$ . The figure also shows the best fit model. The measured spectrum consists of several peaks originating from acoustic waves in the baryon-photon fluid before the photon decoupling. These oscillations result from two competing effects: gravity and photon radiative pressure. Baryons

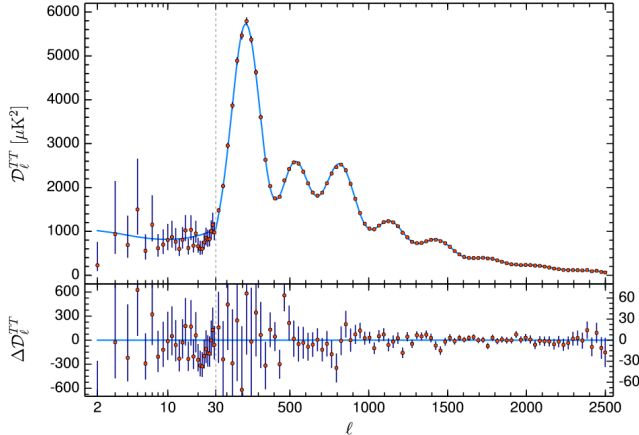


**Figure 3.5:** Power spectrum of temperature fluctuations in the Cosmic Microwave Background. Figure taken from [34]

tend to form clusters of matter that create gravitational wells that pull the baryon-photon liquid, compressing it and increasing its temperature. The matter accumulation and consequent compression of the baryon-photon fluid are slowed by the increasing photon radiative pressure, which eventually expands the fluid, cooling it and erasing temperature anisotropies. The position, relative height and shape of the peaks in the multipole expansion are used to infer the values of the cosmological parameters. The position of the first peak, for example, is sensitive to  $\Omega_K$  and, to some extent, the amount of Dark energy. The shape of the spectrum is determined by the densities of baryonic and Dark Matter, which are found to be

$$\Omega_b h^2 = 0.02337 \pm 0.00015 \text{ and } \Omega_c h^2 = 0.1200 \pm 0.0012$$

respectively, by the Planck collaboration [27].

This section reviewed only a few of the observations that seem to confirm the CDM model, which postulates DM is responsible for all these gravitational effects. Other models, instead of introducing new matter in the Universe, suggest that modifying the gravitational laws at large scales could explain several of the observed phenomena. These models, however, do not explain all the observations. DM, is the only solution that explains all the observations consistently, even though no particle candidate has been detected yet.

### 3.3 Candidates for Dark Matter

The experimental observations and the study of structure formation of the Universe put constraints on the nature of the DM particle candidates. For a new particle to be a suitable DM candidate, besides being able to be experimentally probed, it must be neutral, stable and have the right mass abundance to yield the observed relic density. Moreover, to explain the formation of galaxies, DM must be *cold* (non-relativistic)<sup>2</sup> during the time of decoupling.

A potential DM candidate among the fundamental particles of the SM appears to be the neutrino. Besides being neutral, the neutrinos have a non-vanishing mass and interact only weakly with the other SM particles. They do not comply, however, with the rest of the requirements, being relativistic particles with too small abundance to account for the total Dark Matter mass in the Universe. The upper bound on neutrino abundance, according to Planck [33], is  $\Omega_\nu h^2 \lesssim 6 \cdot 10^{-4}$ , while the upper bound of neutrino masses, estimated from a combination of cosmological observations and particle physics experiments, is  $\sum_i m_{\nu_i} < 0.264$  eV, and the corresponding abundance is  $\Omega_\nu h^2 \lesssim 0.00285$  [35]. These abundance values are too small for neutrinos to be the dominant component of DM.

Another particle suggested as a viable DM candidate was the *sterile neutrino* (right-handed neutrinos) [36]. They do not interact with SM particles except left-handed neutrinos, with which they are allowed to mix. Sterile neutrinos overcome the constraints that ruled out the SM neutrinos as viable DM candidates. Their mass is expected in the keV range, and there are many constraints on the mass and mixing angle, leaving only a limited phase-space range available for future search [37].

One more possible candidate for DM is the *axion*, originally proposed [38] to provide a solution to the *strong CP problem*<sup>3</sup>. The authors of Ref. [38] postulated the existence of a new global  $U(1)$  symmetry which is spontaneously broken at some scale,  $f_a$ . This mechanism leads to a new boson, the axion [39, 40], which is expected to have very weak interactions with SM particles.

One of the most popular and studied candidates for DM are the *Weakly Interactive Massive Particles* (WIMPs), often denoted as  $\chi$ . WIMPs are found in many BSM theories, fulfil all the requirements discussed at the beginning of this section, and can be detected in many ways, that will be discussed in the next section. They have masses ranging between few GeV to few TeV [29, 41], and cross-sections at the electroweak scale. If WIMPs are produced thermally in

---

<sup>2</sup>The term *hot* describes relativistic DM particles, while *warm* refers to intermediate states.

<sup>3</sup>In principle CP violation is allowed in strong interactions, but this is not observed in Nature.

the early universe, their relic density after freeze-out is calculated as described in 3.1 (Eq. 3.11). For a WIMP candidate with mass in the allowed range that interacts only weakly with the SM particles, its estimated relic density matches the one observed. This is known as the *WIMP miracle* and is one of the reasons why WIMPs are so widely searched for.

Many BSM theories predict new particles that can be identified as WIMPs. SUSY models are usually among the most popular. A notable example is the lightest supersymmetric particle (LSP) predicted by the minimal supersymmetric Standard Model (MSSM). The LSP is a Dark Matter candidate because it can not decay due to the conservation of the so-called  $R$ -parity. The  $R$ -parity enforces the baryon number conservation in the theory and prevents proton decay, and is defined as  $PR = (-1)^R$ . The quantum number  $R$  is given by  $3(B - L) + 2S$ , where  $B$  denotes the baryon number,  $L$  the lepton number, and  $S$  the spin. Thereby, SM particles have  $R$ -parity equal to 1 and supersymmetric  $-1$ . There are two sparticles that could be viable candidates, the sneutrino and the neutralino, however, the first has been already ruled out by experiments.

There are many theories that introduce particles that satisfy the requirements listed in the beginning of this section, and the candidates briefly reviewed here correspond only to a subset of those. In the following sections and chapters (including the data analysis for the DM search presented in this thesis) a generic WIMP candidate is considered.

### 3.4 WIMP searches

There are three general classes of experiments searching for WIMPs, that are based on different detection techniques: the direct detection experiments that measure the elastic scattering of DM with nuclei in a target volume, the indirect detection experiments that look for the products of WIMP pair annihilation, and the collider searches where the production of WIMP pairs would be probed as a signal of missing transverse momentum. Figure 3.6 illustrates the different approaches. All the search strategies mentioned above aim to detect interactions between SM and DM and are complementary. The direct and indirect detection experiments can establish the galactic origin of a WIMP signal but have limited sensitivity to the details of the interaction. On the contrary, collider searches are sensitive to the details of the interaction between Dark Matter and SM particles. However, they can not probe the lifetime of the DM particles when it exceeds the time required for the DM particles to exit the detector [42]. In 3.4.1 and 3.4.2 there is a brief overview of the general techniques for direct and indirect searches respectively. This section will close with a presentation of the

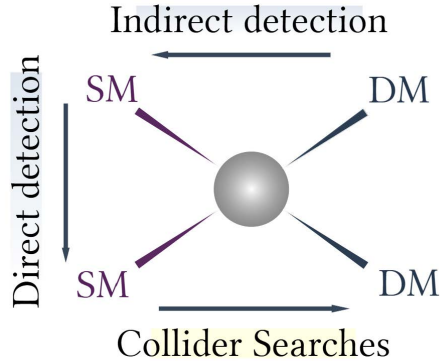


**Figure 3.6:** Illustration of the DM search strategies. The arrows denote the time axis of the diagram for each of the strategies, while the circle in the middle represents a generic coupling between SM and DM particles.

collider searches in 3.4.3 with a focus on the DM search program in the ATLAS experiment.

### 3.4.1 Direct Searches

Direct detection experiments look for events produced by WIMPs from the Milky Way’s Dark Matter halo. From the experimental observations of the rotation curves, it is known that WIMPs are gravitationally trapped within galaxies. As the Milky Way rotates and crosses the DM halo, which does not rotate, it generates a wind of WIMPs that flows in the opposite direction relative to the solar system motion, as seen by an observer on Earth.

The mean velocity in the region of the solar system with respect to the centre of the Milky Way is of the order of  $\sim 100$  km/s. Due to these velocities, the primary signal is nuclear recoils. The elastic recoil energies of the nuclei depend on the WIMP mass and range from 1 keV to 100 keV for WIMPs with masses in the range between 10 GeV to 10 TeV.

The interaction rate depends on the number of target nuclei in the detector volume and the product of the interaction cross section and the local WIMP flux. The ratio of the detector mass over the atomic mass of the nucleus gives the number of target nuclei in the detector volume. The flux is linked to the local density of Dark Matter,  $\rho_{\text{DM}}$ , the mean WIMP circular velocity,  $v_c$ , the galactic escape velocity  $v_{\text{esc}}$ , and the WIMP mass,  $m_\chi$ . The typical values in direct detection experiments for  $v_c$  is 220 km/s, for  $v_{\text{esc}}$  is 544 km/s, while  $\rho_{\text{DM}}$  is assumed to be  $0.3 \text{ GeV}/\text{cm}^3$  [43]. The remaining free parameters, after these assumptions, are the WIMP-nucleon interaction cross-section and the WIMP

mass. Therefore, the exclusion limits are plotted as contours in the plane of these two variables.

The nuclear recoils are studied via the detection of scintillation light, phonons or ionisation charge. Typically two of those techniques are used at the same time to achieve discrimination against backgrounds such as electron recoil, exploiting the different energy releases between nuclear and electron recoil. These experiments require, in general, a very low background environment. For this reason, they are placed in deep underground laboratories to suppress any background from cosmic radiation and are shielded against radioactivity from the rocks.

Their sensitivity depends on the WIMP mass: the best performance is reached for  $m_\chi$  close to the nucleus mass. On the contrary, the sensitivity decreases for small WIMP masses because, in this case, there is not any detectable recoil of the nucleus. The sensitivity will also decrease at high DM masses because the WIMP flux scales as  $1/m_\chi$ .

There are many direct detection experiments, each using different technologies depending on whether they target higher sensitivity to small cross-sections or small masses. Some of the those are the XENON1T [44], LUX [45], PandaX-II [46], DEAP-3600 [47], DarkSide-50 [48], CRESST-II [49], SuperCDMS [50], CDMSlite [51] and the DAMA/LIBRA [52] experiment. The DAMA/LIBRA has reported positive results which are, however, contradicted by the resulting exclusion limits obtained from other experiments. A detailed review of the direct searches for Dark Matter can be found in Ref. [53] and [43].

### 3.4.2 Indirect Searches

Indirect experiments aim to observe the annihilation products of WIMPs, such as gamma rays, neutrinos, positrons, anti-protons or anti-nuclei, by looking for excesses in the flux of gamma rays, neutrinos, or cosmic rays. These experiments complement the direct search efforts, as they are sensitive to the signatures of Dark Matter decay and they can probe low-velocity DM particles. Low-velocity WIMPs can be gravitationally captured in regions like the galaxy centre, the Sun or the Earth. Due to their high density in these objects, WIMP pair annihilation is more likely to occur.

While most annihilation products are immediately absorbed, neutrinos can traverse a large amount of matter without interacting. Some of the produced neutrinos interact in the Earth, resulting in upwards going muons, which can be detected in neutrino telescopes such as IceCube [54]. Neutrino telescopes are looking for annihilation that took place in the Sun or the Earth, with the primary background consisting of neutrinos produced in cosmic ray interactions

in the atmosphere of the Sun. On the contrary, searches for gamma-ray emission focus on dwarf spheroidal galaxies, which are assumed to be satellites of the Milky Way. In these cases, the potential signal manifests as a nearly mono-energetic line in the spectrum, with an energy close to the WIMP mass and a width proportional to the Dark Matter velocity.

There is a variety of indirect detection experiments, each using different detection techniques depending on the channel they use. Dedicated to probing the gamma-ray spectrum for WIMPs are the Fermi Large Area Telescope (LAT)[55], a space observatory, and the ground-based facilities HESS [56], MAGIC [57], VERITAS [58], and HAWC [59]. The Fermi LAT reported the observation of an excess in the gamma-ray flux from the galactic centre at energies of a few GeV. There were interpretations that suggested the excess was compatible with a potential signal [60, 61], however, other possible interpretations contest this claim [62]. Another space experiment looking for indirect detection is the Alpha Magnetic Spectrometer (AMS) [63], which is mounted on the International Space station. Detailed reviews of indirect DM experiments can be found in Ref. [64].

### 3.4.3 Collider Searches

Collider searches aim to detect signals of DM particles produced in SM particle collisions in a controlled environment. WIMPs produced in such collisions will be able to cross the detector surrounding the interaction point without producing any signal since they are stable and interact feebly with SM particles. Unless there is some additional activity in the event, it would be impossible to detect DM.

When DM is produced together with one or more SM particles, its presence can be inferred using momentum conservation in the plane transverse to the colliding beams: the net transverse momentum before the collision is zero and must also be zero after. Any imbalance in this plane, obtained from the negative vector sum of the transverse momenta of all detected particles, can be a hint of DM. The experimental signature, in this case, is a large amount of missing transverse momentum due to the escaping WIMP pair, and an object with high- $p_T$ , and is known as “ $E_T^{\text{miss}} + X$ ”. The interaction between SM and DM particles is assumed, typically, to involve a spin-1 or spin-0 mediator, and  $X$  can be a photon, a jet, a heavy boson or even a Higgs boson. In the ATLAS and CMS experiments, there is a variety of “ $E_T^{\text{miss}} + X$ ” searches carried out:

- $E_T^{\text{miss}} + \text{jets}$ . These searches [65, 66] consider final states with one or more jets originating from initial state radiation (will be explained in Chap.

4) and large amount of missing transverse momentum. The  $E_T^{\text{miss}} + \text{jets}$  search is one of the most inclusive, being sensitive to a large number of WIMP production scenarios, due to the large cross section to produce an initial state radiation jet at hadron colliders.

- $E_T^{\text{miss}} + \text{weak vector boson}$ . Here, the Dark Matter particles are produced along with a vector boson. These searches investigate either leptonic decay modes of the produced boson [67, 68] which benefit from a clean signature, or hadronic decay modes [69, 70] that are characterised from larger branching ratio compared to the leptonic channels. The search described in Ref. [67] also probes the invisible decay of the Higgs boson, as another test of the WIMP hypothesis.
- $E_T^{\text{miss}} + \text{photon}$ . The main advantage of these searches [71, 72] is the very clean signatures of  $E_T^{\text{miss}}$  and high-energetic photon. In this search, the much lower backgrounds compared to  $E_T^{\text{miss}} + \text{jets}$  compensate for the smaller production cross-section of an initial state radiation photon.
- $E_T^{\text{miss}} + \text{SM Higgs boson}$ . These searches tag the presence of DM by requiring a Higgs boson in the final state. They focus on different decay modes of the Higgs boson: the decay to  $b$ -quarks has the highest branching ratio, while the decay to two photons is a very clean channel (see 2.6) [73]. CMS searches explore a combination of  $h \rightarrow \tau^\pm \tau^\mp$  and  $h \rightarrow \gamma\gamma$  channels.

There is an important difference between  $E_T^{\text{miss}} + \text{SM Higgs}$  searches and the other mentioned above: it is highly unlikely for a Higgs boson to be produced from initial state radiation, due to its small Yukawa coupling to the quarks. As a result, in the case of a positive signal, this search would provide insights on the interaction between SM and DM.

Besides the  $E_T^{\text{miss}} + X$  searches, another approach is searching for the visible decays of the mediators. If such a mediator exists and is produced in SM particle collisions, it can also decay back into SM particles, such as quarks, gluons or leptons. The experimental signature is a narrow excess (resonance) on the otherwise smoothly falling background distribution of the invariant mass of the two jets (dijet) [74, 75] or leptons (dilepton) [76, 77] with the highest momentum.

So far, there have been no claims of discovery of DM particles from collider searches. In the absence of positive results, these searches, instead, set limits on the DM couplings and mediators masses.

## 3.5 Simplified models for the $E_{\text{T}}^{\text{miss}} + H(b\bar{b})$ search for Dark Matter

Subsection 3.5.1 contains a brief overview of the two simplified models that are used to interpret the results of the data analysis presented in this thesis, while 3.5.2 overviews the two mediator Dark Matter model, which is used for the reinterpretation studies presented in Chapter 13. The contents of 3.5.1 are largely inspired from References [78, 79].

### 3.5.1 Two-Higgs-Doublet extensions to Standard Model

So far, all the experimental measurements of the Higgs-boson are in agreement with the SM predictions. However, as discussed in 2.7, the choice to introduce only one isospin doublet of scalar fields in the spontaneous symmetry breaking mechanism (discussed in 2.6) was not theoretically well-motivated. There are different ways to extend the Higgs sector, the simplest is to introduce two complex isospin doublets of scalar fields,  $\phi_1, \phi_2$ , with  $Y = 1$  and  $I = 1/2$ . This scenario is known as the *Two Higgs Doublet Model* (2HDM)[80].

This model is restricted by two experimental constraints. The first one comes from electroweak precision measurements and it is related to the parameter  $\rho$  which is defined as

$$\rho = \frac{\sum_{i=1}^n [I_i(I_i + 1) - \frac{1}{4}Y_i^2] v_i}{\sum_{i=1}^n \frac{1}{2}Y_i^2 v_i} = \frac{m_W}{m_Z \cos \theta_W}, \quad (3.13)$$

where  $n$  is the number of Higgs multiplets,  $I_i$ , is the weak isospin,  $Y_i$  the hypercharge, and  $v_i$  is the vacuum expectation value of the  $i$ -th doublet [80]. Equation 3.13 stands also for scalar singlets, triplets or other multiplets that have different values of weak isospin and hypercharge. The value of  $\rho$  is found to be  $\approx 1$  from precision measurements of the  $m_W$  and  $m_Z$ . This condition must also be met for the Higgs doubles in this model.

The second constraint comes from the fact that no flavour-changing neutral currents (FCNC) are observed. Even though such current can occur in the 2HDM model, they can be avoided by making suitable choice of the Higgs-fermion couplings (given by eq. 2.17). Based on the Paschos-Glashow-Weinberg theorem, these currents are absent when all right-handed fermions of a given charge couple only to a single Higgs doublet

The two models used to interpret the results of the data analysis presented in this thesis, are based on the 2HDM model, specifically the so-called Type II

2HDM model. In this type, the CP symmetry is conserved in the Higgs sector, while up-type quarks couple only to one Higgs doublet, which by convention is  $\phi_1$ , and down-type quarks and charged leptons to  $\phi_2$ .

The potential is given by

$$\begin{aligned}
V_H = & \mu_1 \phi_1^\dagger \phi_1 + \mu_2 \phi_2^\dagger \phi_2 + \left( \mu_3 \phi_1^\dagger \phi_2 + \text{h.c.} \right) \\
& + \lambda_1 \left( \phi_1^\dagger \phi_1 \right)^2 + \lambda_2 \left( \phi_2^\dagger \phi_2 \right)^2 + \lambda_3 \left( \phi_1^\dagger \phi_1 \right) \left( \phi_2^\dagger \phi_2 \right) \\
& + \lambda_4 \left( \phi_1^\dagger \phi_2 \right) \left( \phi_2^\dagger \phi_1 \right) + \left[ \lambda_5 \left( \phi_1^\dagger \phi_2 \right)^2 + \text{h.c.} \right],
\end{aligned} \tag{3.14}$$

where  $\mu_i, i = 1, 2, 3$  and  $\lambda_i, i = 1, \dots, 5$  are free parameters. The potential  $V_H$  contains the two Higgs doublets terms in the same form as in Equation 2.15 for the SM Higgs potential. The parameters  $\lambda_i$  are restricted by the requirements that the 2HDM potential has a stable minimum and does not diverge to minus infinity. The Higgs doublets have vacuum expectation values

$$\langle \phi_i \rangle = \left( 0, v_i / \sqrt{2} \right),$$

where  $i = 1, 2$  and  $v = \sqrt{v_1^2 + v_2^2} \approx 246$  GeV, in order to reproduce the  $W$  and  $Z$  boson masses as in the SM. The ratio of  $v_2$  and  $v_1$  defines the parameter  $\tan \beta = v_2 / v_1$ . In the 2HDM model, there are eight scalar fields. Three of these give masses to the  $Z$  and  $W$  boson, and the other five correspond to physical Higgs bosons. There are two physical CP-even (scalar) electrically neutral states,  $h$  and  $H$ , one CP-odd (pseudo-scalar),  $A$ , and two electrically charged states,  $H^\pm$ .

The SM Higgs boson is given by

$$H^{SM} = h \sin(\beta - \alpha) - H \cos(\beta - \alpha).$$

From the above follows that in the limit  $\cos(\beta - \alpha) \approx 0$ , known as the *alignment limit*, the boson  $h$  is identical to the SM Higgs boson. In Ref [81], the measurements of the Higgs boson couplings restrict the available parameter space for  $\tan \beta$  and  $\cos(\beta - \alpha)$ , allowing for arbitrary values of  $\tan \beta$  only in the region around the alignment limit, as seen in Figure 3.7. Also, there is a lower bound on  $\tan \beta$  of  $\sim 0.3$  obtained by requiring the Yukawa coupling of the top-quark to be perturbative [80]. In both 2HDM based models reviewed in this section, the alignment limit  $\cos(\beta - \alpha) = 0$  is assumed. The masses of the Higgs bosons, the mixing angles and  $v$  can be obtained from the parameters  $\mu_i$  and  $\lambda_i$ . Usually models based on 2HDM are parameterised using the parameters:  $v, m_h, m_H, m_A, m_{H^\pm}, \cos(\beta - \alpha), \tan \beta, \lambda_3$ .

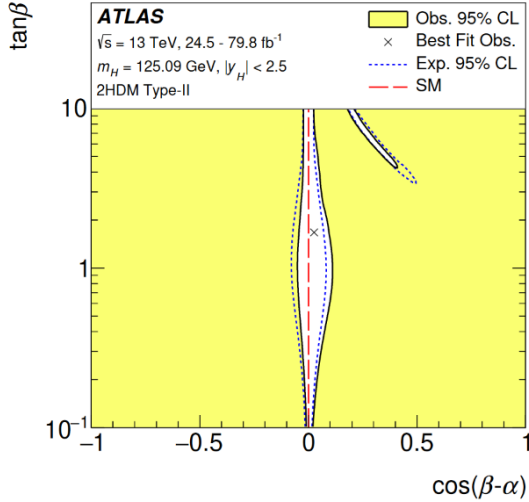


**Figure 3.7:** The excluded region (yellow) in  $(\tan\beta, \cos(\beta - \alpha))$  plane for type II 2HDM. Figure taken from Ref.[81]

The following paragraphs will review two different models complemented by a DM mediator sector. The Dark Matter particles,  $\chi$ , in both cases are assumed to be Dirac fermions. A new  $\mathbb{Z}_2$  symmetry is introduced to guarantee the stability of the DM. The DM particles transform under the  $\mathbb{Z}_2$  symmetry as  $\chi \rightarrow -\chi$  [82, 83]. The corresponding quantum number must be conserved at each interaction vertex, as a result, DM particles can only be produced in pairs and they can not decay into other particles [84].

### $Z'$ -2HDM model

The  $Z'$ -2HDM [85] is a simplified model with an additional DM sector based on the  $U(1)_{Z'}$  symmetry which gives rise to a  $Z'$  boson. This additional spin-1 mediator can mix with the  $Z$  boson.

The process of interest for this search is illustrated in the Feynman diagram shown in 3.8. Here, a  $Z'$  boson is produced resonantly and then decays into the  $H$  boson and the CP-odd boson  $A$ . The latter subsequently decays to a pair Dark Matter particles, due to its large branching fraction to DM. The additional parameters introduced in this model are the mass of the  $Z'$  boson,  $m_{Z'}$ , its coupling strength  $g_{Z'}$ , and the DM particle mass,  $m_\chi$ .

Due to the mixing with the  $Z$ -boson, the constraint  $\rho \approx 1$  implies an upper limit

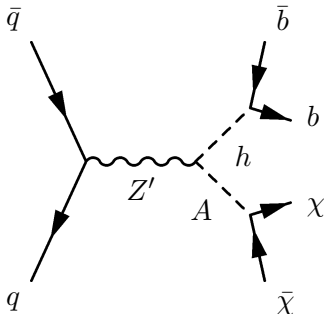


**Figure 3.8:**  $Z'2HDM$  model Feynman diagram

on the universal coupling strength of the  $Z'$ -boson,  $g_{Z'}$ .

## 2HDM+a model

In the  $2HDM + a$  [82, 86] simplified model the pseudo scalar mediator,  $P$ , couples to DM via the interaction

$$\mathcal{L}_\chi = -ig_\chi P \bar{\chi} \gamma_5 \chi$$

where  $g_\chi$  is the dark-sector Yukawa coupling. A general scalar potential for the  $2HDM + a$  can be written as

$$V = V_H + V_{HP} + V_P,$$

where  $V_H$  is the potential described by Eq. 3.14,  $V_{HP}$  describes the potential relating the Higgs doublets  $\phi_1$  and  $\phi_2$  with the pseudo-scalar mediator  $P$  and  $V_P = \frac{1}{2}m_P^2 P^2$  is the free potential term for  $P$ .

The potential  $V_{HP}$  can be written as

$$V_{HP} = P \left( ib_P \phi_1^\dagger \phi_2 + \text{h.c.} \right) + P^2 \left( \lambda_{P_1} \phi_1^\dagger \phi_1 + \lambda_{P_2} \phi_2^\dagger \phi_2 \right), \quad (3.15)$$

where  $m_P$  is the pseudo-scalar mass parameter,  $b_P, \lambda_{P_1}, \lambda_{P_2}$  are the *portal* and *quartic* couplings. The physically observable mediator in this model is not  $P$  but a mixture of  $P$  and the CP-odd state  $A$  in the extended Higgs sector. The resulting state is the pseudo-scalar mediator  $a$ . The corresponding mixing angle is denoted as  $\theta$ .

In this model the production mechanisms relevant for this work are illustrated in Figure 3.9 by two representative Feynman diagrams. In both cases  $A$  is resonantly produced and decays into  $h$  and  $a$ . The later subsequently decays into DM particles while  $h$  decays into a  $b\bar{b}$  pair. In the left diagram of Fig.

3.9, the mediator  $A$  is produced via gluon-gluon fusion ( $ggF$ ), while in the right diagram  $A$  is produced from the annihilation of a  $b\bar{b}$  pair. The pairs of  $b$ -quarks, on the right diagram, are produced via gluon splitting  $g \rightarrow b\bar{b}$ , leading to signatures with two additional  $b$ -quarks.

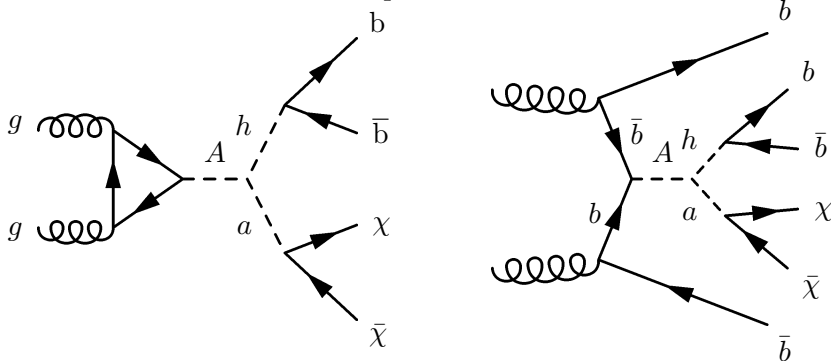


**Figure 3.9:** Representative Feynman diagrams of the 2HDMa model

To specify the model, besides the 2HDM parameters discussed in the beginning of the section, the following additional parameters are needed: the Dark Matter particle mass  $m_\chi$ , the Yukawa coupling of Dark Matter particle  $g_\chi$ , the mixing angle of neutral CP-odd weak eigenstates  $\theta$ ,  $\lambda_3, \lambda_{P_1}, \lambda_{P_2}$  quartic couplings of scalar bosons.

The  $2HDM + a$  model is characterised by a rich phenomenology and it can be probed by all  $E_T^{\text{miss}} + X$  searches, discussed in 3.4.3. From all the signatures, those with a Higgs boson or a  $Z$  boson in the final state are expected to provide constraints in the theoretically best-motivated region of the parameter space.

### 3.5.2 Dark Higgs model

The two mediator Dark Matter model [87, 88] (2MDM model) is a simplified model with a  $Z'$  boson and a dark Higgs boson mediator. DM particles,  $\chi$ , in this model are considered to be Majorana fermions<sup>4</sup>. The model also postulates a new complex Higgs field  $S$  and an additional  $U(1)_{Z'}$  gauge group. The Higgs field  $S$  carries a charge  $q_S$  under the  $U(1)_{Z'}$  gauge group.

The vacuum expectation values of the field  $S$  spontaneously break the  $U(1)_{Z'}$  gauge group, and generate the masses of the  $Z'$  gauge boson and the DM particles. The symmetry breaking gives rise to a new physical Higgs boson  $s$ . Furthermore, the DM particle couples to the  $Z'$  via an axial coupling. As

<sup>4</sup>A Majorana fermion also referred to as a Majorana particle, is a fermion that is its own antiparticle

a result, all three particles,  $Z'$ ,  $\chi$ , and  $s$  couple to each other. The interaction Lagrangian is given by:

$$\mathcal{L}_\chi = -\frac{1}{2}g_\chi Z'^\mu \bar{\chi} \gamma^5 \gamma_\mu \chi - g_\chi \frac{m_\chi}{m'_{Z'}} s \bar{\chi} \chi + 2g_\chi Z'^\mu Z'_\mu (g_\chi s^2 + m_{Z'} s),$$

where  $m_\chi$  is the DM particle mass,  $m_{Z'}$  is the mass of the  $Z'$  boson. In the above, the Dark Matter coupling is  $g_\chi = g_{Z'}, q_\chi$ , where  $g_{Z'}$  is the  $U(1)_{Z'}$  gauge coupling, and  $q_\chi$  charge of the Dark Matter particle. The charge of the DM particle due to the gauge invariance is required to be  $q_S/2$ . Therefore, there are four independent parameters in the Lagrangian:  $m_\chi$ ,  $m_{Z'}$ ,  $m_s$ , and  $g_\chi$

The two mediators allow the dark sector to be coupled to the SM in three different ways. The first is by direct couplings of the  $Z'$  to SM particles, the second by mixing of the  $Z'$  with the neutral gauge SM bosons, and the third is by mixing between the dark Higgs boson and the SM Higgs boson.

The dominant interactions result from vector couplings of the  $Z'$  to quarks ( $q$ ), and the corresponding interaction Lagrangian is

$$\mathcal{L}_q = -g_q Z'^\mu \bar{q} \gamma_\mu q,$$

where  $g_q$  is the coupling strength of the  $Z'$ -boson to quarks. The non-zero mixing between the dark Higgs boson and the SM Higgs boson with mixing angle  $\theta$  ensures that the dark Higgs boson is unstable and can instantly decay into SM states. The dark Higgs boson inherits the branching fractions of an SM-like Higgs boson with mass  $m_s$ .

### 3.5.3 Constrains on Two-Higgs-Doublet models

From the two models discussed in 3.5.1, the  $Z'$ -2HDM model is strongly constrained by dijet searches. Additional (indirect) constraints on the model are placed by flavour-physics searches [89] and electro-weak precision measurements [85], reducing a lot the available phase space.

The main advantage of the  $E_T^{\text{miss}} + X$  searches lies in constraining models such as the  $2HDM + a$  simplified model in which the interaction between SM particles and DM particles is mediated by a pseudo-scalar mediator.

Figure 3.10 shows the exclusion contours at 95%CL<sub>s</sub> in the  $m_A - m_a$  plane and for  $\tan \beta = 1.0$ ,  $m_\chi = 10\text{GeV}$ , and  $\sin \theta = 0.35$ . In addition to the  $E_T^{\text{miss}} + X$  searches limits, the figure also displays a limit contour derived from searches for invisible decays of the Higgs boson ( $H + \text{invisible}$ ). From Fig. 3.10 follows that the exclusion sensitivity is dominated by the  $E_T^{\text{miss}} + Z(\ell\ell)$  and  $E_T^{\text{miss}} + H(b\bar{b})$

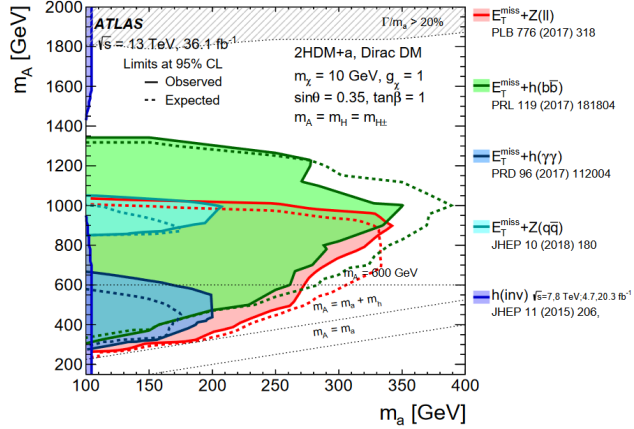


**Figure 3.10:** Exclusion limits (95 % CLs) for the  $2HDM + a$  simplified model in the two-dimensional  $m_A - m_a$  plane for  $\tan\beta = 1.0$ ,  $m_\chi = 10\text{ GeV}$ , and  $\sin\theta = 0.35$ . The limits are obtained from  $E_T^{\text{miss}} + X$  searches as well as searched for the invisible decays of the Higgs boson. The regions where the width of any of the Higgs bosons exceeds 20 % of its mass are marked with dashed grey lines. Figure taken from Ref. [83].

searches. It should be noted that the limits displayed in Fig. 3.10 result from the reinterpretation of the results of the DM searches listed on the figure.

The analysis strategy of the  $E_T^{\text{miss}} + H(b\bar{b})$  search shown in Fig 3.10, was defined to optimise the sensitivity to the  $Z' - 2HDM$  model, and despite the fact that both  $2HDMa$  and  $Z' - 2HDM$  models give rise to a  $E_T^{\text{miss}} + H(b\bar{b})$  signature the final state kinematics is different - as will be discussed in Chapter 8. As a result the results presented in Fig. 3.10 might not be optimal. On the contrary, the data analysis that will be presented in this thesis is optimised for the  $2HDM + a$  signals.

# Chapter 4

## Proton-proton collisions

This chapter provides an overview of the key concepts involved in the description of proton-proton collisions and their simulation. The first section, 4.1, presents the overall picture of two colliding protons and establishes the related terminology. Section 4.2 briefly discusses the initial state of the colliding protons, which is described by the parton density functions. Section 4.3 introduces the main concepts involved in calculating the hard scatter cross-section. Section 4.4 presents the processes characterised by lower momentum transfer than the hard scatter. Finally, Section 4.5 contains a short description of the event simulation procedure and brief reviews of the main event generators used in this work.

### 4.1 Description of a $pp$ collision

The description of proton-proton collisions is quite complex because protons are composite objects. In Chapter 2 (Sec.2.1), protons were introduced as a combination of three quarks ( $uud$ ), but this picture is not entirely accurate. Besides these three quarks, also called *valence quarks*, quantum fluctuations and interactions between valence quarks create a *sea* of gluons and quark-anti quark pairs. All the proton constituents are collectively called *partons*.

When the protons collide at energies of a few TeV, the corresponding timescale of the interaction is much shorter than that of the fluctuations, enough to resolve the internal structure of the incoming protons. In such a  $pp$  collision, the hard scattering is primarily between (any) two partons from the incoming protons. The momentum scale of the hard scatter is high, and the process can be treated perturbatively. On the contrary, the interactions that confine the coloured partons to hadrons occur at low momentum scales - much lower than the hard

scatter- that correspond to a non-perturbation regime. Moreover, the debris of the incoming proton can create additional activity. This rather complicated picture can be decomposed into various sub-processes and stages, reviewed in the next paragraph.

Figure 4.1 is an illustration of a proton-proton collision event. This example shows the production of a Higgs boson and a top-quark pair in the hard scatter. The incoming protons are depicted as green ellipses and the valence quarks as three straight incoming lines. The hard scatter is shown as a red circle and is the process with the highest momentum transfer. Before the partons interact, they can produce additional radiation either via gluon splitting or gluon emission from a quark. This additional radiation is known as *initial state radiation* (ISR) and is marked with blue colour. Likewise, the products of the collision produce QCD radiation with the same mechanisms, which is called *final state radiation* (FSR) and is colour-coded red in the figure. Partons can continue emitting radiation further via these processes leading to the so-called *parton showers*. The result of the parton showers is quarks and gluons with a momentum of few GeV. At these scales, the quarks and gluons are confined into hadrons, in a process called *hadronization*, denoted in the picture with light green ellipses. These initial hadrons decay further into stable particles creating cascades of hadrons, and leading eventually to the formation of *jets*.

Finally, the purple blob in the lower half of the figure is additional activity caused by secondary interactions between some of the proton remnants. These also create parton showers, that hadronise and decay into stable particles. These interactions are much softer than the primary interaction, and together with the rest of the proton remnants, shown as small light blue ellipses, form the so-called *underlying event* (UE).

To be able to describe the outcome of the collision, it is necessary to know the state of the protons before the collision, and therefore the momentum carried by their constituents. This will be the focus of the following section.

## 4.2 Before the collision: from protons to partons

To describe the hard scatter, we first need to consider the energy available for the interaction of the two participating partons, which is smaller than the centre-of-mass energy,  $\sqrt{s}$ , of the colliding protons. The relation between the entire centre-of-mass energy and the partonic,  $\sqrt{\hat{s}}$ , can be expressed as

$$\hat{s} = x_1 x_2 s,$$

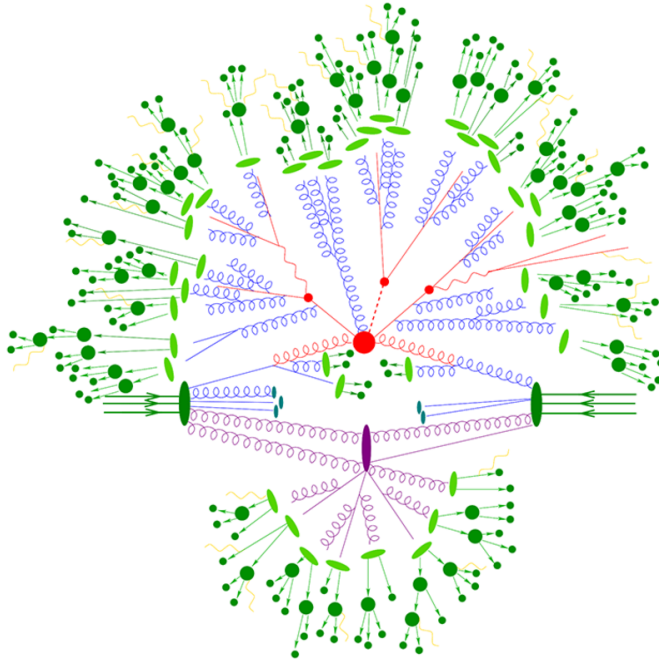


**Figure 4.1:** Sketch of a  $pp$  collision event. The green lines show the incoming valence quarks of the colliding proton, that are illustrated as green ellipses. The various process are shown with different colours. Listed in order of decreasing momentum transfer,  $Q^2$ , these processes are: the hard scatter (red), ISR (blue), FSR (red), hadronization (light green), hadron decays (green), and underlying event (purple). The yellow wavy lines represent electromagnetic radiation, which can be emitted at any stage by electrically charged particles. Figure from Ref. [90]

where  $x_1$  and  $x_2$  are the so-called Bjorken variables. The Bjorken variable,  $x$ , can be interpreted as the fraction of the proton momentum carried by each parton when its mass and transverse momentum are negligible. The probability to find a parton type  $i$  with momentum fraction  $x$ , when a proton is probed at some scale  $Q^2$ , is given by the *parton density functions* (PDFs),  $f_i(x, Q^2)$ . The PDFs can not be derived from first principles because the dynamics of the system inside the proton is not known a priori. Instead, they are determined from experimental measurements.

Various collaborations provide up-to-date estimations for the PDFs. Each group uses a different approach or type of experiment to determine the PDFs, however, the main procedure is the same. The first step of this procedure is to work the ideas on the general expected shape of the distributions into a model with several free parameters. Then, using the connection between PDFs and cross-section

(which will be discussed in 4.3), the parameters are extracted from fit to data. Finally, the calculated PDFs are evolved towards lower or higher scales using their dependence on  $Q^2$ .

The dependence of the PDFs on the scale  $Q^2$  of the scattering is described by the *DGLAP* equations:

$$\begin{aligned}\frac{\partial q_i(x, Q^2)}{\partial \log Q^2} &= \frac{\alpha_S}{2\pi} \int_x^1 \frac{dz}{z} \{P_{q_i q_j}(z, \alpha_S) q_j\left(\frac{x}{z}, Q^2\right) + P_{q_i g}(z, \alpha_S) g\left(\frac{x}{z}, Q^2\right)\} \\ \frac{\partial g(x, Q^2)}{\partial \log Q^2} &= \frac{\alpha_S}{2\pi} \int_x^1 \frac{dz}{z} \{P_{g q_j}(z, \alpha_S) q_j\left(\frac{x}{z}, Q^2\right) + P_{g g}(z, \alpha_S) g\left(\frac{x}{z}, Q^2\right)\}\end{aligned}$$

where  $q_j\left(\frac{x}{z}, Q^2\right)$  is the quark PDF,  $g\left(\frac{x}{z}, Q^2\right)$  is the gluon PDF and  $P_{ab}$  are the *splitting functions*. The splitting functions using perturbation theory are written as:

$$P_{ab}(x, \alpha_S) = P_{ab}^{(0)}(x) + \frac{\alpha_S}{2\pi} P_{ab}^{(1)}(x) + \dots$$

Figure 4.2 shows the PDFs from NNPDF group, estimated at two different scales  $10 \text{ GeV}^2$  and  $10^4 \text{ GeV}^2$  at next-to-next-to-leading order (NNLO) - the term will be explained in 4.3. In both scales the valence quark PDFs dominate at high  $x$ -values, while the gluons and sea-quarks dominate at low  $x$ . In fact,

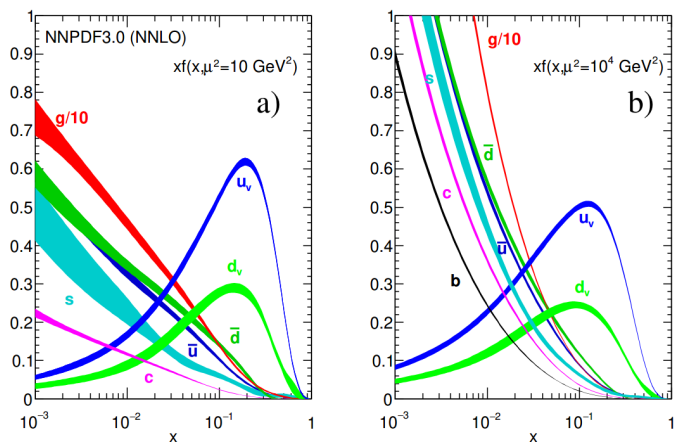


**Figure 4.2:** NNPDF3.0 Parton distribution functions for quarks, antiquarks and gluons, at  $Q^2 = 10 \text{ GeV}^2$  (left) and  $Q^2 = 10^4 \text{ GeV}^2$  (right). For sea quarks and antiquarks the PDFs are assumed to be identical. Figure taken from Ref. [91].

by comparing the sea-quark and gluon contributions, at low  $x$ , between the two  $Q^2$  scales, we observe that those at higher scales are larger. Qualitatively this effect can be explained as follows: higher momentum transfer corresponds to smaller probing distances, which means more of the proton internal structure

is revealed, which carry overall smaller momentum fractions  $x$ . The PDF4LHC working group recommends [92] three PDF sets as primary choices to describe collisions at the LHC, namely the CT14 [93], MMHT14 [94] and NNPDF3.0 [95]. Figure 4.3 presents a comparison of the gluon (left) and quark (right) PDFs between the three benchmark sets estimated at  $Q^2 = 100 \text{ GeV}^2$ . The sets MMHT14 and NNPDF3.0 are presented with respect to the CT14 set. The discrepancies in the figure are caused from the use of different input data, and different choices for the parameters. The sets also use two different approaches. The more conventional approach, adopted by CT14 and MMHT14 groups, is to choose a functional form for the PDFs with ten to thirty free parameters that are determined via a fit to data. The Neural Net PDF (NNPDF) collaboration uses an alternative method: Monte Carlo replicas are created from the original data set and then used to train and validate a neural network. The result is an ensemble of PDFs from which the average is used. For searches beyond the standard model, the authors of the PDF4LHC report recommend the use of the NNPDF3.0 set. From Figure 4.3, we see that the three sets agree within

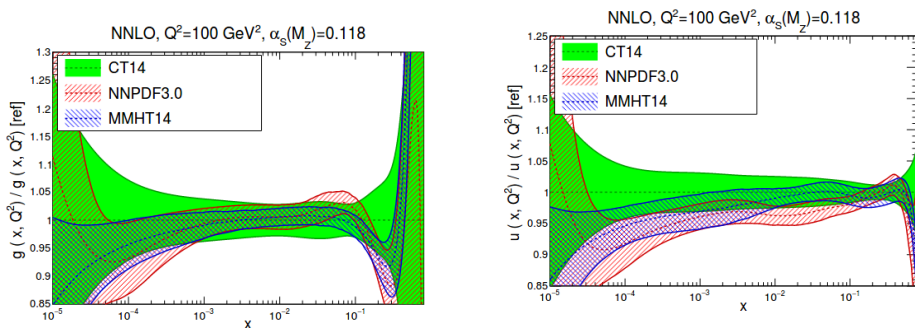


**Figure 4.3:** Comparison of the gluon (left) and up-quark (right) PDFs from the three benchmark sets CT14, MMHT14 and NNPDF3.0 at NNLO and a scale of  $Q^2 = 100 \text{ GeV}^2$ . The CT14 set is the central value and MMHT14 and NNPDF3.0 are shown with respect to it. Figure taken from Ref. [95]

their uncertainties. The uncertainties for the gluon pdfs are lower for  $x$  between  $\sim 10^{-3}$  and  $\sim 10^{-2}$ , and become very large for  $x < 10^{-3}$  and  $x > 10^{-1}$ . The uncertainties of the up-quark PDFs increase for low  $x$  values ( $x < 10^{-3}$ ) and again at much higher  $x$  values, almost  $x \sim 0.7$ .

Each collaboration provides, besides the central values for the PDF set, the associated error sets. The error sets incorporate the uncertainties on the experimental data used for the fits, as well as, effects from parametrisation and finite order calculations. There are also specific error sets for alternative values of the running coupling  $\alpha_s$ . In Ref. [92] the authors provide, also, explicit formu-

lae for the quantification of the associated uncertainties for physical quantities. Chapter 11 will explain how these error sets are used to estimate the uncertainty on specific quantity.

### 4.3 The hard scatter

The main ingredient for the cross-section calculation is the transition rate from the initial to the final state, which, according to Fermi's Golden Rule, is given by the integral of the square of the absolute value of the transition matrix element integrated over the available phase space. For a scattering process with two incoming particles and  $n$  outgoing, the cross-section can be written as [96]

$$\sigma = \frac{S}{4\sqrt{(p_a \cdot p_b)^2 - (m_a m_b)^2}} \int |\mathcal{M}_{ab \rightarrow n}|^2 (2\pi)^4 d\Phi_n.$$

In this expression the incoming particles are labelled as  $a$  and  $b$ ,  $\mathcal{M}_{ab \rightarrow n}$  is the matrix element,  $S$  is a statistical factor added to take into account identical particles in the final state <sup>1</sup> and  $d\Phi_n$  is the phase space element, which is written as

$$d\Phi_n = \delta^4(p_a + p_b - p_1 \cdots - p_n) \times \prod_{j=3}^n 2\pi \delta(p_j^2 - m_j^2) \Theta(p_j^0) \frac{d^4 p_j}{(2\pi)^4}.$$

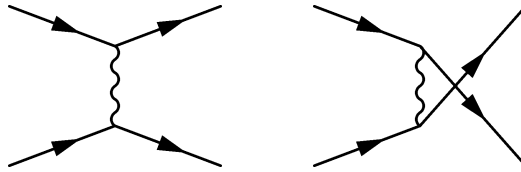
The term  $\delta^4(p_1 + p_2 - p_3 \cdots - p_n)$  in the phase space element ensures the conservation of energy and momentum, the term  $\delta(p_j^2 - m_j^2)$  forces all outgoing particles to be *on-shell*, while the  $\Theta$  function ensures positive energy for the outgoing particles.

The mathematical expression of the matrix element amplitude for a specific process can be derived in the framework of QFT and is graphically represented through *Feynman diagrams*. These graphs depict an interaction using different lines to represent the various particles and vertices to describe the couplings. Every element of the Feynman diagram corresponds to a specific term in the amplitude of the process. A set of rules, known as *Feynman Rules* can be used to write the expression of the matrix element for any Feynman diagram. The rules for the different theories can be found in many textbooks, for example, in Ref. [5]. To calculate the matrix element for a given process, for example  $2 \rightarrow n$  we need to take into account all the possible Feynman diagrams for this process. This will be illustrate in the next paragraph using the example of electron-electron scattering, using only approximations and not rigorous mathematical calculations for the ME.

---

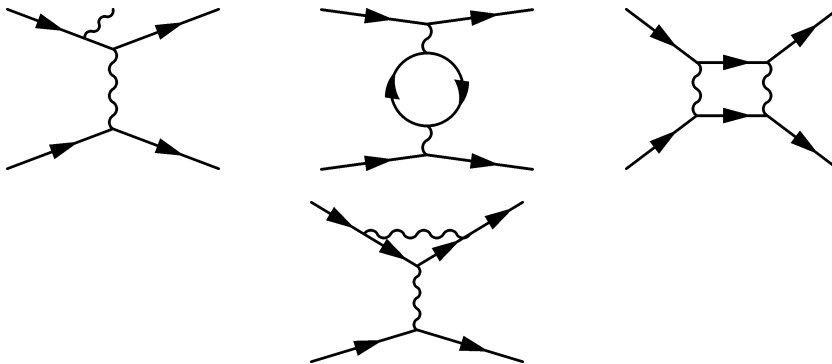
<sup>1</sup>for every group of  $j$  identical particles there is a factor  $1/j!$

Figure 4.4 shows the simplest Feynman diagrams that contain the lowest number of vertices for the electron-electron scattering, which is mediated by a photon or a  $Z$ -boson. Besides these simple cases, it is possible, for example, that the



**Figure 4.4:** Examples of leading order Feynman diagrams for electron scattering

electrons emit a photon before or after the interaction, as shown in Figure 4.5 (top left) along with other diagrams that contain loops. To calculate the cross-section of the electron-electron scattering, every possible diagram needs to be taken into account. That should also include even more complicated diagrams than in Fig. 4.5. To simplify the discussion, it is assumed that the momentum transfer is much lower than the  $Z$ -boson mass, and consider only the photon propagator terms.



**Figure 4.5:** Examples of next-to-leading order Feynman diagrams for electron scattering

According to Feynman Rules, every QED vertex contributes to the amplitude by a factor  $-ig\gamma^\mu$ , where  $g$  is the coupling. Taking only the diagrams of Fig 4.4 into account, the matrix element will be proportional to the coupling squared. The calculation of the cross-section (or an observable in general) using only contributions from the simplest diagram contains terms of coupling constant at the lowest order and is characterised as *leading-order*(LO). The matrix elements corresponding to diagrams of Fig. 4.5 contain more than two vertices and lead to matrix elements that contain higher orders of the coupling constant. The corresponding calculations, in this case, are characterised as *next-to-leading or-*

der (NLO). Due to the small value of the QED coupling constant, higher-order diagrams are suppressed, however, the large number of such diagrams, especially when additional radiation or more loops are considered, leads to a significant contribution to the cross-section. Including higher-order terms increases the precision of the theoretical predictions. Currently many processes are calculated at *next-to-next-to-leading order* accuracy.

Cross-sections for QCD processes can be estimated in the same way as illustrated above using the corresponding Feynman rules, only when the strong coupling constant is sufficiently small, i.e. in the perturbative regime. For proton-proton collisions, however, to estimate the cross-section we need the factorisation theorem [97], which allows to “separate” the perturbative and non-perturbative terms. The physical cross-section for two colliding partons,  $A$  and  $B$ , factorises into the parton-level cross section  $\hat{\sigma}_{ab \rightarrow X}$  and the parton density function of the partons  $a$  and  $b$  via

$$\sigma_{AB} = \int dx_a dx_b f_{a/A}(x_a, \mu_f^2) f_{b/B}(x_b, \mu_f^2) \hat{\sigma}_{ab \rightarrow X},$$

where  $\mu_f$  is the *factorisation scale*, which can be interpreted as the scale that distinguishes the perturbative and soft processes. The parton cross section can be written in orders of the strong coupling constant,  $a_s(\mu_R^2)$ , via

$$\hat{\sigma}_{ab \rightarrow X} = [\hat{\sigma}_0 + a_s(\mu_R^2)\hat{\sigma}_1 + \dots]_{ab \rightarrow X}$$

In the expression above,  $\mu_R$  is the renormalisation scale of the strong coupling constant. In principle, the cross-section should be independent of the scales  $\mu_R$  and  $\mu_f$ , which applies when all the orders are included in the perturbation series, and compensate the scale dependence of the PDFs. Since it is impossible to consider all terms in the series, the dependence remains. Selecting reasonable values for the scales depends on the characteristics process, while it is common to set  $\mu_R = \mu_f$ . Different values for the scales result in different numerical estimates for the cross-section, which means there should be one uncertainty in the cross-section that reflects the effect from the neglect of higher orders in the perturbation series.

The following section will outline the remaining processes in  $pp$  events introduced in 4.1, which are characterised by softer momentum transfers than the hard scatter.

## 4.4 From partons to hadrons

As explained in Section 4.1, parton showers describe additional emissions of the incoming and outgoing partons of the hard interaction. When a gluon of very small energy is emitted, or when the splitting angle between the gluon and one of the quarks is very small, the perturbation theory breaks down. These higher-order effects, not covered by the matrix element calculations, are addressed by the framework of parton showers.

The parton showers describe the evolution from the scale of the hard scatter down to scales of roughly 1 GeV, at which the partons are confined in hadrons. During this evolution process, the probability of transitioning to a lower state without splitting or emitting a gluon is calculated. This probability determines whether or not an additional parton is produced. Initial state showers, however, are evolved backwards: the interacting partons are dressed with further radiation iteratively, starting from a lower scale, until the non-perturbative regime is reached. In this case, we are interested in the probability of the interacting parton at a given momentum fraction and scale to originate from a higher momentum fraction at a lower scale.

The matrix element calculations describe the hard interactions including diagrams up to a fixed order, and, therefore, a small number of external partons. On the contrary, parton showers, which describe correctly soft-collinear emissions, involve an arbitrary number of additional partons. The two approaches are combined, consistently avoiding double-counting via a procedure called *matching*. There are different matching schemes, such as the CKKW technique [98–100], which usually involve a scale that separates the regimes in which the two approaches are applicable.

Confinement forces particles that carry colour to form hadrons. However, the hadron-production mechanism is a non-perturbative QCD process, which cannot be predicted from first principles. Describing, therefore, the transition of a coloured partonic system into colourless hadrons demands the use of phenomenological models. Two of the most commonly used models are the Lund string model, and the cluster model. The underlying idea of the Lund string model is that when attempting to separate a pair of quarks the field lines are attracted, because of the gluon self-coupling, resulting in a tube-like structure called string. As the quarks move apart, the string is stretched, increasing its potential energy. Once the potential energy becomes higher than the mass of a quark-antiquark pair, the string breaks into two new strings, each connecting a pair of quarks. These new strings stretch further and break into new strings, creating more pairs, and so on. This repetitive procedure stops when all the potential

energy in the strings turns into quark pairs connected by gluon strings, that are assumed to correspond to mesons. While the string model produces hadrons directly from the quark pairs, the cluster model has an intermediate step. First, a cluster is formed through the non-perturbative splitting of gluons produced from the parton showers into quark-antiquark pairs. The cluster, then, decays leading to additional light-flavour pairs.

When describing the final state of collisions, it is necessary to address the remaining activity that occurs from partons that do not partake in the hard scatter, also called spectators. Due to the high collision energy, these spectators can lead to additional partonic interactions. These parton-parton interactions are part of the underlying event and are assumed to be  $2 \rightarrow 2$  QCD processes with relatively small momentum transfer. The values of the parameters and scales used in the modelling of the UE and the hadronization have to be adjusted to describe the experimental data closely. This adjustment requires the comparison of theoretical predictions to observations which is made possible using software simulation tools known as *event generators* (or simply generators), discussed in the following and final section of this chapter.

## 4.5 Event generators

The simulation of the final states of high energy proton-proton collisions is a complex problem considering the large number of produced particles and the vast range of their momenta which spans over many orders of magnitude. As explained in the first section of this chapter, the events are divided into different regimes, each simulated with different approaches. The simulations of processes in all these regimes employ Monte Carlo techniques [101]. The matrix element calculations, for example, are solved numerically via Monte Carlo integration, while the parton shower evolution involves the use of Markov chains. When all the simulation algorithms are consistently combined in a single framework they form a general-purpose Monte Carlo event generator. In the following there is an outline of the two general-purpose generators used in this work, as well as matrix element generators that only produce and calculate the ME of specific processes.

**SHERPA** SHERPA [100] is a general-purpose generator that can be used to model all SM processes, as well as various BSM processes. It has two different matrix element generators, which generate the code for the ME calculations, and use some of the most advanced phase-space integration techniques. The software has its own description of the parton shower. It also contains a hadronisation model, which is based on cluster models, and a description of the underlying

event based on multiple-parton scattering.

**PYTHIA** PYTHIA [102], is also a general purpose generator. It provides a list of hard-coded subprocesses, from which the user selects. Just like SHERPA, it has its own parton shower and hadronization models, using though different approaches. It also comprises modelling of soft processes, providing an inclusive description of the total  $pp$  cross section. Because of this, PYTHIA is quite often used to generate events with multiple collisions, besides the hard scatter, known as pile-up events- these will be discussed further in Chapter 5. As PYTHIA has no automated code generation capabilities, it is designed to use external input from ME generators.

**MadGraph** MadGraph is a matrix element generator. This means that the software generates the Feynman diagrams and the code for the calculation of the matrix element for a user-specified process, such as  $2 \rightarrow n$  scattering. This code can, then, be used for the cross section calculation, or for event generation. When used for the later, the simulation of parton showers, hadronization etc, is performed by an external programme, for example PYTHIA.

**MC@NLO** MC@NLO [103] calculates the hard QCD process in NLO accuracy. Its has the advantage of providing its own algorithm for parton showering, and an additional package aMC@NLO that automates its matching procedure.

**MadGraph5\_aMC@NLO**[104] As the name suggests, this software combines in one framework all the features of MadGraph5 and aMC@NLO, superseding both of them. For event generation, the output is usually interfaced with PYTHIA.

The output of the event generation is used for several distinct purposes in particle physics experiments, such as designing the data analysis strategy, extracting a signal of new physics from the background of SM processes or performing measurements of the SM parameters. Comparing the output of event generators to data, however, requires the additional steps of simulating the detector response, digitisation and reconstruction. Before discussing these topics, Chapter 5 will provide an overview of the Large Hadron Collider, the accelerator that produced the proton-proton collisions used in this thesis.



# Chapter 5

## The Large Hadron Collider

The Large Hadron Collider (LHC)[105] is the largest accelerator build at present with a circumference of approximately 27 km. It is located at CERN near Geneva, Switzerland and was installed 100 m beneath the French-Swiss border in the existing tunnel of the Large Electron Positron (LEP) collider. Two superconducting rings accelerate particle beams by rotating them in opposite directions and collide them at designated points around the rings to extraordinary high centre-of-mass-energies. The LHC was designed to accelerate proton beams to centre-of-mass-energies up to 14 TeV and heavy ions up to 2.8 TeV per nucleon and deliver luminosities of  $10^{34} \text{ cm}^{-2}\text{s}^{-1}$  and  $10^{27} \text{ cm}^{-2}\text{s}^{-1}$  respectively. The designed luminosity and energies are necessary for the discovery of new physics and higher precision measurements of the Standard Model parameters.

The proton beams, before being injected at the LHC, they are accelerated to energies of 450 GeV. A sequence of accelerators is used for this purpose which is briefly described in Section 5.1. Section 5.2 contains an overview of the experiments located around the ring. Section 5.3 discusses the definition of luminosity. Finally, Section 5.4 has a short performance overview of the LHC operation mostly focusing on the years 2015-2018.

### 5.1 Accelerator complex

The protons are accelerated gradually at several steps before being injected into the LHC rings. Figure 5.1 is a schematic representation of the acceleration sequence. Protons are produced by ionising hydrogen gas and then are inserted to a linear accelerator, called Linac 2, which brings them to the energy of 50 MeV.

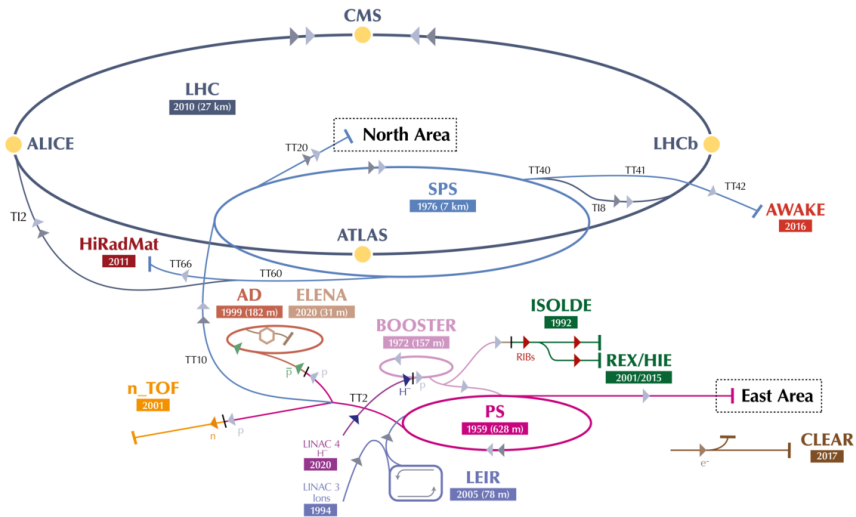


**Figure 5.1:** The accelerator complex at CERN [107]. The acceleration chain is described in the text

The next step in the sequence is the Booster followed by the Proton Synchrotron (PS) where the beam energy reaches 1.4 GeV and 25 GeV, respectively. These two steps also prepare the LHC bunch structure. Protons are organised in 72 bunches spaced at 25 ns (7.5 m) [106]. After that, beams pass through the Super Proton Synchrotron (SPS), which accelerates them at energies of 450 GeV. The next and final step is the LHC. In total 2808 bunches are injected into two beam pipes and are circulated in opposite directions for several minutes until they reach the maximum energy of 6.5 GeV. The beams are bent by a magnetic field of more than 8.3 T generated by superconducting NbTi dipole magnets. Quadropole magnets are used to focus the beam and direct them to the four collision points that are indicated in Figure 5.1, where collisions occur at a rate of 40 MHz.

## 5.2 The LHC experiments

There are seven experiments in total situated around the LHC. The four larger experiments, are located on each of the collision points. Two of them, the ATLAS [108] (A Large Toroidal Lhc ApparatuS) and the CMS [109] (Compact Muon Solenoid) are general-purpose experiments: their main goal is to cover a wide range of physics searches and measurements. The other two experiments are: ALICE [110] (A Large Ion Colliding Experiment), that focuses on studying

QCD interactions at extreme energy densities and temperatures, and LHCb [111] that specialises on heavy flavour physics (study of  $b$  and  $c$  quarks). The three smaller experiments are TOTEM (TOTal Elastic and diffractive cross section Measurement) [112], LHCf (LHC forward) [113], MoEDAL ( Monopole and Exotics Detector At the LHC ) [114]. The main focus of TOTEM are studies related to the products of inelastic collisions and it consists of four detector pairs placed very close to the beam pipe at either side of the CMS detector. MoEDAL is a detector primarily looking for (hypothetic) magnetic monopoles and is close to LHCb. A similar design is adopted for LHCf: its detectors are placed on both sides of the ATLAS detector at 140 meters distance from the collision point. Finally, a new experiment, FASER [115] (ForWArD Search ExpeRiment), will be installed 480 meters from the collision point of ATLAS, close to the beam axis, aiming to search for elementary particles that couple weakly with matter and study the interactions of high-energy neutrinos.

### 5.3 Luminosity

For all the experiments in the LHC luminosity is an important measure of the performance of the accelerator as it connects the event rate,  $R$  at any time with the cross-section  $\sigma$  for a specific process,  $R = \sigma \cdot \mathcal{L}$ . The luminosity depends on several parameters related to the beam. Assuming the two incoming beams with identical bunches (with Gaussian distributed protons in each beam) Luminosity can be written as [105]

$$\mathcal{L} = F \cdot \frac{N_b^2 \cdot n_b \cdot f_r \cdot \gamma}{\epsilon \cdot \beta}, \quad (5.1)$$

where  $N_p$  is the number of protons in each (assuming they have the same number of particles),  $n_b$  the number of bunches in a beam,  $\gamma$  is the relativistic factor of colliding particles and  $f_r$  is the revolution frequency. The additional factor  $F$  is a geometrical correction that takes into account the angle of the two bunches at the crossing. The quantity  $\epsilon$  that appear in the denominator is the transverse normalised beam *emittance* at the collision point, which describes if the particles are well confined to a small distance and if they have similar momenta. Finally, in the denominator there is also the function  $\beta$  at the collision point. The term *integrated luminosity* is used to describe a the luminosity over a period of time :  $L = \int \mathcal{L} dt$

## 5.4 Performance overview

The beams injected to the LHC, after they are accelerated to the desired energy, start to collide as soon as they are stable. The collisions last for several hours and during all this time the experiments record the output of the collisions. As time progresses the beams degrade and the luminosity drops. When the luminosity falls below a certain level the beams are dumped, the magnets are readjusted for new beams to be inserted. This scenario describes a so called *physics run*.

Besides the physics runs there are several other types of runs for technical tests. The collider operates almost continuously<sup>1</sup> for few years - a time period known as *LHC Run* - before it is shut down for maintenance and upgrades for few years - these periods are called *Long Shutdowns*. The LHC so far had two Runs, as illustrated in Figure 5.2a and two Long Shutdowns. The second Long Shutdown ended recently and we are now collecting data for Run-3. This work uses data collected over the full Run-2 period which started at 2015 when the beam energy reached 6.5 TeV and ended in 2018. Figure 5.2a also shows

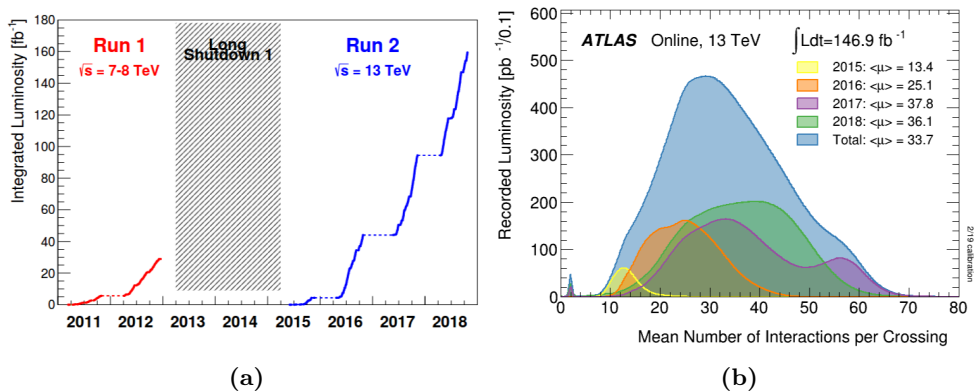


**Figure 5.2:** Integrated luminosity during Run 1 and Run-2 (left) Ref.[116] and the distribution of the average number of interactions per crossing  $\langle \mu \rangle$  (right) [117].

a comparison of the integrated luminosity between Run-2 and Run-1. During Run-2 LHC produced 160 fb<sup>-1</sup> integrated luminosity for ATLAS and CMS. We also see that the collider managed to exceed its designed luminosity in 2018, when the highest peak luminosity reached  $2.1 \cdot 10^{34}$ .

To increase the luminosity the space between bunches has to become smaller. In

<sup>1</sup>Occasionally, during Runs, the operation of the collider can be interrupted for few days due to technical problems

some cases, therefore when the detector is recording an event it might also read contributions from other bunch crossings. This is known as *out-of time pile-up*. At the same time due to the high number of protons in each beam, there are going to be multiple p-p interactions in a single bunch crossing. Between these interactions the most energetic is considered to be the hard scatter and the rest are the so-called *in-time pile-up* or simply pile-up in the following. The pile-up is quantified by the number of interactions per bunch crossing, which is shown in Figure 5.2b for the Run-2. By looking at both plots in Figure 5.2 we can see how the increase of luminosity is increase of the pile-up.



# Chapter 6

## The ATLAS Experiment

This chapter starts with a general overview of the ATLAS detector in section 6.1, then, sections 6.2-6.5 describe its main components. Section 6.6 contains a brief description of the trigger system. A short description of the data taking and processing procedures in the ATLAS experiment is given in section 6.7 and Section 6.8 describes the reconstruction of physics objects. Finally, 6.9 outlines the detector simulation chain.

### 6.1 Detector Overview

The ATLAS experiment has a detector that weighs 7000 tonnes and measures 44m in length and 25m in height. The cylindrical shape, with a forward-backward symmetry, covers almost the full solid angle around the interaction point <sup>1</sup>. The ATLAS detector is designed with multiple layers of cylindrical, coaxial sub-detector elements built with different materials, as shown in Fig. 6.1. Because different types of particles have different types of interactions with the detector material, we are able to distinguish the particles based on the signal they leave - if they leave any- in the different detector components. Neutrinos, which do not interact at all with the detector, escape detection. The following sections give an overview of the main sub-detector elements.

---

<sup>1</sup>Such detectors are also known as *hermetic* or  $4\pi$  detectors

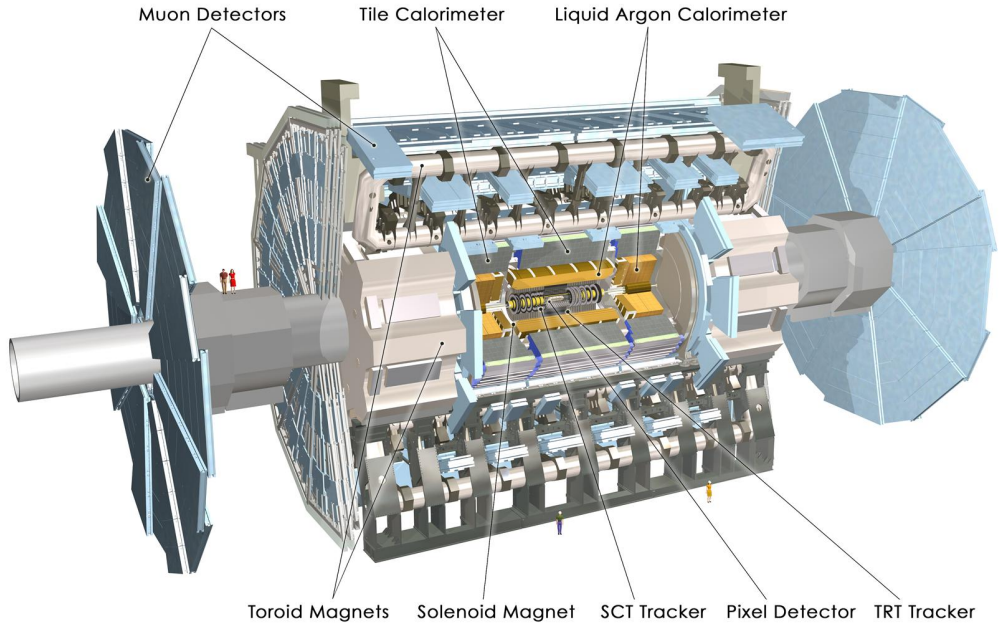


**Figure 6.1:** Cutaway illustration of the ATLAS detector showing the layout [108].

### 6.1.1 Coordinate System and kinematic variables

The origin of the coordinate system is placed at the nominal interaction point within ATLAS (geometric centre of the detector). The z-axis is aligned with the beam line creating a right-handed coordinated system with the x-axis pointing towards the centre of the LHC and the y-axis upwards. The positive and negative of the z-axis define the so-called "A-side" and "C-side" of the detector. The azimuthal angle,  $\phi$ , is measured in the transverse XY plane with respect to the positive x-axis. The polar angle,  $\theta$ , is measured relative to the positive z-axis.

The momentum of the partons participating in the collisions is not known exactly along the z-axis. It is therefore necessary to use quantities that are Lorentz invariant. The differences in polar angle do not satisfy that requirement. Instead, *pseudorapidity* is used for position measurements defined as

$$\eta = -\ln [\tan (\theta / 2)] .$$

Another kinematic quantity commonly used is the *rapidity*, which is defined as  $y = \frac{E+p_z}{E-p_z}$ . Pseudorapidity results from the rapidity in the limit where the particle mass can be neglected. A Lorentz invariant way to describe distances

inside the detector is using  $\Delta R$  which is defined by

$$\Delta R = \sqrt{\Delta\eta^2 + \Delta\phi^2}.$$

Finally, we need to define projection of the momentum on the XY transverse plane, called *transverse momentum*, which is  $p_T = \sqrt{p_x^2 + p_y^2}$ . One can safely assume that the transverse momentum of the partons is negligible compared to the longitudinal one. Therefore, the sum of the transverse momenta of all the collision products must also be zero, due to momentum conservation. However, when invisible particles are produced the sum of the momenta of the visible collision products will be non-zero. The negative vector sum of the momenta of all visible particles inside the detector is called *missing transverse momentum* and is denoted as  $\vec{p}_T^{\text{miss}}$ . The magnitude of the the missing transverse momentum,  $E_T^{\text{miss}}$ , is called *missing transverse energy*

## 6.2 Inner detector

The inner detector (ID) tracking system consists of three subsystems that exploit different particle detection techniques and are the pixel detector, the semiconductor tracker (SCT) and the transition radiation tracker (TRT). The ID is divided into three regions, the central barrel region and two end-caps. The main purposes of the ID are to reconstruct the trajectories of charged particles (also referred to as tracks for brevity) and to determine the positions of interaction vertices. Additionally, it is also used for electron identification. The ID is embedded in a 2 T magnetic field created by a superconducting solenoid magnet. The following paragraphs will review each sub-detector of the ID separately, starting with the innermost system, which is also the one with the highest granularity and spacial resolution.

### 6.2.1 The Pixel detector

The pixel detector consists of four layers in the barrel region and three disks in each of the end-caps. Figure 6.2 shows the position of the barrel pixel layers with respect to the beam pipe along with the rest of the ID subsystems. The innermost layer of the detector, the insertable B-layer (IBL) [118], is located at a radial distance of 33.25 mm from the  $z$ -axis and its outermost layer is at a distance of  $R = 122.5$  mm. Out of all three sub-detectors of the ID, the pixel detector has the highest granularity. Its pixels have a minimum size of  $50 \mu\text{m}$  in the transverse plane and  $400 \mu\text{m}$  in the longitudinal  $z$ -direction, and the spatial resolution achieved is  $10 \mu\text{m}$  in the transverse plane and  $115 \mu\text{m}$  in  $z$ . The pixel

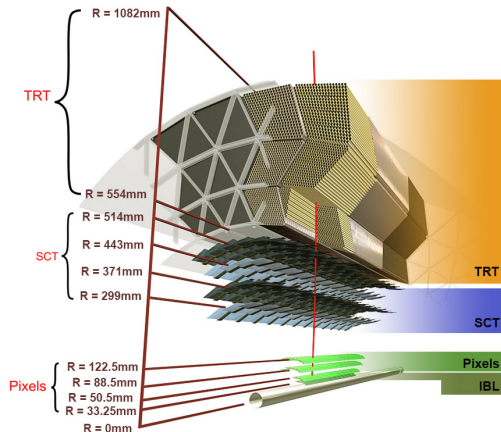


**Figure 6.2:** 3D drawing of the sensors and structural elements of the ID barrel region. A track of  $10\text{GeV}p_T$ , shown with a red line, traverses successively the beam-pipe, the IBL, pixel, SCT and TRT layers at  $\eta = 0.3$ .

detector is vital for the reconstruction of the primary interaction and secondary decay vertices and the high precision measurement of the impact parameter of the track. The secondary vertices are needed to identify jets from heavy-flavour quarks and  $\tau$ -leptons.

## 6.2.2 The Semi-Conductor Tracker

The middle subsystem of the ID is the silicon microstrip Semi-Conductor Tracker (SCT). The detector has four layers in the barrel region. Each layer has two sets of strips, one aligned parallel to the beam axis and the second askew by  $40\text{ mrad}$  stereo angle with respect to the first, to allow for two-dimensional position measurement. The distance of each barrel layer from the beam axis is shown in Figure 6.2. The spatial resolution achieved in the barrel region is  $17\mu\text{m}$  in  $(R-\phi)$  and  $580\mu\text{m}$  in  $z$ . The SCT has 9 disks in the end-cap region that provide a spatial resolution of  $17\mu\text{m}$  in  $(R-\phi)$  and  $580\mu\text{m}$  in  $z$ .

## 6.2.3 The Transition Radiation tracker

The outermost part of the ID is the Transition Radiation Tracker (TRT). The subdetector consists of straw tubes filled with either a Xe-based or an Ar-based gas mixture, which function as proportional drift chambers. The TRT provides track measurement in  $(R-\phi)$  up to  $|\eta| = 2.0$ . It was designed to achieve a position resolution of  $130\mu\text{m}$  per straw.

Even though the TRT has a lower position resolution than the SCT and pixel, it contributes significantly to the high precision track measurement by extending the length of the tracks (for charged particles with  $|\eta| = 2$  the track radius is extended by approximately 1 m.) One of the advantages of using drift tubes as detector technology in the outer layer is that they have a comparably lower cost than silicon detectors. Chapter 7 contains a more detailed description of the TRT detector.

Besides tracking, the detector contributes to the identification of electrons by detecting transition radiation. The transition radiation is the electromagnetic radiation a charged particle emits when it crosses the boundary between two media with different dielectric constants. The intensity of the emitted radiation depends on the mass of the traversing particle, with lower mass particles emitting more transition radiation photons. As a result, the energy deposits from electrons can be distinguished from other particles, such as pions, using two different read-out thresholds.

### 6.3 Calorimeter System

The ATLAS calorimeter system covers a range of  $|\eta| < 4.9$ , its geometry is fully symmetric in  $\phi$ , and consists of the Electromagnetic Calorimeter (ECal), the Hadronic Calorimeter (HCal), and the Forward Calorimeters, (FCal), as illustrated in figure 6.3. The system has a length of 12.2 m and an outer radius of 4.25 m. All the components are *sampling calorimeters*, i.e. they have alternating layers of high-density *passive* material, which produces avalanches of particles, and *active* material, which is used to detect the produced particles. The electromagnetic calorimeter has a fine granularity for central regions, that match the coverage of the inner detector, to provide precision energy measurements for electrons and photons. The rest of the calorimeter is mostly used for the reconstruction of jets and the missing transverse momentum, and a lower granularity is sufficient. An important feature of the calorimeters is their depth, which must be sufficient to contain the showers reducing the particle flow that can reach the muon system. For electromagnetic calorimeter, the depth is expressed in terms of the *radiation length*,  $X_0$ .  $X_0$  is the mean length at which the energy of an electron travelling through the material is reduced, via bremsstrahlung, by a factor of  $1/e$ . The depth of the HCal is typically expressed in terms of the *interaction length*,  $\lambda$ , which is the mean distance a hadron travels in a material before it interacts inelastically with a nucleus. The ECal has a total depth that exceeds  $22 X_0$  in the barrel and  $24 X_0$  in the end-caps. The depth of the HCal is  $9.7 \lambda$  in the barrel and  $10 \lambda$  in the end-caps. The design features of the calor-

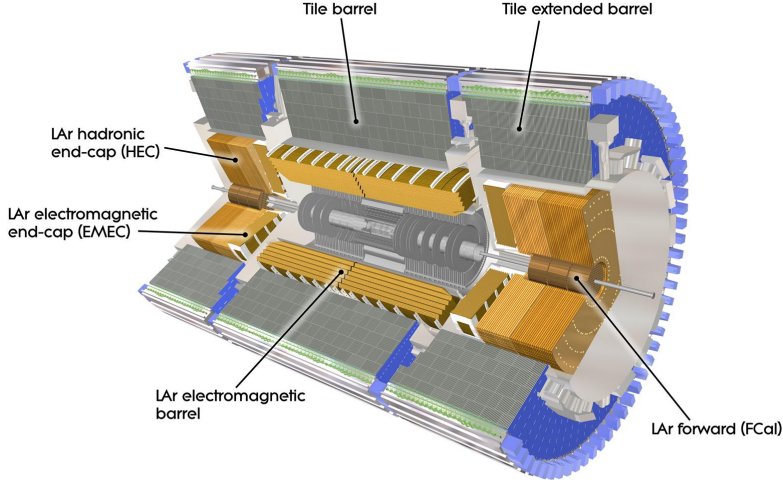


**Figure 6.3:** Schematic view of the ATLAS Calorimeter system [108].

imeters provide high-resolution measurements for the highly energetic jets and assure the precise measurement of missing transverse momentum, which is very important for BSM searches, such as the one presented in this work.

### 6.3.1 Electromagnetic Calorimeter

The electromagnetic calorimeter is divided into two parts, the *ElectroMagnetic Barrel* (EMB) which covers a region of  $|\eta| < 1.47$  and the *ElectroMagnetic End-Caps* (EMEC) covering a region of  $1.37 < |\eta| < 3.2$ . Figure 6.4 shows the layers and the cell segmentation for a barrel module. The EMB consists of two half-barrel calorimeters, while two coaxial wheel calorimeters are placed on each side of the forward areas. The active material of the electromagnetic calorimeter is liquid argon (LAr), while the passive is lead. This technology is chosen because it combines high performance with resistance to radiation, and to work the temperature must be kept low. For this reason, the calorimeter is placed inside three independent cryostats. Kapton electrodes, interleaved with lead absorber plates, collect the charge yielded in the calorimeter. These electrodes are folded in an accordion geometry to avoid dead zones and minimise electronic dead-time.

In the region  $|\eta| < 2.5$ , which is covered by the ID and is most important for precision measurements, the ECal is divided into three longitudinal layers. The first layer is finely segmented into strip cells to improve the measurement in the

$\eta$ -direction.

The second layer consists of square tower cells and collects the largest energy fraction of an electromagnetic shower. The cells of the third layer have double the size in  $\eta$  compared to the cells of the second layer, as it collects the tails of the shower.

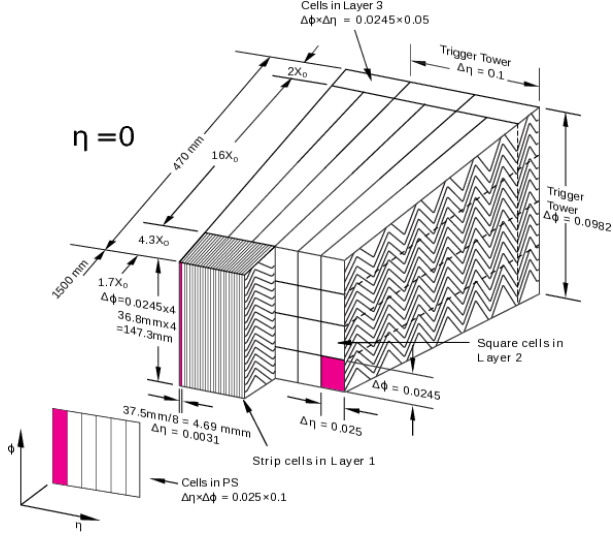


**Figure 6.4:** Sketch of the Liquid Argon Calorimeter [108]

The general structure of the EMEC is the same as the EMB, but it is rotated into the radial direction (instead of the axial direction of the EMB). The transition region between the EMB and EMEC ( $1.37 < |\eta| < 1.52$ ) contains a large amount of inactive material, which results in non-negligible energy losses and reduces calorimeter performance. For this reason, it is usually recommended that physics analyses that need high precision electrons and photons should exclude this particular region. Between the ID and the electromagnetic calorimeter there is a presampling calorimeter, in a region of  $|\eta| < 1.8$ , which is used to estimate the energy loss of electrons and photons from their interactions with the preceding material. The presampler has a 1.1 cm thick layer of LAr in the barrel and 0.5 cm in the end-cap region. The combined energy resolution in the ECAL is

$$\frac{\sigma}{E} = \frac{10\%}{\sqrt{E}} \oplus 0.7\%, \quad (6.1)$$

where  $\oplus$  denotes quadrature sum.

### 6.3.2 Hadronic Calorimeter

The hadronic calorimeter is located just outside the ECAL and comprises three parts, the Tile Calorimeter (TileCal), the Hadronic End-Cap Calorimeter (HEC) and the Forward Calorimeter (FCal). Depending on the detector region they cover, each part is using different technologies. The TileCal is a sampling calorimeter that uses steel as the absorber and scintillating tiles as active material. It consists of a central barrel that covers a region of  $|\eta| < 1.0$  and two extended barrels at  $0.8 < |\eta| < 1.7$ . The TileCal has an inner radius of 2.28 m, and an outer radius of 4.25 m, and, just like the EM calorimeter, is segmented into three layers with different depths. The central barrel layers have respective thicknesses of  $1.5\lambda$ ,  $4.1\lambda$  and  $1.8\lambda$ , while for the extended barrels the corresponding depths are  $1.5\lambda$ ,  $2.6\lambda$ , and  $3.3\lambda$ . The HEC covers an  $|\eta|$ -range from 1.5 to 3.2 and overlaps with both the tile and forward calorimeter. It consists of two wheels at each detector side segmented into two longitudinal sections. The HEC uses copper plates as absorber and LAr as the active medium. The resolution of the barrel and end-cap calorimeters is

$$\frac{\sigma_E}{E} = \frac{50\%}{\sqrt{E}} \oplus 3\%.$$

Finally, the FCal covers the region  $3.1 < |\eta| < 4.9$ , and consists of three layers per end-cap. The active medium is LAr. The first layer, closest to the interaction point, uses copper as the absorber and is designed for electromagnetic measurements, while the other two use tungsten, to measure mainly hadronic showers. Behind the FCal there is a brass layer used to absorb the remaining of the hadronic showers. The FCal energy resolution is

$$\frac{\sigma_E}{E} = \frac{100\%}{\sqrt{E}} \oplus 10\%.$$

## 6.4 Muon Spectrometer

The Muon Spectrometer (MS) is located in the outer part of the detector where only muons can reach since all the other particles are stopped in the calorimeter system. It consists of high-precision tracking chambers and is also equipped with separate trigger chambers that provide fast signals.

Crucial to the function of the system are the superconducting toroid magnets that provide the necessary magnetic field for the momentum measurement. The magnet system consists of three magnets, the large barrel toroid ( $|\eta| < 1.4$ )

and two end-cap toroids on each detector side ( $1.6 < |\eta| < 2.7$ ). Each magnet contains 8 coils. While the barrel coils have their own cryostat, a common cryostat is used for the end-cap coils on each side. Figure 6.5 shows the layout of the muon system. The symmetry of the muon system reflects the geometry

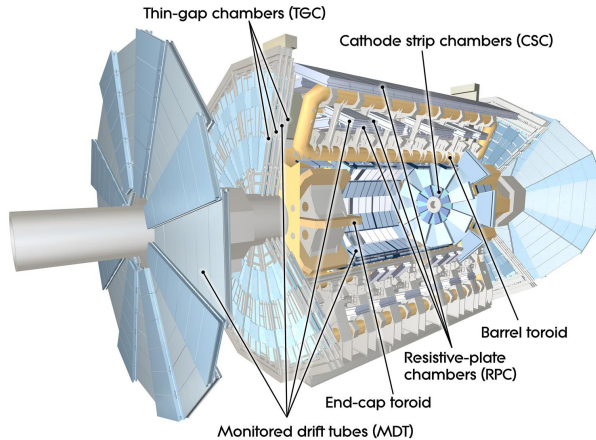


**Figure 6.5:** Schematic cut-away view of the ATLAS muon system [108].

of the magnets and is divided into octants. The tracking chambers in the barrel are placed in three cylindrical layers around the beam axis, while in the end-caps, there are four wheels perpendicular to the beam axis. The MS consists of four different chamber types, the Monitored Drift Tubes (MDTs), the Cathode Strip Chambers (CSCs), the Resistive Plate Chambers (RPCs) and the Thin Gap Chambers (TGCs). The first two, MDTs and CSCs, are used for tracking, while the rest, RPCs and TGCs, are used for triggering.

The Monitored Drift Tube chambers provide the track coordinates in most of the detector regions at  $|\eta| < 2.7$  with high precision. They are, also, simple to construct and have predictable mechanical deformations. A typical MDT chamber consists of two multi-layers, each containing three or four layers of drift tubes. The drift tubes are made of aluminium and the anode is a tungsten-rhenium wire in the centre of the tube. The average resolution is about  $35 \mu\text{m}$  per chamber.

The Cathode Strip Chambers are used in the innermost layer of the forward region at  $2.0 < |\eta| < 2.7$ . These are multi-wire proportional chambers the cathode planes of which are divided into strips in orthogonal directions. This allows them to measure both coordinates simultaneously, with a resolution of  $40 \mu\text{m}$  per chamber in the bending and of  $5 \mu\text{m}$  in the transverse plane.

The Resistive Plate Chambers provide trigger information in the barrel region,

while the Thin Gap Chambers in the forward region. Both triggering chambers deliver signals within 15 – 25 ns after a particle passes through. For this reason, they can be used, also, to tag the beam-crossing. Additionally, they deliver well-defined  $\vec{p}_T^{\text{miss}}$  thresholds and provide coordinate measurements in the bending  $\eta$ -plane and the non-bending  $\phi$ -plane.

## 6.5 Forward Detectors

Several detectors and sensors are placed in the forward regions of the ATLAS detector, which are used to measure particles at high absolute values of pseudo-rapidity and to provide information about the beams.

The LUMInosity Cherenkov Integrating Detector-2 (LUCID-2) [119], is the main detector used for luminosity monitoring during Run 2 in the ATLAS experiment. LUCID-2 consists of two detectors placed around the beam-pipe on both ends of the ATLAS detector at approximately 17 m from the interaction point. It measures luminosity by detecting Cherenkov light signals from charged particles from the debris of inelastic proton-proton collisions. LUCID can provide online monitoring of instantaneous luminosity.

The Zero-Degree Calorimeter (ZDC) [120] has two modules located at a distance of  $\pm 140$  m from the ATLAS IP. This location is where the two separate beam pipes transition to a common straight section pipe. The ZDC can measure neutral particles at  $|\eta| \geq 8.2$ , which is very important for determining the centrality of heavy-ion collisions. For  $pp$  collisions it can be used to tag minimum-bias events. The ZDC is a sampling calorimeter made of alternating layers of quartz rods (active medium) and tungsten plates (absorber).

The ATLAS Forward Proton (AFP) [121] consists of two parts placed in each detector side at 204 m and 217 m with respect to the ATLAS IP. The project extends the physics reach of ATLAS by measuring very forward protons, and mostly focuses on the study of diffractive processes where one or both protons remain intact after the collision.

The Absolute Luminosity For ATLAS (ALFA) detector [122] is situated at a distance of  $\pm 240$  m from the interaction point. It consists of scintillating fibre trackers placed in four Roman pots stations, which can be moved very close to the beam, up to 1 mm distance from it. The main purpose of the detector is to determine the total proton-proton cross-section, and the luminosity, by measuring the proton scattering at very small angles.

The Beam Conditions Monitor (BCM) diamond sensors were primarily designed to protect the detector from damage that could be caused by a potential uncon-

trolled beam but were also used to measure the instantaneous rate of collisions.

## 6.6 Triggering and Data Acquisition

The LHC is designed to operate at a bunch crossing rate of 40 MHz. Limited resources to process and store events at this rate, lead to the implementation of a triggering system that excludes any uninteresting events and reduces the rate from 40 MHz down to approximately 1 kHz. The ATLAS triggering system consists of a hardware-based Level 1 (L1) trigger and a software-based high-level trigger system (HLT) [123].

The L1 triggering system consists of custom electronics and programmable hardware that reduce the event rate down to approximately 100 kHz. The decision to accept an event is made, in  $2.5 \mu\text{s}$ , by the central trigger processor (CPT) using signals from the L1 calorimeter trigger and the L1 muon trigger as well as information from the forward detectors such as the LUCID and ZDC. When an event is accepted from the L1 system, information is sent to the HLT in form of *Region-of-Interest* (RoI): an area in  $\eta - \phi$  where the activity occurred.

The full event information is available at the HLT level, where fast algorithms are deployed to reconstruct tracks and physics objects such as electrons, muons, jets or even missing transverse energy. The decision to accept an event is based on the requirements imposed on the online reconstructed objects. The HLT further reduces the output rate to  $\mathcal{O}(1 \text{ kHz})$ . Events are selected by *trigger chains* (often called triggers), which are combinations of algorithms used to obtain the L1 trigger item and to reconstruct and select physics objects at the HLT level. Each trigger selects a specific physics signature, such as leptons, photons, jets, missing transverse momentum or  $B$ -meson candidates. All the chains used for data taking form a list called *trigger menu*.

Often it is necessary to control the rate of accepted events. In this case, a *prescale factor*,  $n$ , is used so that each event has a  $1/n$  probability to be accepted by the trigger. The values of the prescale factors can be larger or equal to one. Individual prescale factors can be given to each chain at the L1 or the HLT. Trigger with prescale factor equal to one are called *unprescaled triggers* and are used for physics analyses. On the other hand, prescaled triggers are used, mostly in performance studies. For example, low transverse energy electron performance studies use  $J/\psi \rightarrow ee$  events recorded with prescaled triggers [124].

## 6.7 Data taking and processing

Once all the subsystems are ready and the LHC has stable beams, the so-called *run* starts. The term *run* for the ATLAS detector has a different meaning than the LHC Run defined in 5.4. In this case, it is used to describe a period that lasts for several hours, and during which the detector continuously records data. Each run is tagged by a unique *run number*.

The data recorded during different runs with similar conditions are grouped into a *period* which is marked by a capital letter, for example, D. Within each period the runs are grouped into sub-periods of five to ten runs denoted by a number. Each period contains five to ten sub-periods.

Furthermore, the events recorded in a single run are divided into groups of approximately one minute of data-taking, called *luminosity blocks*, to prevent data loss if problems occur during the run, such as sub-detector failures which affect the collected data. Based on data quality requirements, a list is formed for each run that contains only the “good” luminosity blocks and is known as *Good run list* (GRLs) files [125] to use for physics analysis. To further avoid data loss, some of the luminosity blocks in a GRL can still contain corrupted data which are flagged to be removed before using the data set in a process called *event cleaning*. Chapter 9 will describe the event cleaning process applied to the data set used in this work.

The framework ATLAS uses for data processing as well as event simulation is Athena [126], which is a C++ software based on the Gaudi framework [127] that was developed originally for the LHCb experiment. The following paragraphs will describe the main data processing steps and data formats.

When an event is recorded, the read-out from all the detector is delivered in RAW data in byte-stream format. The size of an event in this format is  $\sim 1.6$  MB. To process the enormous amount of data recorded by the LHC experiments, large-scale computing resources are necessary. The LHC *Grid* is a worldwide network of computing resources, designed for processing, storing and distributing LHC data. It is structured hierarchically in different tiers. The Tier-0 is located at CERN and is used for the first step of data processing which includes data calibration and reconstruction. All the event information is stored in Event Summary data (ESD) in the form of reconstructed objects. The next step is producing Analysis Object Data (xAOD) [128], which contains only the information necessary for physics analysis, such as reconstructed physics objects and their properties. This step is needed because the size of ESD is still too large  $\sim 1$  MB per event. The size of an event in AOD format is 200 kB.

Tier-0 is also responsible for copying RAW data to permanent storage and Tier-1 for storage and reprocessing. In addition, Tier-1 receives the output of the reconstruction. Data are further distributed to the over 160 computing centres of Tier-2, that are used to run physics analysis tasks and simulations. These centres keep AODs on the disk together with other file formats such as the so-called Derived AOD format (DxAOD) [129]. DxAODs are produced from physics analysis groups to reduce the event size and only contain physics objects and information relevant to a specific analysis.

The data files used in the analysis presented in this work are produced from DxAOD files after applying specific selection requirements discussed in detail in 10.2.1. The output is stored in ROOT [130] format. Finally, Tier-3 provides access to grid resources and local storage to individual users.

## 6.8 Reconstruction of detector objects

This section contains an overview of the reconstruction process of the objects that are used in the analysis presented in this work. The first subsection, 6.8.1, reviews the track and vertex reconstruction process. Section 6.8.2 discusses the topological clusters. Jets are discussed in section 6.8.4, electrons muons and  $\tau$ -leptons in sections 6.8.5, 6.8.6 and 6.8.7 respectively. Finally, the reconstruction of missing transverse energy is presented in section 6.8.8.

### 6.8.1 Tracks and vertices

The main goal of the ATLAS ID is the reconstruction of the trajectories of charged particles. The track reconstruction starts by forming clusters from raw measurement in the pixel and SCT detectors [131, 132]. The clusters are formed by grouping together pixels and strips, with an energy deposit above a given threshold, that share a corner or an edge. The clusters are used to create three-dimensional space points. For the pixel detector, one cluster corresponds to one space point, while for the SCT a combination from clusters from both sides of the strip layer corresponds to one point. Three space points are used as a seed for the combinatorial Kalman filter [133]. This algorithm creates the track candidates by propagating the measurements through the detector layers while incorporating additional space points that are compatible with the preliminary trajectory. The algorithm creates multiple track candidates, from all the realistic combinations of space points. Several of these candidates have overlapping or wrongly assigned hits. For this reason, a stage follows where an ambiguity solver assigns a tracking score to each candidate using several quality requirements.

For example, the algorithm penalizes tracks that do not have clusters in each detector layer and tracks with poor fit quality (based on the  $\chi^2$  of the track) or large number of shared clusters, while promotes the energetic tracks<sup>2</sup>.

After the ambiguity solving step follows the reconstruction using measurements from the TRT which completes the so-called inside-out track reconstruction technique in ATLAS, which is mostly sensitive to primary charged particles produced in the  $pp$  interaction.

The reverse approach is also used and is known as outside-in reconstruction technique [132]. In this case, the reconstruction starts from seeds in the TRT and propagates the track backwards. This method is more sensitive to tracks with few or no hits in the silicon detectors, that could be created, for example, from secondary vertices or photon conversion.

To describe the tracks a set of five parameters, the so-called perigee parameters, is used  $(z_0, d_0, \theta, \phi, q/p)$ . The perigee is the point of the closest approach of the track to the beam axis. The track parameters are illustrated in Figure 6.6. The distance  $z_0$ , along the  $z$ -axis (beam axis), to the origin is called longitudinal impact parameter. The distance,  $d_0$ , to the beam axis in the transverse plane is called transverse impact parameter.  $\theta$  is the polar angle and  $\phi$  the azimuthal angle. Finally, the parameter  $q/p$  is the charge over the particle momentum and is related to the track curvature.

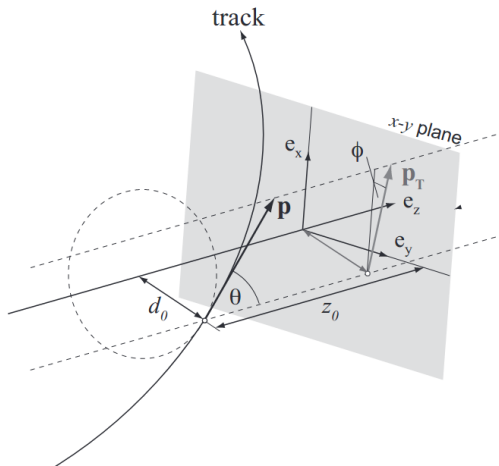


**Figure 6.6:** Track parametrization in ATLAS. Figure taken from Ref. [134].

<sup>2</sup>Tracks with incorrectly assigned clusters have typically a low  $p_T$ .

**Vertex Reconstruction.** The vertex reconstruction begins with a set of tracks that fulfil specific requirements and a seed position. An iterative fit is used to estimate the position of the vertex. In each iteration, any incompatible track is down-weighted by the algorithm and the position of the vertex is recomputed. After finding the vertex position any incompatible track is removed and then used for the reconstruction of another vertex. These steps are repeated until there are no tracks left. [135–137]

## 6.8.2 Topological cell clusters

The first step to reconstruct objects such as jets, photons, electrons and tau leptons, is creating clusters from energy deposits in the calorimeters cells. The clustering algorithm [138] forms the so-called topoclusters from topologically connected cells in the calorimeters in all three dimensions. The main observable is the so-called cell significance which is the ratio of the cell energy,  $E_{\text{cell}}$  over the expected noise,  $\sigma_{\text{cell}}$ . The expected cell noise includes the electronic noise, as well as, a contribution from pile-up, estimated for specific run conditions. To create the clusters the algorithm first locates all the cells with energy at least four times higher than the expected noise. Next, it collects any neighbouring<sup>3</sup> cells with significance higher than two. This step is repeated until there are no neighbouring cells with  $|E_{\text{cell}}| > 2\sigma_{\text{cell}}$ . Finally, the neighbouring cells are added, independently of their significance. Figure 6.7 shows a schematic example of how the clustering algorithm works.

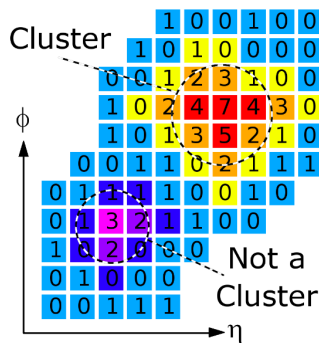


**Figure 6.7:** Two dimensional example, in the  $\eta - \phi$  plane, of the clustering algorithm. Figure from Ref. [139]

<sup>3</sup>Two cells are neighbours if they share a side on the same layer or, if they are in adjacent layers, they must (at least partially) overlap in the  $\eta - \phi$  plane

The cluster energy is reconstructed, by default, in the *electromagnetic* (EM) scale. However, to account for the non-compensating nature of the ATLAS calorimeter, the topoclusters can be further calibrated to match the expected energy deposition from hadronic showers, using the so-called *local cluster weighting* (LCW or LC) method. With this method, the clusters are classified as electromagnetic or hadronic and for each cell a correction factor is derived from simulated, single charged and neutral pions.

An additional origin correction is applied to topoclusters that modifies their momentum to point to the primary vertex instead of the detector centre [140].

### 6.8.3 Particle Flow objects

To reconstruct jets dedicated algorithms (discussed in the next subsection) read inputs from a list and group them together in one object. The inputs for these algorithms can be topoclusters, tracks of charged particles, or a combination of both creating the so-called *particle flow* (PFlow) objects [131]. The PFlow objects benefit from the properties of both the tracking and the calorimeter systems. The ID offers better momentum and angular resolution for low  $p_T$  particles and allows to distinguish tracks originating from the hard scatter vertex. On the other hand, calorimeters offer better energy resolution at high  $p_T$  and can detect neutral particles. The algorithm that combines tracks and topoclusters must not double-count the energy. For this reason, when the tracking information is used for a particle, the corresponding shower from the calorimeter is removed. This is a quite challenging task since subtracting the expected energy from the calorimeter cells must not affect the deposits from other particles.

The first step is the track selection: the algorithm considers only tracks that fulfil tight selection requirements (more hits are required in the first two layers of the ID and no missing hits on the pixel detector) and must have  $p_T < 40$  GeV. This limit is set because energetic particles are not well isolated from nearby activity making the subtraction complicated. The next step is matching the tracks to the clusters. There is a probability that a single particle deposits energy in multiple clusters. This probability is calculated by the particle flow algorithm and depending on the result more clusters might be added to the track-topocluster system. For each track-topocluster system the algorithm subtracts the expected energy deposit from the calorimeter cell-by-cell. Whole clusters can be removed during this process if the energy after this subtraction is equivalent to the fluctuation of a single particle deposit. The selected tracks and remaining topoclusters are the particle flow objects that are used as inputs to jet finding algorithms.

## 6.8.4 Jet reconstruction

Tracks, topoclusters or PFlow objects can be used as inputs to reconstruct jets. A jet finding algorithm takes these inputs and combines them to jets. In this work jets are created using the anti- $k_T$  algorithm [141] which is a sequential recombination algorithm. All sequential recombination algorithms are infrared and collinear safe, i.e. emissions of soft gluons and collinear splitting of partons do not change the outcome. The algorithms use two parameters,

$$d_{ij} = \min(p_{Ti}^{2p}, p_{Tj}^{2p}) \frac{\Delta R_{ij}^2}{R^2}, \quad (6.2)$$

$$d_{iB} = p_{Ti}^{2p}, \quad (6.3)$$

where  $R$  is the distance parameter that determines the maximum allowed distance between the two objects,  $\Delta R_{ij}^2 = \Delta\phi_{ij}^2 + \Delta\eta_{ij}^2$ ,  $d_{ij}$  is the distance between the input objects,  $d_{iB}$  is the distance between object and beam and the exponent  $p$  can be  $-1, 0$  or  $1$ . The algorithms proceed via the following steps:

1. The distances  $d_{ij}$  and  $d_{iB}$  are calculated for all possible combinations of the input objects.
2. If  $d_{ij}$  is smaller than  $d_{iB}$  the objects  $i$  and  $j$  are combined.
3. If  $d_{iB}$  is the smallest, then  $i$  is a jet and it is removed from the input list

These steps are repeated until there are no more objects in the list. The value of the exponent determines the type of the algorithm: anti- $k_T$  corresponds to  $p = -1$ . Setting  $p = -1$  in Equations 6.2 and 6.3 the components with the higher transverse momentum are combined first. Since the direction of the jet axis is mostly determined by the highest  $p_T$  object, the axis of high- $p_T$  jets is determined from the beginning. For this reason, jets with high  $p_T$  have a circular shape, as shown in Figure 6.8, while jets with lower  $p_T$  might have more irregular shapes.

There are two more sequential recombination algorithms, the  $k_T$  algorithm [142, 143] with  $p = 1$  and the Cambridge/Aachen [144] with  $p = 0$ . The  $k_T$  algorithm clusters the softer object first and the jet direction is changing as higher  $p_T$  objects are added, leading to the random shapes of jet active area. The Cambridge/Aachen is independent of the objects' transverse momentum and depends only on the angular separation between them. In this case pairs with lower  $\Delta R_{ij}$  are combined first, resulting in irregular shapes as well. Figure

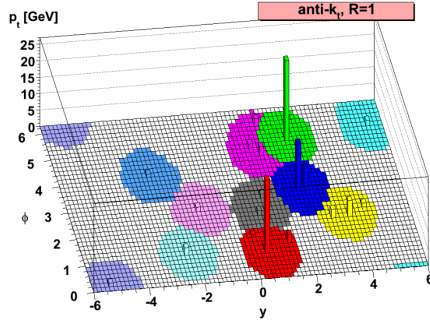


**Figure 6.8:** Example of the jet active area for simulated parton-level event clustered using the anti- $k_T$  algorithm. Figure from taken from [141].

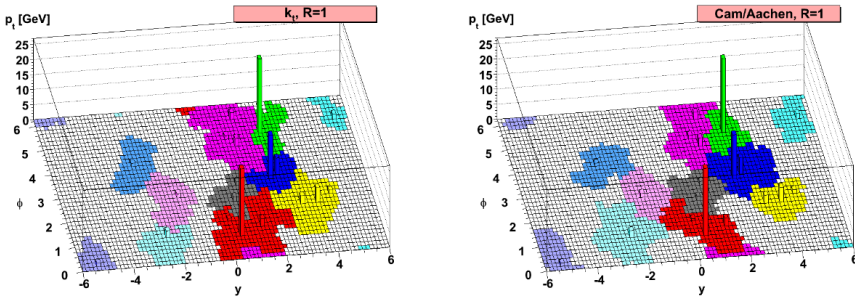


**Figure 6.9:** Example of active areas of jet clustered with the  $k_T$  algorithm (left) and Cambridge/Aachen (right). Figure from taken from Ref. [141].

6.9 illustrates examples of jets created using the  $k_T$  algorithm on the left, and Cambridge/Aachen on the right.

Different types of jets can be defined, depending on the inputs, jet finding algorithm and distance parameter  $R$  that is used. In this work, all the jets are reconstructed using the anti- $k_T$  algorithm. They are classified as *small- $R$*  jets that are reconstructed from PFlow objects with a distance parameter of  $R = 0.4$  or as *large- $R$*  jets reconstructed from LCW weighted topoclusters with a distance parameter of  $R = 1.0$ .

The energy of the reconstructed jets needs to be calibrated further to account for the different responses across the calorimeters, the presence of inactive material, cases where the showers extend beyond the calorimeter volume, pile-up effects, noise and out-of-cone radiation. The calibration for the jet energy scale (JES) consists of several steps, each compensating for different effects. In the following

paragraphs there is a brief description of the calibration process for small- $R$  and large- $R$  jets.

**Calibration of small- $R$  jets.** The first step of the calibration procedure [145, 140] addresses pile-up effects, and aims to remove excess energy from in-time and out-of-time pile up. In this step, corrections are estimated and then subtracted from the jet’s transverse momentum, without affecting  $\eta$  or  $\phi$  [146]. The next step removes residual pile-up dependence, using a correction derived from a Monte Carlo simulation. After that follows a correction of the four-momentum of the reconstructed jet, to match the four-momentum of truth jets, i.e jets created with the same clustering algorithm using as inputs stable particles from simulated events. This is done by accounting for the non-compensating nature of the calorimeter, energy losses in the dead material, out-of-cone effects, and biases in the jet  $\eta$  reconstruction. The following step mitigates energy leakage and flavour dependence of the jets, i.e. variations on the calorimeter response and jet reconstruction that depend on which particle initiated the jet. The corrections, in this step, are derived using the structure of the energy deposits in the calorimeters and information from both the tracking and muon systems. Finally, the so-called *in situ* calibration is applied that accounts for differences between the jet response in data and simulations, which occur due to imperfect simulation of the detector and the physics processes involved. The correction is obtained by calculating the response in data and simulation separately, using events with a jet recoiling against a well-measured reference object, for example a photon, and then applying the ratio of these responses as an additional correction in data.

In addition to the central value of the JES, another important quantity is the jet energy resolution (JER), which depends on the stochastic nature of the showers, the irreducible pile-up contributions and the electronic noise, and can be parametrised as

$$\frac{\sigma_{p_T}}{p_T} = \frac{N}{p_T} \oplus \frac{S}{\sqrt{p_T}} \oplus C.$$

Here,  $N$  is the term for the noise,  $S$  is the stochastic term and  $C$  is a constant term related to the design of the detector and the geometry.

**Calibration of large- $R$  jets.** The jets, in this case, undergo a so-called “*grooming*” procedure to reduce pile-up contributions. For the grooming the trimming algorithm [147] is used, which re-clusters the jet constituents using the  $k_T$  algorithm with  $R = 0.2$  and removes those that carry less than 5% of the jet transverse momentum. The jet mass for large- $R$  jets is derived from the

weighted average of a calorimeter-based term and a track-assisted, one using the tracks associated to the jet [148]. Large- $R$  jets are also calibrated to match the truth jets, which are reconstructed using the anti- $k_T$  algorithm and are also trimmed, as described above. The calibration brings the jets to the particle-level energy scale, mass scale and  $\eta$ . The last step is the in situ calibration that accounts for differences between data and simulations. The uncertainties associated with the Jet Mass Scale (JMS) calibration are estimated by calculating the ratio of the calorimeter-based mass term over the track assisted term and then comparing the ratio estimated for data and simulated events [148]. The JES related uncertainties are estimated from the in situ calibration, as described in Ref. [149].

**Variable-Radius track jets** Another type of jets used in this work is the so-called *Variable radius track jets* [150]. These jets are reconstructed using as inputs tracks associated to the large- $R$  jets described in the previous section, and a variable distance parameter,  $R_{eff}$ , that is  $R_{eff} = \frac{\rho}{p_T}$ , where  $p_T$  is the jet transverse momentum.

## ***b*-tagging**

In this work the ability to correctly identify jets from  $B$ -hadrons, also called  $b$ -jets, is very important. The identification of such jets takes advantage of the unique characteristics of the  $B$ -hadrons: they have an average life-time of approximately 1.5 ps [151, 152] which means that they travel a few millimetres before they decay, creating a secondary vertex as illustrated in Figure 6.10. There are two steps in the identification of  $b$ -jets. In the first, the algorithms (known as *low-level*) use the tracks associated to a jet and their impact parameters to determine if they are coming from a secondary vertex. In the second step multivariate classifiers are used to increase the efficiency, also called *high-level* algorithms. There are several low-level algorithms, listed bellow.

- The impact parameter (IP) based algorithms IP2D and IP3D which use the information of the impact parameter of the tracks associated to the jets. [153].
- The SV1 algorithm which is based on the reconstruction of the secondary vertex [154].
- The JetFitter algorithm [155] which reconstructs the full decay chain of  $b$ - and  $c$ -hadrons.

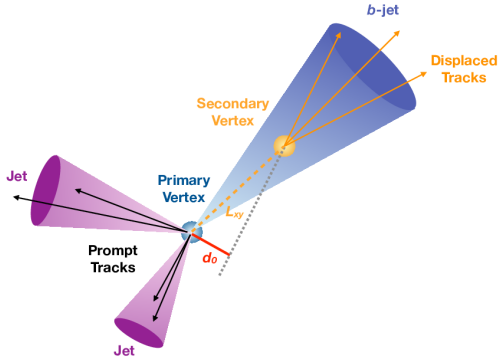


**Figure 6.10:** Example of the production of two light jets and a  $b$ -jet in the transverse plane. Figure from Ref. [156] .

The outputs of the low-level algorithms are used as input to the high-level. There are two main high-level algorithms used in ATLAS called MV2 and DL1. The first is using Boosted Decision Tree (BDT), while the DL1 uses Deep Neural Network (DNN) [157]. DL1 uses the same inputs as MV2 as well as input from the JetFitter which improves the rejection of the  $c$ - and light jets with respect to the MV2.

The performance of an algorithm is accessed in terms of the *efficiency* and the ability to reject light-flavour and  $c$ -jets. The  $b$ -tagging efficiency is the probability that the algorithm correctly identifies a  $b$ -jet. The probability of mistakenly tagging a  $c$ -jet or light-flavour jet as a  $b$ -jet, is called the mistag rate. The  $b$ -tagging efficiency is estimated from simulations and collision data separately, and the ratio between data and simulation, called Scale Factor (SF), is used to weight simulated events on a jet-by-jet basis. To estimate the  $b$ -tagging efficiency and mistag rates in data,  $t\bar{t}$  events are used with two opposite sign leptons and two jets in the final state. The efficiencies and mistag rates for the MV2 algorithm are provided in Ref. [158, 159].

### 6.8.5 Electrons

The analysis presented in this thesis uses electrons in a central region of the detector with  $|\eta| < 2.47$ . This subsection contains an overview of the electron reconstruction, identification and isolation based on Reference [124]. An electron signature is characterised by a track in the inner detector that is matched closely

in  $\eta - \phi$  with an energy deposit in the electromagnetic calorimeter. The first step in the electron reconstruction, is forming topoclusters from energy deposits in the electromagnetic calorimeter, as explained in 6.8.2. After the topoclusters are selected, tracks that match loosely the cluster are refitted to account for bremsstrahlung effects. This step distinguish electrons from photons: if there is no matching track the topocluster is considered as a photon. However, photons can produce electron pairs in the ID, and in this case, are called converted. The electrons from a photon conversion will have tracks that point back to the conversion vertex, instead of the primary vertex. Whether the track points to a secondary or primary vertex determines if the cluster is considered as an electron or a converted photon. The next step is to build the so-called super clusters. Topoclusters with specific requirements on the transverse energy and on the matched track, described in [124], are used as seeds. All clusters in windows of  $3 \times 5$  towers ( $\Delta\eta \times \Delta\phi = 0.075 \times 0.125$ ) around the barycenter of the topocluster are collected. The clusters inside the window are called satellite clusters. For electrons, the window can be bigger,  $5 \times 12$  towers, if the satellite cluster in this extended window shares the best-matched track with the topocluster. The seed together with the satellite clusters are the super clusters. After this step the super cluster energy and position are calibrated, and the cluster is matched to tracks, for electrons and conversion vertices for converted photons.

The electron identification uses a likelihood-based multivariate analysis (MVA) technique. This method uses the probability density functions (pdfs) of several discriminating variables described in Ref. [124], to estimate the probability of a given object to be signal or background. In this case, the signal is electrons from the primary vertex or from decays of heavy resonances, while the background is misidentified hadronic jets, electrons from photon conversion or from the decays of heavy flavour hadrons. The identification depends on the value of a likelihood based (LH) discriminant calculated for each electron which has a sharp peak at one for signal and at zero for background. A set of four threshold values defines four operating points, with specific identification efficiency and background rejection. The operating point are “*VeryLoose*”, “*Loose*”, “*Medium*”, “*Tight*”. For the last three working points the identification efficiency for an electron of 40 GeV transverse energy is 93%, 88% and 80% respectively. For the analysis described in this work, the working point is a variation of the Loose, called LooseAndBLayer, which has the additional requirement that the tracks must have a hit in the BLayer of the pixel detector.

Electrons produced in the initial collision or heavy resonance decays (for example decays of  $W/Z$  bosons or  $\tau$ -leptons) are called *prompt*. Usually, prompt electrons are characterised by little activity in the nearby area in  $\eta - \phi$ . The activity near the tracks and clusters is quantified using two variables:  $p_T^{cone20}$  and  $E_T^{cone20}$ , for

the track and calorimeter isolation respectively. The  $p_T^{cone20}$  is defined as the sum of the transverse momenta of tracks with  $p_T > 1 \text{ GeV}$  in a cone around the electron track with variable distance:  $\Delta R < \frac{10 \text{ GeV}}{p_T}$  with a maximum of 0.2. The  $E_T^{cone20}$  is defined as the sum of transverse energy of all the clusters in distance  $\Delta R < 0.2$  from the electron cluster barycenter. These variables are used to distinguish prompt electrons from the background.

The calibration of electrons and photons consists of an optimization of the energy resolution with a multivariate algorithm based on the EM shower properties, corrections for differences between data and simulation, and estimation of energy corrections using  $Z \rightarrow e^+e^-$  and  $J/\psi \rightarrow e^+e^-$  events [124].

### 6.8.6 Muons

This section contains an overview of the muon reconstruction, identification and isolation based on Reference [160]. First tracks are reconstructed in the ID, as described in 6.8.1, and in the MS independently. The first step of the track reconstruction in MS is to search for hit patterns inside each muon chamber and form track segments. Next, to build the track candidates hits from segments in different layers are fitted. Since the same segment can be used to form different track candidates an overlap removal algorithm is used to either allow a segment to be shared between two tracks or assign the segment to a single track candidate. Finally, the hits from each track candidate are fitted and candidates are accepted based on the fit quality. The information from ID and MS are then combined to reconstruct the muons. The following muon types are defined:

- Combined muons (CB). For this type, the tracks are reconstructed independently in the ID and MS and then are combined.
- Segment-tagged (ST) muons. The track from the ID is first, extrapolated to the MS. Then, if there is at least one track segment in the MDT or CSC chambers it is determined as a muon track. This type is used either for muons with low  $p_T$  or muons that cross one layer of the MS.
- Calorimeter-tagged (CT) muons. In this case, the track from the ID must match an energy deposit in the calorimeter compatible with a minimum-ionizing particle. This type of muon can be used to recover acceptance in regions where the MS is not well-instrumented, because no information from the MS are used for the reconstruction.
- Extrapolated (ME) muons. For this muon type the reconstruction is based on the MS tracks for which only a loose requirement is applied on their

compatibility with the primary vertex. As no information from the ID is required, this type of muons is used to recover acceptance in the forward region that is outside of the ID coverage.

All the types mentioned above are reconstructed independently which results in overlaps between muon candidates. To resolve the overlaps that occur when two muon types share an ID track, preference is given first to CB muons, then to ST and finally to CT muons. To resolve overlaps with ME muons, the algorithm examines the properties of the tracks and the fit quality. Similar to electrons, the analysis is interested in prompt muons. To distinguish them from non-prompt muons several sets of criteria are defined. The criteria aim to reject mostly muons from pion and Kaon decays and select prompt muons with high efficiency. The tracks, in these cases have a characteristic “kink” making the quality of the fitted track very poor. Therefore one of the most important variables for the requirements definitions is the quality of the fit for the combined track. Two more variables, equally important are the  $q/p$  significance and the compatibility of the momentum of the muon  $p_T$  measured in the ID and MS independently. The  $q/p$  significance, where  $q$  is the charge and  $p$  the momentum, is defined as  $|q/p|/\sigma(|q/p|)$ , where  $\sigma(|q/p|)$  is the quadrature sum of all the corresponding uncertainties. To ensure a robust momentum measurement there are specific requirements on the number of hits in each layer of the ID and the number of hits in MS tracks are used.

Each combination of requirements defines an identification working point. There are five such WPs: Medium, Loose, Tight, Low- $p_T$  and High- $p_T$  [161]. The three first are the most commonly used in physics analyses. Each of the Loose, Medium, and Tight WPs selects muons in a subset of the previous category (for example muons in Medium also pass Loose selection). Finally, isolation requirements are also defined for the muon candidates, based on quality requirements of the tracks and the variables  $p_T^{cone30}$  and  $E_T^{cone20}$ , for the track and calorimeter isolation respectively. The variables are defined similarly to electrons, only changing the distance variable for the  $p_T^{cone30}$  to  $\Delta R < \max(\frac{10\text{GeV}}{p_T}, 0.3)$ .

The calibration procedure, described in Ref. [161], uses  $Z \rightarrow \mu^+\mu^-$  and  $J/\psi \rightarrow \mu^+\mu^-$  events to calculate and validate scale factors that correct differences in the momentum of the reconstructed muons between data and simulation, and to estimate the momentum scale and resolution.

### 6.8.7 Taus

When a tau lepton is produced in a collision, because of its really short life time of  $2.9 \times 10^{-13}$  s, it decays before reaching the IBL of the pixel detector. Therefore

taus are observed via their decay products. Taus decay either leptonically with a BR of  $\sim 35\%$  or hadronically with a BR of  $\sim 65\%$ . The leptonic decays produce well isolated electrons and muons that are reconstructed as it was explained previously. In this work the focus will be on the hadronically decaying taus because they can be a significant background contribution because of the jet-like signature they create. This signature has several characteristics that can be used to identify and veto them. Hadronic tau decays involve one or three pions<sup>4</sup>, which are called *1-prong* and *3-prong* respectively [162] and the jet is usually narrow.

To reconstruct the tau-candidates, the first step is to form jets using the anti- $k_T$  algorithm (as described in 6.8.4) with a distance parameter of  $R = 0.4$  using LCW topoclusters as inputs. The jets must have  $p_T$  above 10 GeV and  $|\eta| < 2.5$ . The vertex of the tau lepton is identified among the PV candidates and is associated to the candidate. Next tracks from ID with  $p_T > 1$  GeV that fulfil the requirements listed in Ref. [162], are matched to the jet if they are within  $\Delta R < 0.2$  of the jet axis.

Once the tau-candidates are reconstructed several identification requirements are applied to distinguish them from other jet-like signatures. For the identification a Recursive Neural Network (RNN) is used, described in Ref. [163], which uses as inputs variables and observables calculated from the associated tracks or the topoclusters. Four working points are defined: “*VeryLoose*”, “*Loose*”, “*Medium*”, “*Tight*” with decreasing signal efficiency and increasing background rejection. In this work the Very Loose working point is used which has an efficiency of 95% for both 1- and 3-prong. Finally, an energy calibration is applied.

### 6.8.8 Missing Transverse Energy

In proton-proton collisions the partons that participate in the hard interaction have momentum along the beam axis ( $z$ -axis) and almost zero momentum in the transverse plane. Because of momentum conservation, it is expected that the vector sum of the transverse momenta of all the collision products is negligible. If there is an imbalance, the negative of the vector sum is called missing transverse momentum and is denoted as  $\vec{E}_T^{miss}$ . The reconstruction of the missing transverse momentum starts after the objects mentioned previously (jets, photons and leptons) are reconstructed and calibrated. Because the objects are reconstructed independently some energy deposits or associated tracks can be used for multiple objects. Therefore, before proceeding with the estimation of the  $\vec{E}_T^{miss}$  there is a step to remove any overlaps.

---

<sup>4</sup> $\tau \rightarrow \pi^0 \pi^- \nu_\tau$  or  $\tau \rightarrow \pi^+ \pi^- \pi^- \nu_\tau$

The reconstructed electrons, muons, hadronic decaying visible taus, photons, muons and jets, i.e the high  $\vec{p}_T$  physics objects, are the so-called *hard*-term of  $\vec{E}_T^{miss}$ . On the other hand tracks from the primary vertex that are not associated with any of the “hard” objects are the *soft* component. The expression for the  $\vec{E}_T^{miss}$  reads:

$$\vec{E}_T^{miss} = - \sum \vec{p}_T^e - \sum \vec{p}_T^\gamma - \sum \vec{p}_T^\tau - \sum \vec{p}_T^\mu - \sum \vec{p}_T^{\text{jets}} - \sum \vec{p}_T^{\text{soft}} \quad (6.4)$$

The soft term is very important for estimating the  $E_T^{miss}$  scale and resolution, especially in events that have low multiplicities of hard objects. It is reconstructed using tracks from the ID associated to the PV. The magnitude of the missing transverse momentum,  $E_T^{miss}$ , is defined as ( $|\vec{E}_T^{miss}| = \sqrt{E_x^{miss} + E_y^{miss}}$ ). The corresponding azimuth angle is :  $\phi^{miss} = \arctan(E_x^{miss}, E_y^{miss})$ . The total transverse energy in the detector  $\sum E_T$  quantifies the total event activity and is an important observable for understanding the resolution of the  $E_T^{miss}$ . Finally, the scalar sum of the transverse momenta of the reconstructed objects is denoted as  $H_T$ :

$$H_T = \sum p_T^e - \sum p_T^\gamma - \sum p_T^\tau - \sum p_T^\mu - \sum p_T^{\text{jets}} \quad (6.5)$$

## 6.9 Event simulation chain in ATLAS

The output of the event generators, described in Chapter 4, consists of final state particles, i.e. particles that do not decay immediately after being produced, and is stored in a form of HepMC files [164] readable by the Athena framework called *EVNT* files. For some processes the generator output is “filtered” to increase statistics in a particular region of phase space for the specific process. In such cases, a so-called *event filter* or *generator filter* is applied at the event generation step that keeps only events that fulfil specific requirements (such filters are used in the analysis and are discussed in 9).

The EVNT files are the input to the detector simulation [165], which is performed with the help of the GEANT4 particle simulation toolkit [166]. GEANT4 contains many models for the interaction processes inside the detector, as well as cross sections for a large range of energies, which are collected in *physics lists*. The geometrical description of the detector and the running conditions are stored in databases. The detector geometry database contains information on the volume and position of each detector component, its material and maps of the magnetic fields. On the other hand, the condition database has information on inactive/dead material, calibration constants or misalignments

and distortions. The output of the detector simulation step is energy deposits and is stored using the HITS file format. The next step is the digitization of these energy deposits which converts them to what the detector would actually record: pulses and currents in byte-stream format. The file format for this step is the so-called Raw Digital Object (RDO). From that point on the file formats used for the simulated events is the same as those used for data, as the same reconstruction software is used.

In the experiment, there are two types of derived objects for simulated events. One is the created from the xAOD files generated from the reconstruction of simulated events. The other is produced directly from the output of the generators before the detector simulation step described above and is referred to as *truth* DxAOD. There are four types (centrally produced) of truth DxAOD, with different amounts of information retained. For example, Truth0 is a copy of the full generator output, while Truth1, Truth2, and Truth3 contain reduced versions of the output.

The truth-level information is a key ingredient for the study of the acceptance of a physics analysis, as well as the estimation of the associated systematic uncertainties related to the modelling of background and signal processes. Truth3 is recommended for these studies, however, in this work a modified version of Truth3 is used because the centrally produced ones did not contain all the necessary information. Chapter 10 (Sec. 10.1) describes in detail the truth-level definitions implemented in this case. Chapter 11 discusses how the systematic uncertainties related to the modelling are estimated from the results of the work described in Ch. 10 and then implemented in the statistical data analysis model.



## Chapter 7

# Calibration of the Transition Radiation Tracker

As described in Section 6.2, the Transition Radiation Tracker (TRT) contributes significantly to the momentum measurement of charged particles and to particle identification. The detecting elements of the TRT, the straw tubes, register time information, which is corrected for several effects and then translated to distance of the charged particle to the wire of a straw tube through the calibration procedure. In fact, two parameters are estimated with the calibration, the correction to the time measurement, called  $T_0$ , and a relation between distance from the wire and time, called  $r$ - $t$  relation. The calibration is necessary to ensure the best position resolution and hence momentum measurement in the TRT.

This chapter presents studies of the performance of the calibration procedure using simulated event samples. The first section of this chapter, 7.1, contains an overview of the detector design and layout, and Section 7.2 describes how the time information is recorded by the TRT readout electronics. Section 7.3 introduces quantities that are used in the TRT time calibration, and to evaluate the performance of the calibration procedure. Section 7.4 describes the calibration procedure used for data and simulated events. Section 7.5 presents the method to validate the output of the calibration procedure, and estimate a time offset  $\hat{\mu}$ , which is used to improve the position resolution in data.

Part of my work for the TRT software development and performance group was to perform a calibration of simulated events, the results of which are reported in section 7.6. The main part of my work was to re-estimate  $\hat{\mu}$  after varying the  $p_T$  threshold of the reconstructed tracks used in the calibration. Section 7.7 presents the results of this study using simulated events without a pile-

up contribution, while section 7.8 shows the results of the same study using simulated events that contain a pile-up contribution.

## 7.1 Detector design

The TRT detector consists of approximately 300000 thin-layered straw tubes of a 2 mm radius. The detector is divided into three parts, shown in Figure 7.1: the barrel and two end-caps. The barrel covers a region of  $|\eta| < 1$  and consists of 52544 straw tubes aligned parallel to the  $z$ -axis, organised into three layers. The two end-caps cover a region of  $0.8 < |\eta| < 2$ . They consist of 122880 straws oriented radially to the beam axis, and they are placed on 14 wheels. This orientation was selected because it maximises the number of straws a particle will cross as it passes through the detector.

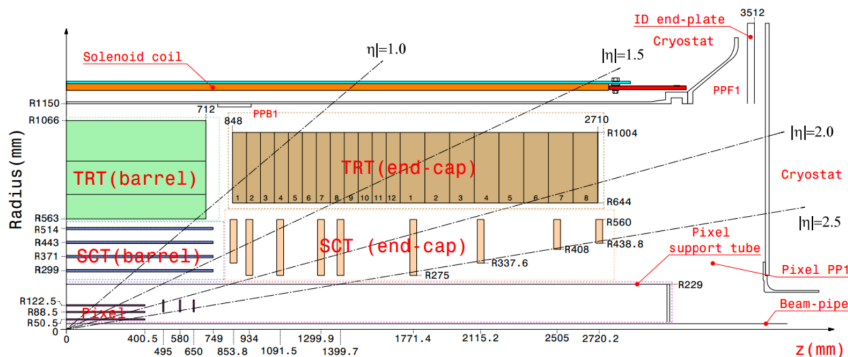


**Figure 7.1:** Schematic representation of the ATLAS Inner Detector in the  $r$ - $z$  plane [167]. Only the A-side of the detector is shown

The straw tubes work as proportional gas chambers. Their walls are made of two layers of polyamide film supported by carbon fibres, and each tube is filled with gas. In the centre of each straw tube, there is a  $30 \mu\text{m}$  thick tungsten wire coated with a thin layer ( $0.6$ - $0.7 \mu\text{m}$ ) of gold. The walls are placed at a negative voltage of  $-1.5 \text{ keV}$  with respect to the wire, which is kept at ground voltage, creating a radial electric field.

When a charged particle crosses a straw tube, it interacts with the atoms of the gas and creates several ionisation clusters along its path. The electric field inside the straw tubes forces the electrons from the ionisation clusters to drift towards the wire (anode). Closer to the wire, the electric field is stronger, and the electrons drifting toward it produce further ionisations that lead to a cascade and a detectable signal - this is discussed in Section 7.2. This signal is then

used to measure the time it takes these electrons to reach the anode, which is called *drift time*, and to identify electrons. Particle identification is achieved, as discussed in Sec. 6.2, by detecting the so-called *transition radiation* [168].

The transition radiation is emitted when a charged particle moves through a non-uniform electric field, such as crossing the boundary between two media with different dielectric constants. The probability of a particle emitting transition radiation depends on the material properties and the Lorentz  $\gamma$ -factor,  $\gamma = E/m$ .

When a relativistic charged particle crosses a single boundary from vacuum to a medium with some dielectric constant  $\epsilon$ , the energy of the emitted transition radiation is given by

$$E = \frac{1}{3}\alpha Z^2\omega_p\gamma, \quad (7.1)$$

where  $\alpha$  is the fine structure constant,  $Z$  is the atomic number, and  $\omega_p$  is the so-called plasma frequency, which is given by

$$\omega_p = \sqrt{4\pi N_e r_e^3 m_e / \alpha}. \quad (7.2)$$

Here,  $N_e$  is the electron density of the medium and  $r_e$  is the classical radius of the electron [169].

To increase the amount of transition radiation, the charged particle needs to cross a large number of boundaries. For this reason, the spaces between the straw tubes of the TRT are filled with polypropylene fibres in the barrel region and polypropylene foils in the end-cap regions.

The number of transition radiation photons produced from an electron is considerably larger than those created from a pion, due to the much higher Lorentz factor. This allows us to distinguish electrons from pions.

Once the transition radiation photons are produced they enter the straw tubes and interact with the gas producing electron-ion pairs. Since the photo-absorption cross section,  $\sigma_{\text{photo}}$  depends on the atomic number ( $\sigma_{\text{photo}} \propto Z^5$ ), the tubes must be filled with a gas with high  $Z$ . The transition radiation photons typically have energies between 5 keV to 15 keV [170], and the gas that efficiently detects X-ray photons is xenon with  $Z = 54$ .

Instead of pure xenon, a gas mixture of 27% carbon dioxide, 3% oxygen and 70% xenon is used. The carbon dioxide works as a quench gas and absorbs UV photons produced during the avalanche. Based on studies reported in Ref. [171], not all the UV photons are absorbed from the carbon dioxide. For this reason, oxygen is added to the mixture. Even though oxygen does not absorb UV photons, the ozone created in the avalanches absorbs them.

During Run 1, all straws were filled with the xenon-based (Xe-based) gas mixture described above. Due to large leaks that appeared in the system that supplies the gas to the detector elements [172, 173], the xenon-based mixture was replaced in the straws that could not be repaired with a cheaper argon-based (Ar-based) gas mixture for Run-2. The Ar-based gas mixture consists of 27% carbon dioxide, 3% oxygen and 70% argon. Figure 7.2 shows the gas used to fill the straw tubes in the TRT barrel and end-cap regions during 2016. During 2017 there was a

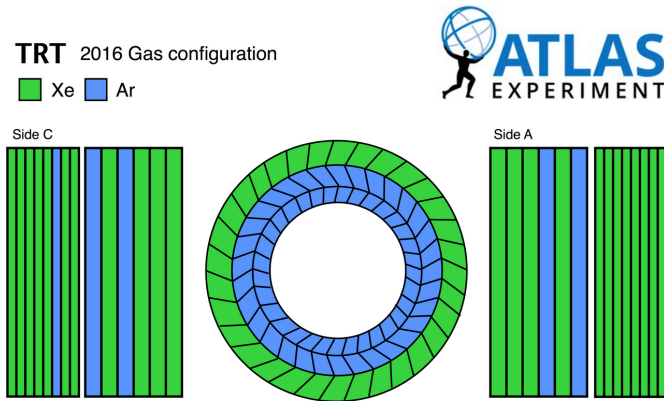


**Figure 7.2:** Gas configuration of the TRT detector used during 2016 [174]. The barrel layers in the middle. On each side of the barrel, the figure shows the 14 wheels of the end-caps. The blue-coloured regions have straw tubes filled with the argon-based gas mixture, while green-coloured have straws filled with the xenon-based mixture.

change in end-cap C: the straw tubes of the third wheel from the barrel were filled with Ar-based gas and the fourth wheel with Xe-based gas.

The argon-based mixture is less efficient in absorbing UV photons, which decreases the particle identification capabilities of the TRT. On the contrary, the tracking capability of the detector is generally unaffected by using the argon gas mixture, with some differences in terms of performance with respect to the xenon gas mixture [172]. One difference is that the drift velocity in the argon-based mixture is higher than in the xenon-based, which leads to shorter measured drift times for argon-filled straw tubes. Additionally, the Ar-based mixture has a lower density than the Xe-based, and the average distance between ionisation clusters is higher, leading to degradation of the drift-time measurement. Finally, the signal shape is different between the two gas mixtures.

## 7.2 Signal description

The front-end electronics record signals in a window of 75 ns, equivalent to 3 bunch crossings. The signal in a single wire consists of a sharp pulse created by the electrons from the avalanche reaching the wire, and a falling tail created by the much slower ions that drifted to the cathode. The recorded signal is first amplified, then shaped to remove the ion tails, and finally discriminated against two predefined thresholds, the *low threshold* (LT) and *high threshold* (HT). Figure 7.3 shows an example pulse, after shaping, from a single straw in a window of 75 ns. The two thresholds are indicated in the figure.

The LT is used to measure the electron drift time, while the HT is used to detect signals from transition radiation photons for the electron-pion separation. Typical values for the LT range from 100 eV to 300 eV. For an Ar-based mixture, the TRT read-out electronics integrate more charge during the signal processing than for a Xe-based mixture (about 15% instead of 5%) because of the different signal shape. As a result, a lower value for the LT can be used for straw tubes filled with Ar-based mixture compared to those filled with Xe-based gas, which leads to an improvement of the drift-time measurement accuracy [172]. Typical values for HT range between 5 keV and 7 keV.

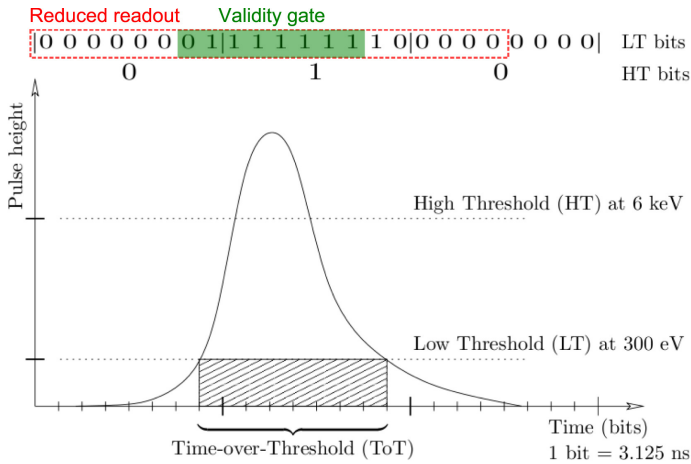


**Figure 7.3:** Example of a pulse from a single TRT straw. Picture modified from [175]

The signal information is recorded in 27 bits, as illustrated on the top of Figure 7.3 covering 75 ns. For each bunch crossing, there are nine bits. Eight of these bits hold the information for the LT and one for HT, as shown in Figure 7.3 (the LT information is 24 bits in total, while HT is stored in 3 bits). The ninth bit is set to 1 only when the pulse exceeds the HT indicating a possible electron and

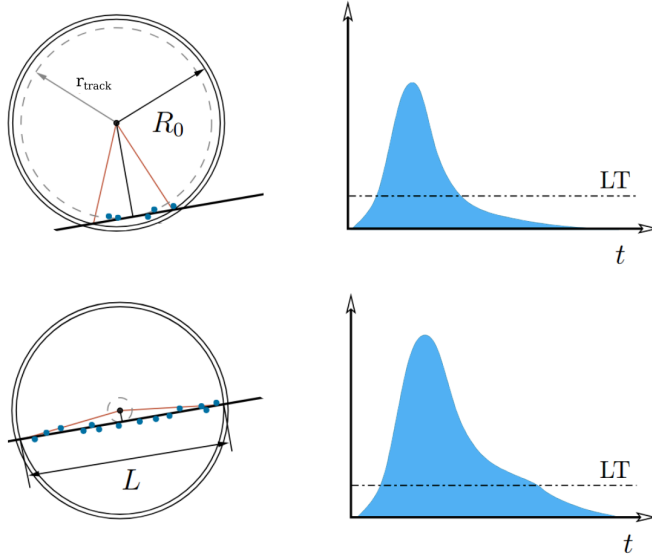


**Figure 7.4:** Signals for tracks close to the walls (top) and to the wire (bottom). The low threshold is marked with a dashed line. Figure modified from Ref. [179]

hence, is used for particle identification. For Run-2 the last 4 bits of the third bunch crossing are dropped [176] to achieve a 100 kHz rate in the level-1 trigger without losing vital timing information. This is the so-called *reduced readout*, shown in Figure 7.3.

The first time the signal rises above the LT is called leading-edge time. This corresponds to the first transition from value 0 to 1, and the measured leading-edge time is the time at the centre of this first 1 bin [177, 178]. On the other hand, the first transition from 1 to 0 is called trailing edge (TE). The time interval between the LE and TE is the so-called *Time Over Threshold* (TOT). The width of the pulse, and hence the TOT, depends on the proximity of the track to the wire. Tracks closer to the wire deposit on average more energy inside the straw tube compared to tracks close to the walls, due to their larger length, as illustrated on Figure 7.4. Therefore, for tracks closer to the wire the corresponding signal, and the ToT, are larger.

Finally, a tunable gate, called *validity gate*, is applied to limit the data flow in the readout drivers (ROD) and to reject hits from the out-of-time pile-up. The drift time information from the straw is considered *valid* if there is at least one low threshold bit set within this gate.

### 7.3 Calibration figures of merit

As discussed in the previous section, TRT electronics measure LE time, which is not equal to the electron drift time. Besides the drift time  $t_D$ , the measured LE time  $t_{LE}$  includes several systematic effects: the time at which the collision took place,  $t_{\text{collision}}$ , the time it takes for a charged particle to reach the straw, known as *time of flight*,  $t_{\text{ToF}}$ , and the time the signal needs to propagate in both directions of the wire<sup>1</sup>, denoted as  $t_{\text{SP}}$ . The LE time is, therefore, given by:

$$t_{LE} = t_D + (t_{\text{collision}} + t_{\text{ToF}} + t_{\text{SP}}) \quad (7.3)$$

The time parameters  $t_{\text{collision}}$ ,  $t_{\text{ToF}}$ ,  $t_{\text{SP}}$  do not change much over a small region of the detector and can be replaced with a single parameter, denoted as  $T_0$ . In the work described here, the  $T_0$

From the relationship 7.3 we can find the measured drift time, for a given  $T_0$  and LE time. The drift time corresponds to a distance known as *drift radius*,  $r_D$ , which is obtained via a relation between the drift time and distance from the wire, called the *r-t* relation. The r-t relation and  $T_0$  are calculated with the calibration procedure, which is discussed in Sec. 7.4. The error on the estimation of the drift circle<sup>2</sup>,  $\delta r_{\text{hit}}$ , is a very important quantity because it is used by the track fitting algorithm to calculate the  $\chi^2$  of the track, as well as to define different types of *hits*<sup>3</sup>. Two of those hit types, which are used in the following, are the *precision* and *tube* hits illustrated in Figure 7.5.

To define these hit types we need, besides  $\delta r_{\text{hit}}$ , the *track to wire distance*,  $r_{\text{track}}$ , which is the distance of the fitted track to the centre of the wire, and the *position residual*,  $\Delta r$ . The position residual, illustrated in Figure 7.6, is the difference between the drift circle and track to wire distance,

$$\Delta r = r_D - r_{\text{track}}. \quad (7.4)$$

Precision hits are those with position residuals within  $2.5 \cdot \delta r_{\text{hit}}$ . On the contrary, hits with position residual larger than  $2.5 \cdot \delta r_{\text{hit}}$ , or without a valid leading edge are called tube hits [180].

Since the main aim of the calibration procedure is to improve the position resolution and, therefore, the momentum measurement of charged particles, the

---

<sup>1</sup>One part of the signal goes directly to the read out electronics, while the other reaches the end of the wire and is reflected back, reaching the read-out later. The electronics cannot distinguish these two signals.

<sup>2</sup>Circle around the wire with radius equal to  $r_D$

<sup>3</sup>The term hit refers to when a charged particle fires a straw

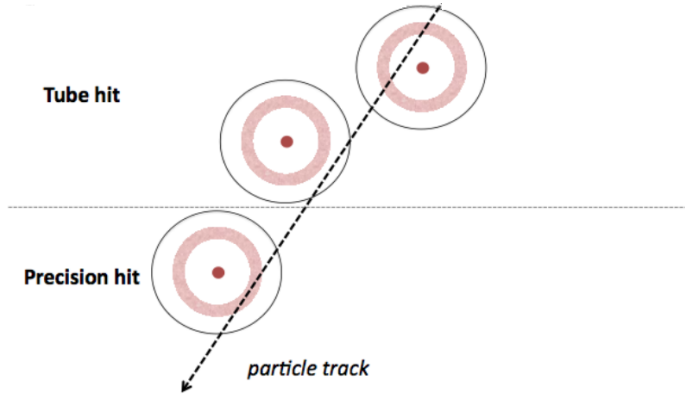


**Figure 7.5:** Illustration of tube and precision hits. The red-shaded disk area in each straw tube corresponds to the drift circle error.

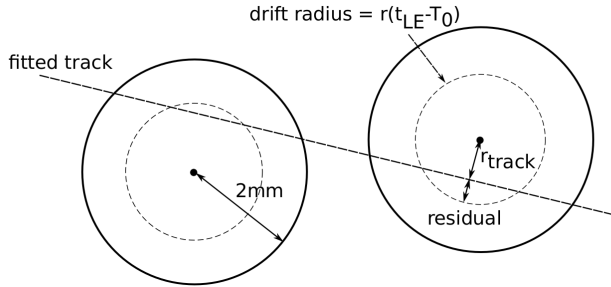


**Figure 7.6:** Two TRT straws crossed by a single track (dashed straight line). The dashed circles represent the drift circle, while the solid circles are used for the walls of the two straws. The distance,  $r_{\text{track}}$ , is marked on the right straw tube, as well as the residual. The wire is shown by a dot in the centre of each straw. Figure from Reference [178]

position residual is very important for the evaluation of the performance of the calibration.

Figure 7.7 shows the distributions of the position residuals for straw tubes filled with Ar-based (7.7a) and Xe-based (7.7b) gas mixture in the barrel region of the detector. The residuals are only estimated using tracks with  $p_T$  above a user-defined threshold (in this example  $p_T > 2$  GeV). The position residuals here are calculated using a so-called *unbiased method*: the track is fitted without considering the information of the hit we want to calculate the residual for. The position residuals estimated this way are more robust against miss-alignment or calibration issues, even though their width is larger than when not using this method [178]. It should be noted that the distributions in fig. 7.7 are symmetric

because the sign in Eq. 7.4 is reversed if the track is on the left of the wire.

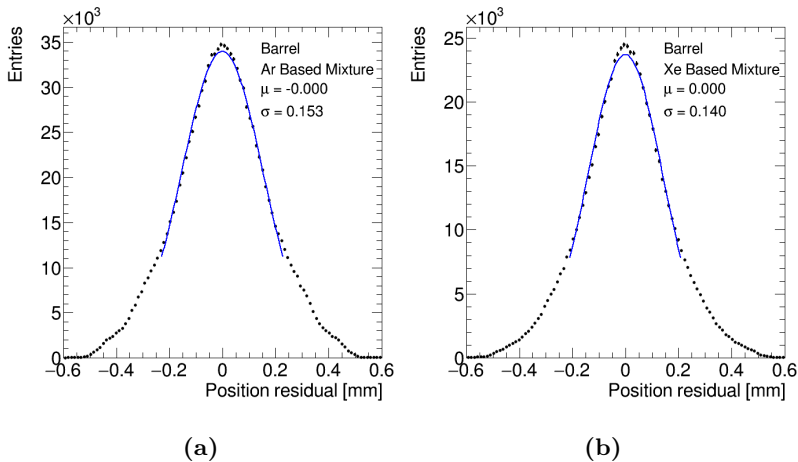


**Figure 7.7:** Position residual in the barrel region from simulated events. The final Gaussian fit is displayed with blue colour. The mean and width estimated from this fit are displayed in each plot.

To estimate the mean and width of the distributions we use a Gaussian fit. However, as can be seen from the figures, the position residual distributions are not perfect Gaussian, because tube hits are included in these distributions. For this reason, the fit is performed iteratively and limited to a region  $\pm 1.5\sigma$  around the mean of the distribution in each iteration. Increasing the range to include the non-Gaussian tails of the distributions degrades the track quality according to Ref. [181]

Another quantity we need to define the so-called *time residual*. To estimate it, we first have to revert the r-t relation to translate the track to wire distance to *track drift time*,  $t_{\text{track}}$ . Then, we take the difference between  $t_{\text{track}}$  and  $t_D$ ,

$$\Delta t = t_D - t_{\text{track}}. \quad (7.5)$$

As was discussed earlier, the ToT depends on the distance of the track from the wire, and it has been shown that hits with a smaller ToT have higher LE time, while hits with longer ToT have lower LE. To account for this we correct the time residual using the so-called *ToT correction*. To calculate this correction the time residuals are accumulated for hits in a specific detector region, gas configuration (Ar-based or Xe-based filled straw tubes) and ToT length. For example, we estimate the time residuals of all the hits from argon-filled straw tubes in the barrel region that have ToT between 0 and 3.125 ns. The hits for each detector region and gas configuration are separated to eighteen ranges of

ToT. The peak of each of these time residual distributions is fitted iteratively with a Gaussian function to estimate its mean. This mean is the so-called ToT correction. The corrections used in this work were derived in Ref. [182].

It has also been shown that hits above the HT threshold, known as HT hits, have smaller values of LE time. Therefore, to account for this systematic effect another correction, called *HT correction*, is applied. The HT corrections are estimated in Ref. [182]. They are the mean of the time residual distribution of HT hits only, estimated for different detector region and gas configuration.

With these corrections, Eq. 7.5 is modified to

$$\Delta t = t_D - t_{\text{track}} - \text{ToT correction} + \text{HT correction}. \quad (7.6)$$

For Run 1 and Run 2, Eq. 7.5 was used to estimate the time residuals of straw tubes filled with Ar-based gas, and Eq. 7.6, was used to for Xe-based straws.

Figure 7.8 shows examples of time residual for straws in the barrel region filled with Ar-based (7.8a without including ToT and HT corrections) and Xe-based (7.8b) gas mixtures. Contrary to the position residuals, the time residual distributions are asymmetric, due to the drift properties of the electrons in the gas and the ionisation clusters. To estimate the mean and width of the time residual we fit the peak of the distribution with Gaussian. The fit is performed iteratively and in each step its range is limited to a region  $\pm 1\sigma$  around the mean of the distribution estimated from the previous step.

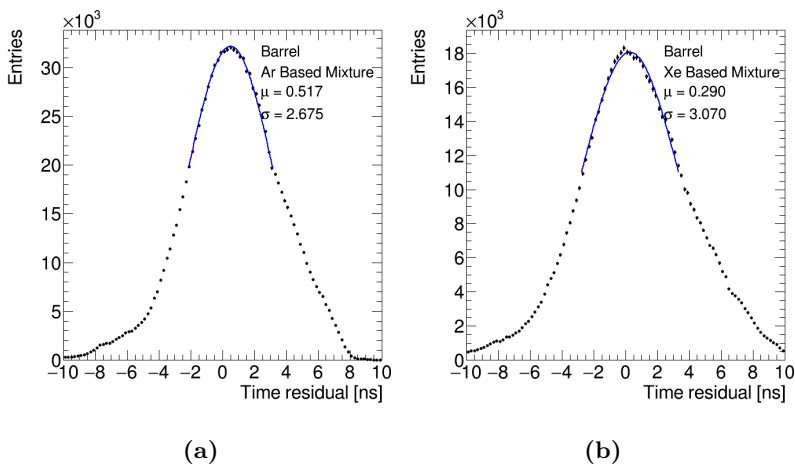


**Figure 7.8:** Time residual in barrel region from simulated events. The final Gaussian function, estimated from the iterative fit is displayed with blue colour. The mean and width of estimated from this fit are displayed on top of each plot.

## 7.4 Calibration procedure

The main aim of the calibration procedure is to provide an estimate for the track-to-wire distance based on the measured LE time. The calibration procedure is performed separately for data and simulated events. The data calibration is performed after every run, to account for small changes that might occur, such as a small change in the gas pressure inside the straw. On the other hand, the calibration of simulated events is performed once and the output is stored in the database. The same calibration output is used for the reconstruction of simulated events, unless some design feature of the detector is changed, for example the value of the low threshold, or if there is some crucial update in the detector simulation. The output of the calibration with simulated events is also used as a seed in data calibration.

The calibration is an iterative procedure, which starts from an initial estimate of the  $T_0$  and r-t relation to reconstruct the tracks in the full Inner Detector. Each iteration uses as input the  $T_0$  and r-t relation estimated in the previous step. In each step a new set of parameters is estimated, as well as the position residuals. The steps are repeated, until the difference in the position residual width between steps is lower than few microns.

### $T_0$ calibration

To estimate  $T_0$ , we have to create time-residual histograms, as those of Fig. 7.8, but for each barrel layer and end-cap wheel separately, and estimate the mean of the distributions along with its associated error with the Gaussian fit described in the previous section.

The  $T_0$  for each iteration  $i$  is shifted by the mean of the time residual:

$$T_0^i = T_0^{i-1} + \mu^i - \hat{\mu} \quad (7.7)$$

The additional shift  $\hat{\mu}$  is an offset estimated in Ref. [177] using data collected in 2011 and was found to be equal to 0.5 ns for tracks with  $p_T > 2$  GeV. The method to estimate this time offset is discussed in Section 7.5. For the results presented in Section 7.6 the offset value was re-evaluated. In Section 7.7  $\hat{\mu}$  was estimated for tracks with  $p_T$  above different thresholds using simulated events without pile up contribution. Section 7.8 presents the results of the same study as Sec. 7.7, this time using events that contain pile up contribution.

## r-t calibration

The first step to estimate the r-t relation is to plot the absolute value of the track-to-wire distance for hits that have a drift time in a specific range, as shown in Figure 7.9 for straw tubes in the end-cap C region filled with Xe-based gas. Figure 7.9 shows the distributions of  $r_{\text{track}}$  in a few selected bins of the drift time. For the calibrations presented in this chapter the drift time is separated in bins of 3.125 ns width. This width is selected because it is equal to the bin width of the readout system. Fig. 7.9 illustrates that higher drift time values correspond to higher distances, and that the width of the distribution is smaller for higher drift times. The width of the distribution is expected to be higher for shorter distances (smaller drift times) since it corresponds to particles that cross the wire closer to the wire. In such cases, the uncertainty on the drift time measurement is higher, because the electrons from the ionisation clusters drift inside the tube for less time and the signal is not amplified properly inside the detector. Figure 7.10 shows the track to wire distance as a function of drift time

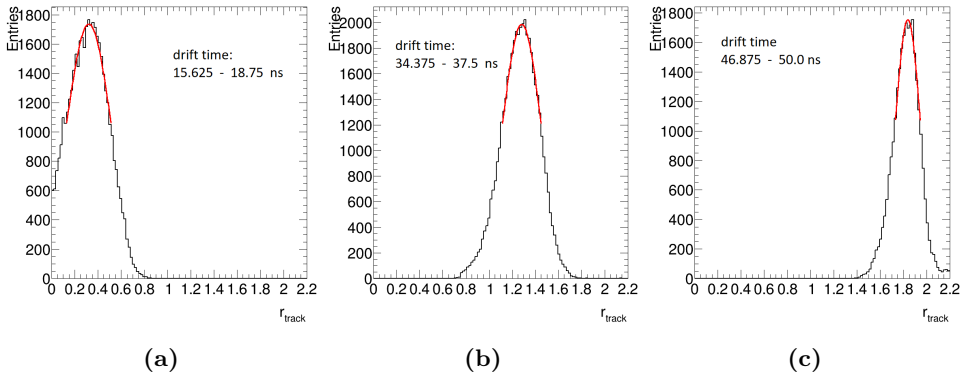


**Figure 7.9:** Distributions of track-to-wire distance for specific bins selected bins of drift time. The red line corresponds to the Gaussian fit used to extract the mean.

for straws filled with Xe-based (7.10a) in the end-cap A and Ar-based (7.10b) mixture in the barrel. The black dots in the figure correspond to the means of the track to wire distance for the specific drift time bin. These points are then fitted with a third degree polynomial,

$$f(t) = a_0 + a_1 t + a_2 t^2 + a_3 t^3. \quad (7.8)$$

The third degree polynomial was selected because it was the simplest function that accurately described the observed data [178]. The r-t relation is finally

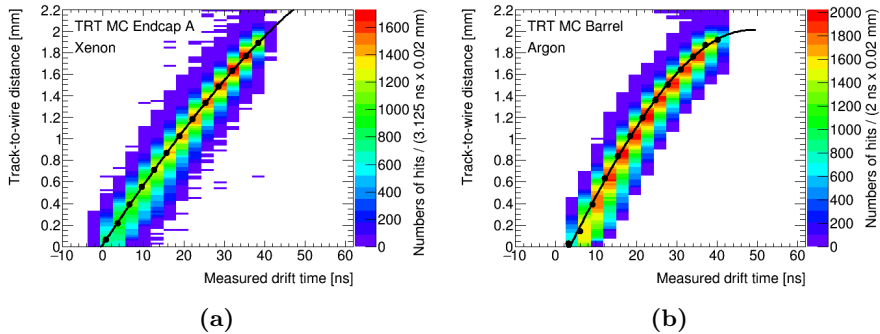


**Figure 7.10:** Example of  $r$ - $t$  relations estimated for straws filled with xenon (left) and straws filled with argon (right) using simulated events and 2016 gas configuration

given by

$$r(t) = \begin{cases} 0, & f(t) < 0 \\ f(t), & 0 < f(t) < R_0, \\ R_0 & f(t) > R_0 \end{cases} \quad R_0 = 2 \text{ mm (straw radius)} \quad (7.9)$$

The distributions of xenon filled straws in Fig. 7.10a are shifted towards higher values of measured drift time with respect to the argon-filled straws in Figure 7.10b. This is expected, since the slope of the  $r$ - $t$  relation is in fact the electron drift velocity in this gas, and the electron drift velocity for the Ar-based gas is higher than for the Xe-based gas mixture.

Despite that the  $r$ - $t$  relation and  $T_0$  are determined independently, shifting the  $r$ - $t$  relation along the time axis changes  $T_0$ , and vice versa: changing  $T_0$  changes the parameters of the  $r$ - $t$  relation. For this reason one point of the  $r$ - $t$  relation is always fixed. The fixed point, in this work is  $f(t = 18 \text{ ns}) = 1 \text{ mm}$ , because Ref. [178] showed that using this fixed point, the estimated  $r$ - $t$  relation for drift time of 0 ns was returning a drift radius of 0 mm for straws filled with Xe-based gas ( $f(t = 0 \text{ ns}) = 0 \text{ mm}$ ).

## 7.5 Validation of the calibration constants

After the calibration is complete, we obtain a set of  $T_0$  values and a set of parameters for the  $r$ - $t$  relation, which should provide the best position resolution when they are used for track reconstruction. The method described in this section is used to determine whether or not the set of estimated  $T_0$  values produces

the smallest possible position residuals. This method was first used in Ref [177], using 2011 data. It is also used in the work described in this chapter.

The first step is to systematically shift the  $T_0$  values up to  $\pm 3$  ns, in steps that range from 0.1 ns to 0.5 ns. Next, we reconstruct tracks for each set of shifted  $T_0$  values, plot the corresponding position and time residuals and estimate their means and widths. The widths of the position resolution and the means of the time residuals are drawn as a function of the  $T_0$  shifts for the barrel region, and for straw tubes filled Xe-based gas. An example from such plots from the first time this method was used in Ref. [177] is shown in Figure 7.11.

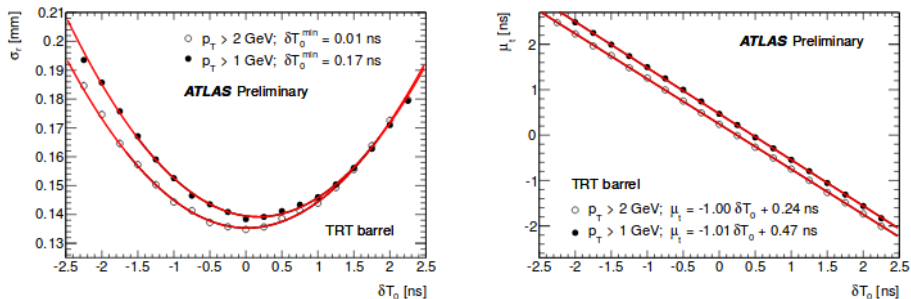


**Figure 7.11:** Dependence of the position residual width (left) and time residual mean (right) on the  $T_0$  shift. Both plots show results obtained from 2011 data. The empty circles correspond to 2 GeV lower thresholds applied on the track  $p_T$ , while the filled dots correspond to 1 GeV. [177]

If the set of the  $T_0$  constants estimated from the calibration is the best value then the minimum of the left plot in Fig. 7.11 should be at  $\delta T_0 = 0$ . To extract the position of the minimum, in this case, we fit with a second-degree polynomial,

$$\sigma_r(\delta T_0) = \sigma_r^{\min} + a(\delta T_0 - \delta T_0^{\min})^2. \quad (7.10)$$

If the minimum is not at  $\delta T_0 = 0$ , but at some value of  $\delta T_0 = \delta T_0^{\min}$ , then we can use these shifted constants to derive a correction for the  $T_0$ , which is the  $\hat{\mu}$  offset in Eq. 7.7. This offset is found from the right plot of Fig. 7.11, by fitting with a straight line ,

$$\mu_t(\delta T_0) = k\delta T_0 + n, \quad (7.11)$$

and evaluating the value of the function at the  $\delta T_0^{\min}$ . The value of  $\hat{\mu}$  was found to be 0.5 ns in Ref. [177] for a 2 GeV requirement on the track  $p_T$  using 2011 data.

## 7.6 Calibration using simulated events with $LT = 100$ eV for straw tubes filled with Ar-based mixture

As explained in Sec. 6.9, the output of the detector simulation is processed by a code, specific to each subsystem, which models not only the detector response, but the signal processing in the electronics as well. The TRT detector simulation and the digitisation package are described in Ref. [183, 184]. The signal shape and the value of the low threshold used in the digitisation step can be adjusted in simulations to obtain better agreement with data.

In previous studies reported in [185], it was found that a low threshold value of 150 eV for straws with Ar-based gas mixture, was providing the best calibration results. The calibration presented in this section uses simulated events produced with a re-optimised signal shape [186] from the previous study, and the low threshold value for the Argon based-mixture set to 100 eV. In Ref. [186], the agreement of the position residual distributions between data and simulated events is better when the low threshold value is set to 100 eV, instead of 150 eV.

The simulated event sample used for this work has an average number of events per bunch crossing  $\langle \mu \rangle < 1$ . Furthermore, at the step of detector simulation the minimum bias trigger is used to record the events. Such simulations are preferred for the calibration because they have fewer and cleaner tracks than samples with pile-up, and hence the track reconstruction can be more accurate.

As it was explained in Sec. 7.5 for the calibration of simulated events the value of the offset is re-estimated. In each iteration the r-t relations are updated as described in Sec. 7.4, but the  $T_0$  parameters are updated via

$$T_0^i = T_0^{i-1} + \mu^i,$$

instead of using Eq. 7.7. After the iterations are complete, we use the method presented in Sec. 7.5 to create the plots shown in Figure 7.12, using only precision hits, to find the  $\delta T_0$  shift that produces the minimum position residual. As it can be seen from Fig. 7.12a the parabolic fit cannot fully describe all the points in the graph. Since we are interested in finding the minimum, the range of the fit was limited to a small region around the lowest position residual width in the graph. The minimum  $\delta T_0$  is displayed on the figure. Figure 7.12b shows the linear fit from which we evaluate the value of  $\hat{\mu}$ . The linear function used in the fit is displayed on the plot of Fig. 7.12b. Once we have the minimum  $\delta T_0$ , we use it to shift the values estimated by the last iteration, and recalculate the position and time residuals. Figure 7.13 shows the position residuals and Fig 7.14 the time residuals, after applying the  $T_0$  shift, for straw tubes filled with

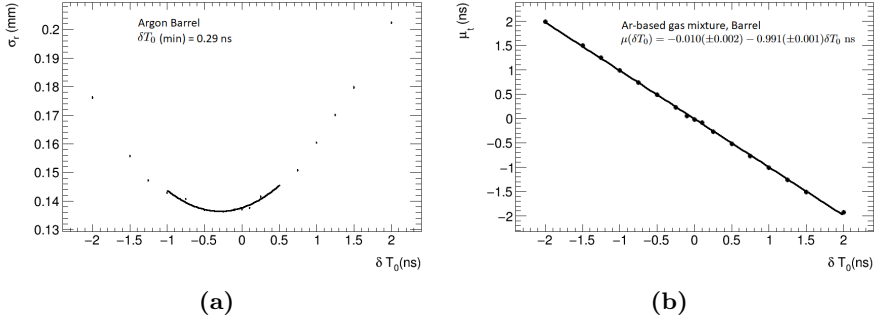


**Figure 7.12:** Dependence of the position residual width (left) and time residual mean (right) on the  $T_0$  shift, for straw tubes filled with Ar-based gas in the barrel region. Both plots are created using simulated events with  $\langle \mu \rangle < 1$ . The tracks used to estimate the residuals have  $p_T > 2$  GeV.

Argon for barrel and end-cap regions. In both figures, the peaks have worse agreement for end-cap regions than for the barrel. This is expected because in the end-caps only few of the wheels have argon filled straw tubes. Additionally, the values of the mean and the width are close since the end-caps are symmetrical, with the only difference being that end-cap C has one more layer filled with argon (see Fig. 7.2).

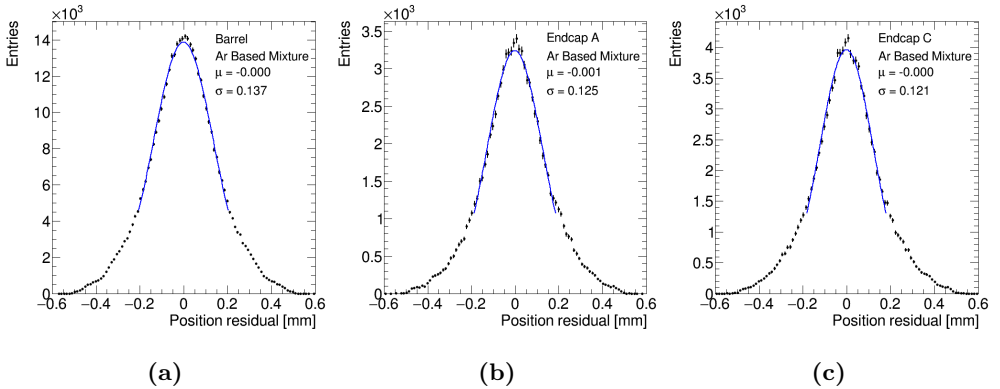


**Figure 7.13:** Position residuals for argon-filled straws for simulated samples with  $\langle \mu \rangle < 1$  and low threshold value of 100 eV

The values of the position residuals are summarised in Table 7.1, and compared to the values obtained from the previous calibration presented in [185]. The results presented in this work show an improvement with respect to the calibration with LT 150 eV and the old argon shape: the position residual width is reduced

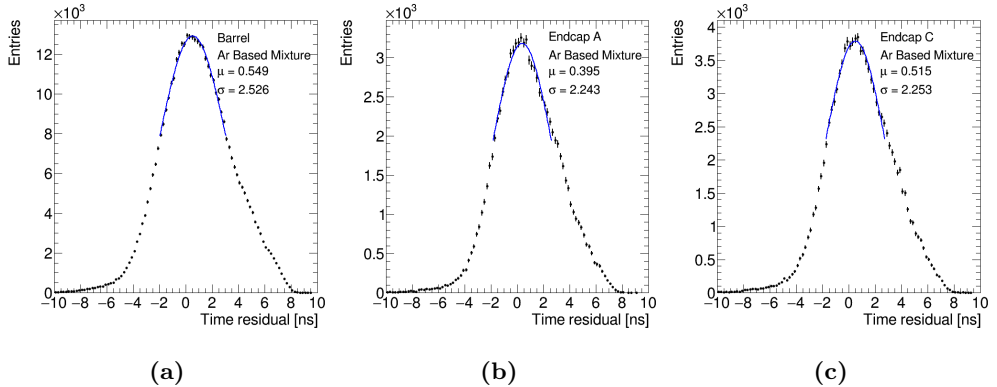


**Figure 7.14:** Time residuals for argon-filled straws for simulated samples with  $\langle \mu \rangle < 1$  and low threshold value of 100 eV

by approximately 10  $\mu\text{m}$  in all detector regions.

LT	$\sigma_r$ barrel	$\sigma_r$ end-cap A	$\sigma_r$ end-cap C
100 eV (new shaping)	137 $\mu\text{m}$	125 $\mu\text{m}$	121 $\mu\text{m}$
150 eV (old shaping)	146 $\mu\text{m}$	134 $\mu\text{m}$	135 $\mu\text{m}$

**Table 7.1:** Comparison of the position residual width between the previous calibration [185] and the new results with improved signal shaping and low threshold value.

## 7.7 Dependence on the $p_T$ of the reconstructed tracks

In this section we use the method of Section 7.5 and the simulated event sample discussed in the previous section, to re-estimate the value of  $\hat{\mu}$  in Eq. 7.7, for straw tubes in the barrel and end-cap regions, separately for those filled with Ar-based and Xe-based gas and using tracks that have  $p_T$  above three distinct thresholds: 1 GeV, 2 GeV and 5 GeV. The aim of this study is to test if there is a dependence of the  $\hat{\mu}$  on the  $p_T$  of the reconstructed track.

Figure 7.15 shows the position residual width (left column) and the time residual mean (right column) as a function of the shifted  $T_0$  constants for straw tubes filled with Ar-based gas, in the barrel and end cap regions. The corresponding plots for straw tubes filled with Xenon are shown in Figure 7.16. In this study we use only precision hits so that the position residual distribution will be more close to a Gaussian.

Figures 7.15 and 7.16 illustrated that the position resolution is overall improved

when we use tracks with higher  $p_T$ . Furthermore, in both figures it is evident that the second degree polynomial fit does not describe well the distributions for the full range of  $T_0$  shifts,  $\pm 3$  ns. This behaviour is more pronounced for the line produced using tracks with  $p_T > 5$  GeV. For this reason, the range is limited in is a small range around the minimum.

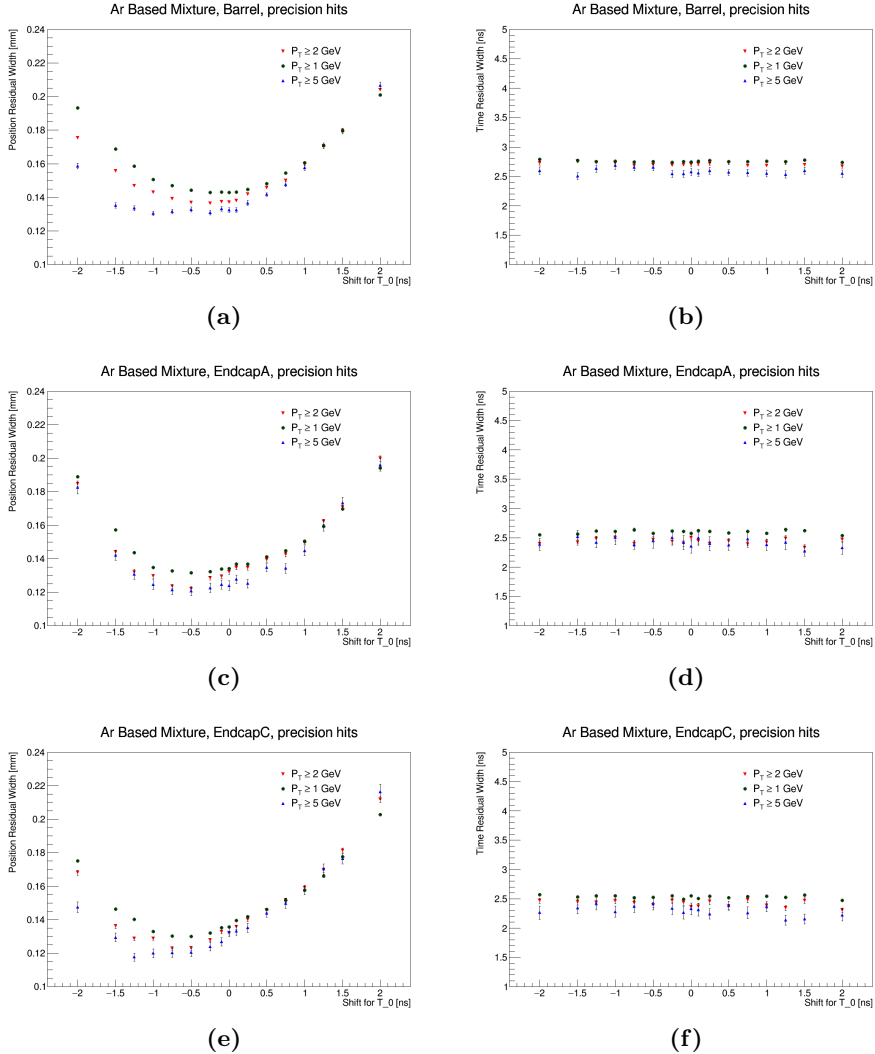


**Figure 7.15:** Position residual width (left column) and time residual mean (right) as a function of the  $\delta T_0$  for straw tubes filled with Ar-based gas. The coloured points correspond to different track  $p_T$  thresholds, 1 GeV-black, 2 GeV-blue and 5 GeV-red. The plots are produced using simulated events with  $\langle \mu \rangle < 1$ .

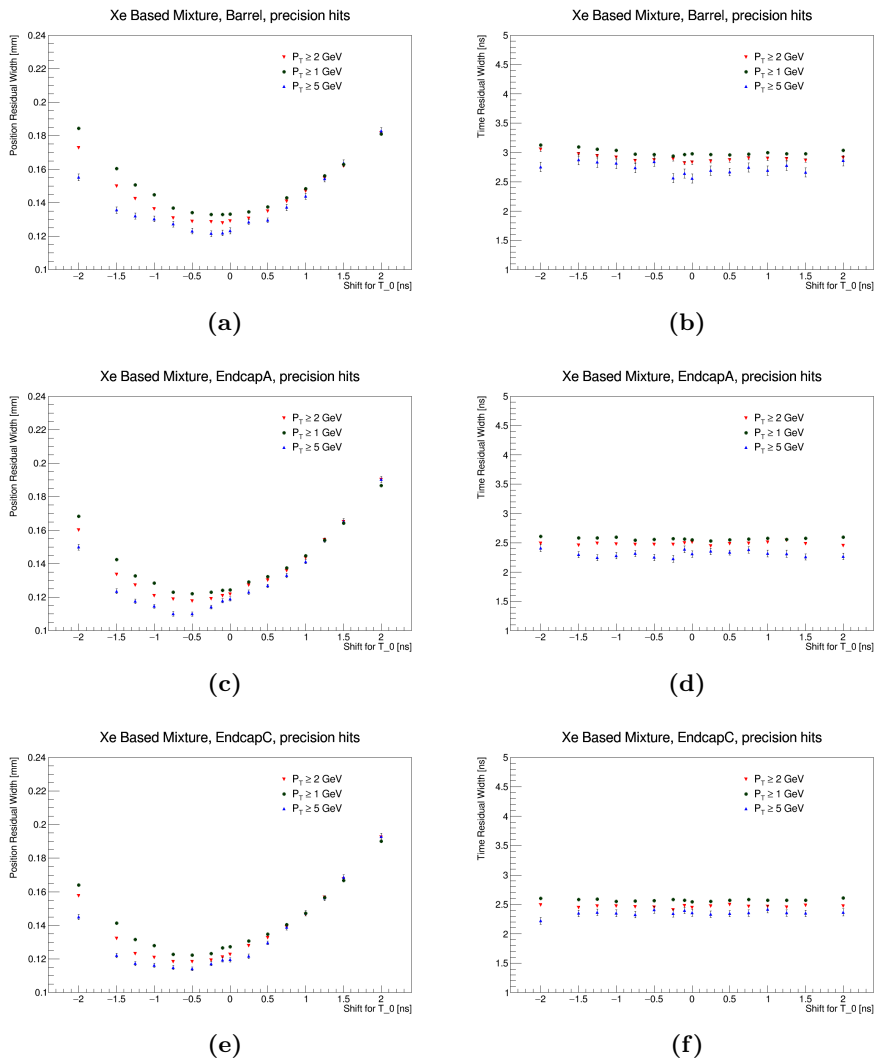


**Figure 7.16:** Position residual width (left column) and time residual mean (right) as a function of the  $\delta T_0$  for straw tubes filled with Xe-based gas. The coloured points correspond to different track  $p_T$  thresholds, 1 GeV-black, 2 GeV-blue and 5 GeV-red. The plots are produced using simulated events with  $\langle \mu \rangle < 1$ .

In Figures 7.15a,c,e , the points for  $p_T > 5$  GeV are flat around  $\sigma_r \sim 0.135 \mu\text{m}$  and  $\delta T_0 \in (-1, 0.5)$  ns, for the barrel and around  $\sigma_r \sim 0.120 \mu\text{m}$  and  $\delta T_0 \in (-1, 0)$  ns, for the end-cap regions. This means that shifting the  $T_0$  constants should not have much of an impact on the position resolution. Also, from Figures 7.15b,d,f we can see that the estimated time offset does not change much with the

increase of the transverse momentum requirement on the reconstructed tracks.

The estimated position resolution minima and the corresponding time offsets are presented for argon-filled straw tubes in Table 7.2. From the Table we

Ar-based gas mixture						
$p_T$ (GeV)	$\sigma_r^{min}$ (mm)			$\mu_t^{min}$ (ns)		
	Barrel	EC A	EC C	Barrel	EC A	EC C
1	0.143	0.131	0.130	0.324	0.518	0.487
2	0.136	0.125	0.124	0.295	0.583	0.512
5	0.131	0.122	0.118	0.364	0.386	0.509

**Table 7.2:** Minimum of the position resolution and estimated offset for straw tubes filled with Ar-based gas mixture, using simulated events with  $\langle\mu\rangle < 1$ .

see that the offset value does not change much with the increase of transverse momentum, and the position resolution improves when using tracks with higher  $p_T$ .

The values of the position resolution minima and the corresponding time offsets for the xenon-filled straw tubes are presented in Table 7.3. From Table 7.3

Xe-based gas mixture						
$p_T$ (GeV)	$\sigma_r^{min}$ (mm)			$\mu_t^{min}$ (ns)		
	Barrel	EC A	EC C	Barrel	EC A	EC C
1	0.133	0.122	0.123	0.265	0.344	0.383
2	0.128	0.118	0.118	0.229	0.349	0.390
5	0.123	0.111	0.115	0.047	0.334	0.367

**Table 7.3:** Minimum of the position resolution and estimated offset for straw tubes filled with Ar-based gas mixture, using simulated events with  $\langle\mu\rangle < 1$ .

we can see that for xenon filled straw tubes, the value of  $\mu_t^{min}$ , for tracks with  $p_T > 5$  GeV is 0.2 ns for the barrel, and  $\sim 0.4$  ns for the end-cap regions, instead of 0.5 ns that is used for data calibration.

## 7.8 Results for simulated events with $\langle\mu\rangle \in (20, 30)$

In this section we check whether or not the offset values remain the same when pile-up is included. For this reason we use a different set of simulated events, that was created with the average number of events per bunch crossing between 20 and 30.

A new set of  $T_0$  parameters and r-t relations was estimated for this simulated event sample. Then, the  $T_0$  parameters were systematically shifted, and for each shifted set we estimated the position residual width and time residual mean for tracks with  $p_T$  above four distinct thresholds: 2 GeV, 5 GeV, 10 GeV and 20 GeV. In this case we could use higher  $p_T$  thresholds because the events were  $Z \rightarrow \mu\mu$  decays, that produce tracks with much higher  $p_T$ . Also the 1 GeV threshold is not used.

Figure 7.17 shows the position residual width (7.17a, c, and e) and time residual mean (7.17b, d, and f) as a function of  $\delta T_0$  for the straw tubes filled with Ar-based gas, while Fig. 7.18 shows the corresponding plots for straw tubes filled with Xe-based gas.

Similar to Fig. 7.15, the second degree polynomial fit does not describe well the points in figures 7.17a, c, and e, for the full range of  $\delta T_0$  values. Thereby, the range of the fit is limited to a small range around the minimum. From Fig. 7.17a, c, e, it is clear that raising the track  $p_T$  threshold above 5 GeV does not lead to a large improvement of the position resolution, and the offset value doesn't seem to differ much. The values of the minimum position residual width and the estimated time offset are presented in Table 7.4. From Table

Ar-based gas mixture						
$p_T$ (GeV)	$\sigma_r^{min}$ (mm)			$\mu_t^{min}$ (ns)		
	Barrel	EC A	EC C	Barrel	EC A	EC C
2	0.155	0.141	0.144	0.188	0.452	0.366
5	0.140	0.124	0.129	0.095	0.332	0.435
10	0.135	0.117	0.123	0.116	0.330	0.465
20	0.134	0.117	0.123	0.234	0.305	0.446

**Table 7.4:** Minimum of the position resolution and estimated offset for straw tubes filled with Ar-based gas mixture, using simulated events with  $\langle\mu\rangle \in (20, 30)$ .

7.4 we can see that the offset value does not change much with the increase of transverse momentum. Furthermore, comparing the position residual widths for tracks with  $p_T$  above 2 and 5 GeV between Tab. 7.2 and 7.4 shows that the position resolution is worse for the simulated event sample which includes pile-up contributions, as expected. Finally, the value of the time offset is overall lower for the event sample that includes pile up. This indicates that with the increase of pile-up the time offset correction  $\hat{\mu}$  in Eq.7.7 should be smaller, if it should be applied at all. However, to draw such a conclusion, one should use simulated event samples with more pile-up, for example with  $\langle\mu\rangle$  of 40, 60 or more, which was not checked for this gas configuration.

A similar behaviour is also observed for the straw tubes filled with Xe-based gas mixture. The values of the position resolution minima and the corresponding time offsets for the xenon-filled straw tubes are presented in Table 7.5. From

Xe-based gas mixture						
$p_T$ (GeV)	$\sigma_r^{min}$ (mm)			$\mu_t^{min}$ (ns)		
	Barrel	EC A	EC C	Barrel	EC A	EC C
2	0.142	0.132	0.132	0.152	0.206	0.214
5	0.128	0.118	0.119	0.107	0.196	0.237
10	0.122	0.115	0.116	0.054	0.205	0.239
20	0.121	0.115	0.116	0.079	0.203	0.248

**Table 7.5:** Minimum of the position resolution and estimated offset for straw tubes filled with Xe-based gas mixture, using simulated events with  $\langle\mu\rangle \in (20, 30)$ .

Table 7.5 we can see that for xenon filled straw tubes, the value of  $\mu_t^{min}$ , for tracks with  $p_T > 5$  GeV is  $\sim 0.1$  ns for the barrel, and  $\sim 0.2$  ns for the end-cap regions, which is different from the 0.5 ns value used during Run 2. Comparing the time offset values from Tab. 7.3 and 7.5, that correspond to track  $p_T$  threshold of 2 GeV and 5 GeV, we see that when we include pile up the value of the shift is lower.

## Adding ToT and HT corrections for straw tubes filled with Ar-based gas mixture

As it was explained in Sec. 7.3, for straw tubes filled with Ar-based gas no ToT nor HT corrections are applied when we calculate the time residual mean. This section presents a comparison of the position residual widths for argon filled straws, for the following cases: without any corrections, after applying ToT corrections, and after both ToT and HT corrections are applied.

The corrections used in this work are estimated in Ref. [182]. The simulated event sample is the same as in the previous section, and the residuals are produced using only tracks with  $p_T$  above 5 GeV, because according to Tab. 7.4, there is no significant improvement in the expected position resolution for higher thresholds.

Table 7.6 shows the estimated position residuals. The first line is retrieved from Tab. 7.4. The position residuals with ToT only and both corrections applied are estimated after dedicated calibrations. The position and time residuals after these calibrations are included in Appendix A.

From table 7.6 it is clear that after adding the ToT corrections the position res-

	Barrel(mm)	EC_A(mm)	EC_C(mm)
no ToT nor HT correction	0.140	0.124	0.129
ToT correction only	0.130	0.116	0.119
ToT and HT correction	0.129	0.113	0.121

**Table 7.6:** Summary of the position residual widths after the calibration without TOT and HT corrections, applying only TOT corrections and apply both TOT and HT, in the various regions of the detector.

olution is improved by  $\sim 10\mu\text{m}$  in all regions, but after adding the HT correction there is almost no improvement of the position resolution.

## 7.9 Study of the pile-up dependence of the time offset values

The offset values estimated in the previous section indicated that the offset values become smaller with the increase of pile-up. This section presents a study that investigates further whether the time offset correction becomes smaller to the point it is unnecessary above some value of  $\langle\mu\rangle$ .

For this study we use simulated events for which all the straw tubes in the detector are filled with Ar-based gas. This is called a *full-Argon scenario*, and it was one of the scenarios studied for Run 3, however it was not used in the end.

In this study we perform the full calibration, iteration and shift of  $T_0$  parameters with a sample without pile-up. Then we use the final set of  $T_0$  parameters as follows: we systematically shift them and use the shifted  $T_0$  sets to reconstruct tracks for two new samples of simulated events, one with  $\langle\mu\rangle = 30$  and one had  $\langle\mu\rangle = 60$ . The next step is to estimate the position residual widths and time residual means as a function of  $\delta T_0$  for both of the aforementioned simulated event samples, following the procedure described in Sec. 7.5 and used in Sec. 7.7 and 7.8. It should be noted that in this work both ToT and HT corrections were used.

The estimated time offsets are presented in Table 7.7. The time offset values reported in the table decrease as the pile-up increases. Especially for  $\langle\mu\rangle = 60$ , the offsets are 0 for the barrel and end-cap C and 0.1 ns for end-cap A. Also the corresponding shift of the  $T_0$  parameters is very close to 0.

Detector Part	$\delta T_0^{min}$ (ns)	$\sigma_r^{min}$ (mm)	$\mu_t^{min}$ (ns)
$\langle \mu \rangle < 1$			
Barrel	-	0.128	0.26
End-cap A	-	0.117	0.38
End-cap C	-	0.117	0.38
$\mu = 30$			
Barrel	0.44	0.155	0.13
End-cap A	0.34	0.140	0.37
End-cap C	0.40	0.143	0.40
$\mu = 60$			
Barrel	0.187	0.190	0.04
End-cap A	0.002	0.174	0.14
End-cap C	0.187	0.178	0.000

**Table 7.7:** Minima of the position resolution and estimated offset for straw tubes filled with Ar-based gas mixture, using simulated events with three different pile-up contributions. The first column shows the position of the minimum.

## Conclusions

This chapter presented studies of the performance of the calibration procedure using simulated event samples. The first part of the work described in this chapter was a calibration of simulated events, after the Argon signal shaping was re-optimised and the LT value was changed to 100 eV. The new calibration showed improved performance for the straw tubes filled with Ar-based gas, since the position resolution width was reduced by roughly 10  $\mu\text{m}$  in all detector regions (barrel, end-cap A and C).

The next part of the work was to re-estimate  $\hat{\mu}$  after varying the  $p_T$  threshold of the reconstructed tracks used in the calibration. Two simulated events samples were used for these studies: one without a pile-up contribution,  $\langle \mu \rangle < 1$ , and one with  $\langle \mu \rangle$  between 20 and 30. In both case the estimated offsets did not change much with the  $p_T$  threshold, since the largest difference was 0.1 ns. Additionally for straw tubes filled with Xe-based gas the estimated values differed from the one used for Run-2.

From these studies it was also concluded that increasing the track  $p_T$  threshold above 5 GeV did not improve much the calibration. As a consequence, for the calibration during Run 3 the track  $p_T$  requirement was raised from 2 GeV (used during Run 2) to 5 GeV.

A comparison of the  $\hat{\mu}$  values estimated using simulated events without and

with pile-up contributions, indicates that the time offset value is smaller when pile-up is included, hinting that the correction perhaps is not necessary for even higher pile-up ( $\langle\mu\rangle > 30$ ). This was confirmed by studying the offset values using simulated events with three different pile-up contributions:  $\langle\mu\rangle < 1$ ,  $\langle\mu\rangle = 30$  and  $\langle\mu\rangle = 60$ . For this study we used the full Argon scenario. The results showed that for high pile-up the offset value was almost 0. Based on these studies it has been decided to no longer use the time offset  $\hat{\mu}$  for the calibrations during Run 3.

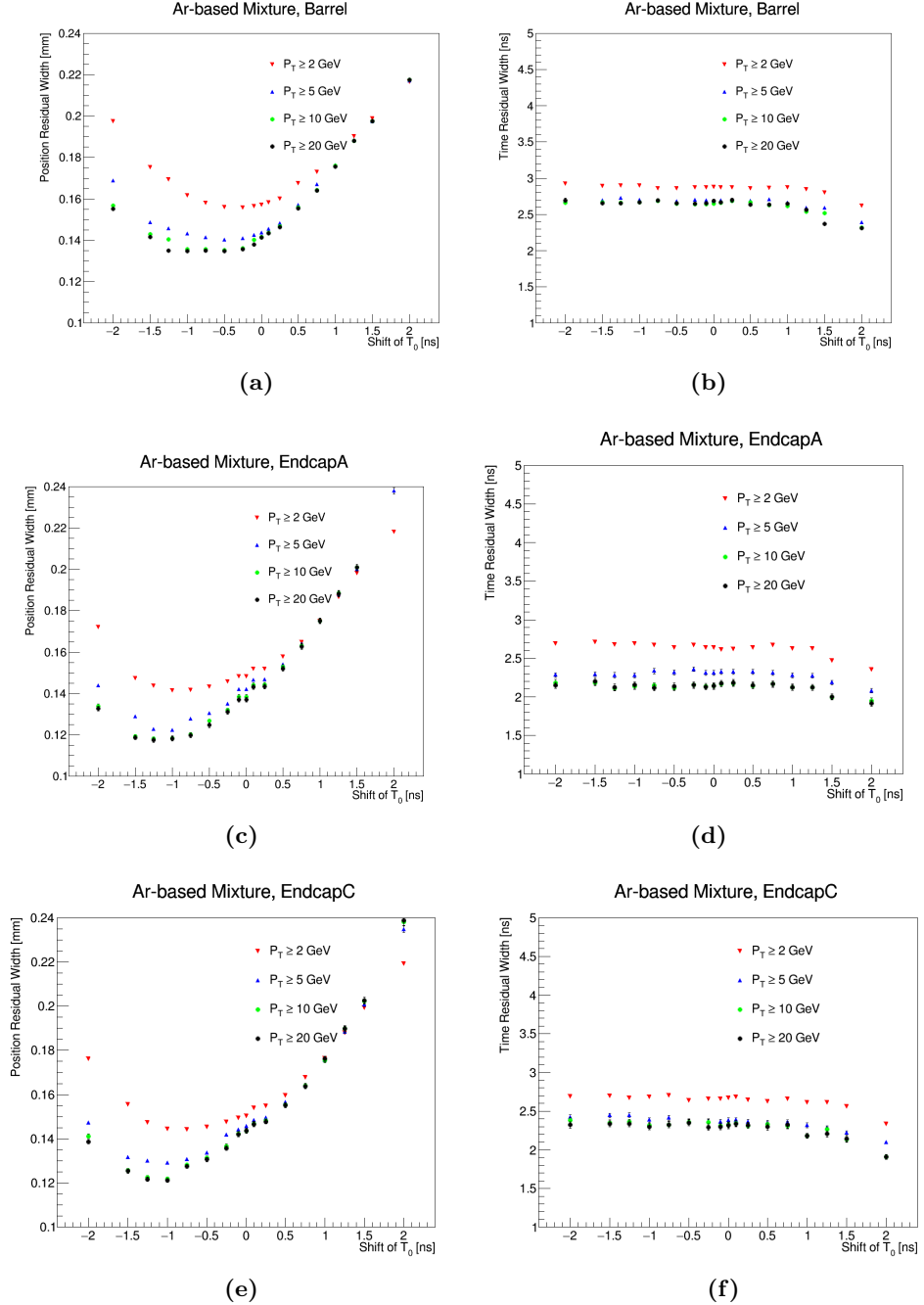


**Figure 7.17:** Position residual width (left column) and time residual mean (right) as a function of the  $\delta T_0$  for straw tubes filled with Ar-based gas. The coloured points correspond to different track  $p_T$  thresholds, 2 GeV-red, 5 GeV-blue, 10 GeV-light green, and 20 GeV-black. The plots are produced using simulated events with  $\langle \mu \rangle \in (20, 30)$ .

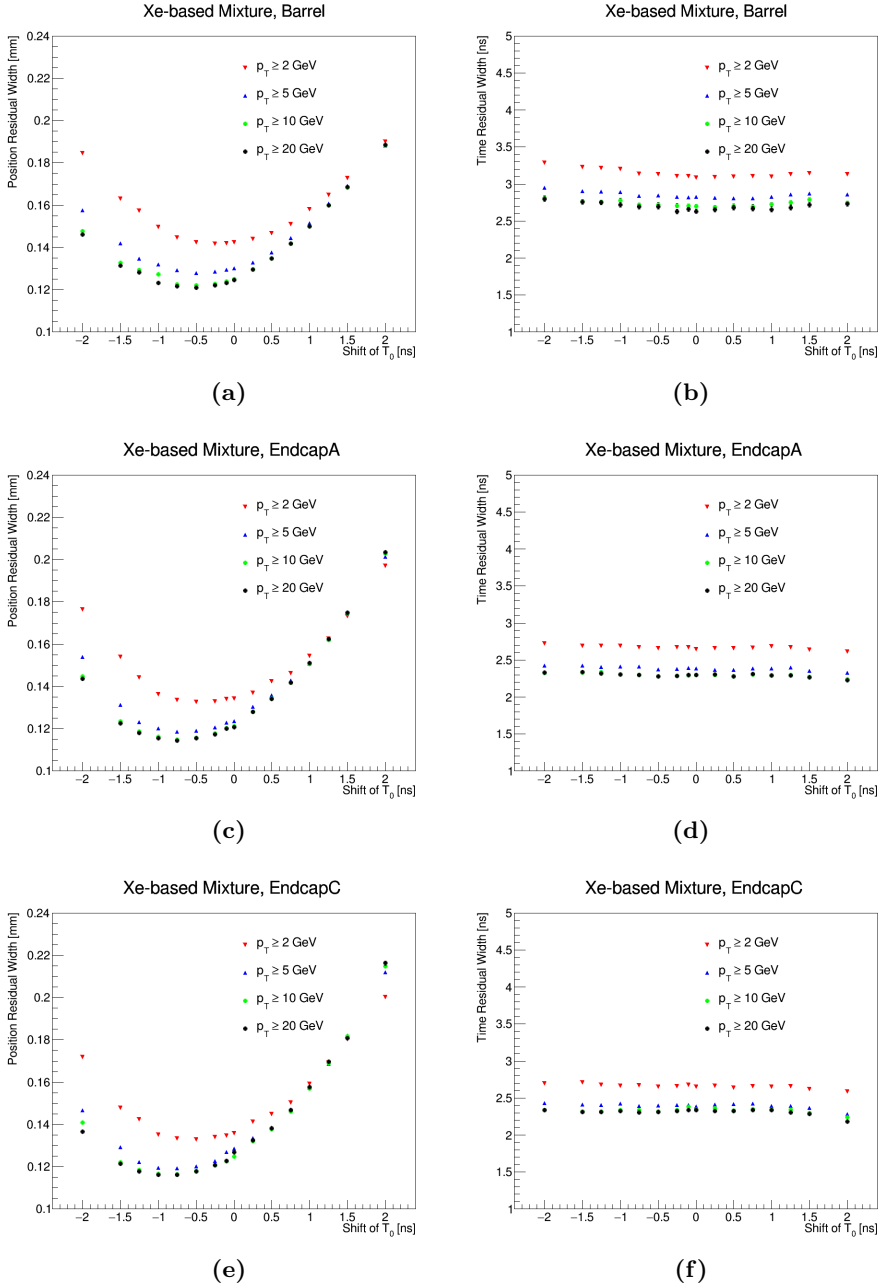


**Figure 7.18:** Position residual width (left column) and time residual mean (right) as a function of the  $\delta T_0$  for straw tubes filled with Ar-based gas. The coloured points correspond to different track  $p_T$  thresholds, 2 GeV-red, 5 GeV-blue, 10 GeV-light green, and 20 GeV-black. The plots are produced using simulated events with  $\langle \mu \rangle \in (20, 30)$ .



# Chapter 8

## Analysis strategy

After the Higgs boson discovery, a new possible channel opened for the  $E_T^{\text{miss}} + X$  searches, the  $E_T^{\text{miss}} + \text{SM Higgs boson}$ . The main difference between this channel and the other  $E_T^{\text{miss}} + X$  signatures is that the Higgs boson is unlikely to be produced from initial state radiation, as mentioned in Section 3.4.3, and can be used as a “probe” for the interaction with the Dark Matter. Out of the possible decay modes, this analysis uses the  $H \rightarrow b\bar{b}$  because it is the channel with the highest branching ratio,  $BR \sim 57\%$  [187].

Furthermore, the  $E_T^{\text{miss}} + H(b\bar{b})$  search is one of the two searches that dominate the exclusion sensitivity of the 2HDMa models, as seen in Sec. 3.5.3, while for the  $Z'$ -2HDM model, it produces complementary results to  $E_T^{\text{miss}} + X$  and resonance searches.

This chapter describes the data analysis strategy to search for Dark Matter with the  $E_T^{\text{miss}} + H(b\bar{b})$  signature. The first step in this analysis is to define a set of selection requirements that will distinguish the process of interest from all the other events produced inside the ATLAS detector. These requirements are defined using the main characteristics of the  $E_T^{\text{miss}} + H(b\bar{b})$  final state signature, described in Section 8.1. This phase space region, referred to as the signal region, is also populated by SM processes that produce similar or identical final states as the signal process. Section 8.2 gives an overview of these SM processes. After estimating the SM predictions in the signal region, we look for deviations between them and the observed data. Section 8.3 describes the statistical analysis model used to estimate the background, extract any possible signal, and set limits when no deviation from the Standard Model expectations is observed.

## 8.1 Signal Characteristics

In this work, we search for events in which dark matter is produced together with a Higgs boson that subsequently decays to a pair of  $b$ -quarks. Thereby, final state signature is tagged by large missing transverse energy and the presence of  $b$ -jets. The missing transverse momentum is correlated with the transverse momentum of the Higgs boson: higher values of  $E_T^{\text{miss}}$  should lead to more energetic Higgs bosons. However, as the boost of the Higgs with respect to the detector frame increases, its decay products, the two  $b$ -jets, become less separated and after some point they can no longer be individually reconstructed. Therefore, the best practice is to reconstruct the Higgs boson candidate using different radius  $b$ -tagged jets depending on the event topology: events with moderate boosts, and relatively low  $E_T^{\text{miss}}$ , should use two small-radius  $b$ -jets, while in cases of highly boosted Higgs, and high  $E_T^{\text{miss}}$ , a single large-radius  $b$ -jet should be used. The event topology with two well-defined  $b$ -jets in the final state, illustrated in Figure 8.1a, is called *resolved*, while the one with a single large- $R$   $b$ -tagged jet, illustrated in Figure 8.1b, is called *merged*. A  $E_T^{\text{miss}}$  boundary of 500 GeV is used to distinguish these two topologies.

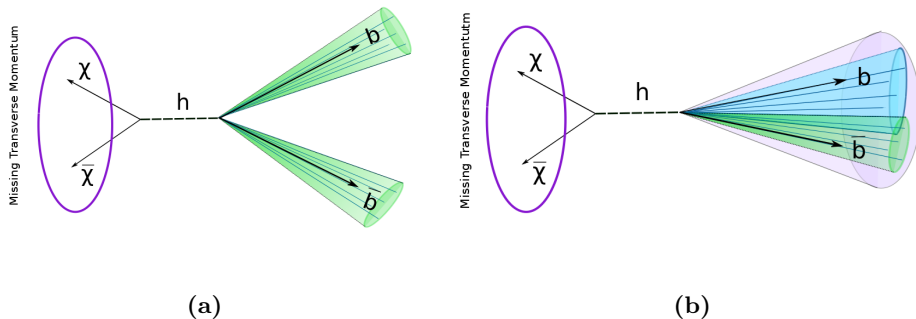


**Figure 8.1:** 8.1a Sketch of the resolved event topology. Here the Higgs decay products can be reconstructed as two well-separate jets. 8.1b Sketch of the merged event topology.

Another distinguishing feature of the  $E_T^{\text{miss}} + H(b\bar{b})$  final state signature is the absence of leptons. As a result, any event with one or more leptons in the final state can be discarded (vetoed).

Section 3.5.1 presented the two main production mechanisms of the 2HDM+ $a$  model relevant to the  $E_T^{\text{miss}} + H(b\bar{b})$  search for DM. The final state signature of the  $b\bar{b}$ -induced processes, as explained in 3.5.1, is expected to have more than two  $b$ -jets. In order to increase the sensitivity of the analysis to this processes, an

additional event topology is included, defined by the presence of three or more  $b$ -tagged jets in the final state. This requirement for events with  $E_T^{\text{miss}} > 500$  GeV (merged topology), translates to two  $b$ -tagged VR-track jets inside the cone of the large- $R$  jet and at least more VR-track  $b$ -jet outside the cone of the large- $R$  jet.

## $E_T^{\text{miss}}$ distributions of the $Z'$ -2HDM and $2HDM + a$ benchmark models

Since  $E_T^{\text{miss}}$  is a key feature of this signature it is necessary to examine its distribution for several representative signal models. All the distributions in this section are produced using simulated events before the detector simulation step, to which only the following requirements are applied:  $E_T^{\text{miss}} > 150$  GeV, no leptons, and  $> 2$  small- $R$  jets or  $> 1$  large- $R$  jet in the event.

The  $E_T^{\text{miss}}$  distributions differ a lot between different signal points within the  $Z'$ -2HDM model, as illustrated in Figure 8.2, for three representative  $Z'$ -2HDM models. From this figure, we see that signal points with larger differences

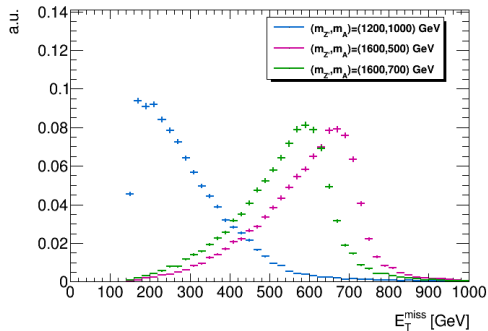


**Figure 8.2:**  $E_T^{\text{miss}}$  distribution for representative signals of the  $Z'$ -2HDM model. The histograms are normalised to unit area.

between  $m_{Z'}$  and  $m_A$ , have harder  $E_T^{\text{miss}}$  spectra. In this model the  $Z$ -boson is produced as a resonance and then decays to  $Ah$ . Therefore, for higher  $m_{Z'}$  there is more energy available for the decay products, and lighter  $A$  will lead to more boosted signature.

The corresponding distributions for the  $ggF$ -induced  $2HDM + a$  models are shown in Figure 8.3. In this figure we see three signal points with mass differences between  $m_a$  and  $m_A$ ,  $(\Delta(m_a, m_A))$  of 200 GeV, 800 GeV, and 1.2 TeV. We see that the average  $E_T^{\text{miss}}$  is very low ( $\sim 200$  GeV) for the signal point with the lower mass splitting,  $(m_a, m_A) = (400\text{GeV}, 600\text{GeV})$ . For the signal model

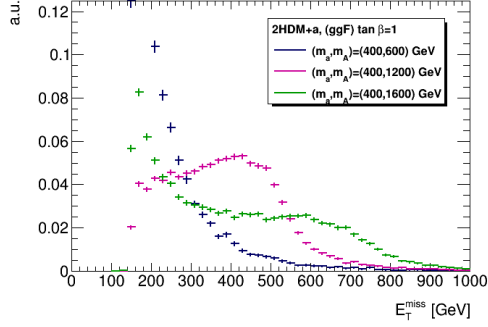


**Figure 8.3:**  $E_T^{\text{miss}}$  distribution for representative signals for the  $ggF$ -induced  $2HDM+a$  model. The histograms are normalised to unit area.

with  $\Delta(m_a, m_A)$ , the peak of the  $E_T^{\text{miss}}$  spectrum moves towards higher values. However, for  $\Delta(m_a, m_A) = 1.2$  TeV, the  $E_T^{\text{miss}}$  distribution moves again to lower values. This behaviour is caused, because for large  $m_A$  the dominant contributions to the  $h + \text{ch}\bar{i}\chi$  final states do not come from the Feynman diagrams shown in Fig 3.9, but from non-resonant production mechanisms [82], such as the off-shell production of  $a$  that decays to  $Ah$ .

Finally, Figure 8.4, shows the  $E_T^{\text{miss}}$  distributions for the  $b\bar{b}$ -induced  $2HDM+a$  model. In this case we see that all the signal models in the figure produce soft  $E_T^{\text{miss}}$  spectra. Comparing the  $(m_a, m_A) = 400, 1200$  point for the  $b\bar{b}$ -induced process to the corresponding point for  $ggF$ -induced processes clearly shows that the  $E_T^{\text{miss}}$  spectra for  $b\bar{b}$ -induced processes is much softer.

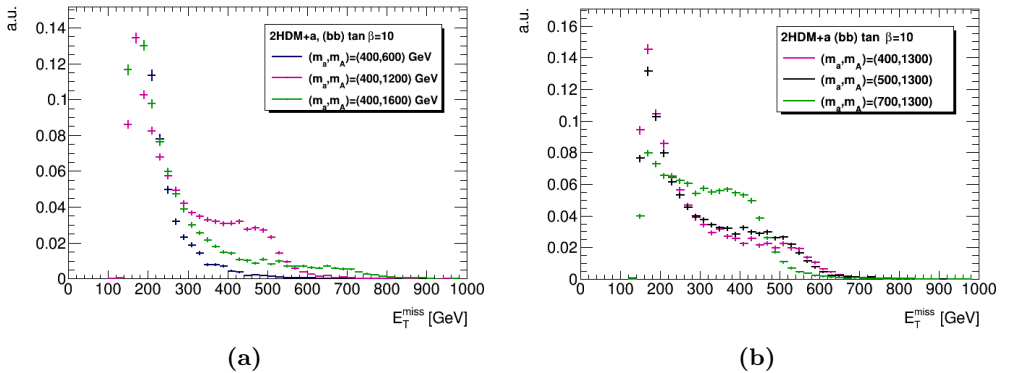


**Figure 8.4:**  $E_T^{\text{miss}}$  distribution for representative signals for the  $b\bar{b}F$ -induced  $2HDM+a$  model. The histograms are normalised to unit area.

From the plots in this section, it is clear that the different models produce different spectra, and for each signal model, the sensitivity can be enhanced if we restrict the  $E_T^{\text{miss}}$  range to values around to the peak of its  $E_T^{\text{miss}}$  spectra. For this reason as the merged and resolved region and further split into more  $E_T^{\text{miss}}$  ranges- will be explained in Chapter 11

## 8.2 Background Contributions

Standard Model processes may create similar or identical signatures with the signal events when neutrinos are involved in the final states. Neutrinos, just like DM particles, escape without detection, leading to real  $E_T^{\text{miss}}$ . In addition, in some events *fake*  $E_T^{\text{miss}}$  can arise from the mis-measurements of the momenta of the reconstructed jets. Events with high jet multiplicities, also called *Multi-jet* events, occur often in hadron collisions and contribute to the background because of fake  $E_T^{\text{miss}}$ . Multi-jet background is suppressed in this analysis by selection requirements that will be discussed in 10.2.2.

Processes that involve neutrinos, jets and leptons in the final state produce a signal-like signature when the leptons fall out of the detector acceptance or are miss-identified as jets. A further complication is introduced when the produced lepton is a muon: if the missing energy in the event is reconstructed with calorimeter information only, then the muon will appear as invisible<sup>1</sup>. Any process with muons in the final state will create a signal-like signature, in this case. In the following paragraphs contain a brief description of the processes that contribute to the background.

The three major background contributions come from the  $Z$ +jets,  $W$ +jets and  $t\bar{t}$  processes. Figure 8.5 shows a representative Feynman diagram for each of the aforementioned processes. Out of the  $Z$ +jets events, those with a  $Z$ -boson

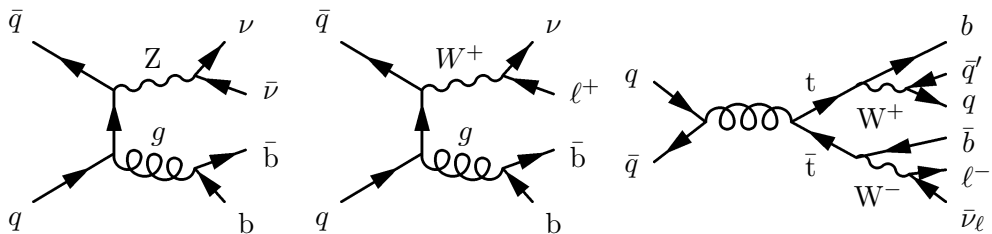


**Figure 8.5:** Examples of Feynman diagrams for  $Z$ +jets(a),  $W$ +jets(b) and  $t\bar{t}$ (c) background processes.

<sup>1</sup>Muons do not produce a significant signal in the calorimeters in contrast to electrons and  $\tau$ -leptons

decaying to neutrinos contribute to the background the most. Other  $Z$  decay channels have small contributions:  $Z \rightarrow q\bar{q}$  decays create final states with low (fake)  $E_T^{\text{miss}}$ , and  $Z \rightarrow \ell^-\ell^+$  events are efficiently suppressed by the lepton veto. The largest contribution from  $W$ +jets events comes from the leptonic  $W$ -boson decays, and the  $W \rightarrow q\bar{q}'$  channel creates final state signatures with low fake  $E_T^{\text{miss}}$ . From the  $t\bar{t}$  processes, the semi-leptonic decays<sup>2</sup> of the top-quark pair have the highest contribution to the total background compared with the other decay channel. Fully-leptonic decays have small contributions because it is less likely that both leptons will be “missed”, while hadronic decays of  $W$ -bosons have lower missing transverse energy, and their contribution is smaller than the semi-leptonic decay.

The other processes contributing to the total background are the production of single  $t$ -quark, two vector bosons (*diboson* production), one vector together with a Higgs boson, and a  $t$ -quark pair together with either a vector boson or a Higgs. These processes are briefly presented in the following.

The production of a single  $t$ -quark is illustrated by the three Feynman diagrams in Figure 8.6 showing the so-called *s-channel*(left), *t-channel*(middle) and *Wt-channel*(right). The associated production of a  $W$  and a top-quark ( $Wt$  channel) is the dominant process and contributes to the background with the final states that contain one-muon.

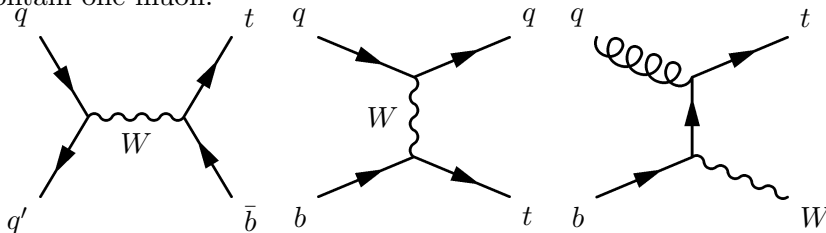


**Figure 8.6:** Single top-quark production Feynman diagrams. On the left is the *s*-channel, the middle diagram correspond to the *t*-channel and the right to the *Wt* channel

The production of two vector bosons (*diboson* production),  $ZZ$ ,  $ZW$ , and  $WW$ , can create a large variety of final states. The larger contributions come events with one or both bosons decaying to neutrinos. Still, their contribution to the total background is small. Likewise, a small contribution comes from the vector boson associated production of a Standard Model Higgs boson ( $VH$ ), shown in Fig. 8.7. In this case, the dominant contribution comes from  $ZH$  events in

<sup>2</sup>The term semi-leptonic is used to describe events where each of the top-quarks decay to  $Wb$  and subsequently one of the  $W$  bosons decays to  $\nu\ell$  and the other to quarks. The terms fully-hadronic (fully-leptonic) refer to cases where both of the produced  $W$  bosons decay to quarks(leptons)

which the Higgs decays to a  $b\bar{b}$  pair and the  $Z$ -boson to neutrinos. Finally, the analysis also considers the associated production of a  $t$ -quark pair and a Higgs ( $t\bar{t}H$ ), or a vector boson ( $t\bar{t}V$ ). Figure 8.8 shows on the left a tree-level diagram of the  $t\bar{t}H$  process and on the right a  $t\bar{t}W$  process. However,  $t\bar{t}H$  and  $t\bar{t}V$  contribute less than all the previously discussed processes, due to their small cross-sections.

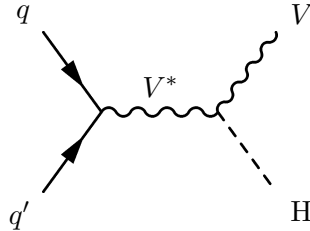


**Figure 8.7:** Vector boson associated production of a Standard Model Higgs

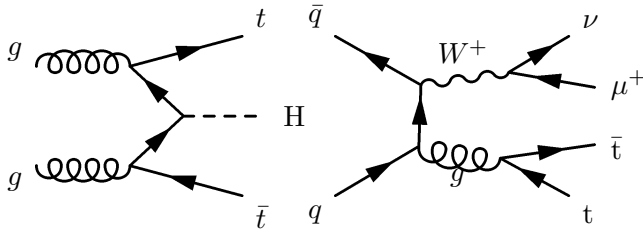


**Figure 8.8:** Associated production of a top-quark pair and a SM Higgs ( $t\bar{t}H$ ) (left) and a  $W^+$  boson ( $t\bar{t}V$ ).

## 8.3 Statistical Analysis

The invariant mass of the Higgs boson is reconstructed from its decay products. To extract any possible signal the analysis compares the mass spectrum obtained from data to the SM predictions. Any differences are quantified in terms of a hypothesis test performed by evaluating a likelihood function. In the absence of any significant deviations, a limit-setting procedure follows. This section describes these statistical procedures, and discusses the tools used to validate the fit results.

### 8.3.1 Likelihood function

There are many ways to extract the value of a parameter from the observed data, and in this analysis we use the so-called maximum likelihood (ML) fit,

which is based on the definition of a likelihood function. The observable that we use in the maximum likelihood fit is the invariant mass spectrum of the two small- $R$   $b$ -tagged jets (large- $R$  jet) in the resolved (merged) region.

The distribution of any observable,  $x$ , is a histogram of  $N$  bins, and each bin can be viewed as the result of an independent measurement that observes a number of  $n_i$  events when  $\mu S_i + B_i$ , are expected. The content of each bin, therefore, follows a Poisson distribution  $p(n_i; \mu S_i + B_i)$ , where  $S_i$  and  $B_i$  are the event yields of the expected signal and background processes respectively, in bin  $i$ . The parameter  $\mu$  is the so-called *signal strength*, and is defined as the ratio of the measured signal cross section over the theoretically predicted one.

With the ML fit the value of the so-called *parameter of interest* (POI) is determined, which in this case is the signal strength, as well as the values of the so-called *nuisance parameters* (NP). The nuisance parameters are added to the fit to account for uncertainties on parameters such as calibration scales, scales used in the event simulation, efficiency and resolution effects, that affect the expected number of events  $S_i$  and  $B_i$ .

The nuisance parameters are called *constrained* when there is prior knowledge on their values from some auxiliary measurement, that provides the central value of the NP and its uncertainties. When there is no prior knowledge for a NP and its value is allowed to free float in the fit, it is called *free-floating*.

The likelihood function for this analysis is built with the HistFactory tool described in Ref. [188]. The invariant mass spectrum, as will be explained in Chapter 11, is produced for different ranges of  $E_T^{\text{miss}}$  and  $b$ -jet multiplicities, creating several distinct signal regions which in HistFactory terminology are called *channels*. The HistFactory tool uses interpolation algorithms to take into account correlations between any combination of nuisance parameters across the different channels. The combined likelihood HistFactory produces for all the channels will be of the form:

$$\mathcal{L}(x; \mu, \alpha, \eta) = \prod_j^{\text{channels}} \prod_i^N (p(n_i; \mu S_i(\alpha, \eta) + B_i(\alpha, \eta))) \prod_k G(\eta_k). \quad (8.1)$$

Here,  $\alpha$  and  $\eta$  are used for the NPs,  $\alpha$  for the background normalisation and  $\eta$  is used for the theory-related and the experimental uncertainties that affect both the signal and background processes. Finally, for each of the  $\eta$  uncertainties the likelihood is multiplied by a term  $G(\eta_k)$  (Gaussian) that constrains the value of  $\eta_k$  around its estimated value (obtained from the control regions) within the uncertainty of this the estimation.

The NPs  $\alpha$  that correspond to the normalisation factors for the background dis-

tributions are free-floating parameters. For the main background contributions they are estimated from the ML fit using dedicated phase-space regions, *the control regions*, that are orthogonal to the signal regions and are also included in Eq. 8.1. The control regions are designed to be populated by background-only events with similar kinematic distributions and event observables to the signal region.

Two such regions are defined in this analysis. The first targets events with one muon in the final state and is called *one-muon control region* (CR1). The processes mainly contributing events in this region are  $W$ +jets and  $t\bar{t}$  production. The second targets final states with two same flavor but opposite sign leptons. This region is populated, mostly by  $Z \rightarrow \ell\ell$  events that are used to provide an estimate for  $Z \rightarrow \nu\nu$  normalisation. In this so-called *two-lepton control region* (CR2), decays to tau-leptons are not used since their reconstruction is more complicated.

### 8.3.2 Hypothesis testing

The constructed likelihood offers an estimation for the signal strength value  $\hat{\mu}$ . The agreement between the estimated and the observed value will be quantified by a hypothesis test with the use of a test statistic. To avoid dependence on nuisance parameters the profile likelihood ratio [189],[190] is used:

$$\lambda(\mu) = \frac{\mathcal{L}(x; \mu, \hat{\eta})}{\mathcal{L}(x; \hat{\mu}, \hat{\eta})} \quad (8.2)$$

In 8.2  $\mathcal{L}(x; \mu, \hat{\eta})$  is the profiled likelihood: the nuisance parameters  $\hat{\eta}$  are estimated by maximising the likelihood  $\mathcal{L}(x; \mu, \eta)$  for a specific  $\mu$  and  $\mathcal{L}(x; \hat{\mu}, \hat{\eta})$  is the likelihood maximised for both  $\eta$  and  $\mu$  simultaneously (global maximum likelihood). From its definition  $\lambda(\mu)$  takes values in the range  $(0, 1)$  with values closer to one indicating better agreement between the observed and the hypothesised  $\mu$ .

### Background-only hypothesis test

In searches like the one described in this thesis, the signal manifests as a significant excess over the SM prediction. To test for a potential discovery, we set as the null hypothesis the *background-only* hypothesis, according to which the observed data are described only by background processes ( $\mu = 0$ ). The test

statistic, in this case, is defined as

$$q_0 = \begin{cases} -2 \ln \lambda(0) & \text{if } \hat{\mu} \geq 0 \\ 0 & \text{if } \hat{\mu} < 0. \end{cases} \quad (8.3)$$

The expression of  $q_0$  is fixed to 0 in the definition above to ensure that cases with fewer events observed than predicted from background-only processes (downward fluctuations of data with respect to the background-only predictions) would not lead to the rejection of the background-only hypothesis.

Higher  $q_0$  values mean that the observed number of events in data is higher than what the background-only hypothesis can explain, and therefore suggest the presence of signal. The incompatibility between data and the hypothesis under test is quantified by the so-called *p-value*. The *p-value* is the probability to measure a value for the test statistic equal or higher than the observed, when the null hypothesis is true. For the background-only hypothesis ( $\mu = 0$ ) the *p-value* is defined as

$$p_0 = \int_{q_{0,\text{obs}}}^{\infty} f(q_0 | 0) dq_0, \quad (8.4)$$

where  $f(q_0 | 0)$  is the probability density function of the test  $q_0$  statistic under the assumption  $\mu = 0$ .

### 8.3.3 Limit setting procedure

For the limit setting procedure, the hypothesis under test is that the data are described only when a signal contribution is added to the background expectation (*signal+background* hypothesis). In this case, the test statistic is defined as:

$$q_\mu = \begin{cases} -2 \ln \lambda(\mu) & \text{if } \hat{\mu} \leq \mu \\ 0 & \text{if } \hat{\mu} > \mu. \end{cases} \quad (8.5)$$

Similarly to the  $q_0$  defined by Eq. 8.3, downward fluctuations of data with respect to the signal+background predictions should not lead to the rejection of the null hypothesis, therefore  $q_\mu$  is set to 0 for  $\hat{\mu} > \mu$ . In Reference [189] the distribution of this test statistic is derived analytically in the asymptotic limit. The corresponding *p-value*, of this hypothesis test is defined as

$$p_\mu = \int_{q_{\mu,\text{obs}}}^{\infty} f(q_\mu | \mu) dq_\mu \quad (8.6)$$

The significance is defined with the help of p-value (Eq. 8.4 and 8.6) as the quantile of the Gaussian evaluated at  $(1 - p)$ :

$$Z = \Phi^{-1}(1 - p)$$

Using the significance any discrepancy can be quantified in units of the standard deviation  $\sigma$  of the Gaussian distribution. This way  $p$ -value of 0.32 corresponds to a significance of  $1 \sigma$ . Typically, to claim a discovery, the background-only hypothesis has to be rejected with a significance of at least  $5 \sigma$  ( $p_0 \leq 2.7 \times 10^{-7}$ ). On the other hand to exclude a specific signal model, the threshold of  $p_\mu = 0.5$  is usually used ( $z = 1.64 \sigma$ ), which correspond to 95% confidence level (CL).

However, if the exclusion is based only of rejecting the signal+background hypothesis, which is also called  $CL_s + b$  method, can be problematic when the signal process produces very small event yields. In such cases the predictions from signal+background and background-only hypothesis are almost identical. The analysis, should not be sensitive to such events. However, downward fluctuations of data with respect to the signal+ background predictions could lead to a small values  $p_\mu$  that lead to the false exclusion of the signal. In the following, the  $CL_s$  method is discussed, which is used in this work and avoids the issues that can occur with the  $CL_s + b$  method.

## CLs upper limits

The  $CL_s$  method [191] is used to set limits in the upper values of  $\mu$ . In this method the first step is to calculate the  $p$ -value by testing the background+signal hypothesis, which here is denoted as  $p_{s+b}$ . The next step is to calculate the  $p$ -value for the background-only hypothesis  $p_b$ . The  $CL_s$  is given by

$$CL_s = \frac{p_{s+b}}{1 - p_b}$$

Any hypothesis for the value of  $\mu$  with  $CL_s \leq 0.05$  is rejected at 95% confidence level.

## Expected limits

Lastly, we need to create an estimate of the expected limit for a given hypothesis. For this purpose the so-called ‘‘Asimov data set’’ [189] is defined so that when it is used in the maximum likelihood estimator the result is the true parameter values. When this data set is used for a statistical test, for example for the background-only hypothesis the result will be the p-value expected when there

is no signal. Likewise, the expected p-value for a specific signal+background hypothesis is given by the fit to the Asimov data set with  $\mu = 1$ .

### Validation of fit results: Nuisance Parameter Pull

The pull of a nuisance parameter  $\theta$ , is a comparison between the central value of the parameter and its uncertainty before and after the fit, and it is defined as

$$\text{pull}(\theta) = \frac{\hat{\theta} - \theta_0}{\sigma_\theta}, \quad (8.7)$$

where  $\hat{\theta}$  is the NP obtained from the fit,  $\theta_0$  is the expectation value of the NP, and  $\sigma_\theta$  is the standard deviation. The pull expresses how far is from the expected value is the one estimated from the fit in units of  $\sigma_\theta$ .

The nuisance parameters with a gaussian constraint, are expected to have an error interval of  $[-1, +1]$ . When a nuisance parameter has error smaller than the expected one, the fit measurement is more accurate than the auxiliary measurement and the corresponding systematic uncertainty is called *constrained*.

To check whether the value of the pulls are suspicious or not, and therefore validate the fit result, a fit is performed using the Asimov dataset. In this case the values of the pulls should be 0, due to the definition of the Asimov data-set, however the systematic uncertainties can still be constrained. The pulls from the Asimov dataset are then compared to those obtained from the background-only fit, to spot any suspicious behaviours.

# Chapter 9

## Data and simulated events

This chapter provides information on the data set analysed in this thesis in Section 9.1 and the configuration used to produce simulated events for the signal and background processes in Section 9.2.

### 9.1 Data

The data set used for this analysis was recorded with the ATLAS detector from 2015 to 2018 (LHC Run2), for proton-proton collisions at 13 TeV centre-of-mass energy. For each year, specific *Good Run Lists* (GRLs) are compiled from the ATLAS Data Quality group, containing runs and luminosity blocks that fulfil quality and other requirements related to the operation of the detector components. The corresponding integrated luminosity for the full data set is  $139 \text{ fb}^{-1}$ .

The rest of this sections describes the different sets triggers used to record events in the signal and control regions.

#### 9.1.1 Trigger naming convention

The triggers discussed in this section follow the general naming convention

$$[\text{Trigger level}]_{-}[\text{object type}][E_{\text{T}} \text{ or } p_{\text{T}} \text{ threshold in GeV}].$$

In the string above the trigger level is either HLT or L1. The object type, for the triggers discussed in 9.1.2 and 9.1.3, can be an either an electron, a muon or  $E_{\text{T}}^{\text{miss}}$  that are denoted as E, MU and XE respectively. The triggers

will select only the events for which the reconstructed object, specified in the [object type], exceeds the threshold indicated in the name string. In some cases, an extra label is added at the end of the name string above to provide additional information, such as which algorithm was used for the object reconstruction or specific identifications and isolation requirements.

### 9.1.2 Single lepton triggers

The analysis uses single electron and single muon triggers to record the events in the two lepton control region. Single muon triggers are also used to record the events used to estimate the efficiency of the  $E_T^{\text{miss}}$  triggers, as will be discussed in 9.1.3.

Changes in the beam condition lead to modification in the trigger algorithms, lepton isolation requirements or threshold requirements in each data taking year. Table 9.1 summarises the single electron triggers [192]. The electron selection and identification in the trigger algorithm are similar to the one described in Section 6.8.5. A likelihood-based multivariate technique is used to select electrons with four working points: very loose (LHVLOOSE), loose (LHLOOSE), medium (LHMEDIUM) and tight(LHTIGHT).

Some of the triggers listed in Tab. 9.1, have additional labels that will be explained in the following. The label NOD0 indicates that the electron identification process uses no information on the impact parameter  $d_0$ . The label IVARLOOSE indicates an additional isolation requirement which is based on the  $E_T$  inside a cone of variable radius around the electron candidate (similar to the offline reconstruction).

Time period	Trigger name
2015	HLT_E24_LHMEDIUM_L1EM20VH
	HLT_E60_LHMEDIUM
	HLT_E120_LHLOOSE
2016 (A-D3)	HLT_E60_LHMEDIUM_NOD0
	HLT_E140_LHLOOSE_NOD0
2016(D4-end),2017,2018	HLT_E26_LHTIGHT_NOD0_IVARLOOSE
	HLT_E60_LHMEDIUM
	HLT_E140_LHLOOSE

**Table 9.1:** Summary of the single electron triggers used to record events in the two lepton control region. For each data-taking period, the events are recorded from at least one of the listed triggers.

Table 9.2 summarises the single muon triggers [193]. There are two procedures

followed to identify a muon. The first is to form candidates from L1 inputs from the Muon Spectrometer and combine them with tracks in the Inner Detector. The first entry of Tab. 9.2 uses this method and for this reason has the additional string L1MU15. The second method, used for the all the other triggers listed in Tab. 9.2, is to extrapolate high precision tracks from the ID to the Muon Spectrometer. An isolation requirement is applied to tracks from the ID in a cone of variable radius around the muon candidate. This is indicated by the strings IARMEDIUM and ILOOSE in the trigger name. The IARMEDIUM was designed to replace the older ILOOSE isolation criterion in the single muon triggers to cope with the high pile-up conditions.

Period	Trigger name
2015	HLT_MU20_ILOOSE_L1MU15 HLT_MU50
2016 (A)	HLT_MU40 HLT_MU50
2016 (B-D3)	HLT_MU24_IARMEDIUM HLT_MU50
2016 (D4-end), 2017, 2018	HLT_MU26_IARMEDIUM HLT_MU50

**Table 9.2:** Summary of the single muon triggers used to record events in the two lepton control region. For each data-taking period the events are recorded from any of the corresponding trigger.

### 9.1.3 $E_T^{\text{miss}}$ triggers

The analysis uses  $E_T^{\text{miss}}$  triggers to record events in the signal region, as the key feature of the mono-H signature is the high missing transverse energy. These triggers reconstruct  $E_T^{\text{miss}}$  using calorimetric information only [194].

Since muons do not produce a significant signal in the calorimeters, the events that contain them will be also recorded by  $E_T^{\text{miss}}$  triggers. For this reason the analysis uses  $E_T^{\text{miss}}$  triggers to also record events in the one-muon control region.

Table 9.3 summarises the  $E_T^{\text{miss}}$  triggers. The luminosity increase translates to higher pile-up conditions that affect the trigger efficiency. To mitigate such effects, similar to the single lepton triggers,  $E_T^{\text{miss}}$  reconstruction algorithms and thresholds are modified as shown in Tab. 9.3.

There are two different algorithms used for  $E_T^{\text{miss}}$  reconstruction, denoted as MHT and PUFIT [194] in Tab. 9.3. The MHT stands for “missing  $H_T$ ”, and  $H_T$  is the scalar sum of the jet transverse momenta. The algorithm uses calibrated jets

Time Period	Trigger name
2015	HLT_XE70_MHT
2016 (A-D3)	HLT_XE90_MHT_L1XE50
2016 (D4-end)	HLT_XE100_MHT_L1XE50
2017 (B-D5)	HLT_XE110_PUFIT_L1XE55
2017 (D6-end)	HLT_XE110_PUFIT_L1XE50
2018	HLT_XE110_PUFIT_L1XE55

**Table 9.3:** Summary of the  $E_T^{\text{miss}}$  triggers used to record events in the signal and one-muon regions for the data-taking time period.

reconstructed from topoclusters with the anti-kt algorithm and a radius parameter of  $R = 0.4$  including deposits from photons, electrons and  $\tau$ -leptons. The missing transverse energy is calculated as the negative vector sum of all the calibrated jets. The “PUFIT” algorithm calculates missing energy using topoclusters combined into  $\eta - \phi$  patches with a size roughly equal to a jet of  $R = 0.4$ . The algorithm assumes that hard scatter produces higher transverse energy deposits than pile-up interactions. For each patch, a fit is used to determine the energy deposits from pile-up and subtracts them. These corrected patches are used to estimate the missing transverse energy.

The analysis considers only events with  $E_T^{\text{miss}}$  higher than 150 GeV, as will be discussed in the next chapter. As can be seen from 9.3 all listed triggers have lower threshold values than 150 GeV, however they are not fully efficient. In this case a trigger might not record events that actually exceed its defined threshold.

The trigger efficiencies, for this analysis, were measured using events recorded with single muon triggers that lie in a phase space region close to the signal region. Since the detector response changes based on the event selection requirements, any differences in the event topology affect the estimated efficiencies. Once this *reference* set of events (also called reference sample, here) is defined, the trigger efficiency,  $\varepsilon$ , is estimated via the ratio

$$\varepsilon = \frac{N_{\text{Reff}, E_T^{\text{miss trig.}}}}{N_{\text{Reff}}},$$

where  $N_{\text{Reff}, E_T^{\text{miss trig.}}}$  is the number of events in the reference sample that fire a specific  $E_T^{\text{miss}}$  trigger and  $N_{\text{Reff}}$  is the number of events in the reference sample.

The efficiency is calculated twice, once using data and once using simulated events. The ratio  $\varepsilon^{\text{data}}/\varepsilon^{\text{MC}}$  is fitted to obtain a smooth function which is used to correct signal and background predictions.

## 9.2 Simulated events

This section includes analysis-specific information on the simulations of signal processes in Section 9.2.1, and background processes in Section 9.2.2.

### 9.2.1 Signal Processes

The results of this analysis are interpreted in terms of the  $Z'$ -2HDM model for a scan over the  $(m_{Z'}, m_A)$  plane, and for fixed choices of the other model parameters, which are presented in Table 9.4 (see 3.5.1 for parameter definitions). The configuration shown in Tab. 9.4 follows the recommendations of the ATLAS/CMS Dark Matter forum [195], and the following paragraph explains the main motivation for these choices. The scan extends in  $m_{Z'}$  from 600GeV to

$Z'$ 2HDM
$m_H = m_{H^\pm} = m_A$
$m_\chi = 100 \text{ GeV}$
$g_{Z'} = 0.8$
$\tan \beta = 1$

**Table 9.4:** Signal theory parameter configuration to generate events for the  $Z'$ -2HDM model

3600GeV, and in  $m_A$  from 300GeV to 1300GeV as shown in Figure 9.1.

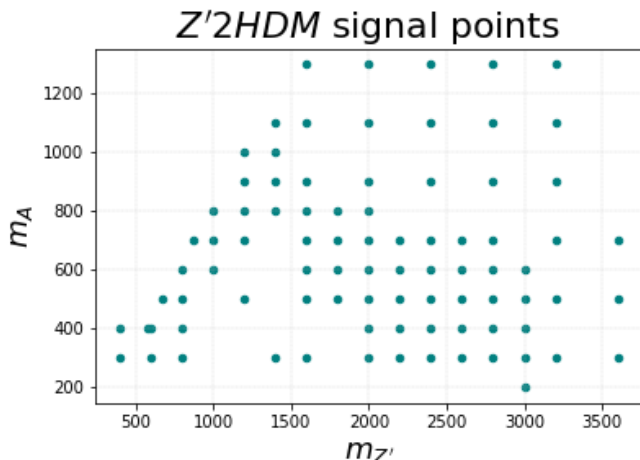


**Figure 9.1:** Grid of signal simulations with different choices of  $m_{Z'}$ , and  $m_A$ . All the other parameters are fixed to the values of Tab. 9.4.

The masses of the charged states were set  $m_H = m_{H^\pm} = m_A$  so that the

analysis results can be easily comparable with the corresponding CMS searches [68]. However, based on the constraints placed by Ref. [196] masses up to 295 GeV are excluded. According to the diagram 3.8 of Section 3.5.1, for the mediator  $A$  to be produced on-shell, it is necessary that  $m_\chi < m_A/2$ . Further the mass of the DM should also be  $m_\chi > m_h/2$ , due to constraints from invisible Higgs decays searches [197]. The value of  $m_\chi = 100\text{GeV}$  is chosen to be able to scan the lower range of  $m_A$ . According to Ref. [195] variations of the coupling or  $\tan\beta$  do not affect the signal kinematics, even though they can affect the production cross-section. For this reason  $g_{Z'}$  is set to an arbitrary value of 0.8 and  $\tan\beta$  to 1.

For the case of the 2HDM $a$  model, the scan is performed over the  $(m_a, m_A)$  plane for the fixed choices of the other model parameters presented in Table 9.5. The scan extends in  $m_a$  from 100 GeV to 600 GeV, and in  $m_A$  from 250 GeV to 2000 GeV, as shown in Figure 9.2. The configuration shown in Tab. 9.5 fol-

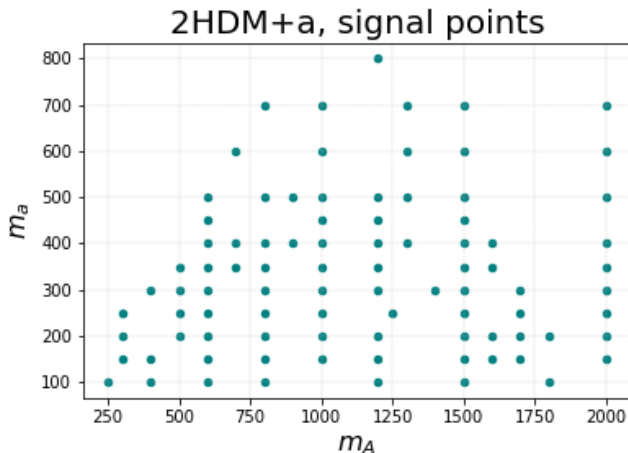


**Figure 9.2:** Grid of signal simulations with different choices of  $m_A$ , and  $m_a$ . All the other parameters are fixed to the values of Tab. 9.5.

lows the recommendations of the LHC DM Working Group [198]. The following paragraph explains the main motivation for these choices. The production rate of  $ggF$  and  $b$ -initiated processes depends on the coupling  $g_{Aah}$  which is a function of  $m_H$ . The coupling decreases when  $m_H < m_A$  reducing the corresponding production rate [86]. For this reason  $m_H = m_{H^\pm} = m_A$  ensures a large production rate for both processes. Constraints from invisible Higgs decays searches [197] allow  $m_a > 100\text{ GeV}$ . The coupling  $g_\chi$  is set to 1 because it is assumed that the mediator  $a$  decays only to DM. To allow for on-shell production of  $a$ , it must hold that  $m_a > 2m_\chi$ . To keep the possibility of studying  $a$  down to

2HDM+a	
$ggF$	b-initiated
$m_A = m_H = m_{H^\pm}$	
$\lambda_{P1} = \lambda_{P2} = \lambda_3 = 3$	
$m_\chi = 10 \text{ GeV}$	
$g_\chi = 1$	
$\sin(\beta - \alpha) = 1$	
$\sin \theta = 0.35$	
$\tan \beta = 1$	$\tan \beta = 10$

**Table 9.5:** Signal theory parameter configuration to generate events for the 2HDMa model via the two production modes considered for this analysis: the gluon-gluon fusion (left) and the b-initiated (right)

low masses,  $m_\chi = 10\text{GeV}$  is chosen. The possible values of  $\lambda_3$  depend on the choice of the Higgs boson masses and  $\sin \theta$ . The benchmark values of  $\lambda_3 = 3$  and  $\sin \theta = 0.35$ , are chosen to allow the  $m_H, m_{H^\pm}$  and  $m_A$  to reach up to order of few TeV.

The production cross section of the  $ggF$  and  $b\bar{b}$ -induced processes, presented in Ch. 3.5.1 Fig. 3.9, depends on  $\tan \beta$ . While the cross section for the  $ggF$  processes decreases with increasing  $\tan \beta$ , for  $b\bar{b}$ -induced increases. The reason for this is the  $t$ -quark loop involved in the  $ggF$  production mechanism:  $A$  has a coupling to  $t$ -quarks that is inversely proportional to  $\tan \beta$ , while its couplings to  $b$ -quarks is proportional to  $\tan \beta$  [86]. According to Ref. [82] the  $ggF$  and  $b\bar{b}$  cross sections are roughly the same for  $\tan \beta \approx 5$ , while the  $b\bar{b}$ -induced production mode becomes dominant for  $\tan \beta = 10$ . On the contrary the dominant production mode for  $\tan \beta = 1$  is the gluon-gluon fusion.

The rest of this section contains information on the event generators, pdf sets, tunes, etc. used for the simulation of the processes described in Chapter 4.

Events are generated for signal Z'2HDM processes with MADGRAPH5\_aMC@NLO 2.6.5 [104] at leading-order (LO) using the NNPDF3.0 NLO PDF set [95] and  $\alpha_s = 0.118$ . The output was interfaced with PYTHIA 8.240 [102] for the simulation of the parton shower and the hadronization. Parton shower and hadronization is simulated with using NNPDF2.3 LO PDF set [199] and the A14 set of tuned parameters (“tune”) [200].

For the simulation of 2HDMa events, matrix elements are calculated with MADGRAPH5\_aMC@NLO 2.6.7 with NNPDF3.0 NLO PDF set and  $\{\alpha_s = 0.118\}$ . The cross-sections were calculated at leading-order (LO) accuracy. The output was interfaced with PYTHIA 8.244 [201] for the simulation of the parton shower and the hadronization. The parton shower model is using the NNPDF2.3 LO PDF set

and the A14 tune. The SM Higgs boson decays into  $b\bar{b}$  pairs were also simulated with PYTHIA 8.240 with a branching fraction fixed to the SM prediction.

Finally, at the event generation an filter is applied that keeps events with  $E_{\text{T}}^{\text{miss}}$  higher than 100 GeV.

## 9.2.2 Background Processes

Table 9.6 summarises the MC generators used for the matrix elements calculations, the order at which cross sections are calculated, the PDF sets, the generators used for the parton showering and hadronisation simulation and the PDF sets used for the parton shower modelling. Events generated with SHERPA [202], in tab 9.6 are not interfaced with other generators, because SHERPA has its own model for parton showering, hadronization and underlying event [203]. The matching of parton showers to matrix elements, for these simulated event samples is done using the MEPS@NLO prescription [204–206]. It should be noted that the decays bottom and charm hadrons for single- $t$  events were simulated with the EVTGEN v1.6.0 program [207] and the  $t\bar{t}H$  events with the EVTGEN v1.2.0. For the processes  $t\bar{t}$ , single- $t$ ,  $t\bar{t}V$  and  $t\bar{t}H$  the A14 set of tuned parameters [200], while for  $VH(b\bar{b})$  the AZNLO tune [208] is used.

**$V$ +jets** Two types event filters are used for these simulated event samples: one filters events based on the quark flavor of the jets and the other based on the the maximum of the boson  $p_{\text{T}}^V$  and  $H_T$ , the MAXHTPTV (here  $H_T$  is the scalar sum of the jets momenta). There are three different flavour filters. The BFILTER which allows only  $b$ -hadrons in the final state with  $p_{\text{T}} > 5$  GeV and  $|\eta| < 2.9$ , the CFILTERBVETO allowing only  $c$ -hadrons with  $p_{\text{T}} > 54$  GeV and  $|\eta| < 3$  and vetoes  $b$ -hadrons, and the CVETOBVETO that vetoes events with  $b$ - and  $c$ -hadrons. The MAXHTPTV requirement is applied so that the final states contain events with  $\max(p_{\text{T}}^V, H_T)$  within a specific range. The ranges used in this work are  $(0, 70)$ ,  $(70, 140)$ ,  $(140, 280)$ ,  $(280, 500)$ ,  $(500, 1000)$ , and above 1000 GeV.  $Z(\nu\nu)$ +jets simulated events are produced, also, in ranges of vector boson  $p_{\text{T}}$  and dijet invariant mass. There are four  $p_{\text{T}}$  ranges,  $(70, 100)$ ,  $(100, 140)$ ,  $(140, 280)$ ,  $(280, 500)$  GeV and three  $m_{jj}$  ranges,  $(0, 500)$ ,  $(500, 100)$ , above 1000 GeV. The slices are defined by creating all the possible combinations of these ranges and the heavy flavour filters.

**$t\bar{t}$ +jets** For these simulated event samples a  $E_{\text{T}}^{\text{miss}}$  filter is used that accepts events with  $E_{\text{T}}^{\text{miss}}$  in the ranges:  $(200, 300)$ ,  $(300, 400)$ , and above 400 GeV

Process	Matrix element	Cross section	PDF(Hard Scatter)	PS + hadron	PDF(PS)
$V + \text{jets}$	SHERPA v2.2 [202]	NLO up to 2 jets LO up to 2 jets	NNPDF3.0 NNLO -	SHERPA v2.2 SHERPA v2.2	-
$t\bar{t}$	POWHEGBOX v2	NNLO	NNPDF3.0 NLO	PYTHIA 8.230	NNPDF2.3 LO
single- $t$ ( $Wt - \text{chan.}$ )	POWHEGBOX v2	NLO	-	PYTHIA 8.230	NNPDF2.3 LO
single- $t$ ( $s\text{-chan.}$ )	POWHEGBOX v2	NLO	NNPDF3.0 NLO	PYTHIA 8.230	NNPDF2.3 LO
single- $t$ ( $t\text{-chan.}$ )	POWHEGBOX v2	NLO	NNPDF3.0 NLO nf4 [95]	PYTHIA 8.230	NNPDF2.3 LO
Diboson	SHERPA v2.2	NNLO	NNPDF3.0 NLO	SHERPA v2.2	-
$Vh(b\bar{b})(q\bar{q})$	POWHEGBOX v2	NNLO(QCD)	NNPDF3.0 NLO	PYTHIA 8.212	CTEQ6L1 [209]
$Vh(b\bar{b})(ggF)$	POWHEGBOX v2	NLO(EW)	-	-	CTEQ6L1
$t\bar{t}V$	MADGRAPH5_AMC@NLO v2.3.3	NNLO	NNPDF3.0 NLO	PYTHIA 8.212	NNLO
$t\bar{t}h$	POWHEGBOX v2	NLO	NNPDF3.0 NLO	PYTHIA 8.210	NLO
		NLO	NNPDF3.0 NLO	PYTHIA 8.230	NLO

**Table 9.6:** Overview of the MC generators used for the matrix elements calculations, the order at which cross sections are calculated (indicated in the “cross section” column), the PDF sets, the generators used for the parton showering and hadronisation simulation and the PDF sets used for the parton shower modelling. For the  $(g\bar{q})$ -initiated  $Vh$  processes, the QCD and electroweak (EW) corrections to the cross section are estimated at different order. Typically, the PDF set used for the modelling of the parton shower (PS) and the hadronisation is different from the one used in ME calculations. The label *NNLO* denotes the next-to-next-to-leading logarithmic order calculations.



# Chapter 10

## Object Definition and event selection

This chapter provides the analysis-specific requirements for the reconstruction of the physics objects in Section 10.1 as well as the truth-level (also referred to as *particle-level*) definitions of physics objects. It also discusses in Section 10.2 the event selection requirements used for the definitions of the signal and control regions. Finally, Section 10.3 presents comparisons of event variables obtained at particle and reconstructed levels to validate the particle-level definitions in signal and control regions.

### 10.1 Physics Objects definition

This section provides information on the requirements the reconstructed objects have to satisfy to be considered in the analysis. The first section, 10.1.1, discusses the primary vertex, Section 10.1.2 the jet, and Section 10.1.3 the leptons definitions. Section 10.1.4 describes the procedure used to resolve cases in which a signal from the detector is reconstructed as two separate objects, known as overlap removal. Finally, Section 10.1.5 discusses the  $E_T^{\text{miss}}$  reconstruction in the analysis and the way we quantify how “genuine” it is.

#### 10.1.1 Primary Vertex

In each event, more than one interaction can be observed. Only the one with the most energetic tracks is considered, and is called *Primary Vertex*. To determine

it, for each vertex we calculate the sum  $\Sigma p_T^2$  for all the associated tracks with  $p_T > 0.5$  GeV. The vertex with the highest sum is the primary vertex.

### 10.1.2 Jets

**Small- $R$  jets** are built using the Particle-Flow algorithm, described in Section 6.8.4. In each event, jets are separated into central with  $|\eta| < 2.5$  and  $p_T > 20$  GeV, and forward with  $2.5 < |\eta| < 4.5$  and  $p_T > 30$  GeV. The Higgs boson decay products have high transverse momentum and populate a central area in the detector. Thereby, only central jets are used to reconstruct the invariant mass of the Higgs candidate and they must not originate from pile-up interactions. To reject pile-up central jets, the analysis uses a multivariate algorithm, the Jet-Vertex-Tagger [210] (JVT). This algorithm provides a likelihood-based discriminant relying on the tracks associated with the jet. The discriminant values range from zero, for pile-up jets, to one for hard-scatter jets. The JVT is used only for central jets with  $20 \text{ GeV} < p_T < 120 \text{ GeV}$ . Additionally the application of the algorithm is limited to jets with  $|\eta| < 2.4$ , due to the use of tracking information. In the analysis, central jets with  $\text{JVT} < 0.5$  is rejected as a pile-up jet.

**Large- $R$  jets** are reconstructed, as explained in Section 6.8.4, from LCW calibrated topological clusters. Only jets with  $p_T > 200$  GeV and  $|\eta| < 2$  are considered. For the variable radius jets associated to the large- $R$  jet the radius parameter was set to  $R = \frac{30 \text{ GeV}}{p_T}$  with a minimum of 0.02 and a maximum of 0.4.

**Muon-in-Jet Correction** When the  $b$ -hadron inside a jet decays through channels such as  $b \rightarrow Wc \rightarrow \mu\bar{\nu}_\mu c$ , which contain muons in the final state, the muon energy and momentum are not included in the jet reconstruction. For small- $R$  jets, this is because the PFlow algorithm does not consider tracks linked to electrons or muons (more details in Sec.6.8.4), while large- $R$  jets are reconstructed from LCW topoclusters using calorimeter-only information.

Not considering the muon contribution affects the measured value of the Higgs boson candidate mass. It can be added, however, after the reconstruction step with the so-called *muon-in-jet correction*. This additional energy correction is applied to the  $b$ -jets that form the Higgs candidate to improve the reconstructed mass resolution [211]. The muons considered in these corrections must pass much looser identification requirements (Loose WP), and since they are pro-

duced inside a jet, no isolation requirement is applied. Muons with  $p_T > 5$  GeV in a region of  $\eta < 2.7$  are considered for this correction.

In the resolved region, if there is a muon within  $\Delta R < 0.4$  of the jet axis of the  $b$ -jet, the correction first subtracts the energy the muon is expected to lose in the calorimeter from the muon four-momentum, and the result is added to the respective jet. If there are more than one muon close to the jet axis, then only the closest is considered. Figure 10.1 shows the distributions of the invariant mass in the resolved signal region with and without muon-in-jet correction for a signal simulation. In the merged region the muon-in-jet correction is applied to the leading  $b$ -tagged large- $R$  jet. In this case we consider the two (or one) muons closest to the large- $R$  jet axis.

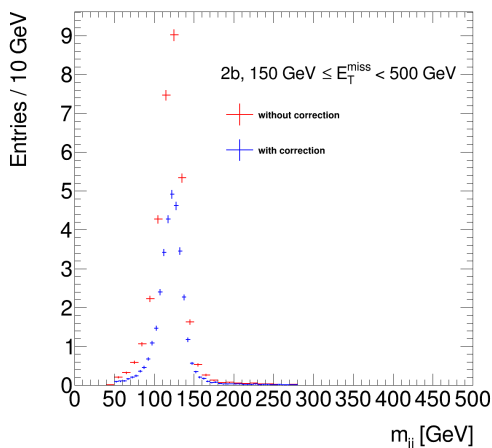


**Figure 10.1:** Distributions of the invariant mass of the Higgs-boson candidate mass, with (blue) and without (red) muon-in-jet correction, in the resolved signal region with exactly 2  $b$ -jets in the final state. The distribution is produced using  $Z'$ -2HDM model with  $m_{Z'} = 800$  GeV and  $m_A = 600$  GeV

**Truth jets** At particle-level, jets are formed by clustering stable particles using the anti- $k_t$  algorithm and are called *truth jets*. From the inputs, muons are excluded since the corresponding physics object deposits very little energy in the calorimeter. In the same way, neutrinos that completely escape detection are excluded as well. A radius parameter of 0.4 is used for small- $R$  jets and 1.0 for large- $R$  jets.

## Identification of $b$ -jets

To identify if a central small- $R$  jet or a variable- $R$  track jet contains a  $b$ -quark the DL1r tagger is used. The working point selected for this multivariate algorithm tags jets containing  $b$ -hadrons with 77% efficiency in  $t\bar{t}$  simulations.

**Particle-level flavour labelling** All truth jets are labelled based on the particle that initiated them (quark or gluon). The flavour of each jet is also stored, and it is determined by the presence of a  $b$ -,  $c$ -hadron or a  $\tau$ -lepton at distance  $\Delta R < 0.3$  from the jet. Using, however, these labels to determine the number of  $b$ -jets in the event does not take into account the efficiency and mistag rates of the  $b$ -tagging algorithm.

Instead of relying only on truth information in this work, a “hybrid” approach is used. For each event, the probability that two or more jets are  $b$ -tagged is calculated using the so-called *efficiency maps*<sup>1</sup>. These maps give the probability for a specific jet to be  $b$ -tagged based on its  $p_T$ ,  $\eta$  and truth flavour label. There are efficiency maps, derived from dedicated measurements, for various tagging algorithms, working points and all flavour hypotheses. The map used here corresponds to the DL1r tagger and 77% working point.

To calculate the probability for an event to contain exactly two  $b$ -tag jets, the first step is to retrieve from the efficiency maps for each jet in the event the probability to be  $b$ -tagged,  $\epsilon_i$ . The next step is to form pairs of jets  $i, j$ , with  $i \neq j$ . The probability of both jets in each pair to be tagged is  $\epsilon_i \epsilon_j$ , while the probability that any of the  $k$  remaining jets in the event is not a  $b$ -jet is  $1 - \epsilon_k$ . Finally, the probability for an event to contain exactly two  $b$ -tag jets is given by

$$w = \sum_{i=1}^{N_{\text{jets}}} \left( \prod_{\substack{i,j=1 \\ i \neq j}}^{N_{\text{jets}}} \epsilon_i \epsilon_j \prod_{\substack{k=1 \\ k \neq i,j}}^{N_{\text{jets}}} (1 - \epsilon_k) \right), \quad (10.1)$$

where  $N_{\text{jets}}$  is the number of jets in the event. This is applied as an additional weight in each event. The formula is also generalised to events that contain three or more jets.

---

<sup>1</sup>The maps are provided by the ATLAS flavour tagging group

### 10.1.3 Leptons

#### Electrons

Electrons in this analysis are used for two purposes: to veto any events in the signal and one-lepton regions, and select events with two electrons in the two-lepton region. For the veto definitions in the signal region loose electron requirements are used to increase the reconstruction efficiency. On the contrary, tighter definitions are needed to have a high purity when selecting electrons for the two-lepton control region.

Electrons are reconstructed from a track which is consistent with a cluster built from energy deposits in the calorimeter. The tracks must have  $\sigma(d_0) < 5$  and  $|z_0 \sin\theta| < 0.5$  mm to be compatible with the primary vertex. As explained in 6.8.5 the LooseAndBLayer identification working point is used. This provides an efficiency of 86% for electrons with  $E_T = 20$  GeV which gradually increases up to 95% for electrons with  $E_T > 100$  GeV [124].

Electrons with  $p_T < 200$  GeV must pass the FCLoose isolation WP, which requires that the energy deposit in a cone of  $\Delta R < 0.2$  ( $E_T^{\text{cone20}}$ ) around the electron cluster must not be more than 20% of the electron  $p_T$ . Electrons with  $p_T > 200$  GeV must pass the FCHighPtCaloOnly, instead, which requires  $E_T^{\text{cone20}} < 3.5$  GeV [124].

Electrons are classified as *baseline*, used for the veto definitions and *signal* used in the event selection of the two-lepton region. Baseline electrons must have a minimum  $p_T$  of 7 GeV to be in a well-understood kinematic regime. For signal electrons the  $p_T$  threshold is increased to 27 GeV. This value is above the higher  $p_T$  threshold of the electron triggers used in this analysis (see Tab. 9.1), and is used to reduce the contributions of fakes electrons and mis-measurements. Both baseline and signal electrons are required to have  $|\eta| < 2.47$ . Table 10.1 summarises the selection requirements for electrons used in the analysis.

	Baseline electrons	Signal electrons
Identification	LooseAndBLayer	
Isolation	FCLoose for $p_T < 200$ GeV FCHighPtCaloOnly for $p_T > 200$ GeV	
$ \eta $	$< 2.47$	
$p_T$	$> 7$ GeV	$> 27$ GeV
Track to vertex association	$d_0/\sigma(d_0) < 5$ and $ z_0 \sin\theta  < 0.5$ mm	

**Table 10.1:** Summary of electron selection requirements.

**Truth electrons** are selected using the so-called PDGID, a unique code assigned to electrons<sup>2</sup> (and all the other particles) during the event generation step [212]. The truth electrons must also be final-state particles which is determined by the so-called *status code*, also assigned at the event generation step. Because we are using truth information to distinguish the electrons no isolation or identification requirements are necessary. Truth electrons are also categorised to baseline and signal with  $p_T$  above 7 GeV and 27 GeV respectively and are required to have  $|\eta| < 2.47$ .

## Muons

Similar to the electrons, two muon definitions are used: baseline muons with looser definitions for vetoing events, and signal muons with tight definitions to ensure a high-purity muon selection in the control regions. All baseline muons must have a minimum  $p_T$  of 7 GeV. Signal muons must pass the baseline  $p_T$  threshold and the most energetic muon must have  $p_T > 25$  GeV. Baseline muons need to pass the Loose identification WP, which uses all types of muons described in 6.8.6, while signal muons are required to pass the Medium WP, that has a lower efficiency than the Loose WP and uses only CB and ME muon types. In terms of isolation, baseline muons are selected with the FCLoose isolation WP which requires  $E_T^{\text{cone}20}$  to be less than 30% of the  $p_T$  of the muon. Signal muons must pass the FCTightTrackOnly isolation WP which requires  $p_T^{\text{cone}30}$  to be less than 6% of the muon  $p_T$ . Both baseline and signal muons are required to satisfy  $|\eta| < 2.5$ ,  $d_0/\sigma(d_0) < 3$  and  $|z_0\sin\theta| < 0.5$  mm. Table 10.2 summarises all the selection requirements applied to muons.

	Baseline muons	Signal muons
Identification	Loose	Medium
Isolation	FCLoose	FCTightTrackOnly
$ \eta $	$< 2.5$	
$p_T$	$> 7$ GeV	$> 7$ GeV for the sub-leading and $> 25$ GeV for the leading
Track to vertex association	$d_0/\sigma(d_0) < 3$ and $ z_0\sin\theta  < 0.5$ mm	

**Table 10.2:** Summary of muon selection requirements.

**Truth muons** are selected, just like the truth electrons, using their PDGID<sup>3</sup>, and the appropriate status code. No isolation or identification requirements are

<sup>2</sup>The number 11 is assigned to  $e^-$  and  $-11$  to  $e^+$ .

<sup>3</sup>13 for  $\mu^-$  and  $-13$  for  $\mu^+$

necessary in this case. Truth muons follow the same categorisation as reconstructed muons and are required to satisfy the same  $p_T$  and  $|\eta|$  requirements.

### Truth $\tau$ -leptons

$\tau$ -leptons that decay to hadrons are used to veto events in the signal region. They are reconstructed from LCW topoclusters using the anti- $k_t$  algorithm with a radius parameter of 0.4.  $\tau$ -lepton candidates are required to have one or three tracks within  $\Delta R < 0.2$  of the jet axis since their hadronic decays can yield either one or three charged pions. A RNN classifier is used to identify the  $\tau$ -leptons and candidates are required to pass VeryLoose WP [163]. Finally, all  $\tau$ -lepton candidates are required to have  $|\eta| < 2.5$  and  $p_T > 20$  GeV.

$\tau$ -leptons are selected, similar to the other truth leptons, by using their PDGID (15 for  $\tau^-$  and  $-15$  for  $\tau^+$  [212]), and the appropriate status code. They are required to satisfy the same  $p_T$  and  $|\eta|$  requirements as the reconstructed  $\tau$ -leptons.

#### 10.1.4 Overlap removal

After the objects are reconstructed possible “overlaps” (cases where the same signal is reconstructed as multiple objects) are resolved. This procedure removes close-by objects based on different criteria. The distance between objects is measured by  $\Delta R = \sqrt{\Delta\phi^2 + \Delta y^2}$ . The procedure is applied in the following order:

1. If two electrons share the same track, the one with the lower  $p_T$  is rejected
2. If the  $\Delta R$  between a  $\tau$ -lepton and an electron or a muon is less than 0.2, the  $\tau$ -lepton is rejected.
3. When an electron and a muon share an ID track, the electron is rejected if the muon is calorimeter-tagged, otherwise the muon is rejected.
4. If there is a small- $R$  jet at distance  $\Delta R < 0.2$  from an electron, the jet is rejected.
5. If the  $\Delta R$  between an electron and a small- $R$  jet is less than  $0.04 + 10 \text{ GeV}/p_T(e)$ , with a maximum of 0.4, the electron is rejected.

6. If a small- $R$  jet with less than three associated tracks is at a distance  $\Delta R < 0.2$  from a muon, or is ghost-associated to the muon, the jet is rejected.
7. If the  $\Delta R$  between a muon and a small- $R$  jet is less than  $0.04 + 10 \text{ GeV}/p_T(\mu)$ , with a maximum of 0.4, then the muon is rejected.
8. If the  $\Delta R$  between a small- $R$  jet and a  $\tau$ -lepton is less than 0.2, the small- $R$  jet is rejected.
9. If the  $\Delta R$  between a large- $R$  jet and an electron is less than 0.1 then, the large- $R$  jet is rejected.

Only the objects that pass through the full sequence described above are used in the analysis.

**Overlap removal for truth particles.** An overlap removal is applied for truth particles as well. The need for such a procedure comes from the way truth-jets are formed: all stable particles in the event are used as inputs to the jet clustering algorithm except muons and neutrinos. As a result, a jet can be formed around a stable electron. For the overlap removal procedure we need to define an isolation requirement for electrons. Here, an electron is considered isolated when the  $p_T$  of the charged particles within a cone of radius 0.2 around it is less than 20% of the electron  $p_T$ . The procedure is applied in the following order:

1. Any small- $R$  truth jet within  $\Delta R < 0.4$  of an isolated electron is rejected.
2. Any muon within  $\Delta R < 0.4$  of the remaining small- $R$  jets is rejected.
3. Any electron within  $\Delta R < 0.4$  of the small- $R$  jets is also rejected.
4. If there is a large- $R$  jet within  $\Delta R < 1.2$  of the remaining electrons, the large- $R$  jet is rejected.

### 10.1.5 Missing Transverse Energy

For this analysis,  $\vec{E}_T^{\text{miss}}$  is reconstructed from baseline electrons and muons and all small- $R$  jets (central and forward as defined in Sec. 10.1.2). The  $\tau$ -leptons are treated as jets in the calculation of  $\vec{E}_T^{\text{miss}}$  and they are not included as a separate term. Also, large- $R$  jets are not used in the reconstruction. The Tight WP is used, which does not include forward jets with  $20 \text{ GeV} < p_T < 30 \text{ GeV}$

to suppress pile-up contributions. Finally,  $E_T^{\text{miss}}$  reconstruction uses a separate overlap removal procedure [213].

**Particle-level missing transverse momentum  $E_T^{\text{miss}}$**  The most straightforward way to calculate  $E_T^{\text{miss}}$  at particle-level is to take the vector sum of all the stable non-interacting particles like neutrinos and DM particles. However, this is not the best approximation of the detector-level  $E_T^{\text{miss}}$  definition. In this work,  $E_T^{\text{miss}}$  is defined by calculating an equivalent to the calorimeter-based only  $E_T^{\text{miss}}$  and then adding the contribution from muons separately. The first term includes all the stable interacting particles within detector acceptance ( $\eta < 5$ ) except muons. The second term uses all final state muons with  $p_T > 6 \text{ GeV}$ .

### Missing Transverse Energy Significance

As it was discussed in Section 8.2, several effects such as the inaccurate reconstruction of physics objects, or measurement inefficiencies and resolution effects, can give rise to fake  $E_T^{\text{miss}}$ . There is a way to quantify how “genuine” the reconstructed  $E_T^{\text{miss}}$  is by using the so-called  $E_T^{\text{miss}}$  Significance,  $\mathcal{S}$ . This event variable was initially defined as

$$\mathcal{S} = \frac{E_T^{\text{miss}}}{\sqrt{H_T}},$$

where  $H_T$  is defined by Eq. 6.5 as the scalar sum of the momenta of the all hard objects entering the  $E_T^{\text{miss}}$  reconstruction. This is called *event-based*  $E_T^{\text{miss}}$  significance. In events with neutrinos or other non-interacting particles,  $E_T^{\text{miss}}$  is expected to be larger than the  $H_T$ . As a result, real  $E_T^{\text{miss}}$  leads to higher values of event-based  $E_T^{\text{miss}}$  significance compared to fake  $E_T^{\text{miss}}$ .

A more sophisticated definition of  $E_T^{\text{miss}}$  significance is used in this work, which takes into account the resolutions of all the objects entering the  $E_T^{\text{miss}}$  reconstruction as well as the correlations between them, and is called *object-based*  $E_T^{\text{miss}}$  significance.

In a coordinate system rotated parallel (longitudinal L) and perpendicular (transverse T) to the direction of the  $\vec{E}_T^{\text{miss}}$ , the definition of  $\mathcal{S}$  can be written as

$$\mathcal{S} = (E_T^{\text{miss}}, 0) \begin{pmatrix} \sigma_L^2 & \rho_{LT}\sigma_L\sigma_T \\ \rho_{LT}\sigma_L\sigma_T & \sigma_T^2 \end{pmatrix}^{-1} \begin{pmatrix} E_T^{\text{miss}} \\ 0 \end{pmatrix} = \frac{|E_T^{\text{miss}}|^2}{\sigma_L^2(1 - \rho_{LT}^2)}, \quad (10.2)$$

where  $\sigma_L^2$  and  $\sigma_T^2$  are the total variances in the longitudinal and transverse directions relative to  $\vec{E}_T^{\text{miss}}$ , respectively, while  $\rho_{LT}$  is the correlation factor of the longitudinal ( $L$ ) and transverse ( $T$ ) measurements [214].

High values of  $\mathcal{S}$  indicate that resolution effects are not enough to account for the observed  $E_T^{\text{miss}}$ , instead, they suggest the presence of an undetected object, such as a neutrino.

**Particle-level  $E_T^{\text{miss}}$  significance** It is possible to implement a definition for object-based  $E_T^{\text{miss}}$  significance using truth particles. In this case, we use the particle-level estimated  $E_T^{\text{miss}}$ , and the resolution of the corresponding reconstructed objects, which is known as a function of  $p_T$  and  $\eta$ . For example, for a truth electron with  $p_T = 100$  GeV and  $\eta = 0$  the relative parallel resolution, in the  $E_T^{\text{miss}}$  significance definition, is set to 1.7% and the perpendicular to 0.4% [214]. No kinematic requirements are applied to the truth particles used for the calculation of the  $E_T^{\text{miss}}$  significance, except to truth small- $R$  jets, which are required to have  $p_T$  higher than 20 GeV and must not be formed around a stable electron.

## 10.2 Event Selection

Only events from the good run list (GRL) that do not have any of the flags explained in Section 6.7 are used in the definition of the signal and control regions. Section 10.2.1 contains a set of baseline event requirements. Section 10.2.2 describes the additional requirements that define the resolved signal region, while Section 10.2.3 contains the event selection requirement for the merged signal region. Section 10.2.4 presents the event selection for the one and two lepton control regions.

### 10.2.1 Baseline event selection

**Event Cleaning.** As explained in Section 6.7 problematic events that are affected by some detector problem are flagged in order to be removed before using the data-set for physics analysis. The flags are placed in any of the following cases :

- When there are noisy cells in the liquid argon calorimeter system, or corrupted cells in the tile calorimeter.
- If the event is corrupted by problems in the SCT.

- When information is missing and the event is incomplete.
- When one or more muons from cosmic rays are recorded, i.e. muons with  $d_0 > 0.2 \text{ mm}$  and  $|z_0 \sin\theta| > 1 \text{ mm}$ .
- When the muons in the event are poorly measured :  $\frac{\sigma(|q/p|)}{|q/p|} > 0.4$

Once the corrupted events are removed the rest of the event selection requirements are applied.

$E_{\text{T}}^{\text{miss}} > 150 \text{ GeV}$ . The analysis uses the  $E_{\text{T}}^{\text{miss}}$  triggers listed in Table 9.3 to record events, and the higher threshold is  $110 \text{ GeV}$ . Requiring  $E_{\text{T}}^{\text{miss}}$  higher than  $150 \text{ GeV}$  ensures that the events are in a  $E_{\text{T}}^{\text{miss}}$  region where the triggers are fully efficient.

**Lepton veto.** In the signal region any events that contain baseline electrons, muons or tau candidates are rejected.

**Extended tau veto.** The extended tau veto rejects any events with a small-R jet that has less than four associated tracks, and its angular separation from  $E_{\text{T}}^{\text{miss}}$  is less than  $22.5^\circ$  ( $\Delta\phi(E_{\text{T}}^{\text{miss}}, \text{jet}) \leq 22.5^\circ$ ). This additional requirement is applied to catch tau-leptons misidentified as jets, mostly from  $W$  decays. Since leptons produced in  $W$  boson decays are almost aligned, any misidentified  $\tau$ -lepton should be relatively close in  $\phi$  to the  $E_{\text{T}}^{\text{miss}}$ .

$\Delta\phi(E_{\text{T}}^{\text{miss}}, \text{jet}_i) > 20^\circ$ . The definition of this selection requirement uses the three most energetic forward and central jets in the event and calculates their angular separation with the  $E_{\text{T}}^{\text{miss}}$ ,  $\Delta\phi(E_{\text{T}}^{\text{miss}}, \text{jet}_i)$ . Events were selected only when the minimum between the three calculated values was higher than  $20^\circ$ . As it was discussed in Section 8.2, mis-measurements in jets can give rise to fake  $E_{\text{T}}^{\text{miss}}$ . If one jet is mis-measured in a multijet event, the  $E_{\text{T}}^{\text{miss}}$  points to the direction of this jet. Therefore signal events should have a minimum angular separation between jets and the reconstructed  $E_{\text{T}}^{\text{miss}}$ .

## 10.2.2 Resolved region

The following requirements are applied in addition to the baseline selection:

- $E_T^{\text{miss}} < 500$  GeV. Events in the resolved region must have missing transverse energy lower than 500 GeV.
- $p_T(H_{\text{reco}}) > 100$  GeV, when  $E_T^{\text{miss}} < 350$  GeV. From the signal event topology discussed in Section 8.1 is evident that the Higgs momentum is correlated with the momentum of the Dark Matter particles. As a result, the Higgs candidate  $p_T$ ,  $p_T(H_{\text{reco}})$ , is also highly correlated with  $E_T^{\text{miss}}$  for signal events, while the same requirement is not necessarily valid for SM background events. Requiring the  $p_T(H_{\text{reco}})$  to be higher than 100 GeV for the resolved region enhances the signal sensitivity.
- $p_T(H_{\text{reco}}) > 300$  GeV, when  $E_T^{\text{miss}} > 350$  GeV. For  $E_T^{\text{miss}}$  values higher than 350 GeV the threshold on  $p_T(H_{\text{reco}})$  is raised to 300 GeV.
- $m_T^{b,\text{min}} > 170$  GeV and  $m_T^{b,\text{max}} > 200$  GeV. This cut is used to remove background contributions from the semi-leptonic decays of pair produced top-quarks (discussed in 8.2). The reconstructed transverse mass of the  $b$ -tagged jet and  $E_T^{\text{miss}}$  is given by:

$$m_T^b = \sqrt{2p_T^{b,E_T^{\text{miss}}} (1 - \cos \Delta\phi(\vec{p}_T^{b,\text{miss}}, \vec{E}_T^{\text{miss}}))} \quad (10.3)$$

$m_T^{b,\text{min}}$  and  $m_T^{b,\text{max}}$  is the transverse mass calculated from 10.3 using the  $b$ -jet with the minimum or maximum  $\Delta\phi(\vec{p}_T^{b,\text{miss}}, \vec{E}_T^{\text{miss}})$  respectively. For events from semi-leptonic  $t\bar{t}$  decays,  $m_T^{b,\text{min}}$  and  $m_T^{b,\text{max}}$  should be approximately equal to the mass of the top-quark ( $\approx 170$  GeV).

- $\mathcal{S} > 12$ . Multi-jet processes are expected to have low values for  $E_T^{\text{miss}}$  significance, and therefore, signal events are required to have  $\mathcal{S} > 12$ .
- A requirement is applied on the number of central small- $R$  jet. A maximum of four jets is allowed when the event has exactly two  $b$ -tagged jets and a maximum of five when the event has three or more  $b$ -tagged jets.
- $50 \text{ GeV} < m_{jj} < 280$  GeV. Finally, the invariant mass of the Higgs candidate must be within the range  $50 \text{ GeV} < m_{jj} < 280$  GeV. Even though the signal events are expected to be centered around  $m_{jj} = 125$  GeV, the range is larger so that we can use the side band of the mass spectrum,  $50 \text{ GeV} < m_{jj} < 70$  GeV, and  $140 \text{ GeV} < m_{jj} < 280$  GeV, for the background estimation. The lower threshold of 50 GeV is chosen because this the lowest mass for calibrated large- $R$  jets.

Figure 10.2 shows the relative background contributions of all the background processes that create a considerable yield of events in the resolved SR. Figure

10.2a shows the yield break down when exactly 2  $b$ -jets are required in the final state. In this case, the dominant process is  $Z$ +jets (40.4%), followed by  $t\bar{t}$  (33.6%) and  $W$ +jets (14.9%). Figure 10.2b shows the background contributions when 3 or more  $b$ -jets are required in the final state. Here,  $t\bar{t}$  (58.6%) is the dominant background followed by  $Z$ +jets(22.6%).

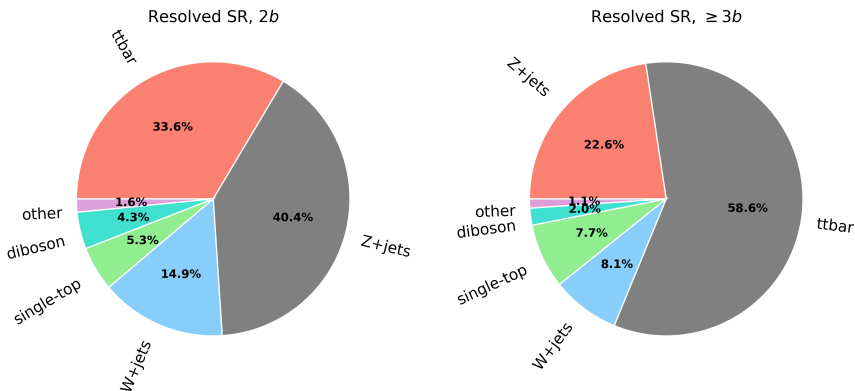


**Figure 10.2:** Relative contributions of the SM background processes in the resolved SR. In these charts, the label “other” describes the relative contributions from  $t\bar{t}V, t\bar{t}H$  and  $VH(bb)$  processes.

### 10.2.3 Merged region

In addition to the baseline requirements the events in the merged region must fulfil the following criteria:

- $E_T^{\text{miss}} > 500 \text{ GeV}$ .
- There must be at least one central large- $R$  jets.
- The invariant mass of the most energetic central large- $R$  jets must be within the range  $50 \text{ GeV} < m_J < 280 \text{ GeV}$ . The different upper bound from the resolved reason was selected because of the different binning adopted in the mass spectrum. The binning in the mass spectrum is coarser in this region due the smaller number of events.

Figure 10.3 shows the relative background contributions of all the background processes with considerable yields in the merged SR when exactly 2  $b$ -jets(10.3a),

and at least 3  $b$ -jets (10.3a) are required in the final state. Similar to the resolved SR, the dominant background contributions in the first case comes from  $Z$ +jets processes, while in the later from  $t\bar{t}$ .

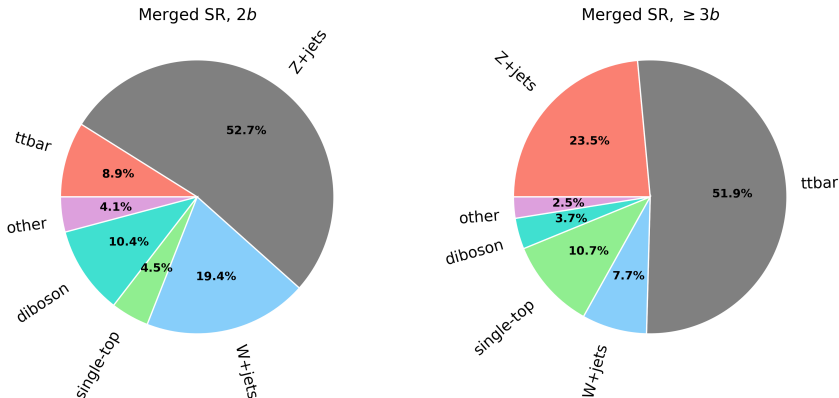


**Figure 10.3:** Relative contributions of the SM background processes in the merged SR. In these charts, the label “other” describes the relative contributions from  $t\bar{t}V$ ,  $t\bar{t}H$  and  $VH(b\bar{b})$  processes.

## 10.2.4 Control region definitions

### One-muon control region

All events in the one-muon control region are required to have exactly one signal muon, no baseline electrons and no  $\tau$ -leptons. The rest of the event selection requirements discussed in Sec. 10.2.2 and Sec. 10.2.3 are also applied to define the resolved and merged CR1, respectively. The only difference is that the offline reconstructed  $E_T^{\text{miss}}$  definition is modified to treat the muon as invisible by removing the contribution of the signal muon from the  $E_T^{\text{miss}}$  calculation in Eq. 6.4. The result is denoted as  $E_{T, \text{lep. invis.}}^{\text{miss}}$  and is used instead of  $E_T^{\text{miss}}$  in the selection requirements. Additionally,  $E_T^{\text{miss}}$  significance is calculated with  $E_{T, \text{lep. invis.}}^{\text{miss}}$  and is denoted as  $S_{\text{lep. invis.}}$ . Modifying these definitions is done to maintain the same kinematic properties between the signal and one-muon control region. To illustrate this we are going to compare the distributions of  $E_T^{\text{miss}}$  in SR and  $E_{T, \text{lep. invis.}}^{\text{miss}}$  in CR1, as well as the distributions of the invariant mass of the two leading  $b$ -jets, which form the Higgs-boson candidate.

For these comparisons, we will use  $t\bar{t}$  and  $W + jets$ . These processes are two

of the dominant in both SR and CR, as can be seen from Fig. 10.2, 10.3 and Figure 10.4. Figure 10.4 shows the relative contributions of the SM processes in the resolved (10.4a and 10.4b) and merged (10.4c and 10.4b) one-muon control regions. The dominant SM processes are the  $t\bar{t}$  and  $W$ +jets, for both merged and resolved regions with exactly 2  $b$ -tag jets in the final state. When at least 3  $b$ -jets are required, single top processes have larger relative contributions than  $W$ +jets processes.

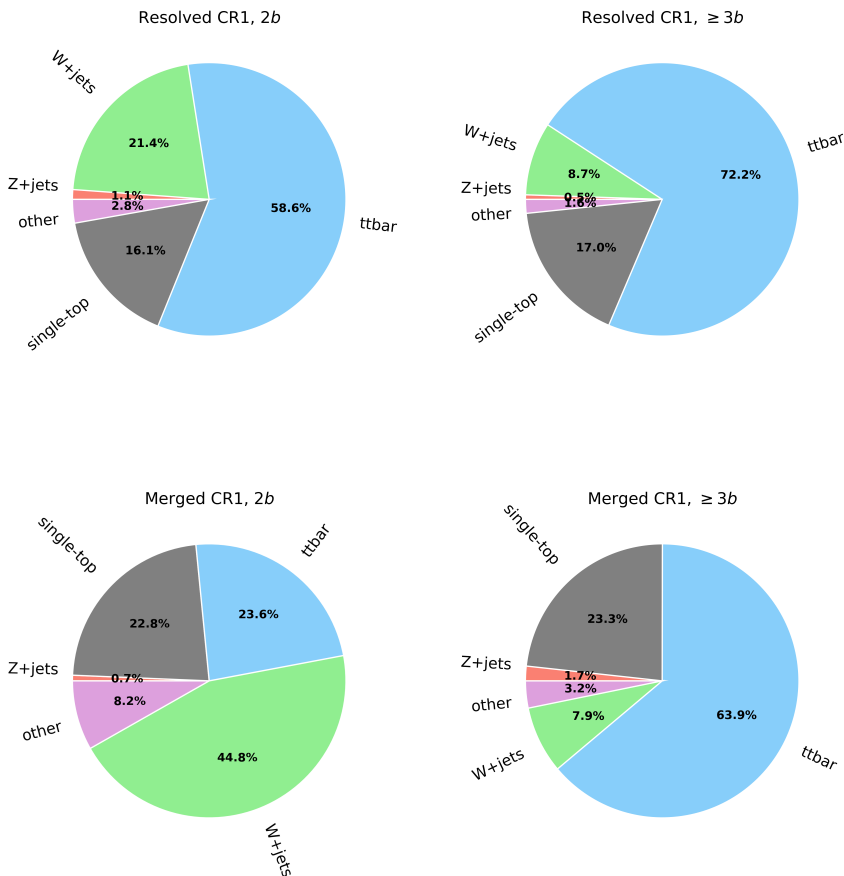


**Figure 10.4:** Relative contributions of the SM background processes in the resolved (top) and merged (bottom) CR1 . In these charts, the label “other” describes the relative contributions from  $VV$ (diboson),  $t\bar{t}V, t\bar{t}H$  and  $VH(b\bar{b})$  processes.

Figure 10.5 shows comparisons between the  $E_T^{\text{miss}}$  definition in the resolved signal region and  $E_{T, \text{lep. invis.}}^{\text{miss}}$  in the resolved one-muon control region, for  $t\bar{t}$

and  $W + jet$  simulated events with exactly  $2b$ -tagged jets (10.5a) and at least  $3b$ -tagged (10.5b) jets in the final state. The corresponding comparisons for the merged region are shown in Fig. 10.5c and 10.5d. From Fig. 10.5a and 10.5b,

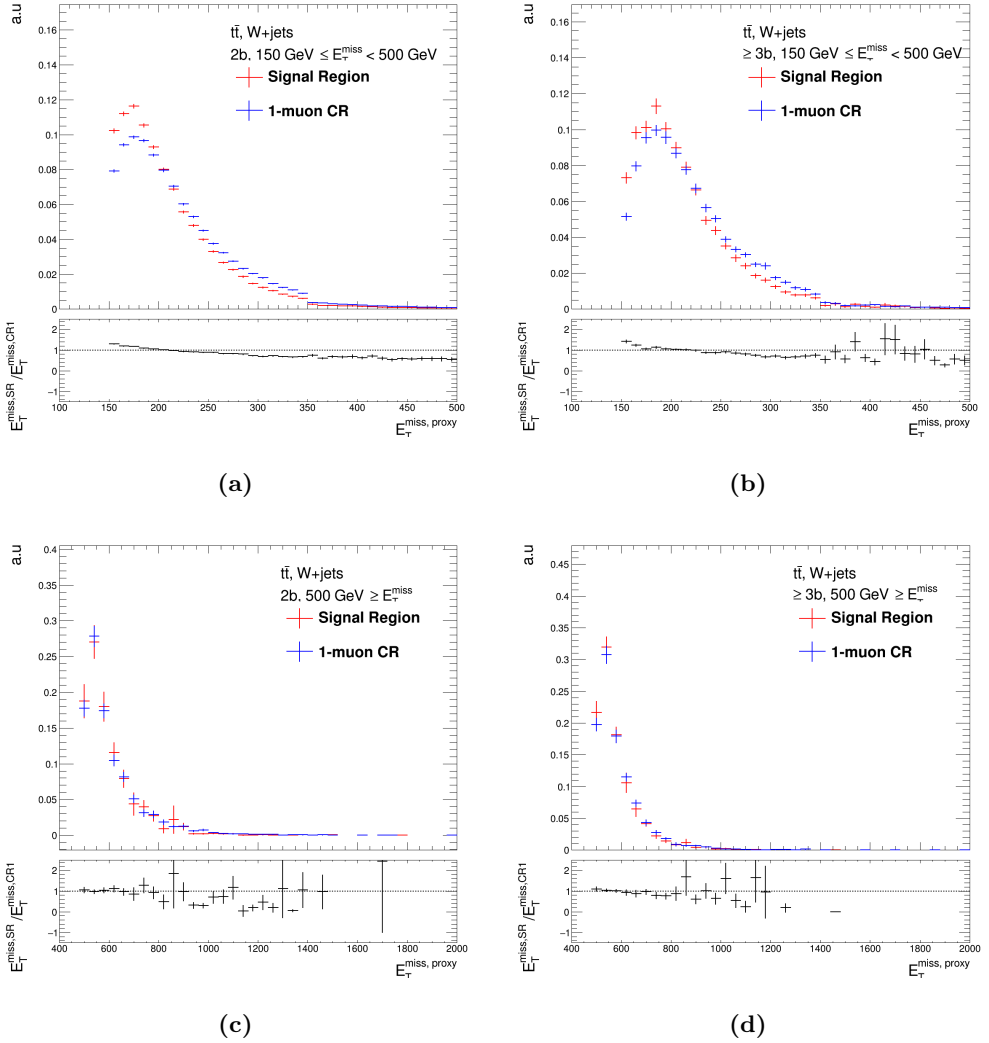


**Figure 10.5:** Comparison of the  $E_T^{\text{miss}}$  and  $E_T^{\text{miss,lep.invis.}}$  distributions as they are defined in the resolved SR (red) and one-muon CR (blue), for  $t\bar{t}$  and  $W$ +jets simulated events with exactly  $2b$ -tagged jets (left) and at least  $3b$ -tagged jets (right) in the final state. The lower panels show the ratio between  $E_T^{\text{miss}}$  and  $E_T^{\text{miss,lep.invis.}}$ . The drop observed in values of  $E_T^{\text{miss}} = E_T^{\text{miss,lep.invis.}} = 350 \text{ GeV}$  is due to the raise of the threshold on  $p_T(jj)$  from  $100 \text{ GeV}$  to  $300 \text{ GeV}$  for  $E_T^{\text{miss}} (E_T^{\text{miss,lep.invis.}}) > 350 \text{ GeV}$ . The error bands show only the statistical uncertainty.

we see that  $E_{T, \text{lep. invis.}}^{\text{miss}}$  has a harder spectrum than  $E_T^{\text{miss}}$ . The ratio between these quantities shows a trend, which can be explained by considering which  $t\bar{t}$  and  $W$ +jets decay modes are relevant in the resolved and merged signal and one-muon control region.

The decay channels for  $t\bar{t}$  events are

$$\begin{aligned} t\bar{t} &\rightarrow W^+bW^-\bar{b} \rightarrow q\bar{q}' b q''\bar{q}'''\bar{b}, \\ t\bar{t} &\rightarrow W^+bW^-\bar{b} \rightarrow q\bar{q}' b \ell^-\bar{\nu}_\ell \bar{b}, \\ t\bar{t} &\rightarrow W^+bW^-\bar{b} \rightarrow \ell^+\nu_\ell b q''\bar{q}'''\bar{b}, \\ t\bar{t} &\rightarrow W^+bW^-\bar{b} \rightarrow \ell^+\nu_\ell b \ell'^-\bar{\nu}_{\ell'}. \end{aligned}$$

For the signal region, a dedicated study in Ref. [215] showed that the largest contribution for  $t\bar{t}$  events comes from semi-leptonic decays and the largest fraction of them involves a  $\tau$ -lepton. On the contrary, the decay modes that involve either two leptons or hadrons-only had minor contributions in the SR, as shown in Fig. 10.6. This is expected because fully leptonic channels are less likely to pass the lepton veto while fully hadronic events are less likely to pass the  $E_T^{\text{miss}}$  selection requirements for the SR. It should be noted that this study did not include  $W$ +jets events. However, since the  $t$ -quarks decay almost always to  $Wb$ , the  $W$ -boson decay modes that contribute the most to the SR are expected to be the same as for  $t\bar{t}$  events.

According to Fig. 10.6, from the semi-leptonic decays that involve a  $\tau$ -lepton, those with the  $\tau$ -lepton decaying to hadrons contribute the most in the resolved SR, while in the merged SR  $\tau \rightarrow$  lepton has a larger contribution than  $\tau \rightarrow$  hadrons. In the one-muon CR, the majority of  $t\bar{t}$  events originate mostly from semi-leptonic decays that involve muons. Additionally, events where a  $\tau$ -lepton is involved that subsequently decays to  $\mu\nu_\mu$ , also are expected to contribute a lot. In these cases, treating muon as invisible leads harder  $E_{T, \text{lep. invis.}}^{\text{miss}}$  spectrum than the corresponding  $E_T^{\text{miss}}$  spectrum in the SR, from hadronically decaying  $\tau$ -leptons ( $\tau_{had} - had$  contribution in Fig. 10.6), explaining the trend observed in the bottom panels of Fig. 10.5.

The corresponding comparisons between  $E_T^{\text{miss}}$  in merged SR and  $E_{T, \text{lep. invis.}}^{\text{miss}}$  in merged CR1 are shown in Fig.10.5c and 10.5d. In this case, the shapes of the distributions are roughly the same, as is illustrate from the flat ratio centred around one on the bottom panels. In the merged SR most of  $t\bar{t}$  events involve  $\tau$ -leptons decaying to leptons, which are reconstructed as missing energy (leptons that fall out of the detectors acceptance), making the  $E_{T, \text{lep. invis.}}^{\text{miss}}$  distribution in CR1 merged and the  $E_T^{\text{miss}}$  distribution in SR merged region more close.

Despite the difference between the shapes of  $E_T^{\text{miss}}$  and  $E_{T, \text{lep. invis.}}^{\text{miss}}$  in the re-

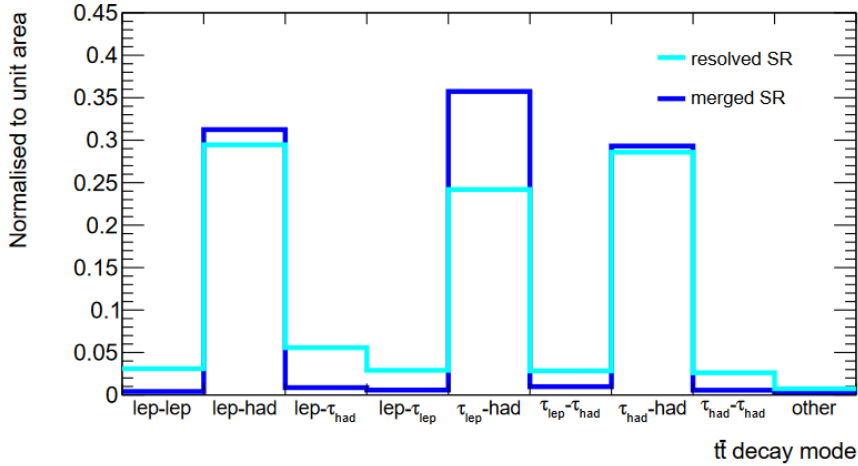


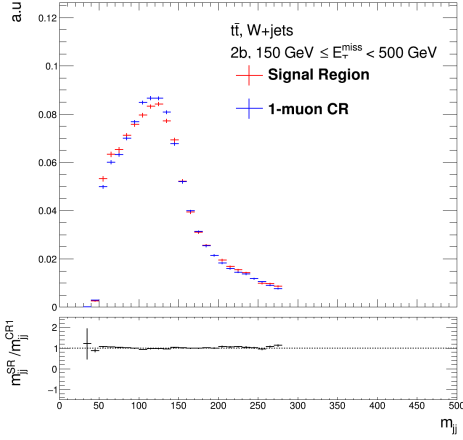
**Figure 10.6:** Fractional contribution of the  $t\bar{t}$  decay modes in the resolved and merged SR, for events that contain 2 or more  $b$ -tagged jets in the final state. The labels indicate the decay modes of each of the  $W$ -boson. The label “lep” is used when either  $e$  or  $\mu$  is produced from the  $W$ -boson decay, while “had” is used for decays into quarks. The label  $\tau_{lep}$  ( $\tau_{had}$ ) describes the  $W$  decays via a leptonically (hadronically) decaying  $\tau$ -lepton. Figure reproduced from Ref. [215].

solved SR and CR1 we can conclude that the two regions have similar kinematic properties. Figure 10.7 shows the distribution of the invariant mass of the two leading  $b$ -jets,  $m_{jj}$  in the event in the resolved (merged) signal and one-muon control region on top (bottom). From the plots in these figures it is clear that the shape of the mass spectra are similar, since the ratio in all cases is flat around one.

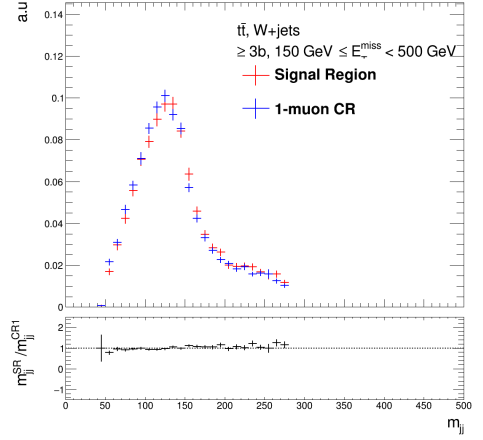
## Two lepton control region

For the two lepton control region, single lepton triggers are used. The first step, in this case, is the *trigger matching*: the offline reconstructed lepton is required to geometrically match a lepton as reconstructed by the single lepton trigger algorithms. For the electron triggers, the offline electron selected for the process should have  $E_T$  at least 5% higher than the threshold of the lowest trigger. The offline muon, on the other hand, must have  $p_T$  at least 1 GeV higher than the threshold of the lowest trigger. Only leptons that are matched to a trigger are considered in the two lepton control region.

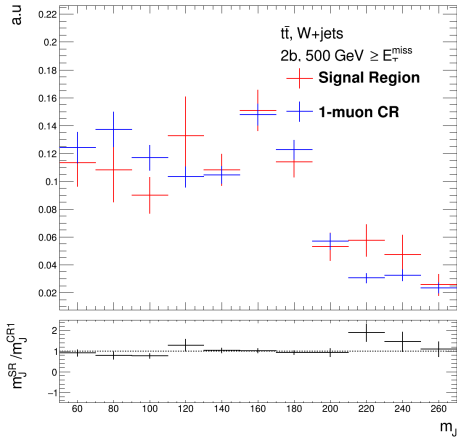
The events are required to have exactly one pair of signal electrons or signal muons with opposite sign, i.e.  $e^+e^-$  or  $\mu^+\mu^-$ . The further event selections



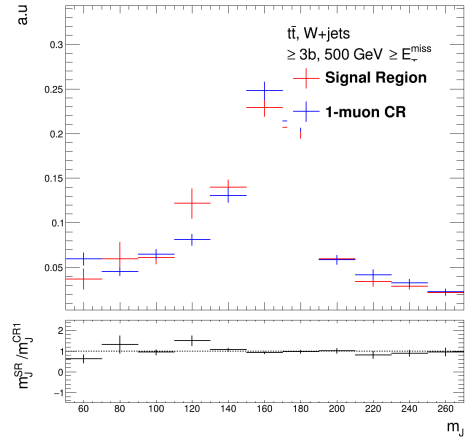
(a)



(b)



(c)



(d)

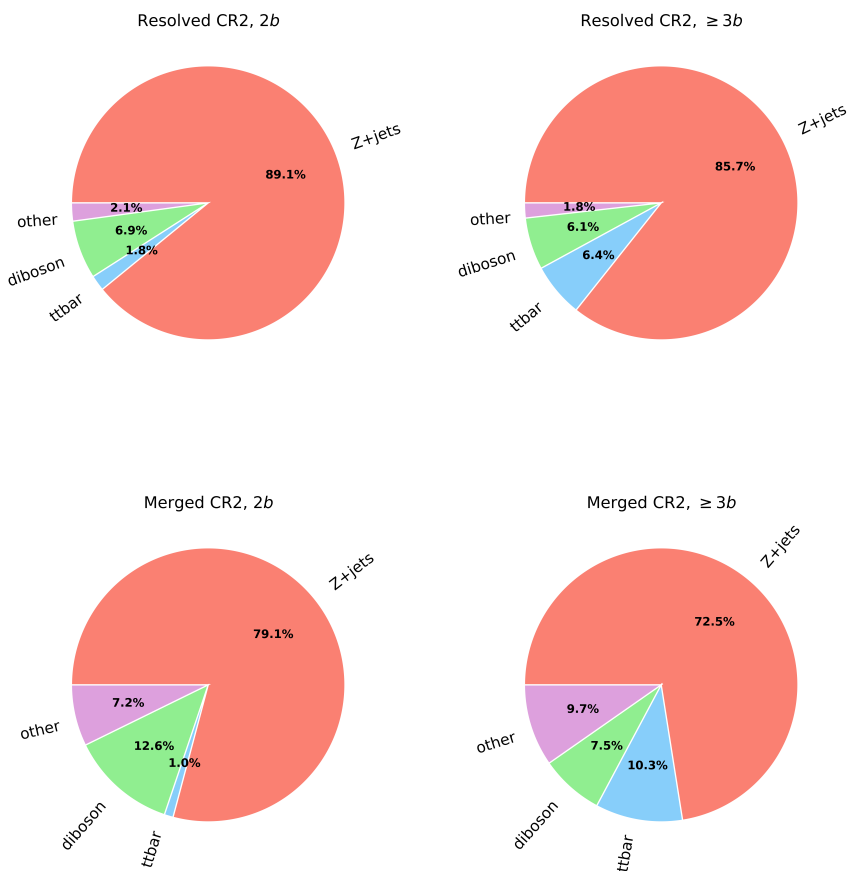
**Figure 10.7:** Comparison of the invariant mass distributions of the two leading  $b$ -jets for  $t\bar{t}$  simulated events in the resolved (top) SR (red) and one-muon CR (blue) for  $t\bar{t}$  and  $W$ +jets simulated events with 2  $b$ -tagged jets (left) and at least 3  $b$ -tagged jets (right) in the final state. The bottom column shows the corresponding distributions in the merged SR and CR1 regions. The lower panel shows the ratio between the  $m_{jj}$  distributions in the SR and CR1. The histograms are normalised to unit area.

described in Sec. 10.2.2 and Sec. 10.2.3 are applied. Here a modified  $E_T^{\text{miss}}$  definition is used, as well, which treats the pair of leptons as invisible by removing the contributions of two signal electrons or muons from the  $E_T^{\text{miss}}$  calculation in Eq. 6.4. This quantity is denoted as  $E_{T, \text{lep. invis.}}^{\text{miss}}$ . For this control region two

definitions of  $E_T^{\text{miss}}$  significance are used: one estimated with the “regular”  $E_T^{\text{miss}}$  definition, denoted as  $\mathcal{S}$  and one with the modified version which is denoted as  $\mathcal{S}_{\text{lep.Invis.}}$ . Events in the CR2 are required to have  $\mathcal{S} > 5$  and  $\mathcal{S}_{\text{lep.Invis.}} > 12$ .

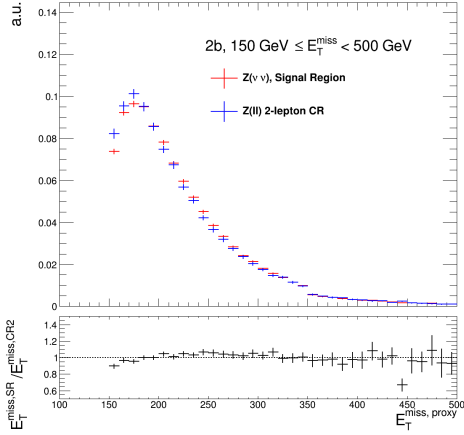
Finally, the invariant mass of the lepton pair ( $m_{\ell\ell}$ ) must be less than 10 GeV different from the invariant mass of the  $Z$  boson:  $|m_Z - m_{\ell\ell}| < 10 \text{ GeV}$ .

Figure 10.8 shows the relative contributions of the SM processes in the resolved (10.8a and 10.8b) and merged (10.8c and 10.8b) two-lepton control regions. From this figure, it is clear that the selection requirements ensure high-purity in  $Z$ +jets events.

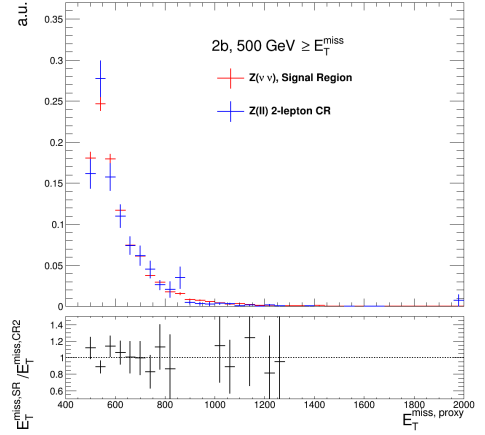


**Figure 10.8:** Relative contributions of the SM background processes in the resolved (top) and merged (bottom) CR2. In these charts, the label “other” describes the relative contributions from  $t\bar{t}V$ ,  $t\bar{t}H$  and  $VH(b\bar{b})$  processes.

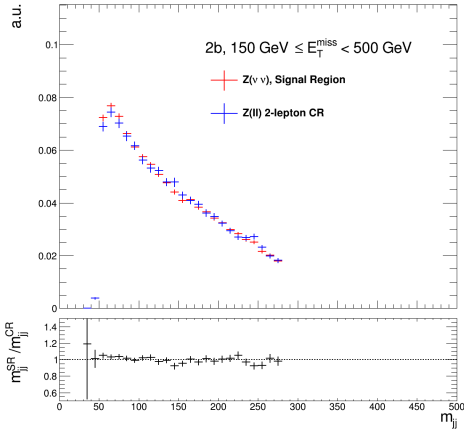
Using  $E_{T, \text{lep. invis.}}^{\text{miss}}$  for the CR2 requirements, leads to selecting  $Z$ +jets events with similar kinematic properties as in the signal region. Figure 10.9a (10.9b), shows on the top panel, the shape of the  $E_T^{\text{miss}}$  distribution in the resolved (merged) signal region and the  $E_{T, \text{lep. invis.}}^{\text{miss}}$  distribution in the resolved (merged) two-lepton control region, for events with exactly 2  $b$ -tagged jets in the final state. The corresponding plots for events with more than 3 $b$  tagged jets have very low statistics for a meaningful comparison and they are not shown here. Their ratio, shown on the bottom panel, is centred around one, with small fluctuations, indicating good agreement between the two distributions. Figure 10.9c (10.9d) shows the invariant mass of the two leading  $b$ -jets, calculated for  $Z(\nu\nu)$ +jets simulated events in the signal resolved (merged) region, and the  $m_{jj}$  for  $Z(\ell\ell)$ +jets events in the two-lepton control region.



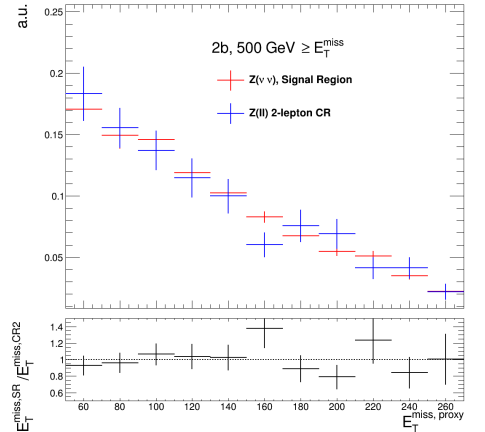
(a)



(b)



(c)



(d)

**Figure 10.9:** Top Column:  $E_T^{\text{miss}}$  and  $E_{T, \text{lep. invis.}}^{\text{miss}}$  distributions for  $Z(\nu\nu)$  events (red) in the signal region and for  $Z(\ell\ell)$  events (blue) in the two-lepton control region, respectively. Bottom Column: corresponding plots for the invariant mass distributions of the two leading  $b$ -jets. The lower panels show the ratios  $E_{T, \text{lep. invis.}}^{\text{miss}} / E_T^{\text{miss}}$  and  $m_{jj}^{SR, Z(\nu\nu)} / m_{jj}^{CR2, Z(\ell\ell)}$ . The histograms are normalised to unit area.

## 10.3 Validation of the particle-level definitions of the event selection requirements

The choices for the PDF sets, scales, parton shower and hadronization modelling, described in Sec. 9.1, for the event simulation have an impact on the final state kinematics. Therefore, alternative choices, for example using a different PDF set, could alter the final states, leading to migrations of events between regions or event loss in the resolved regions (events failing to pass requirements). These differences in the event yields are considered as systematic uncertainties, commonly referred to as *modelling* or *theoretical* uncertainties.

To estimate the theoretical uncertainties on the shape and normalization of the distributions of the event variables we use in the statistical analysis, we need two ingredients: the distributions produced by the *nominal* parametrisation, described in Sec. 9.2.2, and those produced by alternative choices, also referred to as *variations*.

The event yields after the detector simulation and reconstruction are affected not only by the kinematic acceptance, but also by the detector resolution and the reconstruction efficiency. Therefore, to study the effect of the theoretical uncertainties on the kinematic acceptance, we have to use the distributions before the detector simulation step.

For this reason, we use the truth-level objects discussed in Sec. 10.1 to define the signal and control region selections. After these selections are applied to the output of event generators, we use the truth-level event variables to estimate the theoretical uncertainties on their shape and normalisation. The inputs, however, to the statistical analysis are distributions of reconstructed event variables. To use the modelling uncertainties (estimated at truth-level) directly on the statistical analysis model, we need to verify that the kinematic properties in all analysis regions in both levels (truth and reconstructed) are similar.

This section compares particle- and reconstructed-level event variables in the signal and control regions. All the plots in this section follow the same format. They consist of a top panel, where the distributions of a specific event variable (e.g.  $E_T^{\text{miss}}$ ) are shown at particle- and reconstructed-level in a specific phase-space region, and a bottom panel which shows the bin-by-bin ratio of the reconstructed-level over the truth-level variable. In the bottom panel, dashed lines indicate 1, +1.3, and  $-0.7$  for better readability. The simulated processes used for these comparisons are labelled in the top right corner of each plot. Finally, the error bars include only statistical uncertainties.

### 10.3.1 Signal Region

In this section we compare kinematic variables in the resolved and merged signal region to verify that truth- and particle- level definitions select events in the same phase-space. Any simulation could be used for the comparisons, even background simulations, such as  $Z(\nu\nu)$ . However, when the reconstructed DxAOD files are produced for background processes, a set of selection requirements is used to remove some of the events. Since the same treatment is not applied in truth-level events, there are difference between the truth- and particle-level event variables at this stage already. Such requirements are not applied to signal events when DxAOD files are produced, and therefore for comparisons in SR we use signal simulations. For the comparisons we use the following signal simulations:

- 2HDM $a$  with  $\tan\beta = 10$  and  $m_A = 1200$  GeV,  $m_a = 100$  GeV. We select this sample for comparisons in the resolved and merged signal region with at least  $3b$ -tag jets in the event.
- $Z'$ -2HDM with  $m_{Z'} = 2000$  GeV and  $m_{Z''} = 900$  GeV. This model is selected for the comparisons at the merged signal region for events with exactly  $2b$ -tagged VR track jets inside the cone of the large- $R$  jet.

Figure 10.10, shows the truth-level  $E_T^{\text{miss}}$  distributions of the signal points used for the comparisons, after applying only the following preselection requirements:  $E_T^{\text{miss}} > 150$  GeV, lepton veto, and at least two  $b$ -jets in the final state.

In the following we are going to compare event variables in the four analysis region: resolved with exactly  $2b$ -jets, resolved with  $3b$ -jets, merged with  $2b$ -jets (VRtrack-jets) inside the cone of the large- $R$  jet and merged with  $2b$ -jets (VRtrack-jets) inside the cone of the large- $R$  and at least one  $b$ -jet outside. The distributions are produced after applying the full event selection of the respective region. These regions, for brevity, will be referred to as resolved  $2b$ , resolved  $\geq 3b$ , merged  $2b$  and merged  $\geq 3b$ , in the following.

Figure 10.11 shows comparison plots for the  $E_T^{\text{miss}}$  distribution in the four signal regions. The truth and reconstructed distributions agree relatively well in the resolved  $2b$  region, since the ratio in the bottom panel is flat around one with only small fluctuations. In the resolved and merged  $\geq 3b$  regions there are no major differences between the distributions, however, the comparison can not be conclusive due to the large statistical uncertainties. In the merged  $2b$  region, the shape of the reconstructed distribution is shifted towards lower  $E_T^{\text{miss}}$  values. However, this is not considered an issue, given the difference in the way  $E_T^{\text{miss}}$  is defined in the two levels, and the overall similar shapes of the distributions.

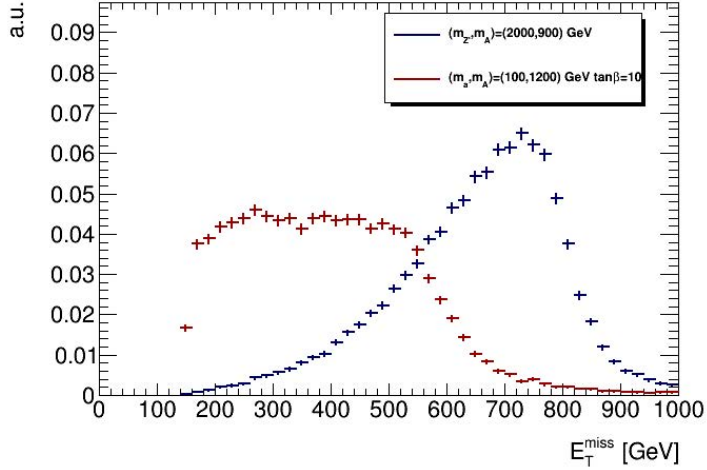


**Figure 10.10:**  $E_T^{\text{miss}}$  distribution for the signal simulations used for the comparisons. These are obtained after applying the preselection criteria discussed in the text.

Figure 10.12 shows comparisons between the distribution of the invariant mass of the Higgs-boson candidate in truth- and reconstructed-level. From the figure we see that the shape of the truth-level Higgs candidate mass, in the resolved  $2b$  and merged  $2b$  cases, has a more steep peak at 125 GeV in the resolved and merged  $2b$  regions. On the contrary, due to resolution effects on the jet mass reconstruction both the  $m_{jj}$  and  $m_J$  distributions at reconstructed-level are smeared.

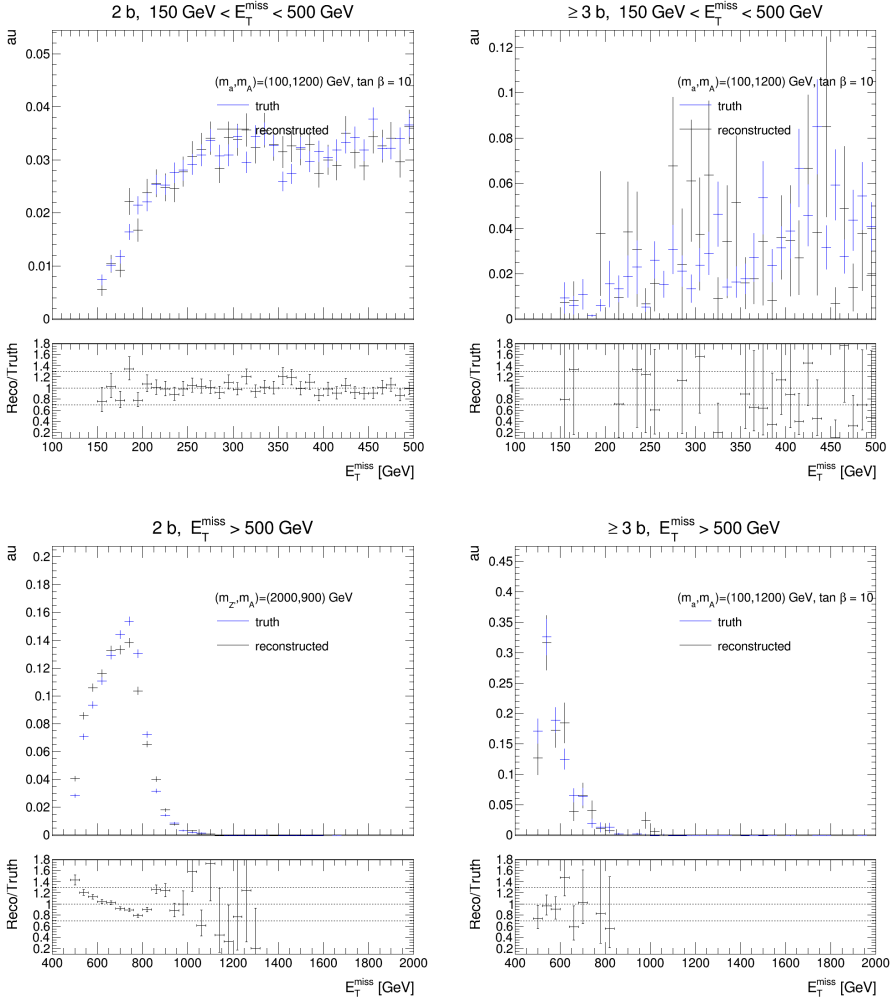
Finally, figure 10.13 shows comparison plots for the  $p_T$  of the Higgs boson candidate in all regions. From the ratio in all picture we can see a relatively good agreement between truth and reconstructed distributions, in all regions.

A similar validation to the one presented in this section for the signal region is performed for the one- and two-lepton control regions in the following sections.

### 10.3.2 One-muon control region

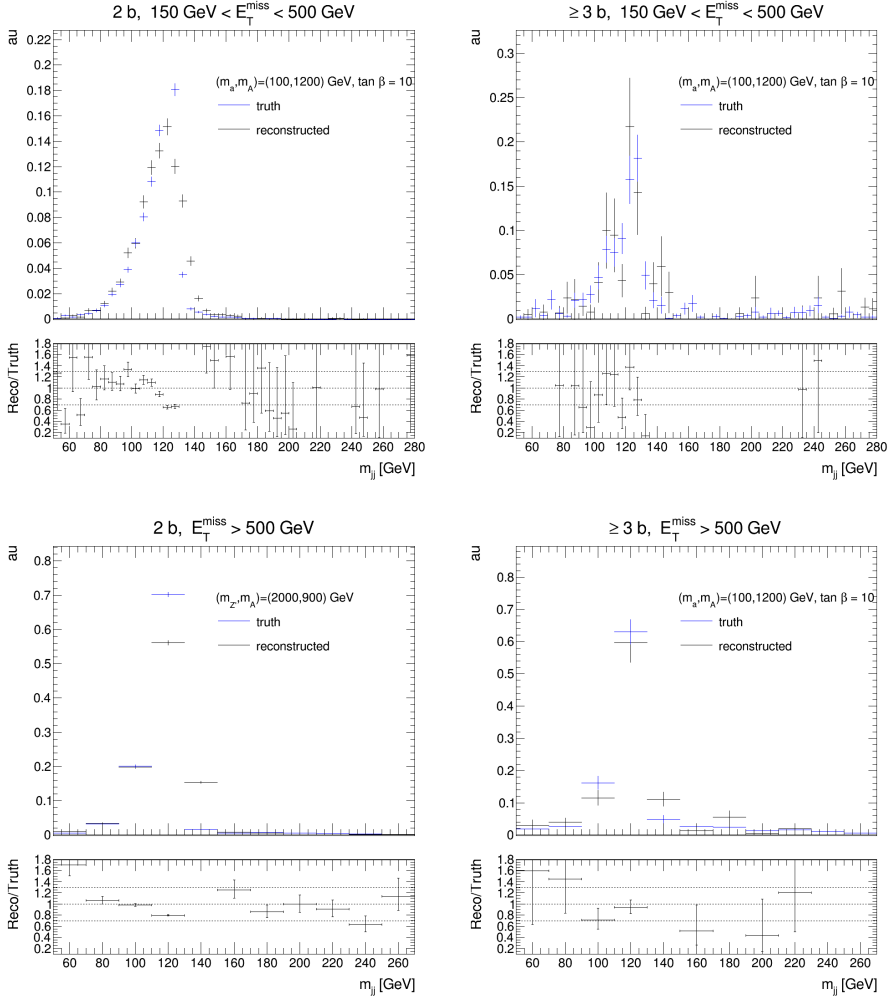
The one-muon control region is designed to constrain the normalisation of the  $t\bar{t}$ +jets and  $W(\mu\nu)$ +jets processes. To validate the truth-level implementation of the one-muon control region, simulated  $W(\mu\nu)$ +jets evens are used.

Figure 10.14 shows the shape of the  $E_{T, \text{lep. invis.}}^{\text{miss}}$  in all the regions. The ratios, in all cases, are relatively flat with only small fluctuations, indicating that the particle- and reconstructed-level definitions are close. In the resolved  $2b$  region, there is drop in the  $E_{T, \text{lep. invis.}}^{\text{miss}}$  shape at 350 GeV. At this point we require the



**Figure 10.11:** Comparison plots for the  $E_T^{\text{miss}}$  distributions in the resolved (top) and merged (bottom) signal region for events with  $2b$ -jets (left) and at least  $3b$ -jets (right).

$p_T$  of the Higgs-boson candidate to be above 300 GeV instead of 100 GeV which is the threshold for  $E_T^{\text{miss}} < 350$  GeV. Figure 10.15 shows the distributions of the invariant mass of the Higgs-boson candidate. In the resolved  $2b$  region, the small differences are due to the mass resolution of the reconstructed small  $R$ -jets. A good agreement is observed in the merged  $2b$  regions. In the resolved  $\geq 3b$  region the shapes look similar, since the ratio is compatible with one within the (statistical) uncertainties, with the exception of few bins. In the merged  $\geq 3b$  region, we see large fluctuations in the ratio, but for most of the bins the ratio is



**Figure 10.12:** Comparison plots for the invariant mass of the Higgs-boson candidate mass in the resolved (top) and merged (bottom) signal region for events with  $2b$ -jets (left) and at least  $3b$ -jets (right).

compatible with one, within the uncertainties. Finally, figure 10.16 shows the  $p_T$  of the combined two leading  $b$ -jet in the event and the leading large- $R$  jet. In all cases there is a good agreement between truth and reconstructed distributions.

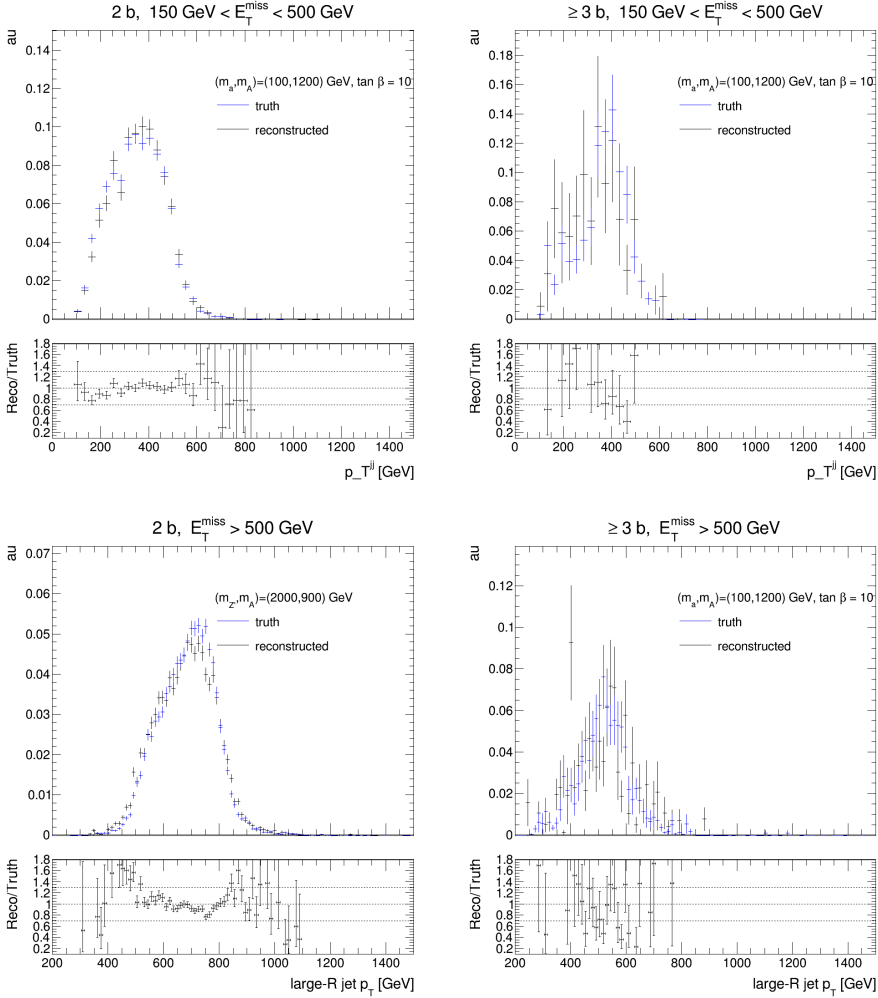
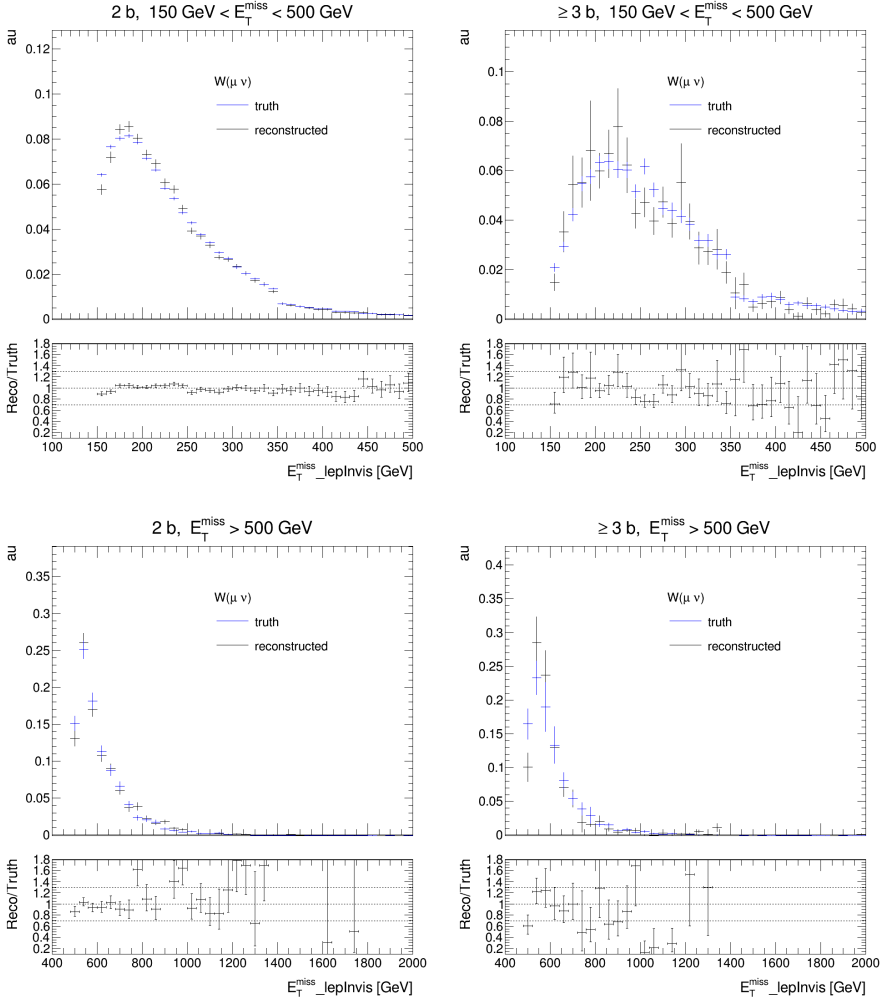


**Figure 10.13:** Comparison plots for the  $p_T$  of Higgs-boson candidate in the resolved (top) and merged (bottom) signal region for events with  $2b$ -jets (left) and at least  $3b$ -jets (right).

### 10.3.3 Two-lepton control region

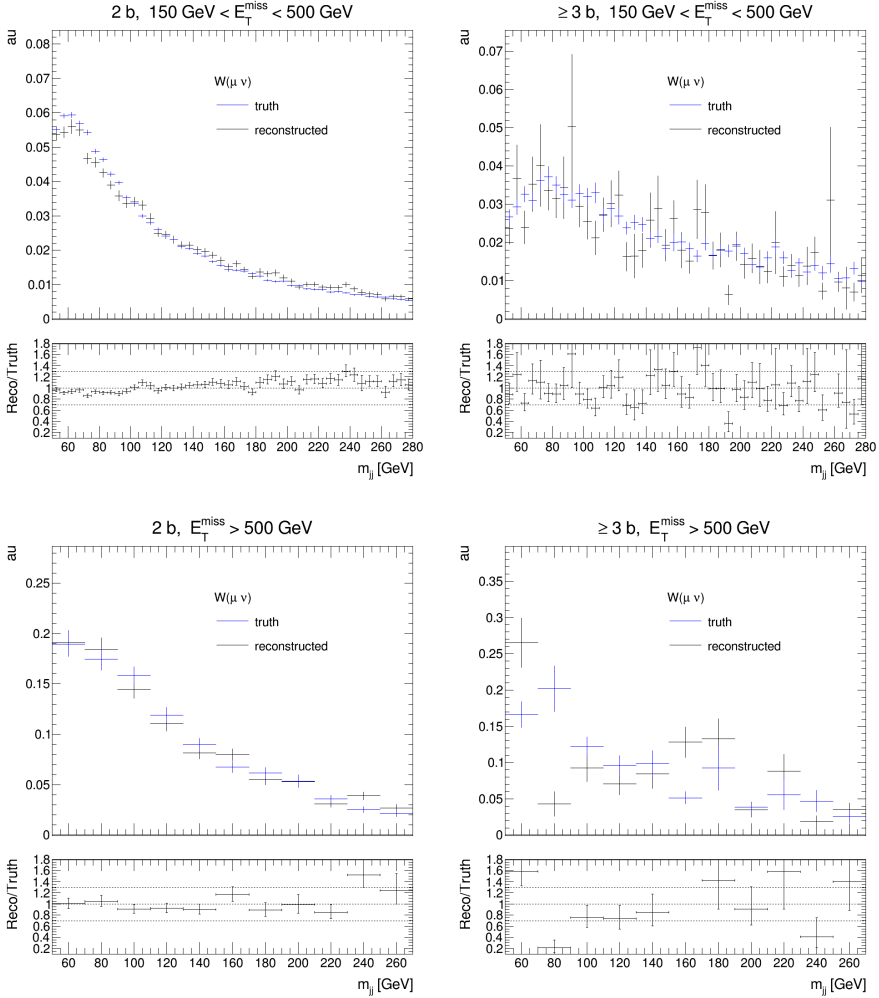
The two-lepton control region is designed to constrain the normalisation of the  $Z$ +jets processes. To validate the truth-level implementation of this control region, we use simulated  $Z(\mu\mu)$ +jets events.

Figure 10.17 shows the shape of the  $E_{T, \text{lep. invis.}}^{\text{miss}}$  in all the regions. In the resolved  $2b$  region, the distributions agree well up to  $\sim 220$  GeV. For  $E_{T, \text{lep. invis.}}^{\text{miss}}$



**Figure 10.14:** Comparison plots for the  $E_{T, \text{lep. invis.}}^{\text{miss}}$  distributions in the resolved (top) and merged (bottom) one-muon region for events with  $2b$ -jets (left) and at least  $3b$ -jets (right).

values above this threshold, however, the ratio drops below one, and the shape of the truth-level  $E_{T, \text{lep. invis.}}^{\text{miss}}$  distribution is interrupted for values above 350 GeV where the  $p_T$  of the Higgs-boson candidate is set to 300 GeV. This can be explained by looking at the corresponding comparison for the  $p_T$  of the two leading  $b$ -jets in Figure 10.18. In the resolved  $2b$  region we see that for values above 300 GeV, there is a steep drop in the truth level distribution. Additionally there is no correlation between the  $E_{T, \text{lep. invis.}}^{\text{miss}}$  and the  $p_T$  of the two  $b$ -jets. The reconstructed distribution of  $E_{T, \text{lep. invis.}}^{\text{miss}}$  in both cases is has very low (but



**Figure 10.15:** Comparison plots for the Higgs-boson candidate invariant mass distributions in the resolved (top) and merged (bottom) one-muon region for events with  $2b$ -jets (left) and at least  $3b$ -jets (right).

still non-zero) values due to the resolution of the objects used in its calculation, and the smearing of the reconstructed  $p_T^{jj}$  distribution. Figure 10.19 shows the distributions for the invariant mass of the Higgs-boson candidate. In all regions there is a relatively good agreement between the truth and reconstructed distributions, as indicated by the ratios, which fluctuate around one. In Appendix B there are comparison plots for more event variables, used in the event selection. From the plots presented in this section, we can conclude that the truth-level implementation of the analysis selects events with similar kinematic properties

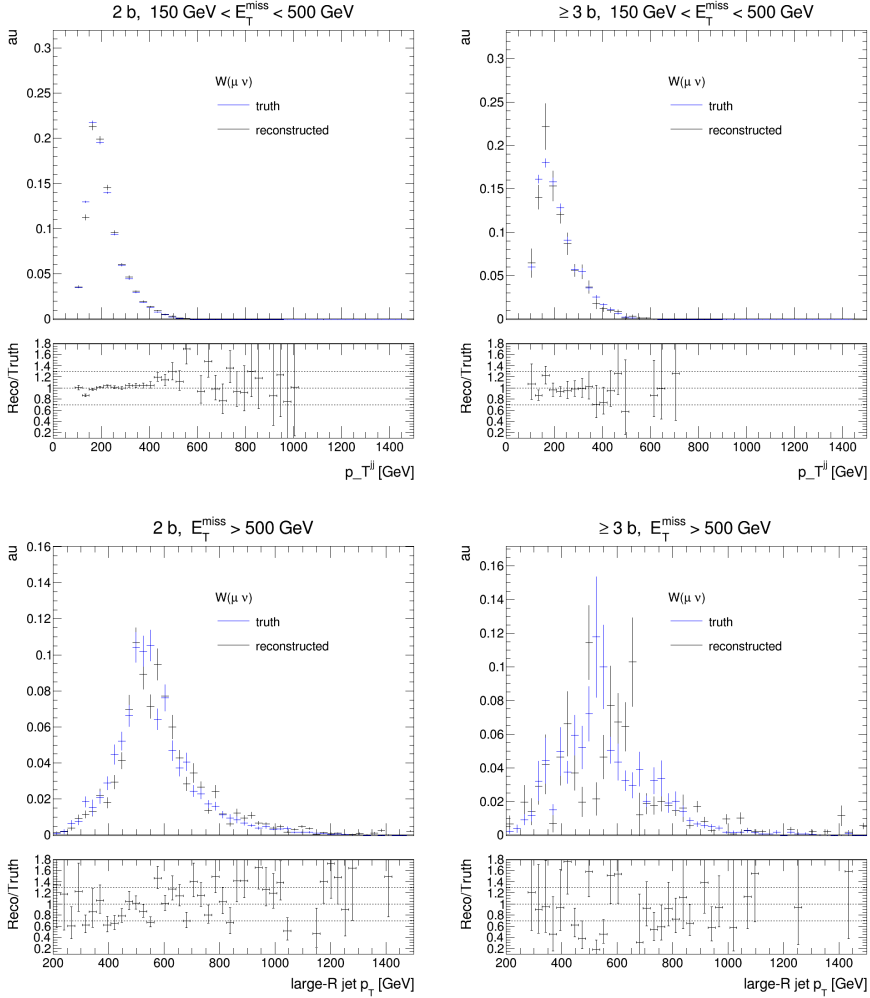


**Figure 10.16:** Comparison plots for the Higgs-boson candidate  $p_T$  distributions in the resolved (top) and merged (bottom) one-muon region for events with  $2b$ -jets (left) and at least  $3b$ -jets (right).

as the definitions discussed in sections 10.2.1-10.2.4.

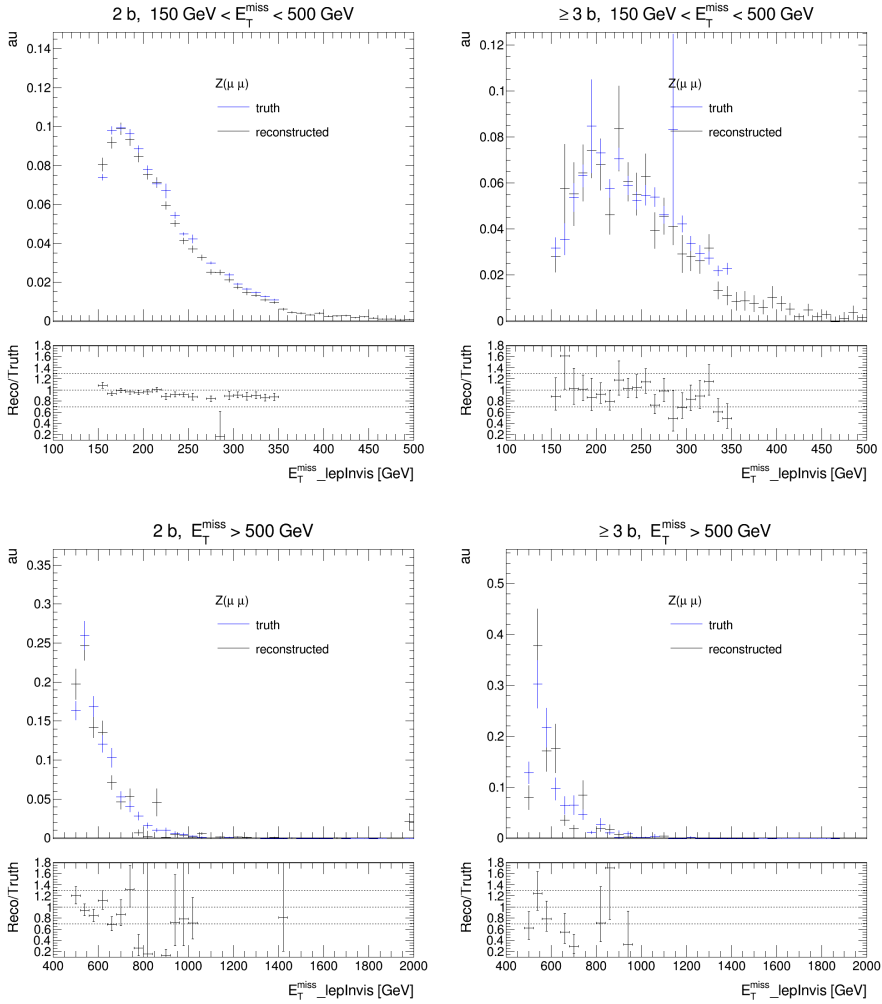


**Figure 10.17:** Comparison plots for the  $E_T^{\text{miss}} \text{ lep. invis.}$  distributions in the resolved (top) and merged (bottom) two-lepton region for events with  $2b$ -jets (left) and at least  $3b$ -jets (right).

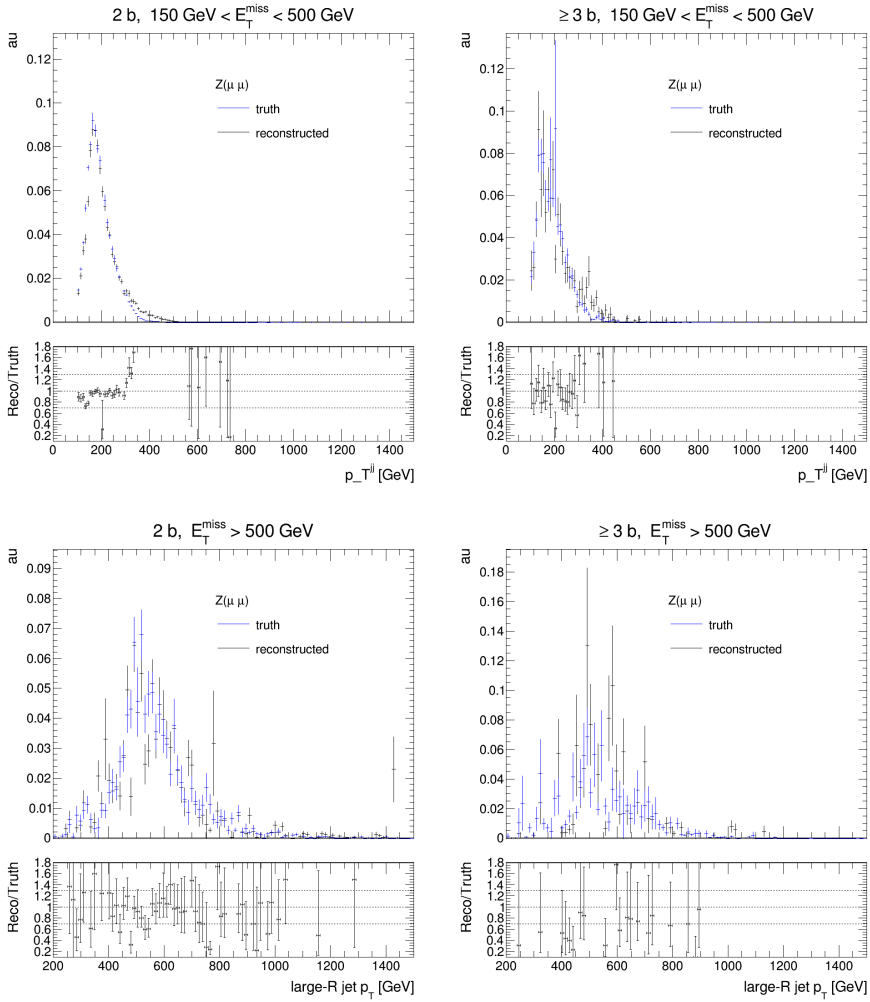


**Figure 10.18:** Comparison plots for the Higgs-boson candidate  $p_T$  distributions in the resolved (top) and merged (bottom) two-lepton region for events with  $2b$ -jets (left) and at least  $3b$ -jets (right).

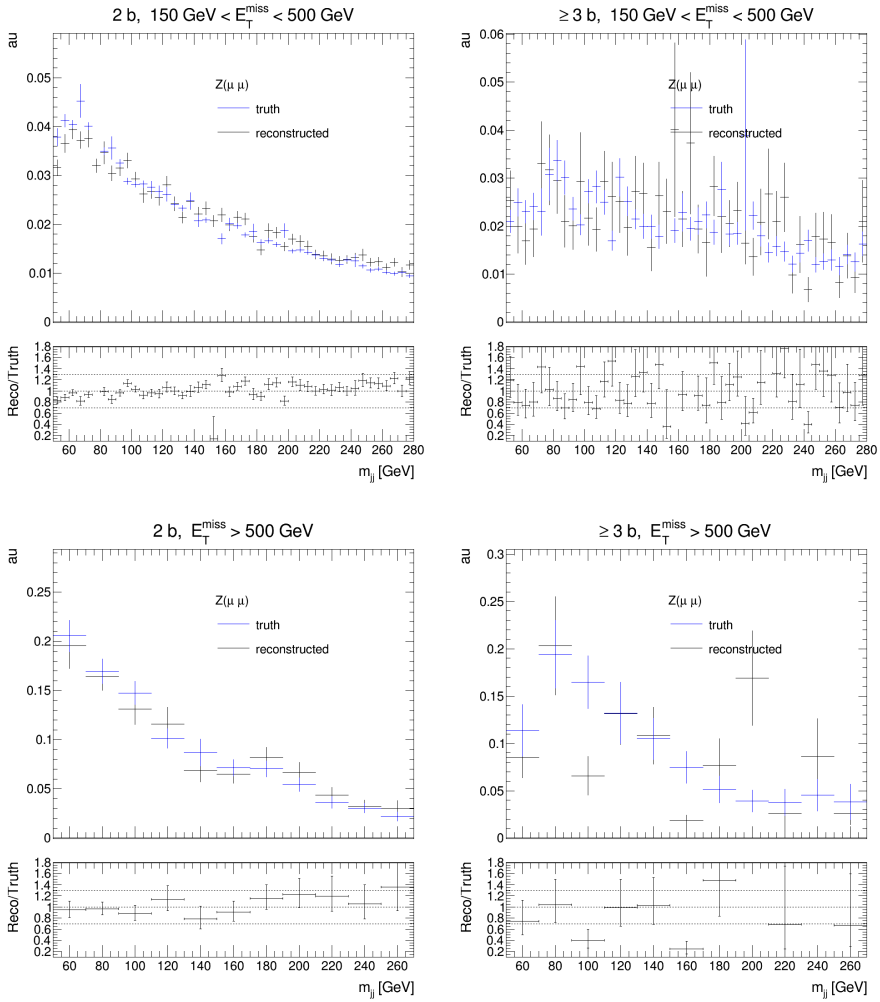


**Figure 10.19:** Comparison plots for the Higgs-boson candidate invariant mass distributions in the resolved (top) and merged (bottom) two-lepton region for events with  $2b$ -jets (left) and at least  $3b$ -jets (right).

# Chapter 11

## Systematic uncertainties, fit setup, and pre-fit data to MC comparisons

This chapter discusses in Section 11.1 the sources of systematic uncertainties considered in the search and the setup of the statistical analysis model, commonly referred to as *fit setup*, in Section 11.2. Section 11.3 presents a comparison between data and MC predictions before performing the profile likelihood fit.

### 11.1 Systematic uncertainties

The main goal is to find any discrepancies between the SM background predictions and the observed data. To assess the significance of any discrepancies, we have to assign uncertainties to all sources that limit the precision and accuracy of the SM predictions. Besides the statistical uncertainty, which limits the precision of the predictions, all the other systematic uncertainties are classified based on their origin into two groups, the experimental and the theoretical, both discussed in this section.

Experimental and theoretical systematic uncertainties on the shape and normalisation of the fit variables are evaluated in all analysis regions for the SM background processes. For the signal processes, uncertainties on the shape of the invariant mass of the Higgs boson candidate, are estimated only in the signal region because almost no signal yields are expected in the control regions.

### 11.1.1 Experimental Uncertainties

While statistical uncertainties are the result of stochastic fluctuations in the data sample, experimental uncertainties are associated with the calibration and resolution of the measurement apparatus. The sources of experimental systematic uncertainties are listed below.

**Luminosity.** As it was discussed in Section 6.5, the luminosity uncertainties for the individual years are between 2.0% and 2.4%. However, these values are correlated leading to 1.7% uncertainty for the integrated luminosity of the full Run-2 data [216].

**Pile-up.** Simulated pile-up interactions are corrected to match the conditions found in the collected data, by the so-called pile-up re-weighting procedure. This procedure corrects the average number of interactions per bunch crossing in the simulated event samples. In this analysis, the uncertainties due to the pile-up re-weighting are estimated by varying the corresponding re-weighting factors by 4%.

**$E_T^{\text{miss}}$  Triggers.** Trigger-related uncertainties arise from the estimation method of the scale factors, described in Section 9.1.3. Two different sources of uncertainties are considered in the calibration: the statistical uncertainty, and a systematic uncertainty associated with the differences between the topology of the signal region and the phase space region used in the calibration.

**Small- $R$  jets.** There are 29 sources of systematic uncertainty related to the JES considered in this analysis. Most of these uncertainties are related to the in-situ calibration. Other sources are related to pile-up effects and the flavour dependence. Figure 11.1 shows some typical values of the JES uncertainty, as a function of  $p_T$  for central jets at fixed  $|\eta| = 0$ , on the left, and as a function of  $\eta$  for jets with  $p_T = 60$  GeV [140] on the right. From the left hand side of Fig. 11.1a, it is clear that the dominant contribution to the total JES uncertainty for jets with  $p_T$  lower than  $\sim 30$  GeV comes from pile-up effects. Above this point and up to  $\sim 400$  GeV the dominant source is the flavor response, while for  $p_T > 400$  GeV are the uncertainties in the jet in-situ calibration. The spikes observed in Fig. 11.1b of the figure are caused by the so called *non-closure* uncertainty, which is assigned to account for the fact that not the full ATLAS simulation was used, but the ATLAS fast simulation [165].

The dominant contribution to the JER uncertainties comes from propagating JES uncertainties to the estimation of the JER. Another significant contribution is the uncertainty associated with the difference between the JER in data and simulations. Finally, a source of uncertainty, is the measurement of the efficiency of the Jet-Vertex-Tagger.

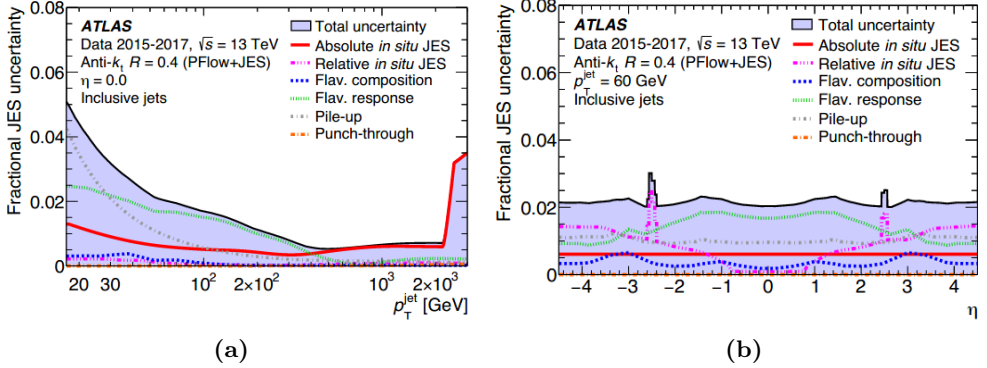


**Figure 11.1:** Fractional jet energy scale uncertainty as a function of  $p_T$  ( $|\eta| = 0$ ) (a), and as a function of  $\eta$  (b) ( $p_T = 60$  GeV). The total uncertainty is the quadrature sum of all components. Figures from Ref. [140]

**Large- $R$  jet.** There are several source of uncertainties related to the JES, JER, jet mass scale (JMS), and resolution (JMR). The JES uncertainties are described by four components that account for: the difference between data and MC simulation, differences between different simulated event samples used in the calibration, uncertainties related to the tracking information, and the total statistical uncertainty. These are calculated from the jet in situ calibration [149]. The JMS uncertainties are estimated by comparing the calorimeter measurements of the jet  $p_T$  with the ID measurements [148]. The JER and JMR uncertainties are described by one component each. The JER component accounts for uncertainties in the jet in situ techniques. The JMR uncertainties are obtained by comparing for different simulated processes, the reconstructed jet properties to the corresponding truth-level. In this analysis we use only the uncertainties obtained from  $H \rightarrow b\bar{b}$  [217].

**Leptons.** There are two main sources of lepton uncertainties: those related to the energy scale and resolution and those related to the efficiency measurements, i.e the identification, isolation and reconstruction efficiency. The estimation of the uncertainties is explained in detail in Ref. [124] for electrons, and Ref. [161] for muons. Other sources considered in the analysis are the efficiency of the electron and muon triggers and, for muons, the track-to-vertex association.

**Flavor tagging.** Differences in the  $b$ -tagging efficiencies between data and simulations, simulated events are corrected by scale factors. These factors also includes an extrapolation procedure to high- $p_T$  jets. Therefore two sources of systematic uncertainties are related to the efficiency measurements and the extrapolation procedure. Additionally, uncertainties associated with the meas-

urement of the rejection efficiency of  $c$ - and light-flavour jets are considered.

$E_T^{\text{miss}}$ . The uncertainties, in this case are associated with the measurement of the energy scale and resolution of the soft term, which are estimated by calculating the difference between data and simulation in  $Z \rightarrow \mu\mu$  events. The uncertainties of the calibrated objects, used in the  $E_T^{\text{miss}}$  reconstruction are propagated to the  $E_T^{\text{miss}}$  uncertainty. Another source of uncertainty is the uncertainty on the  $E_T^{\text{miss}}$  trigger scale factor.

Table 11.1 summarises all the sources of experimental systematic uncertainties, considered in the analysis.

Systematic Uncertainties	
Electrons	Reconstruction, identification and isolation efficiency
	Energy scale and resolution
	Trigger efficiency
Muons	Reconstruction, identification and isolation efficiency
	Trigger efficiency
	Energy scale and resolution
	Track-to-vertex association
$\tau$ -leptons	Energy scale
$E_T^{\text{miss}}$	soft-term scale and resolution
	$E_T^{\text{miss}}$ trigger SF
jets	Jet energy scale (JES) and resolution (JER)
	Quark flavour composition
	Pile-up
	Jet Mass Resolution (JMR)
b-tagging	$b$ -tagging efficiency
	mistag efficiency

**Table 11.1:** Summary of the sources of experimental systematic uncertainties considered in this analysis.

## Estimation of the experimental systematic uncertainties

The uncertainties associated with the sources listed above have to be propagated to the uncertainty of the predicted event yield for each simulated process. The following procedure is used to estimate the uncertainty associated with one source, on the predicted event yields of each simulated process.

- First, the parameter, for example the jet energy scale, is shifted twice by  $\pm 1$  standard deviation,  $\sigma$ .

- The full analysis event selection is applied to the updated simulations.
- The uncertainty is the difference between the event variable distributions corresponding to the shifted values, also called *variations* and the nominal. The term *up (down) variation* is used to describe the distributions that correspond to a parameter shifted by  $+1\sigma$  ( $-1\sigma$ ).

These systematic uncertainties are estimated with the help of software tools provided by the ATLAS combined performance groups.

### 11.1.2 Theoretical systematic uncertainties

Our limited knowledge of the values of various parameters used in the simulation of p-p collisions, creates inaccuracies which can systematically shift predicted production rates and kinematic properties of the simulated processes. The main sources of systematic uncertainties considered in the analysis are listed below.

**Re-normalisation and factorization Scale.** In section 4.3 the renormalisation and factorisation scales were introduced. For the event simulation, these scales are set to  $\mu_R = \mu_F = \mu^{\text{nom}}$ , where  $\mu^{\text{nom}}$  is the nominal value, which depends on the specific process. To estimate the uncertainties we vary the scales independently by a factor of two around their nominal values. In total, six variations are considered:

$\mu_R/\mu^{\text{nom}}$	0.5	0.5	1	2	1	2
$\mu_F/\mu^{\text{nom}}$	0.5	1	0.5	1	2	2

**Table 11.2:** Variations of normalisation and factorisation scales with respect to their nominal value.

To estimate the associated uncertainty on the shape of the event yields in each bin, we estimate the distributions of the variable using the values listed in 11.2. The uncertainties are obtained by taking an envelope, i.e. estimating, in each bin we take the highest and lowest variations. The uncertainty is  $\pm$  the average of the highest and lowest variation in each bin.

**PDF and  $\alpha_s$**  To calculate uncertainties related to the choice of the PDF and  $\alpha_s$  we use the PDF4LHC prescription [218]: The generator weights are re-evaluated for 100 replicas of the nominal PDF. The predicted event yield in each region and bin is re-evaluated with each replica set and the uncertainty of the yield in each bin is estimated by

$$\delta^{\text{PDF}} = \sqrt{\frac{N_{pdf}}{N_{pdf} - 1} (\langle X^2 \rangle - \langle X \rangle^2)}$$

where  $N_{pdf}$  is the number of the PDF replicas, and  $X$  is used to represent the variations. The uncertainty associated with the  $\alpha_s$  is obtained by shifting the nominal value (0.1180) by its uncertainty,  $\pm 0.0015$  [218]. In each bin the uncertainty is the difference between up and down variation divided by two. The combined uncertainty is the square root of the quadrature sum of  $\delta^{PDF}$  and  $\delta^{\alpha_s}$ . Finally, the combined uncertainty is symmetrised by taking in each bin of the average of up and down variation.

**Strong coupling,  $\alpha_s$ , in the Initial State Radiation modelling** For the  $t\bar{t}$  and single-top simulated process, we need to evaluate the effect of varying the value of  $\alpha_s$  used to model initial state radiation (ISR) from 0.1 to 0.15, by using the up and down Var3c A14 tune variation [219]. The associated uncertainty on the expected event yield, in each bin, is equal to half the difference between the two variations.

**Choice of Matrix Element generator.** For the processes that Powheg Box is used to calculate the matrix element and Pythia8 to model the parton shower, we need to evaluate the uncertainty associated with the choice of Powheg as the ME generator. The uncertainty is obtained by taking the difference between the nominal yield predictions, and those evaluated using an alternative ME calculator.

### **Parton shower and hadronization modelling.**

- To calculate uncertainties related to the modelling of parton shower and hadronization we compare event variables or the normalisation estimated with the nominal samples shown in Ch.9 with those estimated with events simulated using different generators. The associated uncertainties are estimated for all BG processes
- Merging scale. The matrix elements are calculated to a fixed order for different jet multiplicities. The merging scale is used to combine these elements into an inclusive sample and to avoid double counting jets from matrix elements and from parton showers. For SHERPA V+jets processes the associated uncertainty on the expected event yields in each bin is estimated by changing the scale value from 20 GeV to 30 GeV for the up variation, and to 15 GeV for the down variation. These uncertainties are only estimated for V+jets and diboson processes.
- Re-summation scale. To calculate the uncertainties, associated with the scale used for the re-summation of the soft gluon emission, the up variation is calculated by doubling the nominal value of the scale while, the down variation the scale is set to half of the nominal value. Similar to the

previous source, these uncertainties are estimated only for  $V$ +jets and diboson.

For the signal processes only uncertainties associated with the choice of PDF and  $\mu_R, \mu_F$ , scale are estimated.

The sources of the theoretical uncertainties discussed above can also alter the shape of the observables that are used to define the analysis region. For example, changes in the shape of the  $E_T^{\text{miss}}$  distribution can cause migrations between adjacent  $E_T^{\text{miss}}$  bins- will be discussed in the next section. For this reason, for each source described above, besides the uncertainty on the shape of the  $m_{jj}$  distribution and the overall normalisation, additional uncertainties are assigned to account for the differences in the  $E_T^{\text{miss}}$  shape, the number of leptons in the event and the number of  $b$ -jets.

## 11.2 Fit Setup

Different variables are fitted in the signal and control regions. For the signal region we chose the mass of the Higgs boson candidate, because for signal events it should have a peak around  $\sim 125$  GeV, while for background events should be more broad, and has good discriminating power.

For the one-muon control region the muon charge is used to allow separation between  $W$ +jets and  $t\bar{t}$  processes for events with  $2b$ -jets. In hadron colliders the production of  $W$  boson is dominated from  $q\bar{q}$  where at least one has to be a valence quark. For proton-proton collisions this will be predominately the  $u\bar{d}$  channel leading to more  $W^+$  bosons, and therefore more  $\mu^+$ . On the other hand,  $t\bar{t}$  processes produce the same amount of  $\mu^+$  and  $\mu^-$ , since the top quark decays to  $W^+b$  and the anti-top to  $W^-\bar{b}$ . Due to the low contributions of the  $W$ +jets processes when  $3b$ -jets are required, the fit variable in these cases is the event yields.

For the two-lepton control region the event yields is fitted. This control region contains very few events, especially in the merged topology, so that a binned distribution can not be used.

The parameter of interest (POI), in the fit is the signal strength. Besides the POI, the following NP are allowed to float in the fit (their prior value is set to 1).

- The background normalisation of  $Z$ +heavy-flavor jets. Due to the event selection requirements, the  $V$ +jets background final states that contribute

the most in the signal region will be those with at least one  $b$  or two  $c$ -quarks <sup>1</sup> These states ( $V+bb$ ,  $bl$ ,  $bc$ ) will be referred to as *heavy-flavor* and will be denoted as HF in the following. Possible miss-modellings of the heavy flavor composition in  $V$ +jets simulations can affect the constraining power of the control regions. For this reason,  $V$ +jets simulated samples are treated separately: the background normalisation factor of the  $V$ +HF is allowed to float in the fit, while the normalisation of  $V$ +light flavor composition ( $c$ -, $u$ -, $d$ -quark decays) is constrained to theory predictions. Two normalisation factors are used one for events with exactly two  $b$ -jets and one for those with at least 3 $b$ -tagged jets.

- The background normalisation of  $W$ +HF. In this case one normalisation region is used for all regions, because the contribution of  $W$ +jets is small in the signal regions with at least 3- $b$  jets in the final state.
- The background normalisation factor of the top-quark pair production. A single normalisation factor is used for all the analysis regions and bins, because  $t\bar{t}$  processes because the production mechanism mechanism of  $t\bar{t}$  events is the same in both cases. In most events with three  $b$ -tagged jets, the third is a misidentified  $c$ -initiated jet, rather than from initial state radiation.

In the fit there are NPs that parameterise experimental and theoretical uncertainties that affect the normalisation and the shape of the fit discriminant. The normalisation factors of the remaining background contributions are constrained to the theory predictions.

Finally, there are NP that parameterise the statistical uncertainties.

### 11.2.1 Pruning and smoothing

For most of the NP, the histograms of variations are smoothed before performing the fit. These procedure has two steps: first, the bins are merged until the distribution of the variation has only one maximum with respect to the nominal, and then they are merged again until the statistical uncertainty in each variation bin is below 5%.

Before performing the fit, the fit-framework compares for each source of systematic uncertainty the relative shift of the up and down variations with respect to the nominal within each analysis region. If the relative shift of both variations is

---

<sup>1</sup>Final states with one  $c$ -quark and one light flavour, or only light flavour quarks consist less than 4% of the total background

lower than 0.5%, then the NP is not included in the fit. This procedure, is called pruning and helps to reduce computational time and minimise instabilities in the fit.

### 11.2.2 Binning strategy

An illustration of the full binning applied to the signal region is shown in Figure 11.2, and to the one-muon and two lepton control regions in Figure 11.3. As was explained so far, events in the signal and control regions are classified, based on the  $E_T^{\text{miss}}$  and  $E_{T, \text{lep. invis.}}^{\text{miss}}$  respectively into resolved ( $E_T^{\text{miss}}$  proxy  $\in (150 - 500)$  GeV) and merged ( $E_T^{\text{miss}}$  proxy  $\geq 500$  GeV). These regions are further divided as explained in the following.

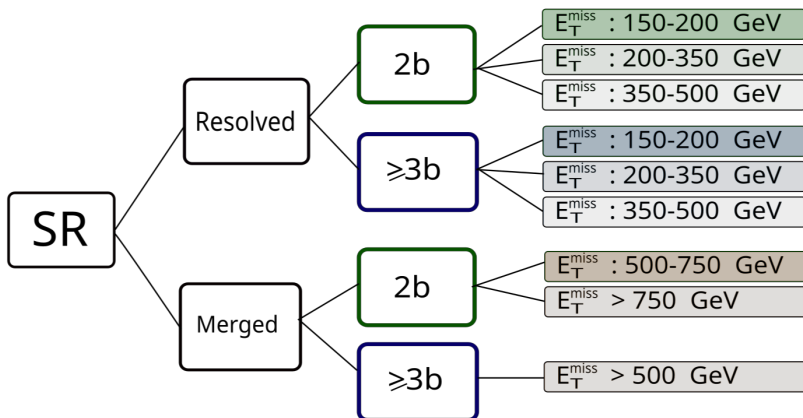


**Figure 11.2:** Illustration of the full binning applied to the signal region.

#### *b*-tag categories

Events in the resolved and merged region are divided into two categories based on the number of *b*-tagged jets in the final state. There are two such *b*-tag categories defined: the *2b*-tag and the  $\geq 3b$ -tag.

**2*b*-tagged** The resolved *2b*-tag region includes events with 2 small-*R* *b*-jets. The merged *2b*-tag region, on the other hand includes events with *2b*-tagged VR-track jets inside the cone of the large-*R*jet and no other *b*-tagged track jet outside the cone.

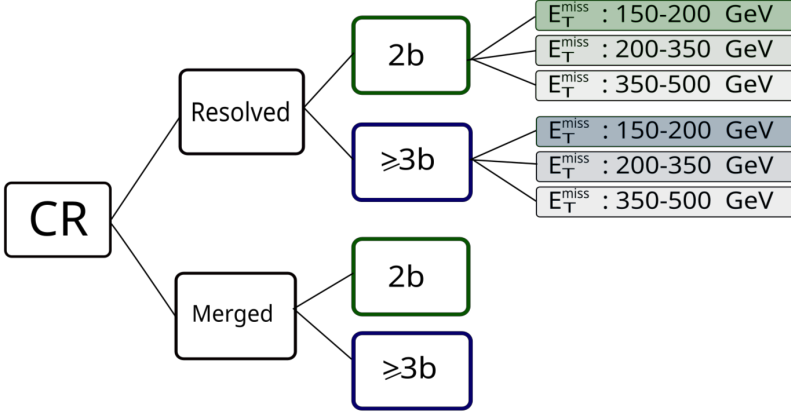


**Figure 11.3:** Illustration of the full binning applied to the one-muon and two-lepton control region.

$\geq 3b$ -tag To increase sensitivity for the case of the 2HDMa signal produced from  $b$ -quarks one additional category is defined, in the resolved region, which includes events with three or more small- $R$   $b$ -tagged jets. Even though  $2HDM+a$  signal models produce softer  $E_T^{\text{miss}}$  and jet- $p_T$  spectrum than the  $Z'$ -2HDM, a  $\geq 3b$ -tag category is defined for the merged region, as well. The  $\geq 3b$ -tag category, in this case, includes events with two  $b$ -tagged track jets inside the larger- $R$  jet cone, and one  $b$ -tagged track jet outside of the jet cone.

### $E_T^{\text{miss}}$ bins

$Z'$ 2HDM signal models with larger  $m_{Z'} - m_A$  mass splitting produce a more boosted signature than the 2HDMa signals. Even within the same model, different parameter choices can lead to significantly different momentum being carried by the dark matter.

To achieve good sensitivity in different regions of phase space, the events that fall in the resolved region in both  $b$ -tag categories, are further divided into three bins based on the  $E_T^{\text{miss}}$ . The first bin contains events with  $E_T^{\text{miss}}$  (or  $E_{T, \text{lep. invis.}}^{\text{miss}}$  for the control regions) in the range (150, 200) GeV, the second in (200, 350) GeV and the third in (350, 500) GeV.

The merged  $2b$ -tag signal region comprises two bins, the first with events that have  $E_T^{\text{miss}}$  in the range (500, 750) GeV, and the second above 750 GeV. The merged  $2b$ -tag one-muon and two lepton control regions are not divided any further. Finally the  $\geq 3b$ -tag merged signal region comprises one bin, as well.

## 11.3 Data and MC comparison

Since the fit is going to use the control regions to constrain the normalisation of the three major backgrounds, it is useful to know before hand how well the SM predictions describe the observed data. This way, we can gain a better understanding of the fit results and the constraining power of the control regions.

The next sections, will discuss the pre-fit distributions of event variables in the signal, and control regions. The format is similar to the one adopted in Sec. 10.3: the distributions of the event variables are shown on the top panel of each plot for data and simulations in a specific phase-space region (e.g resolved CR1), while the bottom panel shows the ratio of data over SM predictions. The hatched bands indicate for each bin the statistical and experimental systematic uncertainties on the predicted background event yields. For their estimation correlations between individual contributions were not considered.

### 11.3.1 Data and MC comparison in SR

Besides the control regions, to determine the background normalisation factors, parts of the invariant mass of the Higgs-boson candidate distribution where no signal is expected are also used. For the signal samples the invariant mass of the Higgs-boson candidate is expected to be  $\sim 125$  GeV. Therefore, the so-called side-band regions that correspond to  $m_{jj} (m_J) < 70$  GeV and  $m_{jj} (m_J) > 140$  GeV, are used in the fit.

The distribution of the invariant mass is not be shown here, but they are included for completeness in Appendix C. The main focus of this section is to examine the distributions of other event variables, such as the  $E_T^{\text{miss}}$  distribution shown in Figure 11.4, which is used in to define the analysis regions and event selection requirements. From the ratio in the bottom panel of figure 11.4a, it is clear that there is a normalisation difference between data and MC in the resolved  $2b$ -tag region. In the resolved  $\geq 3b$  region the larger differences between the distributions are located between  $E_T^{\text{miss}} \sim 200$  GeV and  $\sim 350$  GeV. In the merged  $2b$  region, most of the differences are covered by the large statistical uncertainties on the observed data. Finally, the ratio in the merged  $\geq 3b$  region shows large fluctuations especially up to  $E_T^{\text{miss}} \sim 600$  GeV.

A similar behaviour is observed, also, for the  $p_T$  distribution of the Higgs-boson candidate, which is shown in Figure 11.5. A clear normalisation difference is observed in the  $p_T$  spectrum in the resolved  $2b$ -tag category (Fig. 11.5a), while the differences in the merged  $2b$ -tag and both  $\geq 3b$ -tag categories are covered by the statistical uncertainties on the observed data.

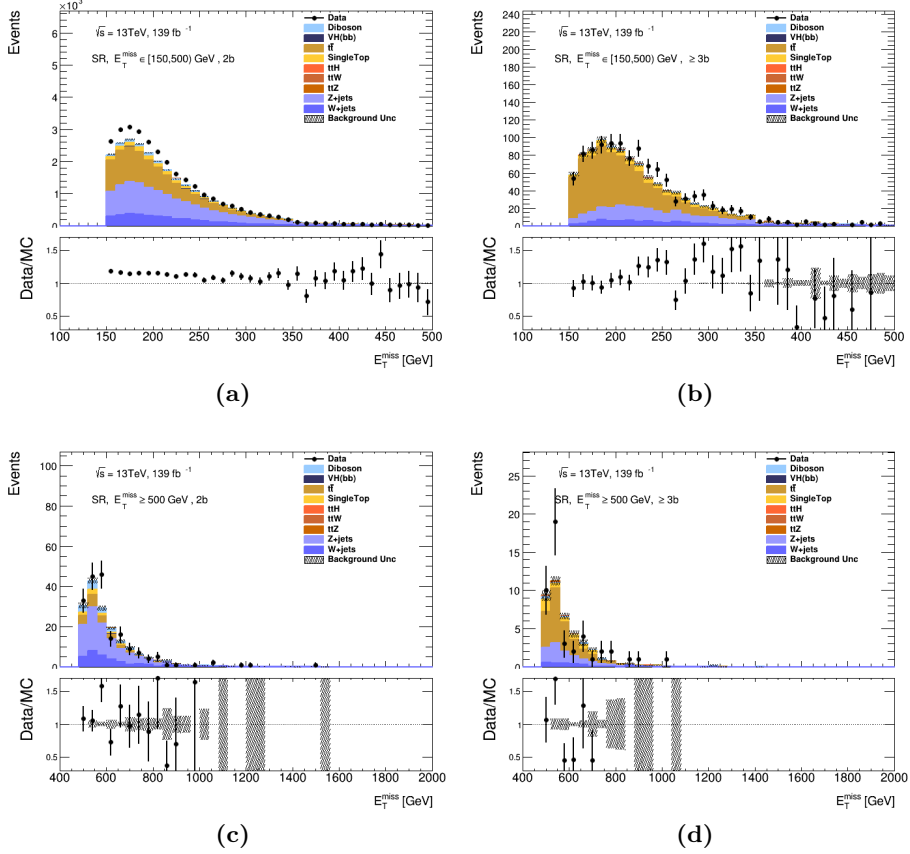


**Figure 11.4:**  $E_T^{\text{miss}}$  spectrum for data and MC backgrounds in the resolved (top) and merged (bottom) signal region for events with exactly 2(left) and at least 3  $b$ -tagged jets(right).

The last distribution presented here, is the  $\Delta\phi$  difference, between the three leading jets in the event and  $E_T^{\text{miss}}$ ,  $\Delta\phi(E_T^{\text{miss}}, \text{jet}_i)$  which is used to select events both in resolved and merged region. The distributions of  $\Delta\phi(E_T^{\text{miss}}, \text{jet}_i)$  are shown in Figure 11.6, in the merged and resolved region for both resolved and merged regions and  $b$ -tag categories

The distributions of the event variables presented in this section hint at normalisation difference between data and the background predictions. To better understand where these differences come we examine in the following sections the distributions of event variables in the control regions.

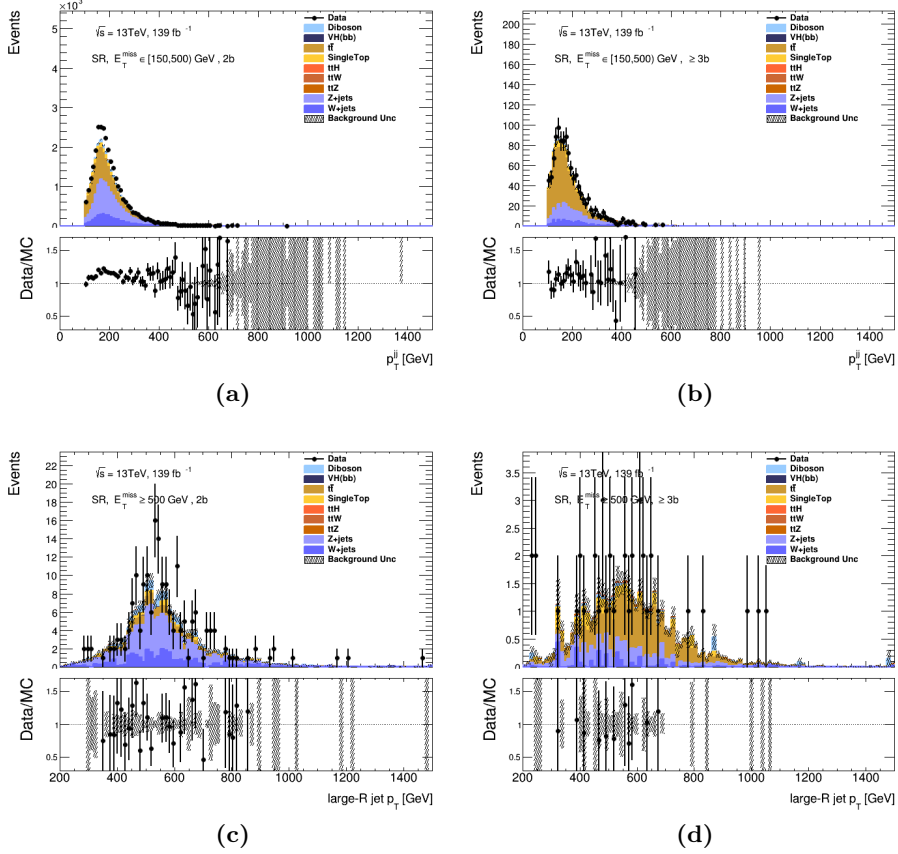


**Figure 11.5:** Higgs-boson candidate  $p_T$  spectrum for data and MC backgrounds in the resolved (top) and merged (bottom) signal region for events with exactly 2(left) and at least 3  $b$ -tagged jets(right).

### 11.3.2 Data and MC comparison in one-muon CR

The fit variable, in this case, as explained in 11.2, is the charge of the observed muons. The muon charge distributions for data and simulated events are shown in Appendix C.

An important variable is the  $E_{T, \text{lep. invis.}}^{\text{miss}}$ , which is used to define the  $E_T^{\text{miss}}$  bins discussed in 11.2. The  $E_{T, \text{lep. invis.}}^{\text{miss}}$  distributions for data and simulations in the resolved and merged control regions, for both  $b$ -tag categories is shown in Figure 11.7. The ratio in Fig. 11.7a is slightly lower than one, for  $E_T^{\text{miss}}$  values up to roughly 300 GeV, and it becomes even smaller for higher  $E_T^{\text{miss}}$  values. In the merged 2 $b$ -tag region in Fig. 11.7c, most differences are covered

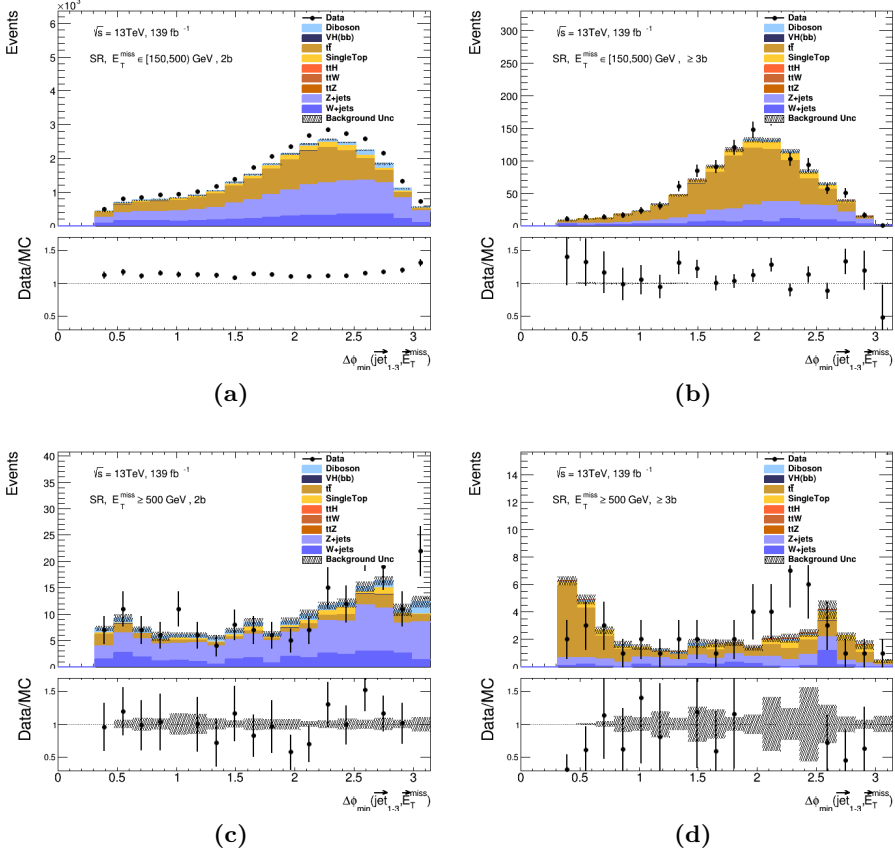


**Figure 11.6:** Distributions of  $\Delta\phi(E_T^{\text{miss}}, \text{jet}_i)$  for data and MC backgrounds in the resolved (top) and merged (bottom) signal region for events with exactly 2(left) and at least 3 b-tagged jets(right).

by the large statistical uncertainties on the observed data. In the 3b-tag resolved region the ratio fluctuates around one, while in the corresponding merged region differences in the  $E_{T, \text{lep. invis.}}^{\text{miss}}$  distributions are covered by uncertainties with the exception of two bins.

Figures 11.7c and 11.7c clearly show that the use of a single met bin in the resolved region is necessary, because there are very few events in the one-lepton control region with  $E_{T, \text{lep. invis.}}^{\text{miss}}$  above 750 GeV. Figure 11.8 shows the distributions of the invariant mass of the Higgs-boson candidate, in the resolved and merged regions and both categories. In this case, we see that the simulated events describe relatively well the observed data since in most of the bins the ratio is very close to one. The only exception is the merged 2b-tag category for

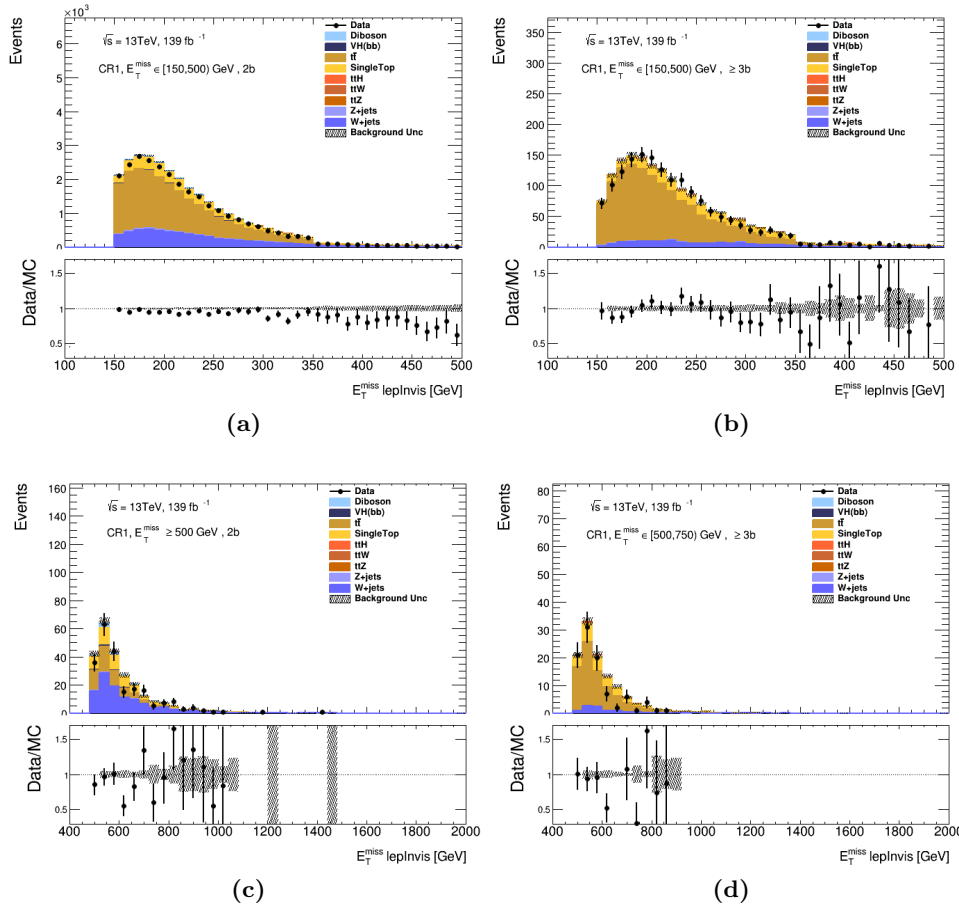


**Figure 11.7:**  $E_{T, \text{lep. invis.}}^{\text{miss}}$  spectra in the resolved (top) and merged (bottom) CR1 for events with exactly 2 (left) and at least 3  $b$ -tagged jets (right).

$m_J > 180 \text{ GeV}$ , shown in Fig. 11.8c. However, since the theoretical systematic uncertainties are not included in this plots, which does not allow to draw safe conclusions.

Despite that the background in some regions to slightly overestimates the data, the background predictions describe relatively the corresponding data distributions.

The distributions of the event variables discussed in this section show that the control region will have a reasonable constraining power for the relevant backgrounds. Appendix C includes the pre-fit distributions of more event variables.

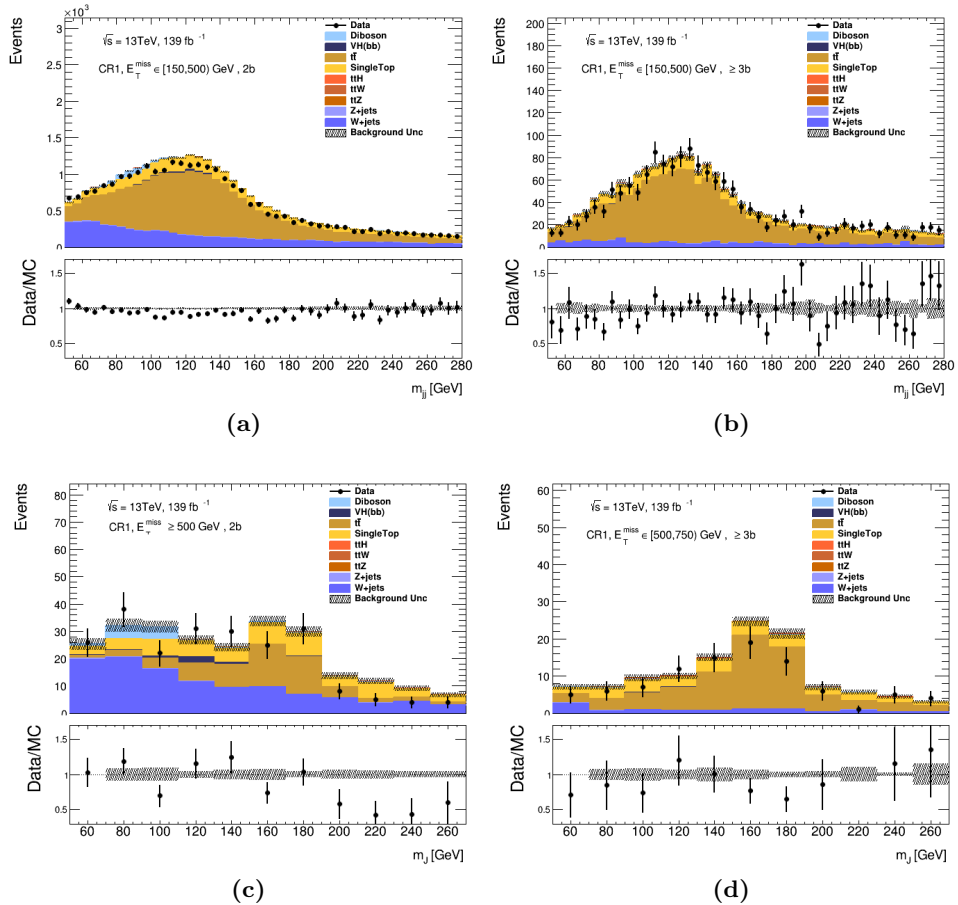


**Figure 11.8:** Distributions of the invariant mass of the Higgs-boson candidate in the resolved (top) and merged (bottom) CR1 for events with exactly 2(left) and at least 3  $b$ -tagged jets(right).

### 11.3.3 Comparison between data and MC predictions in two-lepton CR

The fit discriminant for the two-lepton control region, are the event yields, in each analysis region. Figure 11.9 shows, on the top panels, the invariant mass distributions of the Higgs-boson candidate in both resolved and merged region and for both  $b$ -tag categories. All the distributions in the  $3b$ -tag category, shown in Fig. 11.9, as well as the  $2b$ -tag merged region, are characterised by a very limited number of events in both resolved and merged region, which leads to a drastic increase of the statistical uncertainty on the observed data, covering

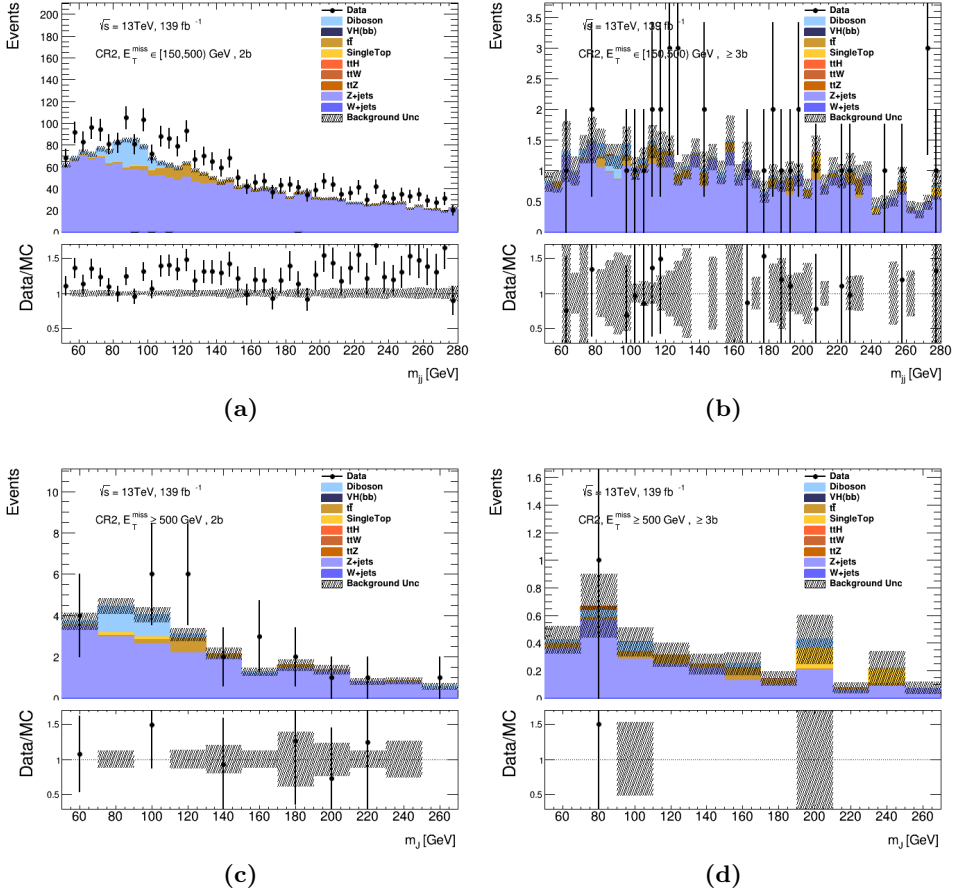
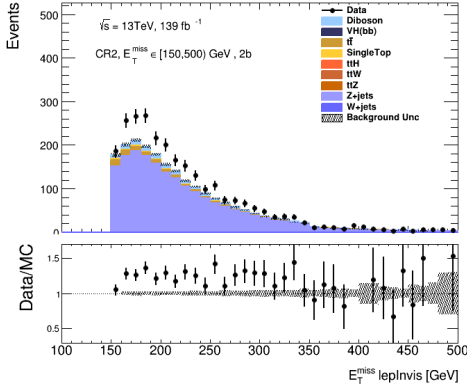


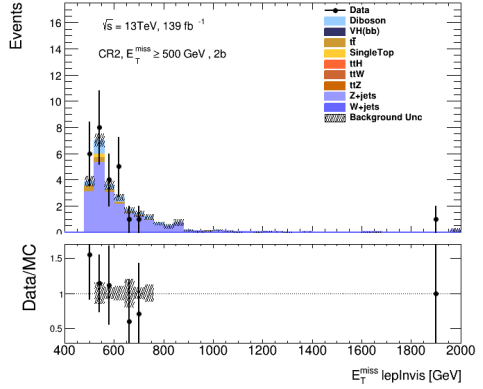
**Figure 11.9:** Distributions of  $m_{jj}$  in the resolved (top) and merged (bottom) two-lepton control region, for events in the  $2b$ -tag (left) and  $\geq 3b$ -tag (right) categories.

any potential differences. Even though, the  $2b$ -tag resolved region appears to have more events than the other regions, we need to keep in mind that the fit is performed in three distinct ranges, in the resolved region, therefore, the events will also be limited there. These plots clearly illustrate why the event yields are used as the fit discriminant in all regions. In the following the event variables are only presented for the  $2b$ -tag category, due to limited statistics in the  $\geq 3b$ -tag category.

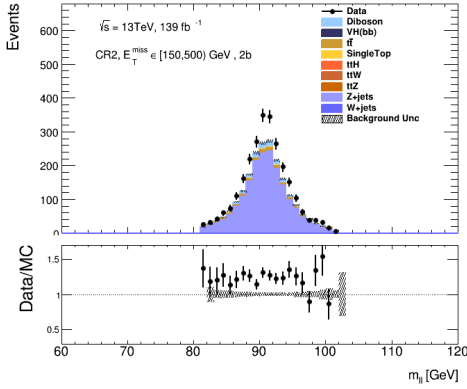
Figure 11.10 shows the distributions of  $E_{T, \text{lep. invis.}}^{\text{miss}}$  (top) and the invariant mass of the two signal leptons in the event (bottom) in the resolved (left) and merged (right) two-lepton control region and for events with exactly  $2b$  jets in the event.



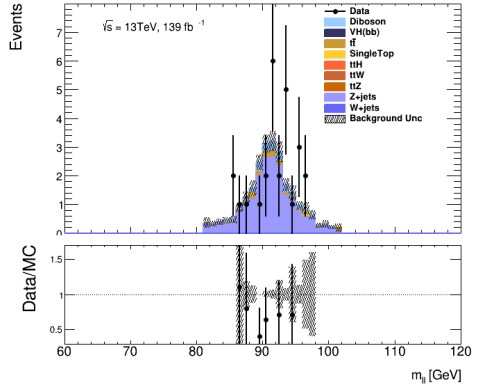
(a)



(b)



(c)



(d)

**Figure 11.10:** Distributions of  $m_{\ell\ell}$  in the resolved (top) and merged(bottom) two-lepton control region, for events in the  $2b$ -tag category.

From all the figures shown in this section we see that in the resolved region, the expected event yields underestimate the observed data, indicating that the fit is necessary. A similar conclusion can not be made for the merged  $2b$  region and the  $3b$ , due to the large statistical uncertainties.

# Chapter 12

## Results and interpretation

This chapter shows the results obtained with the  $E_T^{\text{miss}} + \text{H}(b\bar{b})$  analysis using the full Run 2 dataset. The first section, 12.1, contains the results from the background-only fit, performed to extract the background normalisation factors and to look for deviations from the Standard Model predictions. Section 12.2 presents the results from signal+background fit and the effect of different sources of experimental and theoretical uncertainties on the upper limits of the signal models. Finally, Section 12.3 presents the exclusion limits on the parameter space of the  $Z'$ -2HDM and 2HDM $a$  simplified models for dark matter production and the model independent limits on the production cross section of a Higgs boson and  $E_T^{\text{miss}}$ .

### 12.1 Background-only fit

This section contains the results from the background-only fit, for which the signal strength,  $\mu$ , is set to 0. All the regions introduced in the previous section are fit simultaneously with a profile Likelihood fit, described in Section 8.3.

#### 12.1.1 Nuisance parameters and constraints

In this section, the pulls and constraints of NPs are examined to reveal any issues or features that must be further investigated. The pulls (sec. 8.3, Eq. 8.7) and uncertainties of all the NPs, are estimated once from the background-only fit to data, and then compared to those estimated from the fit to the Asimov dataset with  $\mu = 0$ , in a single plot called *pull-plot*. In this section, only a few interesting cases are shown that either have large pulls or are constrained by

the fit. A pull-plot that contains all NPs, except those that parametrise the statistical uncertainties, is included in Appendix D.

Figure 12.1 shows a pull-plot for some of the NPs associated with theoretical uncertainties of the Z+ light-flavour jets (labelled “Z”) simulation. The NP “Z\_MUR\_MUF” describes the uncertainty due to the choice of normalisation and factorisation scale. The NPs “Z\_ckkw” and “Z\_qsf” describe the uncertainty related to the choice of merging and matching scale respectively. The parameter “Z\_MG” describes the uncertainty associated with the difference between SHERPA and an alternative simulation produced using MC@NLO for ME and PYTHIA for the simulation of the parton shower and hadronisation respectively, and it is constrained to 23% of its size by the fit. The uncertainty on Sec. 11.1.2, This constraint is explained by Figure 12.2, which shows the relative shift of

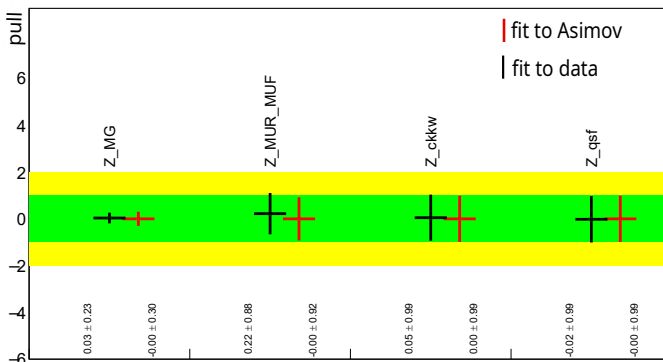
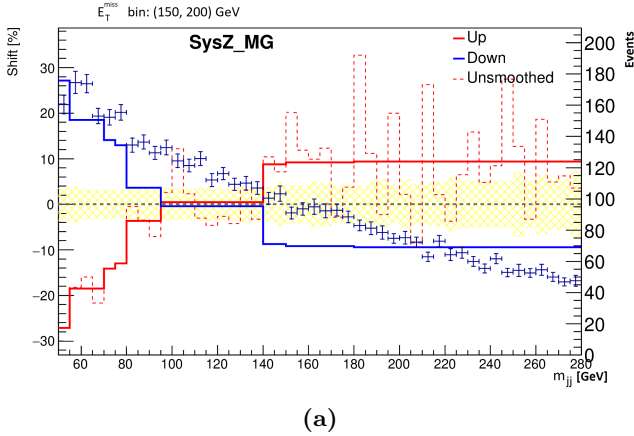


**Figure 12.1:** Z+jets modelling modelling-related nuisance parameter pulls and constraints, obtained from the unconditional fit to the Asimov dataset (red) and the data (black), in the CR and SR regions.

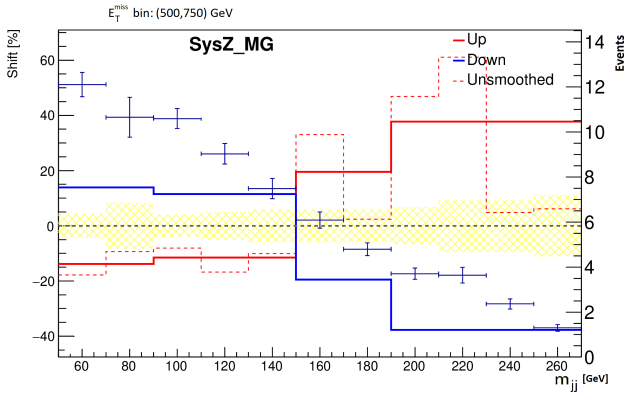
the variations with respect to the nominal distributions, before the fit. The left y-axis shows the relative shift of the variations. The nominal  $m_{jj}$  distribution is also shown with blue points with the error bars that show the statistical uncertainty on the event yields in each bin. The right y-axis corresponds to the values of the nominal distribution. The variations in Fig. 12.2, range from  $\sim 20\%$  to  $\sim 50\%$  before the fit while the statistical uncertainty is only  $\sim 5\%$ , which explains the strong constraint seen in Fig. 12.1. In Figure 12.2, we can also see the effect of the smoothing procedure: before the smoothing, the shape of the variation is affected by the limited statistics of the simulated event sample.

### 12.1.2 Background normalisation factors

The values of the normalisation factors are summarised in Table 12.1. The



(a)



(b)

**Figure 12.2:** Pre-fit  $m_{jj}$  uncertainty from the comparison between SHERPA and MADGRAPH5\_AMC@NLO+PYTHIA comparison in the first  $E_T^{\text{miss}}$  bin of the resolved (left) and merged (right) signal region. The yellow hatched band shows the relative statistical uncertainty on the event yields in each bin of the nominal distribution. The error bars on each point of the nominal distribution show the statistical uncertainty. The dashed red line shows the systematic variation associated with difference between using MC@NLO +PYTHIA and SHERPA. This variation is smoothed and then symmetrised, leading to the up and down variations shown with solid red and solid blue lines respectively.

$t\bar{t}$  (norm\_ttbar) and  $W$ +HF (norm\_Whf) jets normalisation factors, are very close to one, 0.98. This was already hinted by examining the distributions of the event variables before the fit in the one-muon control region (see 11.3). The comparisons indicated that the SM predicted event yields were in some bins higher than the observed data. This small difference between the predicted event yields and data, is also illustrated in Figures 12.4 and 12.5. These figures

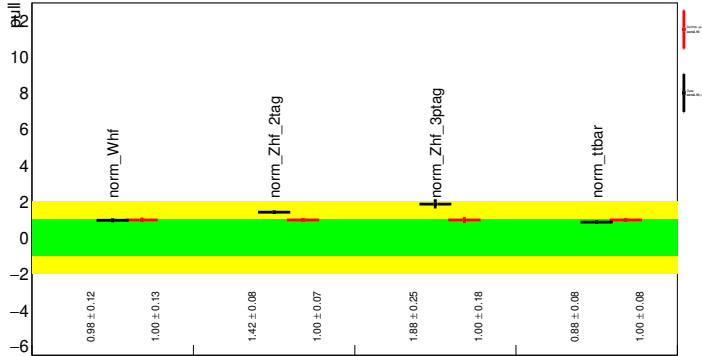


**Figure 12.3:** Post-fit normalisation factors for the free-floating parameters, obtained from the unconditional fit to the Asimov dataset (red) and the actual dataset (black) in the SR and CR regions

Sample	Normalisation factor
$W$ +HF jets	$0.98 \pm 0.12$
$Z$ +HF jets, $2b$ -jets	$1.42 \pm 0.08$
$Z$ +HF jets, $\geq 3b$ -jets	$1.88 \pm 0.25$
$t\bar{t}$	$0.88 \pm 0.08$

**Table 12.1:** Normalisation factors for major backgrounds estimated from the background-only fit.

show the distributions of the muon charge (event yield) in the one-muon CR, for events with  $2b$ -tagged (at-least 3  $b$ -tagged) jets after the fit, in the four  $E_T^{\text{miss}}$  bins used in the analysis. The background expectations before the fit are shown, as well, with a blue dashed line. The pre-fit predictions, in all the plots in Fig. 12.4 and 12.5, are higher than the data especially for events with  $2b$ -tagged jets. For events with at least  $3b$ -jets, the differences between the distributions before and after the fit are covered by the uncertainties in the resolved region, but are noticeable in the merged  $\leq 3b$  region.

On the contrary, the normalisation factors for the  $Z$ +HF background are pulled up. The normalisation for the  $2b$ -jets category is 1.42, while for the  $\leq 3b$ -jets (norm\_Zhf.3ptag) is 1.88. As it was explained in Sec. 11.2, two normalisation factors are used for  $Z$ +HF background normalisation because SHERPA was found to underestimate  $g \rightarrow b\bar{b}$  splitting, and this is the mechanism that produces a third  $b$ -tagged jet in  $Z$ +jets processes.

The observed pulls on the normalisation factors, are compatible with what was observed in the pre-fit distributions of various event variables in the two-lepton CR (Sec. 11.3), in which the normalisation difference between the data and MC predictions was higher than one. This is also illustrated in Figures 12.6 and 12.7

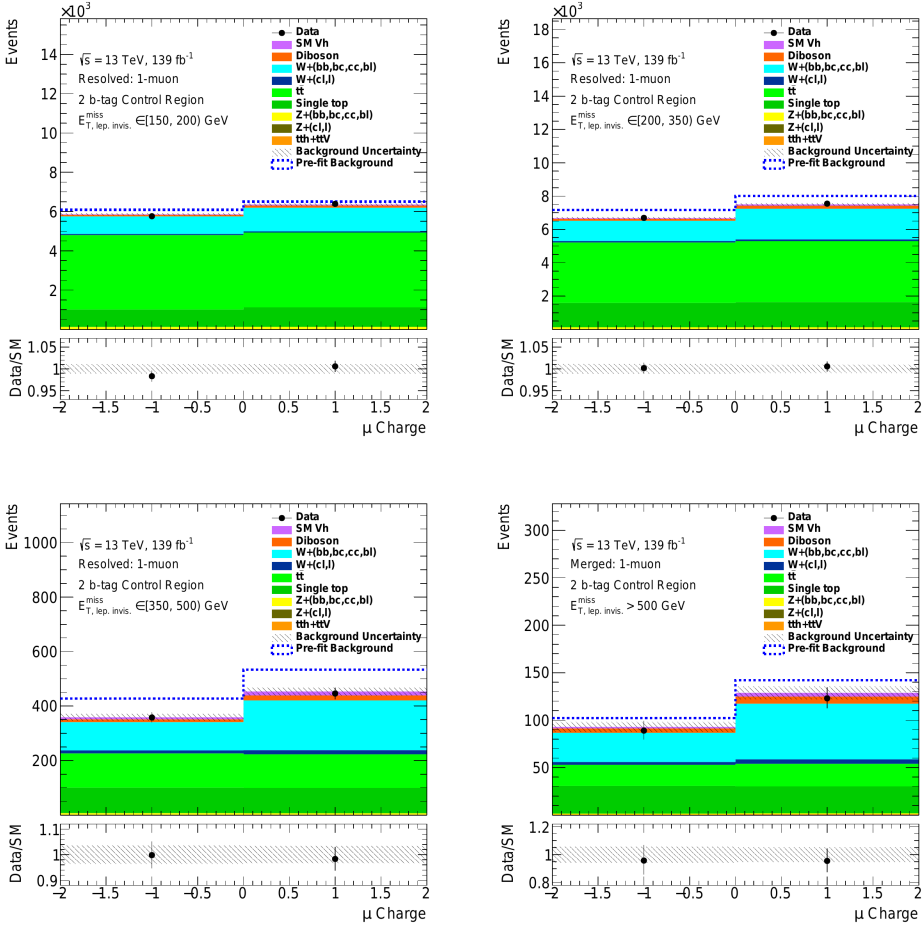


**Figure 12.4:** Distributions of the muon charge in the one-muon CR, for events with  $2b$ -tagged jets after the fit. The distributions are shown in the four  $E_T^{\text{miss}}$  bins used in the analysis. The prefit yields are shown with a dashed blue line. The error bands show the statistical and systematic uncertainties, considering correlations between the individual contributions.

which show the event yields, in the two-lepton control region in the four  $E_T^{\text{miss}}$  ranges used in the analysis, for events with  $2b$ -jets and at least three, respectively. In all the plots shown in Fig.12.6, the predictions before the fit underestimate the observed data. In the first three  $E_T^{\text{miss}}$  bins, the normalisation difference before the fit ranges, roughly, between 1.1, and 1.4., while in the merged region the statistical uncertainty on the observed data hides any potential difference. For events with at least 3  $b$ -jets, the plots in Fig. 12.7 show a considerable difference between the pre-fit expected event yields and the observed data, only

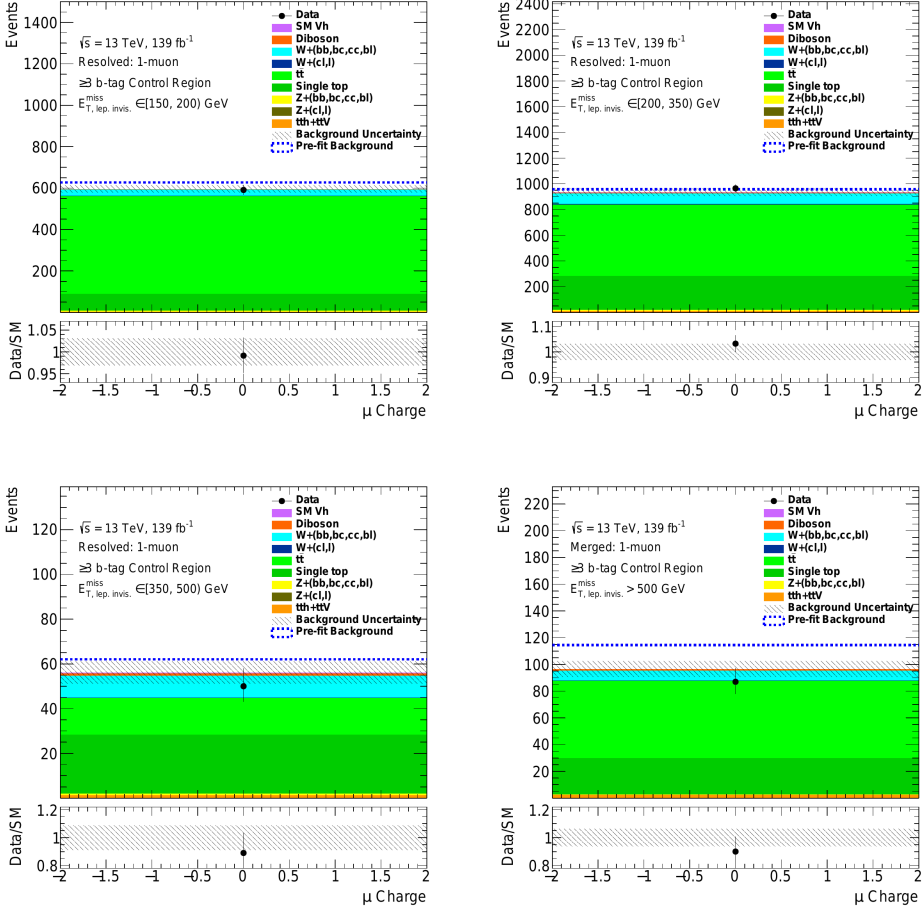


**Figure 12.5:** Event yields (single bin  $\mu$  charge distribution) in the four  $E_T^{\text{miss}}$  bins of the one-muon CR used in the analysis, for events with at least  $3b$ -tagged jets in the final state, after the fit. The prefit yields are shown with a dashed blue line. The error bands show the statistical and systematic uncertainties, considering correlations between the individual contributions

in the second  $E_T^{\text{miss}}$  bin. The high statistical uncertainties on the observed data, in the first and last bin hide any potential differences.

Summaries of the background event yields and observed data events in all  $E_T^{\text{miss}}$  bins and  $b$ -tag categories are shown in Figures 12.8 and 12.9 for the one muon and two-lepton control region, respectively. The ratio of the observed data over the expected event yields from simulations displayed in the lower panels of both figures shows good agreement in all  $E_T^{\text{miss}}$  bins.

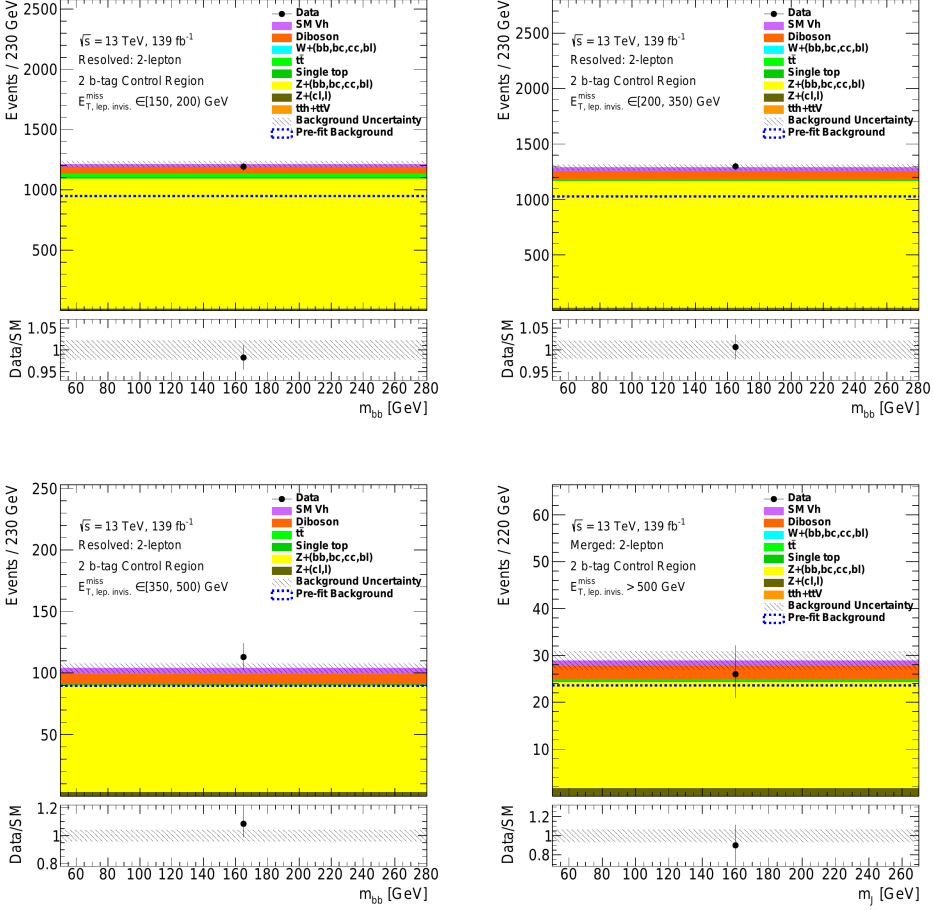


**Figure 12.6:** Comparison of the predicted event yields to the observed data in two-lepton control region, for events with exactly  $2b$ -tagged jets in the final state, in all four  $E_T^{\text{miss}}$  bins used in the analysis. The prefit yields are shown with a dashed blue line.

### 12.1.3 Post-fit distributions in the signal region

Besides determining the background normalisation factors, the background-only fit is used to find whether there are any significant deviations in the signal region from the standard model predictions.

The invariant mass distributions of the of the Higgs candidate ( $m_{jj}, m_J$ ) after the background-only fit, are shown in Figure 12.10 in the five different  $E_T^{\text{miss}}$  bins used in the fit for events with exactly  $2b$ -tagged jets in the final state. Figure 12.11 shows the corresponding plots for the  $3b$ -tag category, in the four

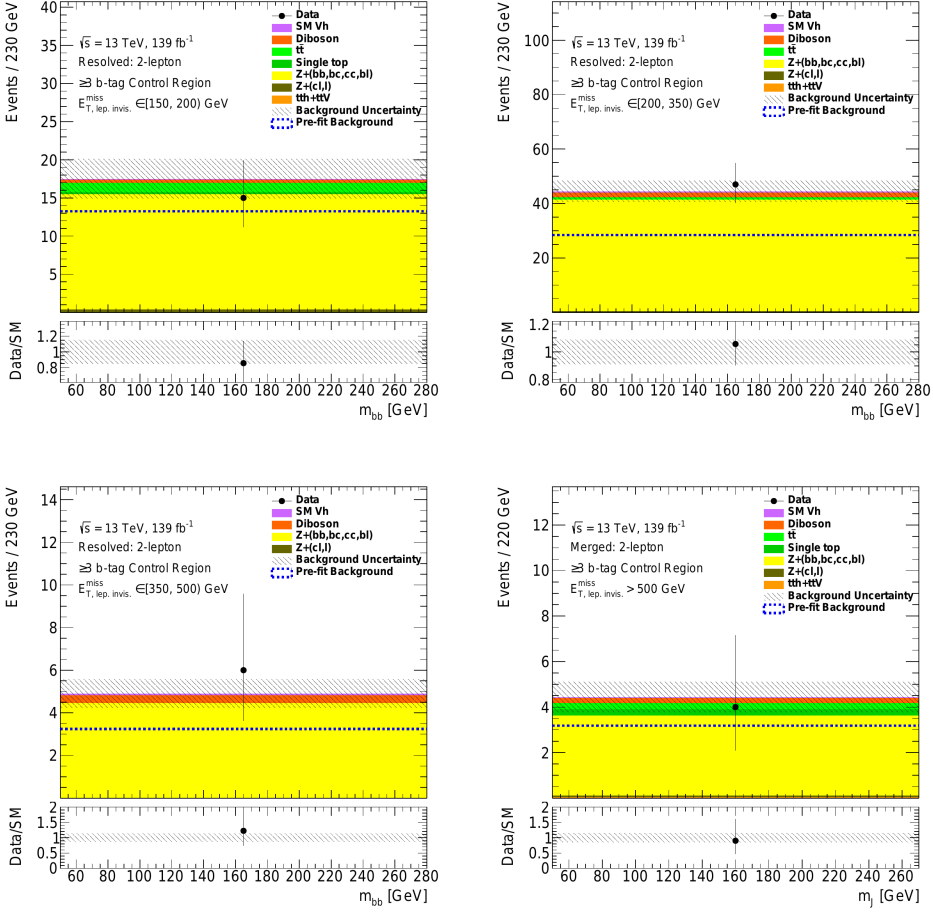


**Figure 12.7:** Comparison of the predicted event yields to the observed data in two-lepton control region, for events with exactly  $2b$ -tagged jets in the final state, in all four  $E_T^{\text{miss}}$  bins used in the analysis. The error bands (hatched lines) show the statistical and systematic uncertainties, considering correlations between the individual contributions.

$E_T^{\text{miss}}$  bins used in this case. The expected mass distributions for a  $Z'$ -2HDM selected signal are overlaid in each  $E_T^{\text{miss}}$  range, scaled by different factors (100, 20, 5, 10, 50 respectively) for visibility. The prefit distributions are displayed, as well, with a blue dash line.

Overall, there is good post-fit agreement between the expected event yields from SM background and the observed data, without any significant difference between the observed data and the SM expectations.

Table 12.2 summarises the expected event yields for each of the background

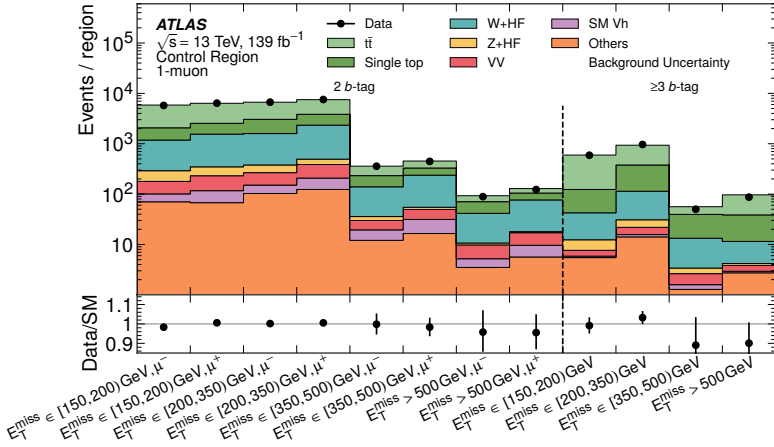


**Figure 12.8:** Comparison of the event yields from all background processes and the observed data as a function of the  $E_T^{\text{miss}}$  for the one-muon control region in both  $b$ -tag categories [220]

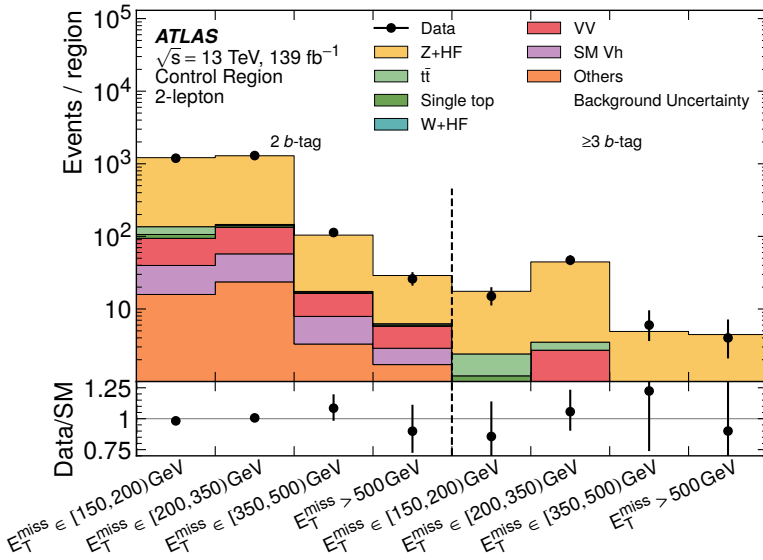


**Figure 12.9:** Comparison of the event yields from all background processes and the observed data as a function of the  $E_T^{\text{miss}}$  for the one-muon control region in both  $b$ -tag categories [220]

processes after the fit and the number of observed data in each  $E_T^{\text{miss}}$  bin for the  $2b$ -tagged jets category. The dominant background contribution is the  $Z$ +jets

process followed by the  $t\bar{t}$  and  $W$ +jets.

2 <i>b</i> signal region	$E_T^{\text{miss}}$ range		
	[150, 200] GeV	[200, 350] GeV	[350, 500] GeV
$Z$ +HF	$6470 \pm 310$	$7200 \pm 310$	$507 \pm 26$
$Z$ +light jets	$72 \pm 15$	$137 \pm 29$	$18 \pm 4$
$W$ +HF	$1590 \pm 210$	$1760 \pm 230$	$106 \pm 14$
$W$ +light jets	$86 \pm 35$	$92 \pm 35$	$14 \pm 5$
Single top-quark	$570 \pm 260$	$570 \pm 260$	$21 \pm 10$
$t\bar{t}$	$4680 \pm 290$	$3280 \pm 240$	$76 \pm 9$
Diboson	$450 \pm 50$	$600 \pm 60$	$56 \pm 7$
$Vh$	$151 \pm 10$	$202 \pm 12$	$26.6 \pm 1.8$
$t\bar{t} + V/h$	$7.6 \pm 0.4$	$11.8 \pm 0.5$	$0.45 \pm 0.06$
Total background	$14070 \pm 110$	$13860 \pm 100$	$825 \pm 19$
Data	14259	13724	799

**Table 12.2:** Background yields in comparison with data in the 2*b* signal regions for different  $E_T^{\text{miss}}$  ranges after a background-only fit to data. Statistical and systematic uncertainties are reported together.

Table 12.3 presents the background contributions for the two  $E_T^{\text{miss}}$  bins in the merged topology for the 2*b*-tagged case. For these two bins a significant background contribution comes from the diboson production.

2 <i>b</i> signal regions	$E_T^{\text{miss}}$ range	
	[500, 750] GeV	[750, $\infty$ )GeV
$Z$ +HF	$94 \pm 7$	$9.2 \pm 1.8$
$Z$ +light jets	$4.5 \pm 1.0$	$1.17 \pm 0.30$
$W$ +HF	$25 \pm 4$	$3.1 \pm 0.6$
$W$ +light jets	$1.6 \pm 0.6$	$0.21 \pm 0.09$
Single top-quark	$2.6 \pm 1.9$	$0.10 \pm 0.16$
$t\bar{t}$	$11.4 \pm 1.6$	$0.38 \pm 0.08$
Diboson	$15.2 \pm 1.9$	$1.61 \pm 0.29$
$Vh$	$5.6 \pm 0.5$	$0.68 \pm 0.12$
$t\bar{t} + V/h$	$0.286 \pm 0.029$	$0.035 \pm 0.006$
Total background	$160 \pm 8$	$16.7 \pm 1.9$
Data	168	19

**Table 12.3:** Background yields in comparison with data in the 2*b* signal region for the two  $E_T^{\text{miss}}$  ranges in the merged topology after a background-only fit to data. Statistical and systematic uncertainties are reported together [220].

Table 12.4 contains all  $E_T^{\text{miss}}$  bins for the 3*b*-tagged category. In the first and third  $E_T^{\text{miss}}$  range the  $t\bar{t}$  productions is the dominant contribution followed by  $Z$ +jets, while the second and third are dominated by  $Z$ +jets.

$3b$ signal regions	$E_T^{\text{miss}}$ range			
	[150, 200] GeV	[200, 350] GeV	[350, 500] GeV	[500, $\infty$ ) GeV
$Z$ +HF	$102 \pm 15$	$278 \pm 28$	$26.4 \pm 3.5$	$15.6 \pm 1.9$
$Z$ +light jets	$0.6 \pm 0.4$	$2.9 \pm 0.8$	$0.34 \pm 0.12$	$0.46 \pm 0.12$
$W$ +HF	$21 \pm 4$	$47 \pm 9$	$4.2 \pm 0.9$	$2.4 \pm 0.4$
$W$ +light jets	$0.01 \pm 0.04$	$1.7 \pm 0.9$	$0.8 \pm 0.4$	$0.031 \pm 0.026$
$t\bar{t}$	$276 \pm 19$	$252 \pm 22$	$5.1 \pm 0.7$	$17.9 \pm 1.8$
Single top-quark	$23 \pm 11$	$55 \pm 25$	$2.9 \pm 1.4$	$3.4 \pm 1.7$
Diboson	$4.8 \pm 1.4$	$12.9 \pm 2.2$	$1.8 \pm 0.4$	$1.26 \pm 0.31$
$Vh$	$0.65 \pm 0.28$	$2.9 \pm 0.5$	$0.40 \pm 0.08$	$0.230 \pm 0.025$
$t\bar{t} + V/h$	$1.78 \pm 0.17$	$3.89 \pm 0.26$	$0.371 \pm 0.035$	$0.78 \pm 0.08$
Total background	$430 \pm 15$	$656 \pm 21$	$42 \pm 4$	$42.0 \pm 2.8$
Data	408	658	42	46

**Table 12.4:** Background yields in comparison with data in the  $3b$  signal regions for different  $E_T^{\text{miss}}$  ranges after a background-only fit to data. Statistical and systematic uncertainties are reported together [220].

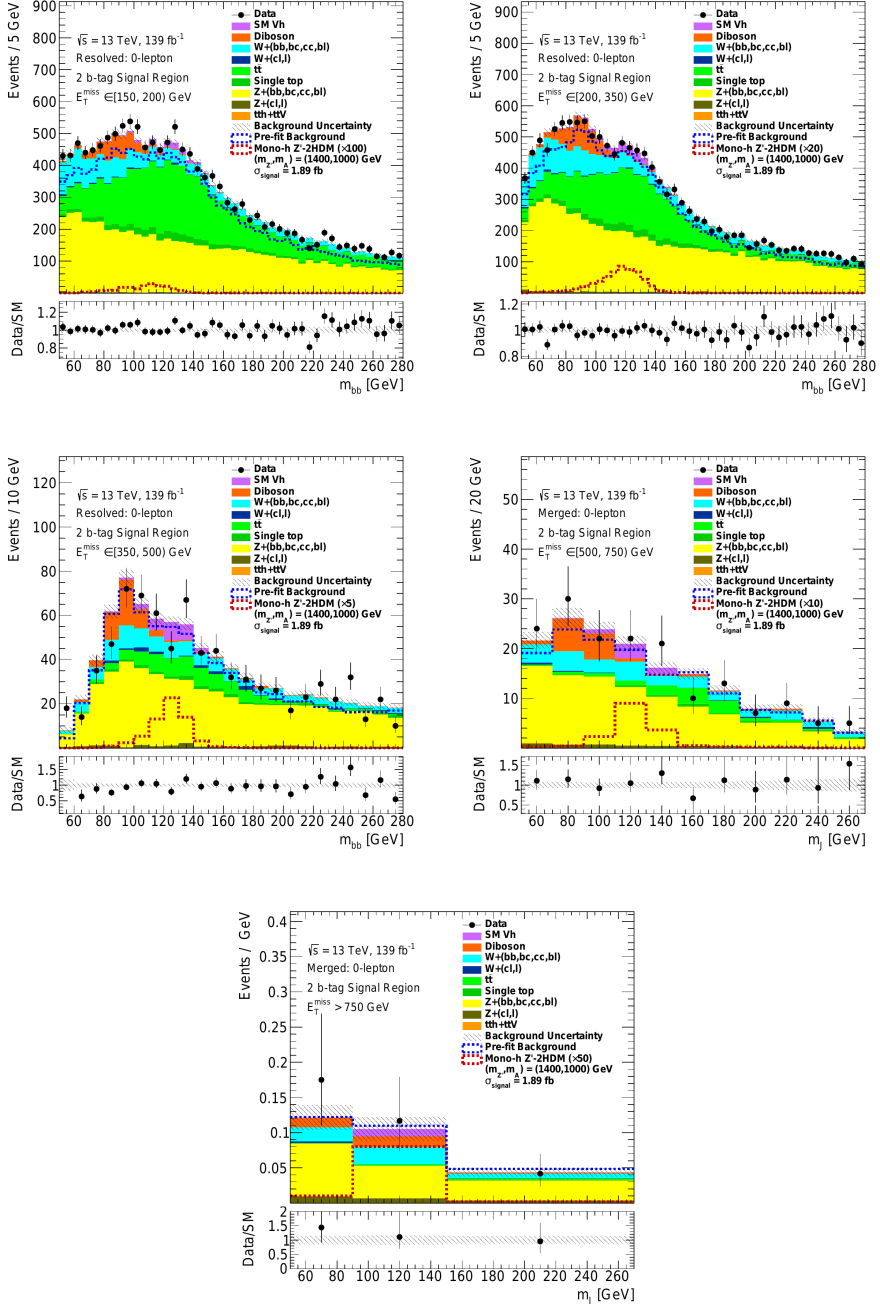


**Figure 12.10:** Distributions of the Higgs candidate mass in the 2*b*-tag signal region in the five  $E_T^{\text{miss}}$  ranges used in the analysis. The pre-fit SM expectations are shown with a blue dashed line. The expected signal from one representative  $Z'$ -2HDM model is shown scaled up by a different factor for each range.

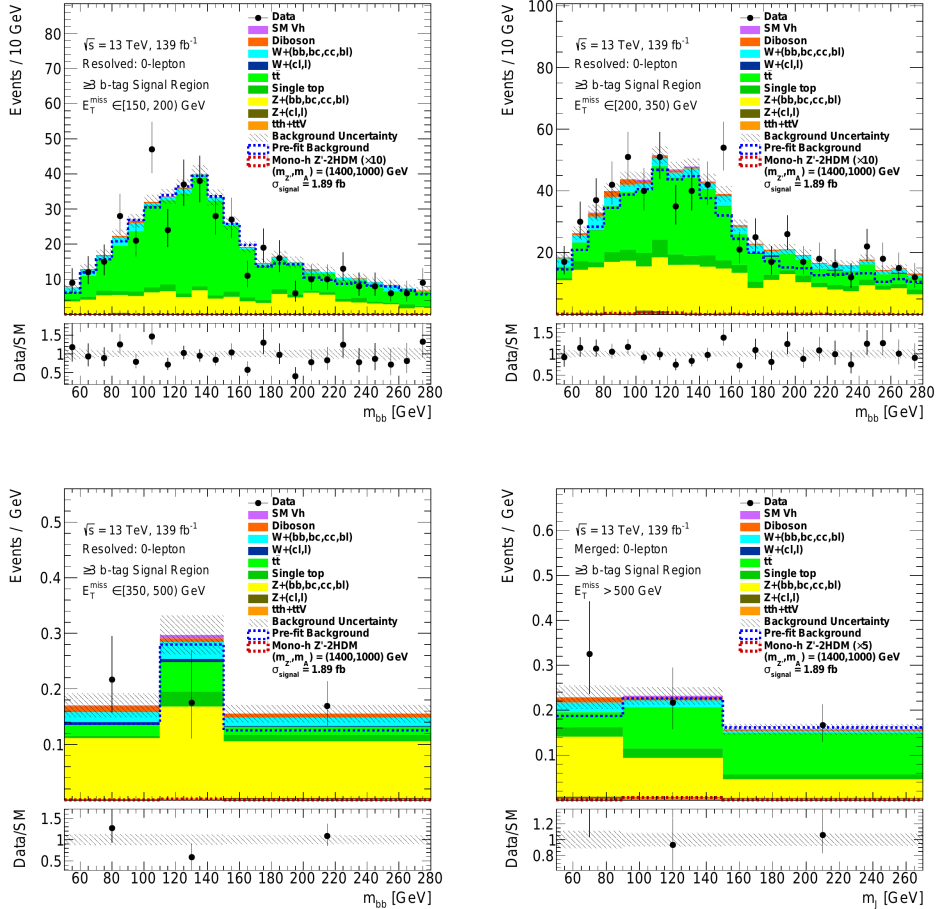


**Figure 12.11:** Distributions of the Higgs candidate mass in the  $\geq 3b$ -tag signal region for the four  $E_T^{\text{miss}}$  ranges used as input to the fit. The pre-fit SM expectations are shown with a blue dashed line. The expected signal from one representative  $Z'$ -2HDM model is shown scaled up by a different factor for each range.

## 12.2 Nuisance parameter impact

To quantify the impact of the systematic uncertainties to the signal strength, a simultaneous signal+background fit is performed for three representative  $Z'$ -2HDM models with  $(m_{Z'}, m_A) = (800, 500)$ ,  $(1400, 1000)$ ,  $(2800, 300)$ . These points correspond to a low, medium and high  $E_T^{\text{miss}}$  range and they are at the edge of the area excluded by the search (exclusion limit plots are shown in Sec. 12.3.1).

The procedure to estimate the impact, using one model, is as follows:

- The observed upper limit on the signal strength for this model is determined.
- A signal+background fit is performed with  $\mu$  set to the observed upper limit for the particular model. From this fit the total uncertainty  $\sigma_{tot}$  is estimated.
- For each source of systematic uncertainty, a new fit is performed, in which the NP associated to the specific source is not included. From this fit the  $\sigma_i$  is estimated.

The fractional impact associated of a specific source of systematic uncertainty on the signal strength is given by:  $(\sigma_{tot}^2 - \sigma_i^2)/\sigma_{tot}^2$ .

Table 12.5 presents the impact on the signal strength of the dominant sources of uncertainty, estimated for the three points signal points. Several sources of uncertainty are grouped together, for example all experimental uncertainties related to jet energy scale and resolution are grouped together in the “Jets” source in the table.

The bottom of the table shows the total systematic uncertainty and the statistical uncertainty. The total systematic uncertainty is smaller than the quadrature sum of the individual sources, due to correlations between the nuisance parameters.

In Table 12.5, the largest impact from the experimental uncertainties comes from the jet related uncertainties for the low  $E_T^{\text{miss}}$  (low mediator mass)  $Z'$ -2HDM point. The systematic uncertainties associated with the normalisation of the three main background also have a large impact on the signal strength for the low  $E_T^{\text{miss}}$  point. From the same table it is also apparent that for higher  $E_T^{\text{miss}}$  values the statistical uncertainty becomes dominant.

Source of uncertainty	Fractional squared uncertainty in $\mu$		
	$Z'$ -2HDM signals, $(m'_Z, m_A)$ [GeV]		
	(800, 500)	(1400, 1000)	(2800, 300)
$Z$ +HF normalisation	0.11	0.03	<0.01
$W$ +HF normalisation	0.02	0.01	<0.01
$t\bar{t}$ normalisation	0.16	0.04	<0.01
$Z$ modelling uncertainties	0.02	0.07	<0.01
$W$ modelling uncertainties	<0.01	0.01	<0.01
$t\bar{t}$ modelling uncertainties	0.13	0.05	<0.01
Single- $t$ modelling uncertainties	0.18	0.02	<0.01
Other modelling uncertainties	0.05	0.01	<0.01
Jets	0.20	0.06	0.01
$b$ -tagging	0.01	0.01	0.04
$E_T^{\text{miss}}$ soft term and pile-up	<0.01	<0.01	<0.01
Other experimental systematic uncertainties	0.01	<0.01	<0.01
Signal systematic uncertainties	<0.01	<0.01	<0.01
MC sample size	0.08	0.07	0.11
Statistical uncertainty	0.27	0.61	0.79
Total systematic uncertainties	0.73	0.39	0.21

**Table 12.5:** Impact of the different sources of uncertainty groups for three different  $Z'$ -2HDM points. The masses  $(m'_Z, m_A)$  are shown in the second row. The sum of the different impacts of systematic uncertainties differs from the total impact of all systematic uncertainties due to correlations [220].

## 12.3 Interpretations

Since no deviation from the Standard Model expectations was observed, the results are interpreted using the two benchmark models, described in Section 3.5.1. The exclusion limits for these two models, also known as *model-dependent* limits are discussed in section 12.3.1.

In addition to the model-dependent limits, we can interpret the results assuming, only that a  $b\bar{b}$  is produced with invariant mass close to the SM Higgs-boson mass together with large amount of  $E_T^{\text{miss}}$ . These type of limits, known as *model-independent limits* is presented in section 12.3.2.

### 12.3.1 Model-dependent exclusion limits

The upper limits presented in this section, are derived using the CLs method described in Section 8.3.3. The procedure to calculate the model independent limits is the following.

The first step is to perform several signal+background hypothesis tests, for a

a particular signal point, assuming different values for  $\mu$  and to estimate the corresponding the CLs values. The goal is to find the signal strength for which the corresponding CLs value is equal to 0.05. This will be the upper limit on the signal strength. If the estimated upper limit on the signal strength is bellow one, then the specific signal point is excluded.

The expected and observed exclusion limits for the 2HDM+a  $b\bar{b}$ -induced,  $ggF$ -induced, and  $Z'$ -2HDM are shown in Figures 12.12, 12.13, and 12.14, respectively.

Figure 12.12 shows the exclusion limits for  $ggF$  induced 2HDM+a scenario. The  $x$ -axis corresponds to the mass of the pseudo-scalar mediator  $a$  and the  $y$ -axis to the mass of mediator  $A$ . The grey dashed line shows the kinematic limit: any  $(m_A, m_a)$  combination bellow this line is excluded. The expected limit is shown with a dashed black line together with the  $\pm 1\sigma$  and  $\pm 2\sigma$  bands. The observed limit is shown with a black solid line. Overall, the observed limit agrees well with the expected, and reaches up to 520 GeV in  $m_a$  for  $m_A = 1.25$  TeV. The figure also shows, for comparison, the area excluded by reinterpretation of the  $36 \text{ fb}^{-1} E_T^{\text{miss}} + \text{Higgs}(bb)$  analysis reported in Reference [83]. With respect to the old result, this analysis extends the exclusion limits in  $m_a$ , by roughly 200 GeV.

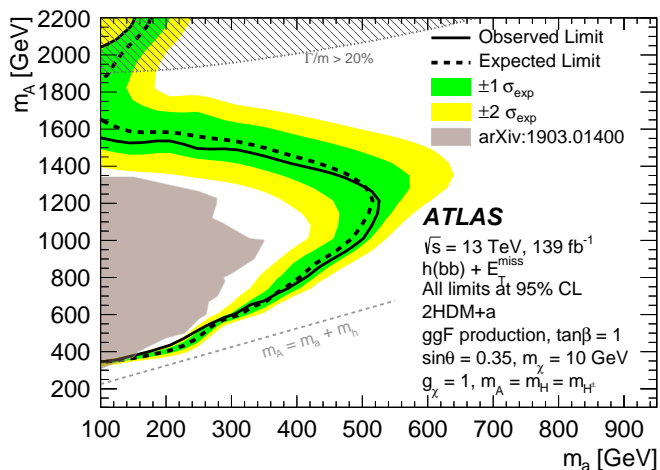


**Figure 12.12:** Observed and expected exclusion limits for the  $ggF$ -induced 2HDM+a signal grid.

For  $m_a$  lower than roughly 250 GeV and  $m_A$  higher than roughly 1700 GeV the exclusion limit becomes stronger again, due to the increase of the cross-section of the  $a \rightarrow ah$  process. Given the parameter choice this analysis, the coupling  $g_{aah}$  becomes higher than  $4\pi$ , for  $m_A \gtrsim 1750$  GeV. Also, according to Ref. [82],

for the potential of Eq. 3.15 to be bounded from below, given the parameter choices in this work (see Tab. 9.5), the values of  $m_A$  have to be  $\lesssim 1250$  GeV for  $\tan\beta = 1$ , and  $\lesssim 2150$  GeV for  $\tan\beta = 10$  [86, 82]. This constraint, however, can be relaxed by changing the values of the quadratic couplings to be closer to the perturbative limit, and as a result it does not affect the validity of the predictions.

The exclusion limits for high  $m_A$  masses, are not shown here, because the width of the additional Higgs-bosons, and the uncertainties associated with the treatment of the width on the theoretical predictions, grow substantially. Therefore, regions of very large widths ( $m_A > 2200$  GeV), are not shown.

The exclusion contours for  $b\bar{b}$ -induced 2HDM+a scenario are presented in Figure 12.13. The limits extend up to  $(m_A, m_a) = (900, 240)$  GeV. In this case, there is a difference between the observed and expected limit, reaching almost the edge of the  $2\sigma$  band. This difference is caused by a deficit in data in the Higgs candidate mass distribution, around 125 GeV, for the  $3b$ -tag category (see Fig. 12.11). Since the  $3b$ -tag category is only sensitive to the  $b\bar{b}$ -induced 2HDM+a model, the deficit does not affect the exclusion limits of the other models. The exclusion contours for the  $b\bar{b}$ -induced 2HDM+a model cover a smaller space in  $(m_A, m_a)$ , compared to the ggF-induced. This model has more contributions from a non-resonant production modes and therefore, a softer  $E_T^{\text{miss}}$  spectrum. This means that there are cases where the  $E_T^{\text{miss}}$  in the event will be lower than the trigger threshold, leading to an overall smaller signal acceptance. The 2HDM+a bb-

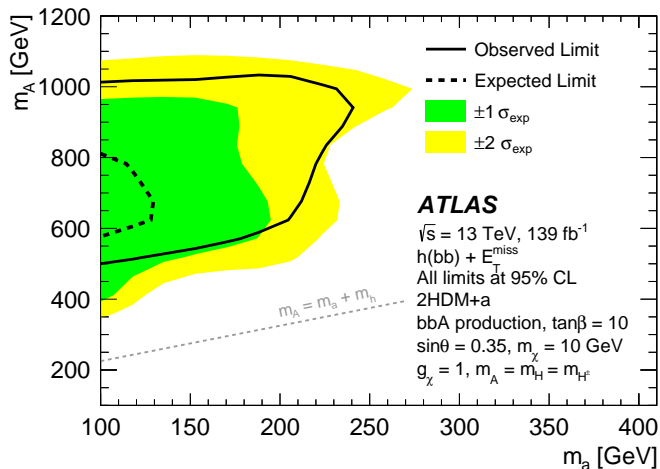


**Figure 12.13:** Observed and expected exclusion limits for the  $b\bar{b}$ -induced 2HDM+a signal grid [220].

induced scenario with  $\tan\beta = 10$  is considered for the first time for the Despite the smaller exclusion area, the limits shown in Fig 12.13, demonstrate that this search is sensitive to the  $b\bar{b}$ -induced 2HDM +  $a$  signals, and this is only due to including the  $3b$ -tag category.

Finally, the exclusion limits for the  $Z'$ -2HDM model are presented in Figure 12.14. The limit extends up to  $m_{Z'}$  of approximately 3 TeV, for  $m_A$  up to 300 GeV). The limit on  $m_A$  reaches and up to approximately 1 TeV for  $m_{Z'}$  up to 2 TeV.

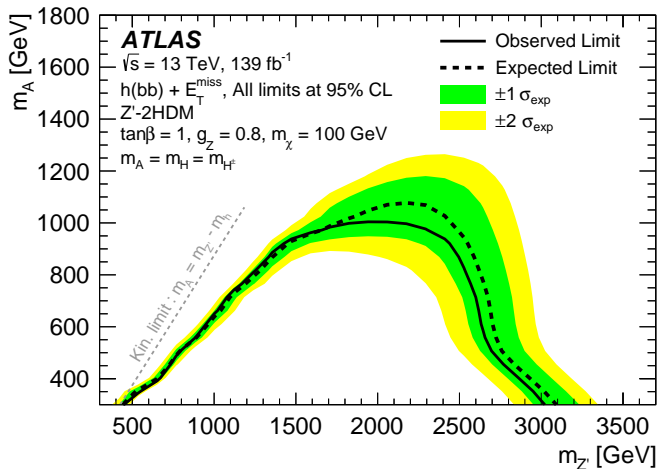


**Figure 12.14:** Observed upper limits on cross-sections for the  $Z'$ -2HDM with the new setup ( $m_H = m_{H^\pm} = m_A$ ) [220].

### 12.3.2 Model-independent limit

The last step is to interpret the results as exclusion limits on the production cross-section of events with a Higgs boson and Dark Matter particles. In this case, only a minimal assumption is necessary for the signal: a  $b\bar{b}$  resonance with mass close to  $m_H = 125$  GeV and is produced together with  $E_T^{\text{miss}}$ . For such an event to be observed the final state objects must end up inside the active volume of the detector and also be recorded, reconstructed, and pass all the kinematic and quality requirements set in the analysis. The visible cross section, which is a fraction of the total cross-section, is given by:

$$\sigma_{\text{vis},h(b\bar{b})+\text{DM}} \equiv \sigma_{h+\text{DM}} \times \mathcal{B}(h \rightarrow b\bar{b}) \times \mathcal{A} \times \varepsilon, \quad (12.1)$$

where  $\mathcal{A}$  is the kinematic acceptance and  $\varepsilon$  the experimental efficiency. Therefore, the term  $\mathcal{A} \times \varepsilon$  represents the probability an event to be reconstructed in a given signal region.

In order to extract the upper limit on the visible cross-section in each signal region, a fit is performed simultaneously to the signal and control regions. In this case, however, the  $m_{bb}$  bins within 90 GeV and 150 GeV are merged into a single bin. Furthermore, a "dummy" signal is injected with cross-section equal to 1 fb in the mass range [90, 150] GeV in each  $E_T^{\text{miss}}$  range and  $b$ -tag category. The signal strength is a floating parameter. Even though, all signal analysis bins and categories are included in the fit, the upper limits are determined for each one separately.

Figure 12.15 shows the upper limit on the visible production cross-section at 95% confidence level (CL) as a function of the  $E_T^{\text{miss}}$  for both  $b$ -tag categories considered in the fit. For the first  $E_T^{\text{miss}}$  met bin in the  $2b$ -tag category, the observed limit is very close to the edge of the  $+2\sigma$  band, due two small excesses in data at  $m_{jj} = 100$  and 125 GeV (Fig. 12.10). In the rest of the  $2b$ -tag category  $E_T^{\text{miss}}$  bins, there is good agreement between the expected and observed limit. For the  $\geq 3$   $b$ -tag category the observed limit is different from the expected (at the edge of the  $2\sigma$  band), due to the data deficit in this region around the peak of the Higgs boson mass (Figure 12.11).

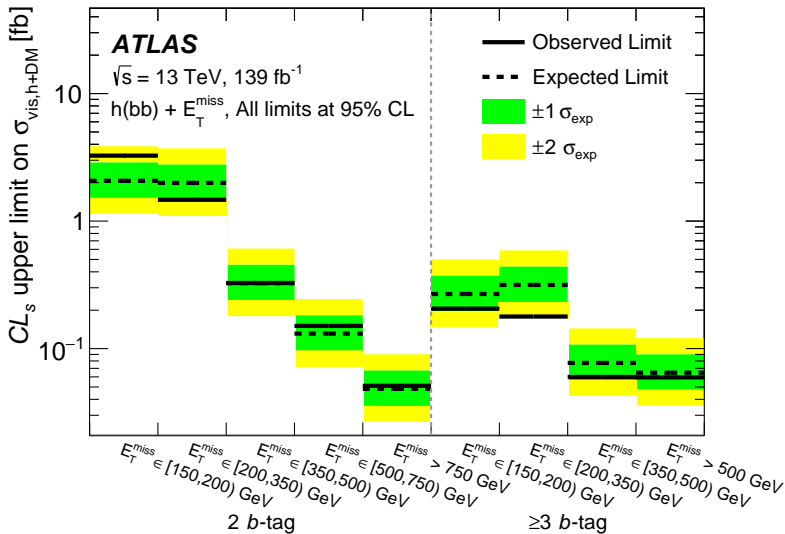


**Figure 12.15:** Observed and expected upper limits at 95% CL on  $\sigma_{\text{vis},h(bb)+\text{DM}} \equiv \sigma_{h+\text{DM}} \times \mathcal{B}(h \rightarrow b\bar{b}) \times \mathcal{A} \times \varepsilon$  of  $h(b\bar{b})$  [220].



## Chapter 13

# Reinterpretation of the MonoH(bb) analysis with RECAST

Even though searches for new physics, such as the one presented in this work, are designed and optimised around specific models, they are often sensitive to alternative theory models. At the same time, there is a plethora of BSM models, and it is difficult to test them all with dedicated searches due to the significant investment of time, human and computational resources needed. In addition to extending the impact of existing searches, reinterpretations provide insight into the design and development of new analyses for dedicated searches. Therefore, it is preferable to reinterpret, when possible, existing analyses before designing a new one.

The work presented in this section is the reinterpretation of the  $E_T^{\text{miss}} + H(b\bar{b})$  analysis in the context of the Dark Higgs model introduced in Sec. 3.5.2. The reinterpretation is performed with the RECAST framework [221], which is briefly introduced in Section 13.1. The RECAST framework uses the data, background and systematic uncertainties estimated from preserved searches to test alternative signal hypotheses. Section 13.2 discusses the manner in which the  $E_T^{\text{miss}} + H(b\bar{b})$  analysis software, and workflow are preserved. Section 13.3.1 contains the parameter configuration used to produce the dark Higgs simulations and Section 13.3.2 presents the results of the reinterpretation.

## 13.1 RECAST

The purpose of RECAST [221], is to organise the systematic interpretation of searches in High Energy Physics in the context of alternative models. The goal is to allow people, even outside the original experiment collaboration, to request a reinterpretation study for a new model. It should be noted here that one of the framework’s goals is to allow a faithful reinterpretation of the analysis, i.e. a reinterpretation that will use the original code developed within the experiment.

The idea, described in Ref. [221] and roughly illustrated in Figure 13.1, is to create a front-end to collect requests, present a list of existing analyses and collect any ready results from accepted and finished requests. Then an application programming interface (A.P.I) connects the front-end to the back-end of the framework that performs the “actual work”. The back-end executes a series of

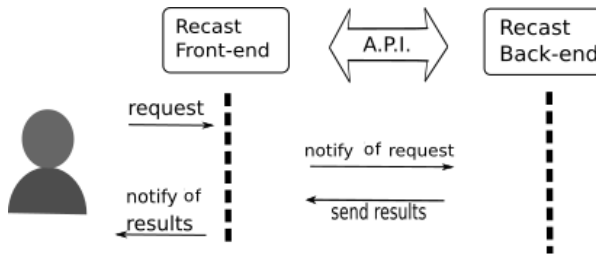


**Figure 13.1:** Illustration of the Recast framework. The diagram outlines the main framework components, the front-end, API and back-end and the interactions between them, time ordered from top to bottom.

processing steps. The first steps prepare the new signal inputs to be run by the analysis code. These steps include running the event generation, detector simulation and reconstruction. The remaining steps run the preserved analysis software to produce limits on the signal strength. These processing steps executed in a specific order comprise the so-called *analysis workflow*. The way that the analysis software and workflow are preserved is explained in the next section.

## 13.2 Analysis Preservation using containerised workflows

The software is preserved in the form of Linux Container images [222] using Docker [223]. The images package the software and any component necessary to run it, such as system tools, environment variables, libraries, dependencies

or files, creating a "snapshot" of the system. This preservation method allows running applications from one operating system to another quickly and safely, since the hosting system limits the physical resources a single container can use.

The  $E_T^{\text{miss}} + H(b\bar{b})$  analysis uses two different software frameworks. The first takes as input DxAOD files and applies the full analysis event selection. This software creates the inputs for the second, which performs the statistical evaluation. Both frameworks were developed using GitLab [224], a manager for Git repositories, and the Continuous Integration (CI) feature, which automatically creates (builds) the Docker images.

The analysis processing steps, i.e the commands to run the software and the order they should be executed are captured in parameterised scripts. This means that the command cannot be altered, but the script can be executed by providing input through a designated interface. A *workflow description language* is used to describe the processing steps and execute them in the correct order which is called *workflow structure*. Out of the many available languages, in this case, `yadage` [225] was used. Within `yadage` the workflow structure and the parametrised scripts are captured in YAML documents [226].

An example of such a parametrised script, using YAML documents is shown in Figure 13.2. In this example the input parameters are the DxAOD file ("in-

```
eventselection:
  process:
    process_type: 'interpolated-script-cmd'
    interpreter: bash
    script: |
      source /recast_auth/getkrb.sh
      source /home/atlas/release_setup.sh
      cd /xampp/XAMPPmonoH
      source XAMPPmonoH/recast/recast_step1_runXAMPPmonoH.sh {input_mc} {dsid} {nEvents}
      sudo rm -f {outputfile}
      sudo cp /xampp/XAMPPmonoH/output_recast/recast_signal_ntuple.root {outputfile}
      echo 'Script done'
  publisher:
    publisher_type: interpolated-pub
    publish:
      selected_signal_mc16: '{outputfile}'
    glob: true
  environment:
    environment_type: 'docker-encapsulated'
    image: gitlab-registry.cern.ch/atlas-mpp-xampp/xamppmonoH
    imagetag: recastScriptsUpdate-c5995b31
    resources:
      - GRIDProxy
```

**Figure 13.2:** Example of step definition. This step is running the framework that applies the event selection. Inside the curly brackets are the parameters the user has to define for this script.

put\_mc”), a unique code assigned to each simulated process by the collaboration

(“DSID”), and the number of events that should be included (“nEvents”). The later is used to limit the number of events in case quick cross-checks are needed. The output is the file called “recast\_signal\_ntuple.root”, and contains the event that pass the selection requirements.

Three such step are defined in total. Besides the one shown in Figure 13.2, there is one step to produce the inputs for the statistical analysis, and one to run the statistical analysis framework. There is one difference with the statistical analysis explained in Sec. 8.3: there are no nuisance parameters in the likelihood for the uncertainties associated with the signal modelling. However, these uncertainties, usually have a small impact on the estimated signal strength. For the  $E_T^{\text{miss}} + H(b\bar{b})$  analysis, Table 12.5, shows that for the three representative signal simulations the impact on the signal strength of the theoretical uncertainties associated with the signal modelling is less than 1%.

The processing steps have to be executed in the correct order. Additionally, some of them have to be executed more than once, while the step that runs the statistical analysis framework depends on the successful execution of previous steps. To schedule their executions we need to define the order in which the steps are processed and their dependencies using a so-called “*directed acrylic graph*”. In such graphs the nodes represent single tasks and the edges denote the dependencies between them. A generic example is shown in Figure 13.3. Here, processing steps B.1 and B.2 depend on the output of step Am and step C depends on the successful execution of B.1 and B.2 and A.

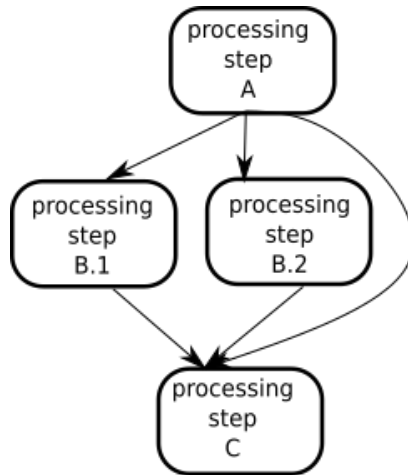


**Figure 13.3:** Example of an abstract acrylic graph. The nodes represent single tasks and the edges denote the dependencies between them.

The corresponding graph for the workflow of the  $E_T^{\text{miss}} + H(b\bar{b})$  analysis is shown

13.4. The three first steps are a repetition of the step shown in Figure 13.2, each is using as input DxAOD files from each campaign (MC16 a,d,e) and run independently from each other and simultaneously. The next step collects the output of the first three steps and creates the inputs for the statistical analysis. The last step is the one running the statistical analysis.

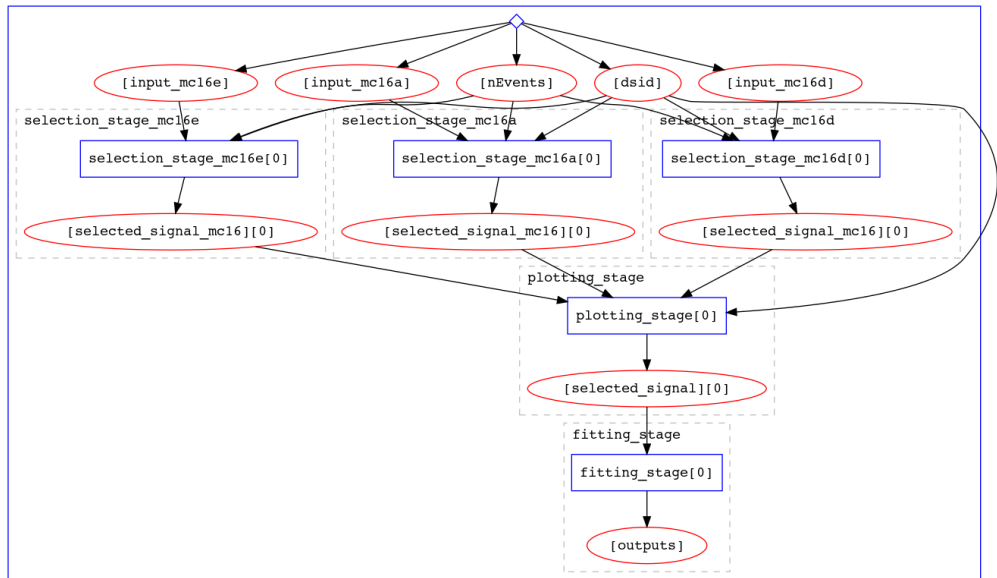


**Figure 13.4:** Workflow DAG for the  $E_T^{\text{miss}} + H(b\bar{b})$  analysis, created with yadage. The red oval-shaped nodes represent the input/output for each step. The blue rectangular nodes show the processing task and the arrows show the dependencies.

### 13.3 Analysis reinterpretation

In this section the preserved workflow and the archived data from the main analysis are used to reinterpret the results. The first step is to generate simulated events using the parameter configuration described in 13.3.1. These sets of simulated events are the inputs to the workflow, which is executed in a dedicated platform for reusable analysis, called *REANA* [227]. The workflow performs a profile likelihood fit simultaneously in all signal and control regions using the alternative dark Higgs hypothesis. In 13.3.2 the results are presented in the form of exclusion limits for the parameter space of the model.

### 13.3.1 Signal simulation

The parameters used to generate the signal samples are shown in Table 13.1. The dark matter mass is set to 200 GeV. The parameter values for  $\theta$ ,  $g_q$  and  $g_\chi$ , follow the choices made in Ref. [228] and the coupling choices for vector mediator simplified model searches at the LHC [198, 229] respectively.

$g_q$	0.25
$g_\chi$	1
$\theta$	0.01
$m_\chi$	200 GeV

**Table 13.1:** Parameter configuration for the simulated samples.

Samples are generated for a grid of  $m_{Z'}$  and  $m_s$  values. The range for  $m_{Z'}$  extends from 500 GeV to 3500 GeV in steps of 500 GeV and for the dark Higgs boson  $m_s$  from 50 GeV to 150 GeV in 20 GeV steps.

The matrix element calculation was performed at leading order with MADGRAPH5\_aMC@NLO 2.6.2 (ATLAS, LCG) [104]. For the modelling of the parton shower and the hadronization, the events are interfaced with PYTHIA 8.230 [201]. The matrix element and parton shower matching and merging is done with the CKKW-L procedure [98, 230] with the matching scale set to 40 GeV. NNPDF3.0 PDF set is used with  $\alpha_S = 0.13$  [95] and the A14 set of tuned parameters. The renormalisation and factorisation scales are set to the MADGRAPH5\_aMC@NLO default values. The EVTGENv1.2.0 program [207] is used to simulate the decays of the bottom and charm hadron. The effect of pile-up interactions is taken into account with overlaying additional inelastic pp collision events are simulated using Pythia 8, with the A3 tune [231] and the NNPDF2.3LO PDF set [199]. The simulated events are weighted to match the pile-up observed in data. For the simulation of the ATLAS detector Geant 4 [166, 232] is used.

### 13.3.2 Reinterpretation results

The analysis workflow was re-executed in the Reusable Analysis Platform (REANA) [227], which is part of a developing CERN infrastructure. The results of the  $E_T^{\text{miss}} + H(bb)$  search, presented in Sec. 12.1 showed that the observed data is compatible with the SM expectations, and no significant excess has been observed. Selected histograms of the invariant mass of the Higgs-boson boson candidate, reproduced using the RECAST implementation of the analysis are shown in Figure 13.5. One signal point with  $m_s = 90$  GeV and  $m_{Z'} = 1000$  TeV

is displayed on the plots. The distributions, as expected, they are identical to those shown in 12.1.3, which illustrates that this is a faithful interpretation of the original analysis.

Figures 13.6a and 13.6b show the expected and observed upper limits on the signal strength of the dark Higgs model. The mass of the  $Z'$  mediator is placed on the  $x$ -axis and the mass of the dark Higgs boson  $m_s$  is on the  $y$ -axis. Any parameter combination with signal strength higher than one is excluded at 95% CL.

In Figure 13.7 the limits are presented as a contour instead. The black solid line shows the observed limit, the dashed line shows the observed limit and the green and yellow bands the  $\pm 1\sigma$  and  $\pm 2\sigma$  uncertainty on the expected limit, respectively. The region to the left of the observed line is excluded at 95% CL. The expected exclusion limit shows that the sensitivity for  $m_s < 70$  GeV is reduced, especially for  $m_s$  values close to 50 GeV.

This is caused by the requirement in the original analysis on the invariant mass of the Higgs candidate, which must be higher 50 GeV. In this case a large fraction of the events from the signal points with  $m_s = 50$  will not pass this requirement, and therefore the sensitivity of the analysis is reduced for this model. Additionally, the sensitivity decreases for  $m_s > 130$  GeV, because the branching ratio for the  $s \rightarrow b\bar{b}$  decreases. The observed exclusion extends up to 3.2 TeV in mediator mass. Finally, the purple dotted line, shows the region of the dark Higgs models parameter space which is compatible with the dark matter relic density measurements performed by the PLANCK collaboration [34]. All the signal points to the right of this line correspond to predicted relic densities higher than these measurements.

## Conclusions

This study demonstrated the sensitivity of the  $E_T^{\text{miss}} + H(b\bar{b})$  analysis to an alternative signal hypothesis, in which a dark Higgs boson is produced and decays to a pair of  $b$ -quarks. Compared to the time and resources necessary for a dedicated analysis the reinterpretation is significantly faster: the estimation of the exclusion limits, once the analysis workflow and software were preserved, took few weeks. However, the exclusion limits of the reinterpretation cannot “compete” with the results of the dedicated analysis, as we saw in Figure 12.12, where the result of reinterpreting an older  $E_T^{\text{miss}} + H(b\bar{b})$  analysis performed with  $36 \text{ fb}^{-1}$  [233] was included. Even though the reinterpretation cannot provide exclusion limits as those of a dedicated analysis, it is still able to exclude a

substantial parameter-space.

At the time the reinterpretations study presented in this section was performed the only available simulated samples, were those described in Section 13.3.1, which as it is later explained in the discussion of the limits correspond to relic densities higher than the measurements performed by the PLANCK collaboration. With the analysis fully implemented in the RECAST framework, the next step would be to produce inputs for the workflow that extend the parameter scan for this model.

These initial studies provided insight to a dedicated search for  $s \rightarrow b\bar{b}$ . The analysis for this search is currently under development, within the ATLAS collaboration. Additionally, this was the first workflow fully implemented and tested in the REANA platform, and influenced other groups to implement their analysis workflow in the same platform.

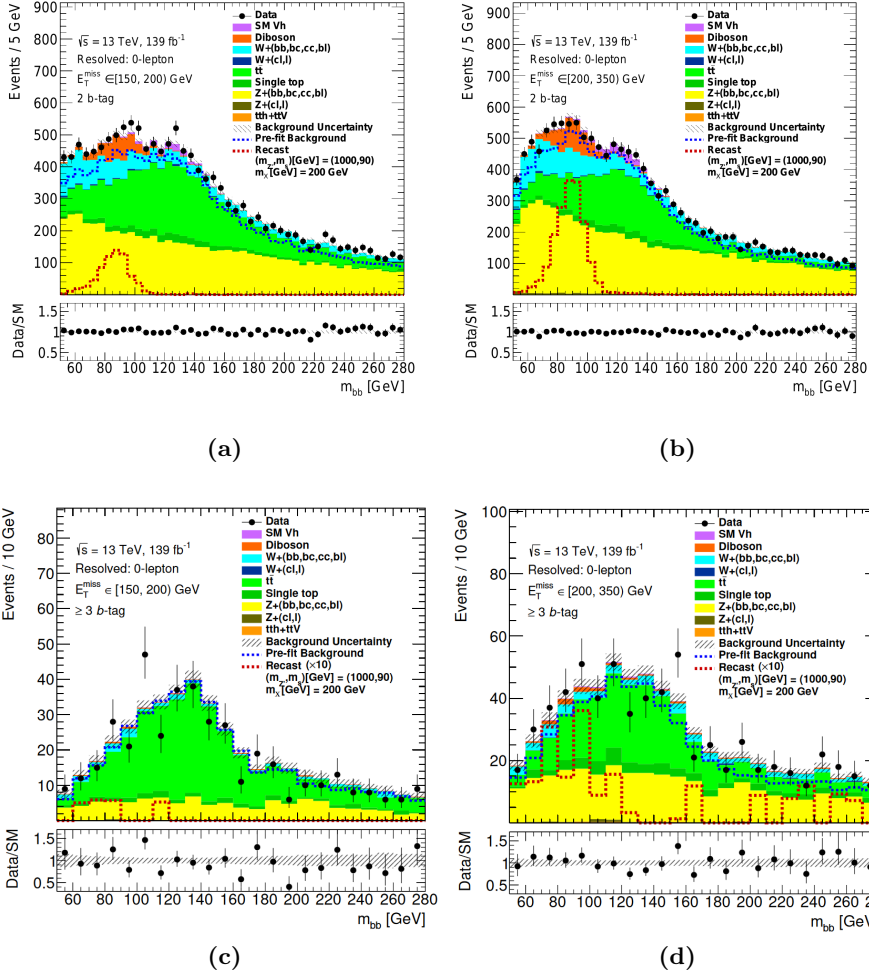


**Figure 13.5:** Distributions of the invariant mass of the Dark Higgs candidate for events in the signal region with two  $b$ -jets(top) and  $\geq 3b$ -jets (bottom) in the two first  $E_T^{\text{miss}}$  bins of the resolved SR. The invariant mass from a representative signal point with  $m_{Z'} = 1400$  GeV and  $m_s = 90$  GeV with cross-section  $\sigma = 356$  fb, is overlaid (red dashed line). The signal in the  $\geq 3b$ -jets category is multiplied by 10 for visualisation.

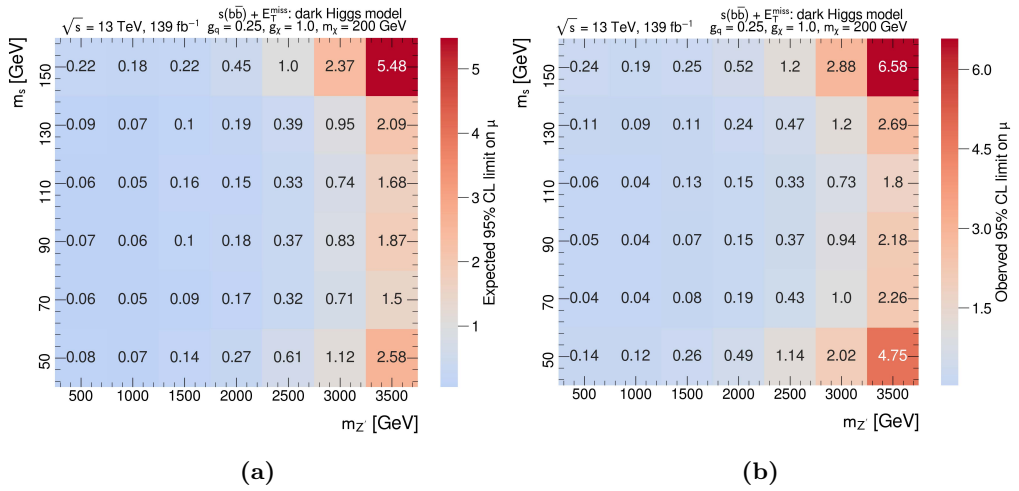


**Figure 13.6:** Upper limits on the signal strength  $\mu$  at 95% signal strength. The plot on the left shows the expected exclusion limits, while the right the observed.

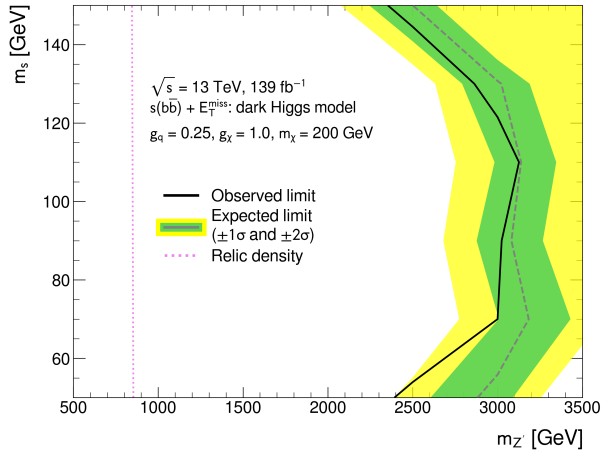


**Figure 13.7:** Exclusion limit contour for the dark Higgs Model with  $g_q=0.2$   $g_\chi=1$   $\theta = 0.01$   $m_\chi = 200 \text{ GeV}$ . The black solid line shows the observed limit, the dashed line shows the observed limit and the green and yellow bands the  $\pm\sigma$  and  $\pm 2\sigma$  uncertainty on the expected limit respectively. The pink curve indicates the points in  $(m'_Z, m_z)$  for which the relic density is consistent to the one predicted by the PLANCK [34] measurement.

# Chapter 14

## Conclusion

The Standard Model of particle physics describes the fundamental constituents of nature and their interactions. Its predictions have been tested for decades and were found to describe the data from collider experiments with remarkable precision. The theory, however, has several limitations. Among others, it does not describe gravity, predict masses for the neutrinos nor explain several other phenomena, like the existence of Dark Matter. Several observations, mostly of gravitational phenomena in a wide range of scales, cannot be explained without assuming the existence of a non-luminous non-baryonic form of matter, which interacts very weakly with ordinary matter. These observations and the study of structure formation of the Universe put constraints on the nature of a possible DM particle candidate: the new particle has to be neutral, stable, and yield the observed DM relic density. Many BSM theories predict Weakly interactive massive particles (WIMPs) as candidates for Dark Matter. Searches for WIMP DM inside collider experiments became increasingly popular in the past decade. A very common signature for Dark matter search at colliders is events with large deficits in the transverse momentum, known as  $E_T^{\text{miss}} + X$  signature.

This thesis presented a search for Dark matter produced together with a Higgs boson that decays into a pair of b-quarks. The analysis used data from proton-proton collisions recorded with the ATLAS detector from 2015 to 2018, that corresponded to an integrated luminosity of  $139 \text{ fb}^{-1}$ .

The event selection was based on the key features of the signature, which are: large  $E_T^{\text{miss}}$ , due to DM escaping detection, the presence of two  $b$ -jets, from the Higgs decay, and the absence of leptons.

For signal events the missing transverse momentum in the event is correlated with the transverse momentum of the Higgs boson candidate, which means that

the Higgs boson will be highly boosted in events with high  $E_T^{\text{miss}}$ . At the same time, as the boost of the Higgs boson increases, its decay products, the two  $b$ -jets, will become collimated. As a result, the analysis considered two distinct topologies, separated by a  $E_T^{\text{miss}}$  threshold. The analysis used events that contained leptons to define dedicated control regions to constrain the dominant Standard Model backgrounds, which are  $t\bar{t}, W + \text{jets}$  and  $Z + \text{jets}$  processes.

To interpret the results two benchmark models were considered in this analysis: the  $Z'$ -2HDM model and the 2HDM+ $a$  model. The  $Z'$ -2HDM predicts a highly boosted Higgs signature, while the 2HDM +  $a$  events present in general a much softer  $E_T^{\text{miss}}$  spectrum. Two production mechanisms were relevant for this analysis for the 2HDM+ $a$  model. In one  $A$  was produced via gluon-gluon fusion ( $ggF$ -induced) and the other from the annihilation of a  $b\bar{b}$  pair. To gain sensitivity to the later the analysis considered also signal events with three or more  $b$ -jets in the final state.

A profile likelihood fit was performed simultaneously in all analysis regions to extract possible signals and estimate the background normalization factors. The main fit discriminant in the signal regions was the mass of the Higgs boson candidate,  $m_h$ . Since the benchmark models produce very different  $E_T^{\text{miss}}$  spectra, the  $m_h$  distribution was fitted in multiple ranges of  $E_T^{\text{miss}}$ , to ensure a good sensitivity to all signals.

Since no deviation from the Standard Model expectations was observed, the analysis produced exclusion limits for the two benchmark models. The analysis also interprets the results as exclusion limits on the visible production cross-section of events with a Higgs boson and Dark Matter particles.

This thesis presented the preservation of the  $E_T^{\text{miss}} + H(b\bar{b})$  analysis in the RECAST framework and a reinterpretation study performed in the REANA platform. This study provided insights to a dedicated  $E_T^{\text{miss}} + \text{dark Higgs}$  analysis, and influence other groups within ATLAS collaboration to use this platform for reinterpretations, since it was the first implemented workflow.

In addition to the search for Dark Matter, this thesis presented studies related to the performance of the drift time calibration of the ATLAS Transition Radiation Tracker. Part of the work was to perform a calibration, using simulations with updated signal shaping and lower threshold value for the straw tubes filled with Ar-based gas. Finally, the dependence of the calibration parameters on the  $p_T$  of the reconstructed tracks and pile-up was studied.

# Chapter 15

## References

- [1] J H Oort. The force exerted by the stellar system in the direction perpendicular to the galactic plane and some related problems. *Bull. Astron. Inst. Netherlands*, 6:249–287, 1932.
- [2] F. Zwicky. Die Rotverschiebung von extragalaktischen Nebeln. *Helv. Phys. Acta*, 6:110–127, 1933.
- [3] Mark Thomson. *Modern particle physics*. Cambridge University Press, New York, 2013.
- [4] Michael E. Peskin. *Concepts of Elementary Particle Physics*. Oxford Master Series in Physics. Oxford University Press, 2019.
- [5] Michael E. Peskin and Daniel V. Schroeder. *An Introduction to quantum field theory*. Addison-Wesley, Reading, USA, 1995.
- [6] Jean Iliopoulos. Introduction to the Standard Model of the Electro-Weak Interactions. In *8th CERN–Latin-American School of High-Energy Physics*, pages 1–30, 2014.
- [7] Guido Altarelli. Collider Physics within the Standard Model: a Primer. 3 2013.
- [8] Antonio Pich. The Standard Model of Electroweak Interactions. In *2010 European School of High Energy Physics*, 1 2012.
- [9] P. A. Zyla et al. Review of Particle Physics. *PTEP*, 2020(8):083C01, 2020.
- [10] Carsten Burgard. Example: Standard model of physics, 2016.

- [11] M. Tanabashi et al. Review of Particle Physics. *Phys. Rev. D*, 98(3):030001, 2018.
- [12] Jeffrey Goldstone, Abdus Salam, and Steven Weinberg. Broken symmetries. *Phys. Rev.*, 127:965–970, Aug 1962.
- [13] Makoto Kobayashi and Toshihide Maskawa. CP-Violation in the Renormalizable Theory of Weak Interaction. *Progress of Theoretical Physics*, 49(2):652–657, 02 1973.
- [14] S. L. Glashow. Partial Symmetries of Weak Interactions. *Nucl. Phys.*, 22:579–588, 1961.
- [15] Steven Weinberg. A Model of Leptons. *Phys. Rev. Lett.*, 19:1264–1266, 1967.
- [16] M. Gell-Mann. The interpretation of the new particles as displaced charge multiplets. *Nuovo Cim.*, 4(S2):848–866, 1956.
- [17] T. Nakano and K. Nishijima. Charge Independence for V-particles. *Prog. Theor. Phys.*, 10:581–582, 1953.
- [18] S. Dittmaier et al. Handbook of LHC Higgs Cross Sections: 1. Inclusive Observables. 1 2011.
- [19] Georges Aad et al. Observation of a new particle in the search for the Standard Model Higgs boson with the ATLAS detector at the LHC. *Phys. Lett. B*, 716:1–29, 2012.
- [20] Serguei Chatrchyan et al. Observation of a New Boson at a Mass of 125 GeV with the CMS Experiment at the LHC. *Phys. Lett. B*, 716:30–61, 2012.
- [21] Morad Aaboud et al. Observation of  $H \rightarrow b\bar{b}$  decays and  $VH$  production with the ATLAS detector. *Phys. Lett. B*, 786:59–86, 2018.
- [22] A. M. Sirunyan et al. Observation of Higgs boson decay to bottom quarks. *Phys. Rev. Lett.*, 121(12):121801, 2018.
- [23] M. Aker et al. Improved Upper Limit on the Neutrino Mass from a Direct Kinematic Method by KATRIN. *Phys. Rev. Lett.*, 123(22):221802, 2019.
- [24] Gianfranco Bertone, Dan Hooper, and Joseph Silk. Particle dark matter: evidence, candidates and constraints. *Physics Reports*, 405(5–6):279–390, Jan 2005.

- [25] Marco Taoso, Gianfranco Bertone, and Antonio Masiero. Dark Matter Candidates: A Ten-Point Test. *JCAP*, 03:022, 2008.
- [26] A. Friedman. On the Curvature of space. *Z. Phys.*, 10:377–386, 1922.
- [27] N. Aghanim et al. Planck 2018 results. *Astronomy & Astrophysics*, 641:A6, Sep 2020.
- [28] Lars Bergström. Non-baryonic dark matter: observational evidence and detection methods. *Reports on Progress in Physics*, 63(5):793–841, Apr 2000.
- [29] Edward W. Kolb and Michael S. Turner. *The Early Universe*, volume 69. 1990.
- [30] K. G. Begeman, A. H. Broeils, and R. H. Sanders. Extended rotation curves of spiral galaxies: Dark haloes and modified dynamics. *Mon. Not. Roy. Astron. Soc.*, 249:523, 1991.
- [31] Douglas Clowe, Maruša Bradač, Anthony H. Gonzalez, Maxim Markevitch, Scott W. Randall, Christine Jones, and Dennis Zaritsky. A direct empirical proof of the existence of dark matter. *The Astrophysical Journal*, 648(2):L109–L113, Aug 2006.
- [32] P. A. R. Ade et al. Planck2013 results. i. overview of products and scientific results. *Astronomy & Astrophysics*, 571:A1, Oct 2014.
- [33] N. Aghanim et al. Planck 2018 results. I. Overview and the cosmological legacy of Planck. *Astron. Astrophys.*, 641:A1, 2020.
- [34] N. Aghanim et al. Planck 2018 results. VI. Cosmological parameters. *Astron. Astrophys.*, 641:A6, 2020. [Erratum: *Astron. Astrophys.* 652, C4 (2021)].
- [35] Arthur Loureiro et al. On The Upper Bound of Neutrino Masses from Combined Cosmological Observations and Particle Physics Experiments. *Phys. Rev. Lett.*, 123(8):081301, 2019.
- [36] Scott Dodelson and Lawrence M. Widrow. Sterile-neutrinos as dark matter. *Phys. Rev. Lett.*, 72:17–20, 1994.
- [37] A. Boyarsky, M. Drewes, T. Lasserre, S. Mertens, and O. Ruchayskiy. Sterile neutrino Dark Matter. *Prog. Part. Nucl. Phys.*, 104:1–45, 2019.
- [38] R. D. Peccei and Helen R. Quinn. CP Conservation in the Presence of Instantons. *Phys. Rev. Lett.*, 38:1440–1443, 1977.

- [39] Steven Weinberg. A new light boson? *Phys. Rev. Lett.*, 40:223–226, Jan 1978.
- [40] F. Wilczek. Problem of strong  $p$  and  $t$  invariance in the presence of instantons. *Phys. Rev. Lett.*, 40:279–282, Jan 1978.
- [41] Kim Griest and Marc Kamionkowski. Unitarity Limits on the Mass and Radius of Dark Matter Particles. *Phys. Rev. Lett.*, 64:615, 1990.
- [42] Oliver Buchmueller, Caterina Doglioni, and Lian Tao Wang. Search for dark matter at colliders. *Nature Phys.*, 13(3):217–223, 2017.
- [43] Marc Schumann. Direct Detection of WIMP Dark Matter: Concepts and Status. *J. Phys. G*, 46(10):103003, 2019.
- [44] Elena Aprile. The XENON1T Dark Matter Search Experiment. *Springer Proc. Phys.*, 148:93–96, 2013.
- [45] D. S. Akerib et al. The Large Underground Xenon (LUX) Experiment. *Nucl. Instrum. Meth. A*, 704:111–126, 2013.
- [46] Andi Tan et al. Dark Matter Results from First 98.7 Days of Data from the PandaX-II Experiment. *Phys. Rev. Lett.*, 117(12):121303, 2016.
- [47] P. A. Amaudruz et al. First results from the DEAP-3600 dark matter search with argon at SNOLAB. *Phys. Rev. Lett.*, 121(7):071801, 2018.
- [48] P. Agnes et al. DarkSide-50 532-day Dark Matter Search with Low-Radioactivity Argon. *Phys. Rev. D*, 98(10):102006, 2018.
- [49] A. H. Abdelhameed et al. First results from the CRESST-III low-mass dark matter program. *Phys. Rev. D*, 100(10):102002, 2019.
- [50] R. Agnese et al. Results from the Super Cryogenic Dark Matter Search Experiment at Soudan. *Phys. Rev. Lett.*, 120(6):061802, 2018.
- [51] R. Agnese et al. Search for Low-Mass Dark Matter with CDMSlite Using a Profile Likelihood Fit. *Phys. Rev. D*, 99(6):062001, 2019.
- [52] R. Bernabei et al. First model independent results from DAMA/LIBRA-phase2. *Nucl. Phys. Atom. Energy*, 19(4):307–325, 2018.
- [53] Jianguai Liu, Xun Chen, and Xiangdong Ji. Current status of direct dark matter detection experiments. *Nature Phys.*, 13(3):212–216, 2017.
- [54] M. G. Aartsen et al. Search for dark matter annihilations in the Sun with the 79-string IceCube detector. *Phys. Rev. Lett.*, 110(13):131302, 2013.

- [55] W. B. Atwood et al. The large area telescope on the fermi gamma-ray space telescope mission. *The Astrophysical Journal*, 697(2):1071–1102, may 2009.
- [56] F. Aharonian et al. H.E.S.S. observations of the Galactic Center region and their possible dark matter interpretation. *Phys. Rev. Lett.*, 97:221102, 2006. [Erratum: Phys.Rev.Lett. 97, 249901 (2006)].
- [57] J. Aleksić et al. The major upgrade of the MAGIC telescopes, part i: The hardware improvements and the commissioning of the system. *Astroparticle Physics*, 72:61–75, jan 2016.
- [58] S. Archambault et al. Dark Matter Constraints from a Joint Analysis of Dwarf Spheroidal Galaxy Observations with VERITAS. *Phys. Rev. D*, 95(8):082001, 2017.
- [59] A. U. Abeysekara et al. A Search for Dark Matter in the Galactic Halo with HAWC. *JCAP*, 02:049, 2018.
- [60] Dan Hooper and Lisa Goodenough. Dark Matter Annihilation in The Galactic Center As Seen by the Fermi Gamma Ray Space Telescope. *Phys. Lett. B*, 697:412–428, 2011.
- [61] Christopher Karwin, Simona Murgia, Tim M. P. Tait, Troy A. Porter, and Philip Tanedo. Dark Matter Interpretation of the Fermi-LAT Observation Toward the Galactic Center. *Phys. Rev. D*, 95(10):103005, 2017.
- [62] Wim de Boer, Léo Bosse, Iris Gebauer, Alexander Neumann, and Peter L. Biermann. Molecular clouds as origin of the Fermi gamma-ray GeV excess. *Phys. Rev. D*, 96(4):043012, 2017.
- [63] Andrei Kounine. The Latest Results from the Alpha Magnetic Spectrometer. *PoS*, EPS-HEP2019:028, 2020.
- [64] Carlos Pérez de los Heros. Status of direct and indirect dark matter searches. *PoS*, EPS-HEP2019:694, 2020.
- [65] Georges Aad et al. Search for new phenomena in events with an energetic jet and missing transverse momentum in  $pp$  collisions at  $\sqrt{s} = 13$  TeV with the ATLAS detector. *Phys. Rev. D*, 103(11):112006, 2021.
- [66] Armen Tumasyan et al. Search for new particles in events with energetic jets and large missing transverse momentum in proton-proton collisions at  $\sqrt{s} = 13$  TeV. *JHEP*, 11:153, 2021.

- [67] Search for associated production of a  $Z$  boson with an invisibly decaying Higgs boson or dark matter candidates at  $\sqrt{s} = 13$  TeV with the ATLAS detector. Technical report, CERN, Geneva, Jul 2021.
- [68] Albert M Sirunyan et al. Search for dark matter produced in association with a leptonically decaying  $Z$  boson in proton-proton collisions at  $\sqrt{s} = 13$  TeV. *Eur. Phys. J. C*, 81(1):13, 2021. [Erratum: *Eur.Phys.J.C* 81, 333 (2021)].
- [69] M. Aaboud et al. Search for dark matter in events with a hadronically decaying vector boson and missing transverse momentum in  $pp$  collisions at  $\sqrt{s} = 13$  TeV with the ATLAS detector. *JHEP*, 10:180, 2018.
- [70] Albert M Sirunyan et al. Search for dark matter produced with an energetic jet or a hadronically decaying  $W$  or  $Z$  boson at  $\sqrt{s} = 13$  TeV. *JHEP*, 07:014, 2017.
- [71] Georges Aad et al. Search for dark matter in association with an energetic photon in  $pp$  collisions at  $\sqrt{s} = 13$  TeV with the ATLAS detector. *JHEP*, 02:226, 2021.
- [72] Albert M Sirunyan et al. Search for new physics in final states with a single photon and missing transverse momentum in proton-proton collisions at  $\sqrt{s} = 13$  TeV. *JHEP*, 02:074, 2019.
- [73] Georges Aad et al. Search for dark matter in events with missing transverse momentum and a Higgs boson decaying into two photons in  $pp$  collisions at  $\sqrt{s} = 13$  TeV with the ATLAS detector. *JHEP*, 10:013, 2021.
- [74] Georges Aad et al. Search for new resonances in mass distributions of jet pairs using  $139 \text{ fb}^{-1}$  of  $pp$  collisions at  $\sqrt{s} = 13$  TeV with the ATLAS detector. *JHEP*, 03:145, 2020.
- [75] Albert M Sirunyan et al. Search for high mass dijet resonances with a new background prediction method in proton-proton collisions at  $\sqrt{s} = 13$  TeV. *JHEP*, 05:033, 2020.
- [76] Georges Aad et al. Search for high-mass dilepton resonances using  $139 \text{ fb}^{-1}$  of  $pp$  collision data collected at  $\sqrt{s} = 13$  TeV with the ATLAS detector. *Phys. Lett. B*, 796:68–87, 2019.
- [77] Vardan Khachatryan et al. Search for narrow resonances in dilepton mass spectra in proton-proton collisions at  $\sqrt{s} = 13$  TeV and combination with 8 TeV data. *Phys. Lett. B*, 768:57–80, 2017.

- [78] John F. Gunion, Howard E. Haber, Gordon L. Kane, and Sally Dawson. *The Higgs Hunter's Guide*, volume 80. 2000.
- [79] M. M. Mühlleitner. Lecture notes: Beyond the standard model physics, February 2015.
- [80] G. C. Branco, P. M. Ferreira, L. Lavoura, M. N. Rebelo, Marc Sher, and Joao P. Silva. Theory and phenomenology of two-Higgs-doublet models. *Phys. Rept.*, 516:1–102, 2012.
- [81] Georges Aad et al. Combined measurements of Higgs boson production and decay using up to 80 fb<sup>-1</sup> of proton-proton collision data at  $\sqrt{s} = 13$  TeV collected with the ATLAS experiment. *Phys. Rev. D*, 101(1):012002, 2020.
- [82] Tomohiro Abe et al. LHC Dark Matter Working Group: Next-generation spin-0 dark matter models. *Phys. Dark Univ.*, 27:100351, 2020.
- [83] M. Aaboud, G. Aad, B. Abbott, D. C. Abbott, O. Abdinov, D. K. Abhayasinghe, S. H. Abidi, O. S. AbouZeid, N. L. Abraham, and et al. Constraints on mediator-based dark matter and scalar dark energy models using  $\sqrt{s} = 13$  tev pp collision data collected by the atlas detector. *Journal of High Energy Physics*, 2019(5), May 2019.
- [84] Tilman Plehn. Lectures on LHC Physics. *Lect. Notes Phys.*, 844:1–193, 2012.
- [85] Asher Berlin, Tongyan Lin, and Lian-Tao Wang. Mono-Higgs Detection of Dark Matter at the LHC. *JHEP*, 06:078, 2014.
- [86] Martin Bauer, Ulrich Haisch, and Felix Kahlhoefer. Simplified dark matter models with two Higgs doublets: I. Pseudoscalar mediators. *JHEP*, 05:138, 2017.
- [87] Michael Duerr, Felix Kahlhoefer, Kai Schmidt-Hoberg, Thomas Schwetz, and Stefan Vogl. How to save the WIMP: global analysis of a dark matter model with two s-channel mediators. *JHEP*, 09:042, 2016.
- [88] Michael Duerr, Alexander Grohsjean, Felix Kahlhoefer, Bjoern Penning, Kai Schmidt-Hoberg, and Christian Schwanenberger. Hunting the dark Higgs. *JHEP*, 04:143, 2017.
- [89] M. Misiak et al. Updated NNLO QCD predictions for the weak radiative B-meson decays. *Phys. Rev. Lett.*, 114(22):221801, 2015.

- [90] Frank Siegert. Monte-Carlo event generation for the LHC, 2010.
- [91] P. A. Zyla et al. Review of Particle Physics. *PTEP*, 2020(8):083C01, 2020.
- [92] Jon Butterworth et al. Pdf4lhc recommendations for lhc run ii. *Journal of Physics G: Nuclear and Particle Physics*, 43(2):023001, Jan 2016.
- [93] Sayipjamal Dulat, Tie-Jiun Hou, Jun Gao, Marco Guzzi, Joey Huston, Pavel Nadolsky, Jon Pumplin, Carl Schmidt, Daniel Stump, and C.-P. Yuan. New parton distribution functions from a global analysis of quantum chromodynamics. *Physical Review D*, 93(3), Feb 2016.
- [94] L. A. Harland-Lang, A. D. Martin, P. Motylinski, and R. S. Thorne. Parton distributions in the lhc era: Mmht 2014 pdfs. *The European Physical Journal C*, 75(5), May 2015.
- [95] Richard D. Ball et al. Parton distributions for the LHC Run II. *JHEP*, 04:040, 2015.
- [96] David Griffiths. *Introduction to elementary particles*. 2008.
- [97] John C. Collins, Davison E. Soper, and George F. Sterman. Factorization of Hard Processes in QCD. *Adv. Ser. Direct. High Energy Phys.*, 5:1–91, 1989.
- [98] Leif Lönnblad. Correcting the color dipole cascade model with fixed order matrix elements. *JHEP*, 05:046, 2002.
- [99] Leif Lönnblad. Combining Matrix Elements and the Dipole Cascade Model. *Acta Physica Polonica B*, 33(10):3171, October 2002.
- [100] T Gleisberg, S Hoeche, F Krauss, A Schaelicke, S Schumann, and J Winter. Sherpa 1. , a proof-of-concept version. *Journal of High Energy Physics*, 2004(02):056–056, Feb 2004.
- [101] D.P. Landau and K. Binder. *A Guide to Monte Carlo Simulations in Statistical Physics*. Cambridge University Press, 2005.
- [102] Torbjorn Sjostrand, Stephen Mrenna, and Peter Z. Skands. A Brief Introduction to PYTHIA 8.1. *Comput. Phys. Commun.*, 178:852–867, 2008.
- [103] Stefano Frixione, Fabian Stoeckli, Paolo Torrielli, Bryan R. Webber, and Chris D. White. The MCanLO 4.0 Event Generator. 10 2010.

- [104] J. Alwall, R. Frederix, S. Frixione, V. Hirschi, F. Maltoni, O. Mattelaer, H. S. Shao, T. Stelzer, P. Torrielli, and M. Zaro. The automated computation of tree-level and next-to-leading order differential cross sections, and their matching to parton shower simulations. *JHEP*, 07:079, 2014.
- [105] Lyndon Evans and Philip Bryant. LHC machine. *Journal of Instrumentation*, 3(08):S08001–S08001, aug 2008.
- [106] R Bailey and Paul Collier. Standard Filling Schemes for Various LHC Operation Modes. Technical report, CERN, Geneva, Sep 2003.
- [107] Esma Mobs. The CERN accelerator complex - 2019. Complexe des accélérateurs du CERN - 2019. Jul 2019. General Photo.
- [108] The ATLAS Collaboration. The ATLAS experiment at the CERN large hadron collider. *Journal of Instrumentation*, 3(08):S08003–S08003, aug 2008.
- [109] The CMS Collaboration. The CMS experiment at the CERN LHC. *Journal of Instrumentation*, 3(08):S08004–S08004, aug 2008.
- [110] F. Carena, W. Carena, S. Chapeland, V. Chibante Barroso, F. Costa, E. Dénes, R. Divià, U. Fuchs, A. Grigore, T. Kiss, G. Simonetti, C. Soós, A. Telesca, P. Vande Vyvre, and B. von Haller. The alice data acquisition system. *Nuclear Instruments and Methods in Physics Research Section A: Accelerators, Spectrometers, Detectors and Associated Equipment*, 741:130–162, 2014.
- [111] A. Augusto Alves, Jr. et al. The LHCb Detector at the LHC. *JINST*, 3:S08005, 2008.
- [112] The TOTEM Collaboration. The TOTEM experiment at the CERN large hadron collider. *Journal of Instrumentation*, 3(08):S08007–S08007, aug 2008.
- [113] O. Adriani et al. The LHCf detector at the CERN Large Hadron Collider. *JINST*, 3:S08006, 2008.
- [114] James Pinfold et al. Technical Design Report of the MoEDAL Experiment. 6 2009.
- [115] Akitaka Ariga et al. Technical Proposal for FASER: ForwArD Search ExpeRiment at the LHC. 12 2018.
- [116] Jorg Wenninger. Operation and Configuration of the LHC in Run 2. Mar 2019.

- [117] LuminosityPublicResultsRun2 < AtlasPublic < TWiki.
- [118] M Capeans, G Darbo, K Einsweiler, M Elsing, T Flick, M Garcia-Sciveres, C Gemme, H Pernegger, O Rohne, and R Vuillermet. ATLAS Insertable B-Layer Technical Design Report. Technical report, Sep 2010.
- [119] G. Avoni et al. The new LUCID-2 detector for luminosity measurement and monitoring in ATLAS. *JINST*, 13(07):P07017, 2018.
- [120] Sebastian White. The ATLAS zero degree calorimeter. *Nucl. Instrum. Meth. A*, 617:126–128, 2010.
- [121] L. Adamczyk et al. Technical Design Report for the ATLAS Forward Proton Detector. 5 2015.
- [122] S. Abdel Khalek et al. The ALFA Roman Pot Detectors of ATLAS. *JINST*, 11(11):P11013, 2016.
- [123] Georges Aad et al. Operation of the ATLAS trigger system in Run 2. *JINST*, 15(10):P10004, 2020.
- [124] ATLAS Collaboration. Electron and photon performance measurements with the ATLAS detector using the 2015-2017 LHC proton-proton collision data. 2019.
- [125] Georges Aad et al. ATLAS data quality operations and performance for 2015–2018 data-taking. *JINST*, 15(04):P04003, 2020.
- [126] R Seuster, M Elsing, G A Stewart, and V Tsulaia. Status and future evolution of the ATLAS offline software. *Journal of Physics: Conference Series*, 664(7):072044, dec 2015.
- [127] M Cattaneo. GAUDI - The Software Architecture and Framework for building LHCb Data Processing Applications. Feb 2000.
- [128] A. Buckley, T. Eifert, M. Elsing, D. Gillberg, K. Koeneke, A. Krasznahorkay, E. Moyses, M. Nowak, S. Snyder, and P. van Gemmeren. Implementation of the ATLAS Run 2 event data model. *J. Phys. Conf. Ser.*, 664(7):072045, 2015.
- [129] James Catmore, Paul Laycock, Eirik Gramstad, Thomas Gillam, Jack Cranshaw, Nurcan Ozturk, and Graeme Stewart. A New Petabyte-scale Data Derivation Framework for ATLAS. Technical report, CERN, Geneva, May 2015.

- [130] R Brun, F Rademakers, and S Panacek. ROOT, an object oriented data analysis framework. 2000.
- [131] M. Aaboud, G. Aad, B. Abbott, J. Abdallah, O. Abdinov, B. Abeloos, S. H. Abidi, O. S. AbouZeid, N. L. Abraham, and et al. Performance of the atlas track reconstruction algorithms in dense environments in the run 2. *The European Physical Journal C*, 77(10), Oct 2017.
- [132] T Cornelissen, M Elsing, I Gavrilenko, W Liebig, E Moyses, and A Salzburger. The new ATLAS track reconstruction (NEWT). *Journal of Physics: Conference Series*, 119(3):032014, jul 2008.
- [133] R. Frühwirth. Application of kalman filtering to track and vertex fitting. *Nuclear Instruments and Methods in Physics Research Section A: Accelerators, Spectrometers, Detectors and Associated Equipment*, 262(2):444–450, 1987.
- [134] T G Cornelissen, N Van Eldik, M Elsing, W Liebig, E Moyses, N Piacquadio, K Prokofiev, A Salzburger, and A Wildauer. Updates of the ATLAS Tracking Event Data Model (Release 13). Technical report, CERN, Geneva, Jun 2007.
- [135] Vertex Reconstruction Performance of the ATLAS Detector at " $\sqrt{s} = 13$  TeV". Technical report, CERN, Geneva, Jul 2015.
- [136] Performance of the ATLAS Inner Detector Track and Vertex Reconstruction in the High Pile-Up LHC Environment. Technical report, CERN, Geneva, Mar 2012.
- [137] Kathryn Grimm, S. Boutle, D. Casper, B. Hooberman, B. Gui, G. Lee, J. Maurer, A. Morley, S. Pagan Griso, B. Petersen, K. Prokofiev, L. Shan, D. Shope, A. Wharton, B. Whitmore, and M. Zhang. Primary vertex reconstruction at the ATLAS experiment. Technical report, CERN, Geneva, Feb 2017.
- [138] Georges Aad et al. Topological cell clustering in the ATLAS calorimeters and its performance in LHC Run 1. *Eur. Phys. J. C*, 77:490, 2017.
- [139] Jeremiah Jet Goodson. Search for Supersymmetry in States with Large Missing Transverse Momentum and Three Leptons including a Z-Boson, May 2012. Presented 17 Apr 2012.
- [140] Georges Aad et al. Jet energy scale and resolution measured in proton–proton collisions at  $\sqrt{s} = 13$  TeV with the ATLAS detector. *Eur. Phys. J. C*, 81(8):689, 2021.

- [141] Matteo Cacciari, Gavin P Salam, and Gregory Soyez. The anti-kt jet clustering algorithm. *Journal of High Energy Physics*, 2008(04):063–063, Apr 2008.
- [142] Stephen D. Ellis and Davison E. Soper. Successive combination jet algorithm for hadron collisions. *Physical Review D*, 48(7):3160–3166, Oct 1993.
- [143] S Catani, Yu L Dokshitzer, Michael H Seymour, and Bryan R Webber. Longitudinally-invariant  $k_{\perp}$ -clustering algorithms for hadron-hadron collisions. *Nucl. Phys. B*, 406:187–224. 38 p, Feb 1993.
- [144] Yu.L Dokshitzer, G.D Leder, S Moretti, and B.R Webber. Better jet clustering algorithms. *Journal of High Energy Physics*, 1997(08):001–001, Aug 1997.
- [145] M. Aaboud et al. Jet energy scale measurements and their systematic uncertainties in proton-proton collisions at  $\sqrt{s} = 13$  TeV with the ATLAS detector. *Phys. Rev. D*, 96(7):072002, 2017.
- [146] Matteo Cacciari and Gavin P. Salam. Pileup subtraction using jet areas. *Physics Letters B*, 659(1-2):119–126, Jan 2008.
- [147] David Krohn, Jesse Thaler, and Lian-Tao Wang. Jet trimming. *Journal of High Energy Physics*, 2010(2), Feb 2010.
- [148] Jet mass reconstruction with the ATLAS Detector in early Run 2 data. Technical report, CERN, Geneva, Jul 2016.
- [149] M. Aaboud, G. Aad, B. Abbott, O. Abdinov, B. Abeloos, D. K. Abhayasinghe, S. H. Abidi, O. S. AbouZeid, N. L. Abraham, and et al. In situ calibration of large-radius jet energy and mass in 13 tev proton–proton collisions with the atlas detector. *The European Physical Journal C*, 79(2), Feb 2019.
- [150] Variable Radius, Exclusive- $k_T$ , and Center-of-Mass Subject Reconstruction for Higgs( $\rightarrow b\bar{b}$ ) Tagging in ATLAS. Technical report, CERN, Geneva, Jun 2017.
- [151] Performance of  $b$ -jet identification in the atlas experiment. *Journal of Instrumentation*, 11(04):P04008–P04008, Apr 2016.
- [152] ATLAS Collaboration. Optimisation and performance studies of the ATLAS  $b$ -tagging algorithms for the 2017-18 LHC run. ATLAS-PHYS-PUB-2017-013, 2017.

- [153] Optimisation of the ATLAS  $b$ -tagging performance for the 2016 LHC Run. Technical report, CERN, Geneva, Jun 2016.
- [154] Secondary vertex finding for jet flavour identification with the ATLAS detector. Technical report, CERN, Geneva, Jun 2017.
- [155] Topological  $b$ -hadron decay reconstruction and identification of  $b$ -jets with the JetFitter package in the ATLAS experiment at the LHC. Technical report, CERN, Geneva, Oct 2018.
- [156] ATLAS Collaboration. Configuration and performance of the atlas  $b$ -jet triggers in run 2, 2021.
- [157] ATLAS Collaboration. Expected performance of the ATLAS  $b$ -tagging algorithms in Run-2. ATL-PHYS-PUB-2015-022, 2015.
- [158] Calibration of light-flavour  $b$ -jet mistagging rates using ATLAS proton-proton collision data at  $\sqrt{s} = 13$  TeV. Technical report, CERN, Geneva, Apr 2018.
- [159] M. Aaboud, G. Aad, B. Abbott, O. Abdinov, B. Abeloos, D. K. Abhayasinghe, S. H. Abidi, O. S. AbouZeid, N. L. Abraham, and et al. Measurements of  $b$ -jet tagging efficiency with the atlas detector using  $t\bar{t}$  events at  $\sqrt{s} = 13$  tev. *Journal of High Energy Physics*, 2018(8), Aug 2018.
- [160] ATLAS Collaboration. Muon reconstruction performance of the ATLAS detector in proton-proton collision data at  $\sqrt{s} = 13$  TeV. *Eur. Phys. J. C*, 76:292, 2016.
- [161] Muon reconstruction and identification efficiency in ATLAS using the full Run 2  $pp$  collision data set at  $\sqrt{s} = 13$  TeV. Technical report, CERN, Geneva, Aug 2020.
- [162] ATLAS Collaboration. Reconstruction, Energy Calibration, and Identification of Hadronically Decaying Tau Leptons in the ATLAS Experiment for Run-2 of the LHC. ATL-PHYS-PUB-2015-045, 2015.
- [163] ATLAS Collaboration. Identification of hadronic tau lepton decays using neural networks in the ATLAS experiment. ATL-PHYS-PUB-2019-033, 2019.
- [164] Matt Dobbs and Jorgen Beck Hansen. The HepMC C++ Monte Carlo event record for High Energy Physics. *Comput. Phys. Commun.*, 134:41–46, 2001.

- [165] G. Aad et al. The ATLAS Simulation Infrastructure. *Eur. Phys. J. C*, 70:823–874, 2010.
- [166] S. Agostinelli et al. Geant4—a simulation toolkit. *Nuclear Instruments and Methods in Physics Research Section A: Accelerators, Spectrometers, Detectors and Associated Equipment*, 506(3):250–303, 2003.
- [167] Basic ATLAS TRT performance studies of Run 1. Technical report, CERN, Geneva, Mar 2014.
- [168] V. L. Ginzburg and I. M. Frank. Radiation of a uniformly moving electron due to its transition from one medium into another. *J. Phys. (USSR)*, 9:353–362, 1945.
- [169] Claus Grupen and Boris Schwartz. *Particle detectors*. Cambridge Univ. Pr., Cambridge, UK, 2008.
- [170] Particle Identification Performance of the ATLAS Transition Radiation Tracker. 9 2011.
- [171] E. Abat et al. The ATLAS Transition Radiation Tracker (TRT) proportional drift tube: Design and performance. *JINST*, 3:P02013, 2008.
- [172] Morad Aaboud et al. Performance of the ATLAS Transition Radiation Tracker in Run 1 of the LHC: tracker properties. *JINST*, 12(05):P05002, 2017.
- [173] Bartosz Mindur. ATLAS Transition Radiation Tracker (TRT): Straw tubes for tracking and particle identification at the Large Hadron Collider. *Nucl. Instrum. Meth. A*, 845:257–261, 2017.
- [174] Trt performance results from 13 tev collision data (2015/2016), 2016.
- [175] Bartosz Mindur. Atlas transition radiation tracker (trt): Straw tubes for tracking and particle identification at the large hadron collider. *Nuclear Instruments and Methods in Physics Research Section A: Accelerators, Spectrometers, Detectors and Associated Equipment*, 845:257 – 261, 2017.
- [176] Keisuke Yoshihara, Bijan Haney, Christopher Meyer, Hugh Williams, Paul Keener, Elodie Deborah Resseguie, George Ian Dyckes, Leigh Schaefer, Khilesh Mistry, Vincent Wai Sum Wong, Daniil Ponomarenko, and Colin Gay. TRT DAQ Performance for Run 2. Technical Report ATL-COM-INDET-2017-041, CERN, Geneva, Sep 2017.
- [177] ATLAS Collaboration. Calibration of the ATLAS Transition Radiation Tracker. ATLAS-CONF-2011-006, 2011.

- [178] Alejandro Alonso, Oxana Smirnova, and Akesson Torsten. Transition Radiation Tracker calibration, searches beyond the Standard Model and multiparticle correlations in ATLAS, Apr 2012. Presented 20 May 2012.
- [179] Daniel Richter. *Energy Loss Measurements with the ATLAS Transition Radiation Tracker Using Test Beam Data*. PhD thesis, Humbolt-Univertät zu Berlin, 2008.
- [180] Performance of the reconstruction of large impact parameter tracks in the ATLAS inner detector. 7 2017.
- [181] T Akesson et al. Straw tube drift-time properties and electronics parameters for the ATLAS TRT detector. *Nucl. Instrum. Meth. A*, 449:446–460, 2000.
- [182] Wen Yi Song. Study of ToT and HT Corrections to the Drift Time in the ATLAS Transition Radiation Tracker (TRT). Technical report, CERN, Geneva, May 2018.
- [183] Thomas H. Kittelmann. *Slepton spin determination and simulation of the Transition Radiation Tracker at the ATLAS experiment*. PhD thesis, Bohr Inst., 2007.
- [184] Esben Bryndt Klinkby. *W mass measurement and simulation of the transition radiation tracker at the ATLAS experiment*. PhD thesis, Copenhagen U., 2008.
- [185] Katja Mankinen. Search for doubly charged higgs bosons in multi-lepton final states with the atlas detector, January 2020. Defence details Date: 2020-01-31 Time: 13:00 Place: Rydberg Lecture Hall (Rydbergsalen), Fysicum, Professorgatan 1, Lund External reviewer(s) Name: Eerola, Paula Title: Professor Affiliation: University of Helsinki, Helsinki, Finland —.
- [186] Christophe Pol A Roland. Optimizing simulation of the argon-based active gas mixture in the Transition Radiation Tracker (TRT). Technical report, CERN, Geneva, Oct 2017.
- [187] D. de Florian et al. Handbook of LHC Higgs Cross Sections: 4. Deciphering the Nature of the Higgs Sector. 2/2017, 10 2016.
- [188] Kyle Cranmer, George Lewis, Lorenzo Moneta, Akira Shibata, and Wouter Verkerke. HistFactory: A tool for creating statistical models for use with RooFit and RooStats. Technical Report CERN-OPEN-2012-016, New York U., New York, Jan 2012.

- [189] Glen Cowan, Kyle Cranmer, Eilam Gross, and Ofer Vitells. Asymptotic formulae for likelihood-based tests of new physics. *Eur. Phys. J. C*, 71:1554, 2011. [Erratum: *Eur.Phys.J.C* 73, 2501 (2013)].
- [190] Glen Cowan. Statistics for Searches at the LHC. In *69th Scottish Universities Summer School in Physics: LHC Physics*, 7 2013.
- [191] Alexander L. Read. Presentation of search results: The CL(s) technique. *J. Phys. G*, 28:2693–2704, 2002.
- [192] Georges Aad et al. Performance of electron and photon triggers in ATLAS during LHC Run 2. *Eur. Phys. J. C*, 80(1):47, 2020.
- [193] Georges Aad et al. Performance of the ATLAS muon triggers in Run 2. *JINST*, 15(09):P09015, 2020.
- [194] Georges Aad et al. Performance of the missing transverse momentum triggers for the ATLAS detector during Run-2 data taking. *JHEP*, 08:080, 2020.
- [195] Daniel Abercrombie et al. Dark Matter Benchmark Models for Early LHC Run-2 Searches: Report of the ATLAS/CMS Dark Matter Forum. *Phys. Dark Univ.*, 27:100371, 2020.
- [196] M. Misiak et al. Estimate of  $\mathcal{B}(\bar{B} \rightarrow X_s \gamma)$  at  $O(\alpha_s^2)$ . *Phys. Rev. Lett.*, 98:022002, 2007.
- [197] Combination of searches for invisible Higgs boson decays with the ATLAS experiment. 10 2020.
- [198] Antonio Boveia et al. Recommendations on presenting LHC searches for missing transverse energy signals using simplified  $s$ -channel models of dark matter. *Phys. Dark Univ.*, 27:100365, 2020.
- [199] Richard D. Ball, Valerio Bertone, Francesco Cerutti, Luigi Del Debbio, Stefano Forte, Alberto Guffanti, Jose I. Latorre, Juan Rojo, and Maria Ubiali. Impact of Heavy Quark Masses on Parton Distributions and LHC Phenomenology. *Nucl. Phys.*, B849:296–363, 2011.
- [200] ATLAS Run 1 Pythia8 tunes. Technical Report ATL-PHYS-PUB-2014-021, CERN, Geneva, Nov 2014.
- [201] Torbjörn Sjöstrand, Stefan Ask, Jesper R. Christiansen, Richard Corke, Nishita Desai, Philip Ilten, Stephen Mrenna, Stefan Prestel, Christine O. Rasmussen, and Peter Z. Skands. An Introduction to PYTHIA 8.2. *Comput. Phys. Commun.*, 191:159–177, 2015.

- [202] Enrico Bothmann, Gurpreet Singh Chahal, Stefan Höche, Johannes Krause, Frank Krauss, Silvan Kuttimalai, Sebastian Liebschner, Davide Napoletano, Marek Schönherr, Holger Schulz, and et al. Event generation with sherpa 2.2. *SciPost Physics*, 7(3), Sep 2019.
- [203] Steffen Schumann and Frank Krauss. A Parton shower algorithm based on Catani-Seymour dipole factorisation. *JHEP*, 03:038, 2008.
- [204] Stefan Hoeche, Frank Krauss, Marek Schonherr, and Frank Siegert. QCD matrix elements + parton showers: The NLO case. *JHEP*, 04:027, 2013.
- [205] S. Catani, F. Krauss, R. Kuhn, and B. R. Webber. QCD matrix elements + parton showers. *JHEP*, 11:063, 2001.
- [206] Stefan Hoeche, Frank Krauss, Steffen Schumann, and Frank Siegert. QCD matrix elements and truncated showers. *JHEP*, 05:053, 2009.
- [207] D. J. Lange. The EvtGen particle decay simulation package. *Nucl. Instrum. Meth. A*, 462:152–155, 2001.
- [208] Georges Aad et al. Measurement of the  $Z/\gamma^*$  boson transverse momentum distribution in  $pp$  collisions at  $\sqrt{s} = 7$  TeV with the ATLAS detector. *JHEP*, 09:145, 2014.
- [209] J. Pumplin, D. R. Stump, J. Huston, H. L. Lai, Pavel M. Nadolsky, and W. K. Tung. New generation of parton distributions with uncertainties from global QCD analysis. *JHEP*, 07:012, 2002.
- [210] Georges Aad et al. Performance of pile-up mitigation techniques for jets in  $pp$  collisions at  $\sqrt{s} = 8$  TeV using the ATLAS detector. *Eur. Phys. J. C*, 76(11):581, 2016.
- [211] ATLAS Collaboration. Evidence for the  $H \rightarrow b\bar{b}$  decay with the ATLAS detector. *JHEP*, 12:024, 2017.
- [212] C. Patrignani et al. Review of Particle Physics. *Chin. Phys. C*, 40(10):100001, 2016.
- [213] ATLAS Collaboration.  $E_T^{\text{miss}}$  performance in the ATLAS detector using 2015–2016 LHC  $pp$  collisions. ATLAS-CONF-2018-023, 2018.
- [214] ATLAS Collaboration. Object-based missing transverse momentum significance in the ATLAS Detector. ATLAS-CONF-2018-038, 2018.

- [215] Andrea Matic. *Search for Dark Matter in association with a Higgs boson decaying into b-quarks with the ATLAS detector*. PhD thesis, LMU Munich (main), 2020.
- [216] Luminosity determination in  $pp$  collisions at  $\sqrt{s} = 13$  TeV using the ATLAS detector at the LHC. Technical report, CERN, Geneva, Jun 2019.
- [217] Jet Mass Resolutions in ATLAS using Run 2 Monte Carlo Simulation. 2018.
- [218] Michiel Botje et al. The PDF4LHC Working Group Interim Recommendations. 1 2011.
- [219] M. Bahr et al. Herwig++ Physics and Manual. *Eur. Phys. J. C*, 58:639–707, 2008.
- [220] ATLAS collaboration. Search for dark matter produced in association with a standard model higgs boson decaying into  $b$ -quarks using the full run 2 dataset from the atlas detector, 2021.
- [221] Kyle Cranmer and Itay Yavin. RECAST: Extending the Impact of Existing Analyses. oct 2010.
- [222] Brendan Burns, Brian Grant, David Oppenheimer, Eric Brewer, and John Wilkes. Borg, omega, and kubernetes. *Queue*, 14(1):10:70–10:93, January 2016.
- [223] Dirk Merkel. Experimental Searches for the Axion and Axion-Like Particles. *Linux J. 2014.239*, March 2019.
- [224] J.M. Hethey. *GitLab Repository Management*. Community experience distilled. Packt Publishing, 2013.
- [225] Kyle Cranmer and Lukas Heinrich. Yadage and Packtivity - analysis preservation using parametrized workflows. jun 2017.
- [226] The Official YAML Web Site.
- [227] Tibor Šimko, Lukas Heinrich, Harri Hirvonsalo, Dinos Kousidis, and Diego Rodríguez. REANA: A System for Reusable Research Data Analyses. Technical Report CERN-IT-2018-003, CERN, Geneva, Dec 2018.
- [228] Michael Duerr, Alexander Grohsjean, Felix Kahlhoefer, Bjoern Penning, Kai Schmidt-Hoberg, and Christian Schwanenberger. Hunting the dark Higgs. *JHEP*, 04:143, 2017.

- [229] ATLAS Collaboration. Constraints on mediator-based dark matter and scalar dark energy models using  $\sqrt{s} = 13$  TeV  $pp$  collision data collected by the ATLAS detector. 2019.
- [230] Leif Lönnblad and Stefan Prestel. Matching Tree-Level Matrix Elements with Interleaved Showers. *JHEP*, 03:019, 2012.
- [231] ATLAS Collaboration. The Pythia 8 A3 tune description of ATLAS minimum bias and inelastic measurements incorporating the Donnachie-Landshoff diffractive model. ATL-PHYS-PUB-2016-017, 2016.
- [232] ATLAS Collaboration. The ATLAS Simulation Infrastructure. *Eur. Phys. J. C*, 70:823, 2010.
- [233] Morad Aaboud et al. Search for dark matter produced in association with a higgs boson decaying to  $b\bar{b}$  using  $36 \text{ fb}^{-1}$  of  $pp$  collisions at  $\sqrt{s} = 13$  tev with the atlas detector. *Physical Review Letters*, 119(18), Nov 2017.



# Appendix A

## TRT auxiliary material

This appendix contains auxiliary material from the TRT calibration studies presented in chapter 7.

### A.1 r-t relations for the calibration with $LT=100$ eV and new signal shaping

This section presents the r-t relations obtained from the calibration of simulated events with  $\langle\mu\rangle < 1$ , presented in Sec. 7.6. Figure A.1 shows the r-t relation for argon-filled and Figure A.2 for xenon-filled straw tubes.

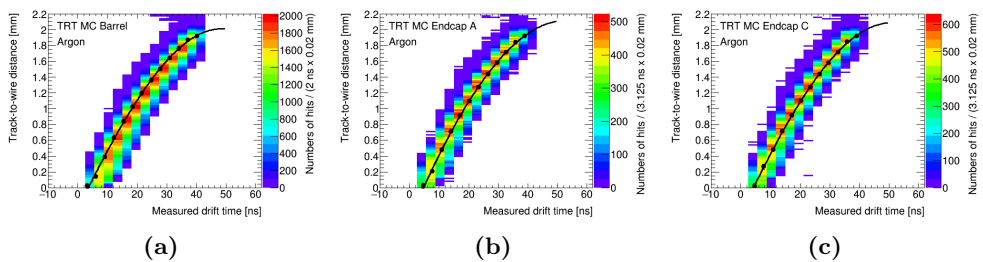


**Figure A.1:** r-t relations for argon-filled straws for simulated samples with  $\langle\mu\rangle < 1$  and low threshold value of 100 eV

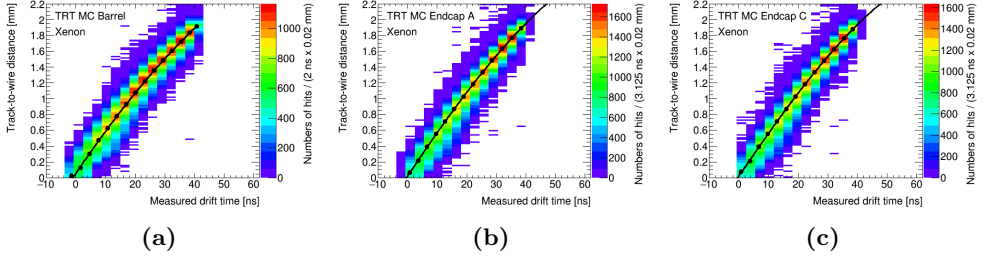


**Figure A.2:**  $rt$  relations for xenon-filled straws for simulated samples with  $\langle\mu\rangle < 1$  and low threshold value of 100 eV

## A.2 Position and time residuals for Xe-based straw tubes using simulated samples without pile-up

This section contains the position and time residuals of Xe-based straw tubes using simulated samples with  $\langle\mu\rangle < 1$ , after the complete calibration, i.e. after 5 iterations and shifting the  $T_0$  parameters. The residuals are estimated for tracks with  $p_T$  above 2 GeV

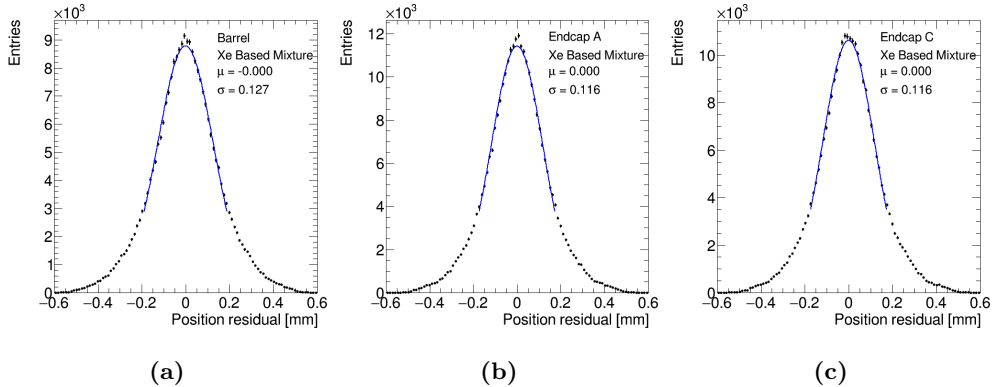


**Figure A.3:** Position residuals for xenon-filled straws for simulated samples with  $\langle\mu\rangle < 1$  and low threshold value of 100 eV

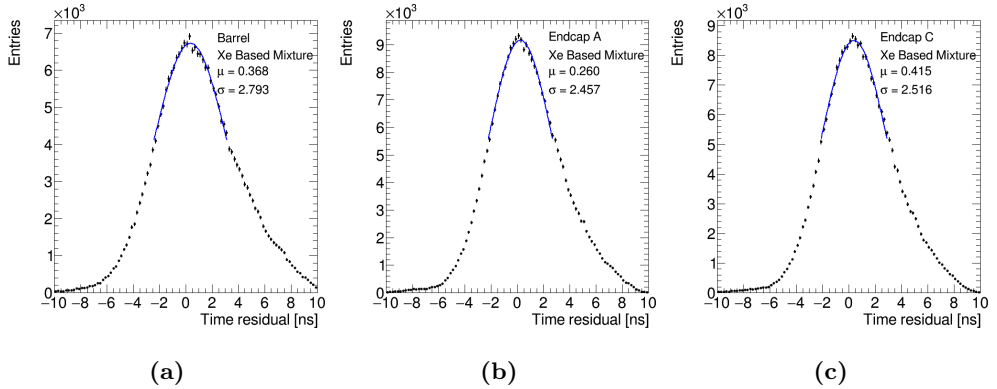


**Figure A.4:** Time residuals for xenon-filled straws for simulated samples with  $\langle\mu\rangle < 1$  and low threshold value of 100 eV

### A.3 Position and time residuals for Ar-based straw tubes with ToT correction only

This section contains the position and time residuals estimated using  $Z \rightarrow \mu\mu$  simulated events with  $\langle\mu\rangle \in (20, 30)$ , for tracks with  $p_T$  above 5 GeV. Figure A.5 shows the residuals for straw tubes filled with Ar-based gas mixture and Fig. A.6 for Xe-based gas mixture.

### A.4 Position and time residuals for Ar-based straw tubes with ToT and HT corrections

This section contains the position and time residuals estimated using  $Z \rightarrow \mu\mu$  simulated events with  $\langle\mu\rangle \in (20, 30)$ , for tracks with  $p_T$  above 5 GeV. Figure A.7 shows the residuals for straw tubes filled with Ar-based gas mixture and Fig. A.8 for Xe-based gas mixture.

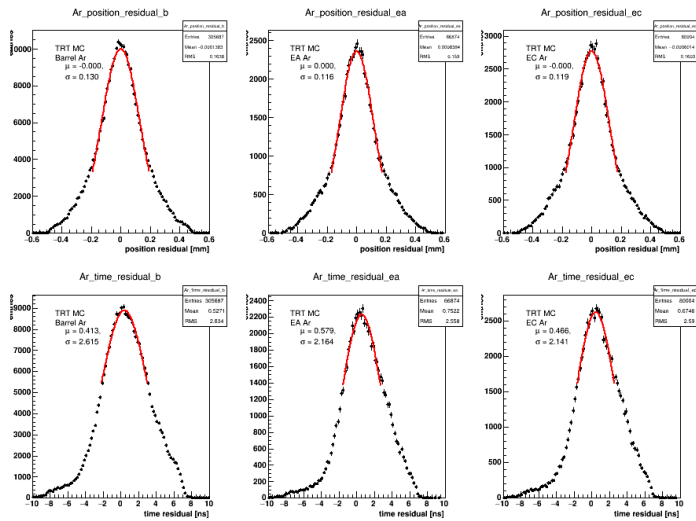


Figure A.5: Position and time residuals for straw tubes filled with Ar-based mixture after applying ToT correction only.

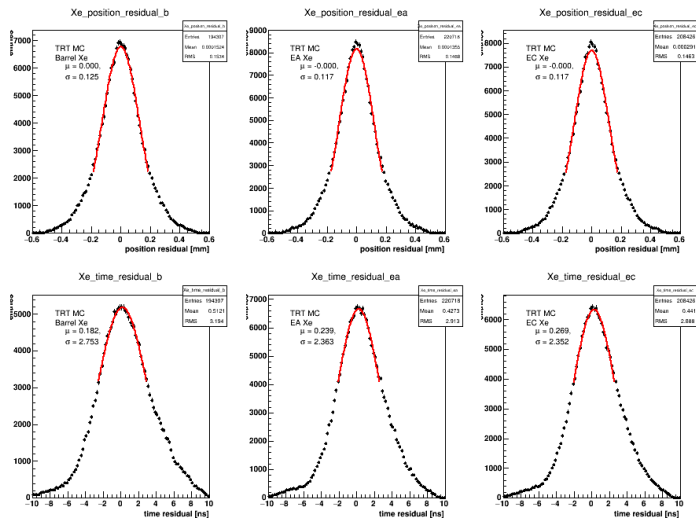
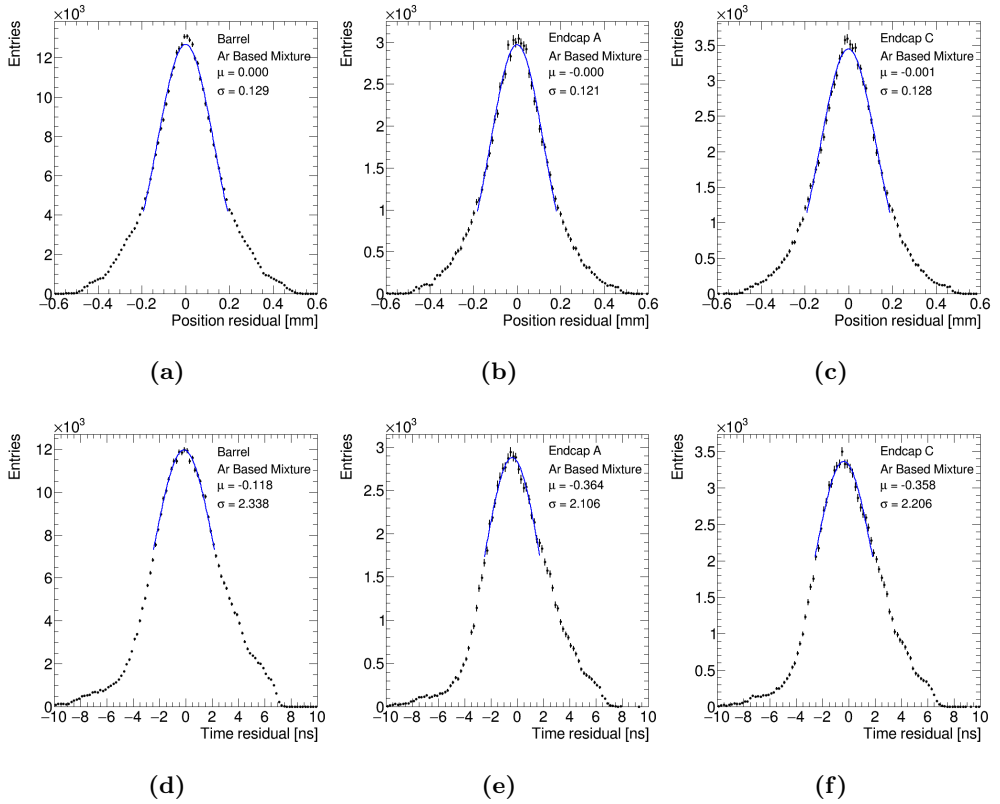
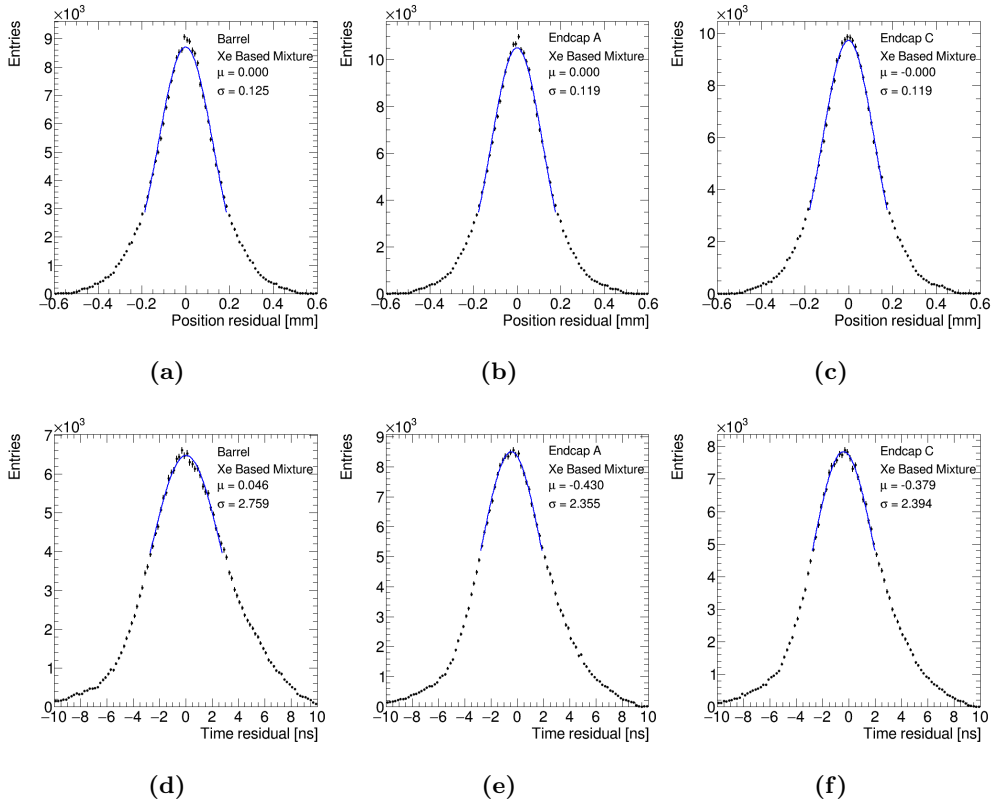


Figure A.6: Position and time residuals for straw tubes filled with Xe-based mixture after applying ToT correction only.



**Figure A.7:** Position (top) and time (bottom) residuals for xenon-filled straws for simulated samples with  $\langle \mu \rangle < 1$  and low threshold value of 100 eV



**Figure A.8:** Position (top) and time (bottom) for xenon-filled straws for simulated samples with  $\langle \mu \rangle < 1$  and low threshold value of 100 eV

# Appendix B

## Comparison plots between reconstructed and truth variables

This chapter contains comparisons between the truth and reconstructed event variables that were not included in the main body of this thesis.

### B.1 Signal region

This section contains comparisons in the signal regions

### B.2 One-muon CR

### B.3 Two-lepton CR

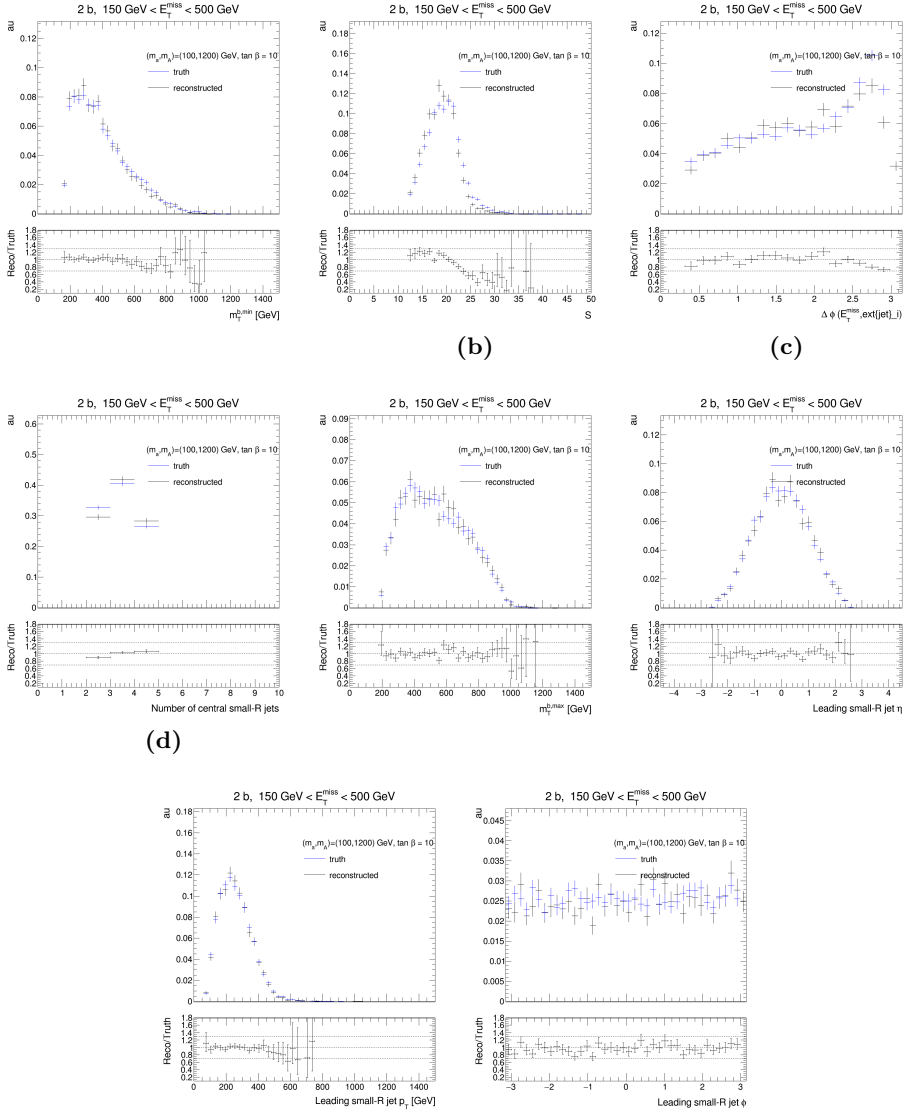


Figure B.1: Comparison of event variable distributions in the resolved 2b signal region.

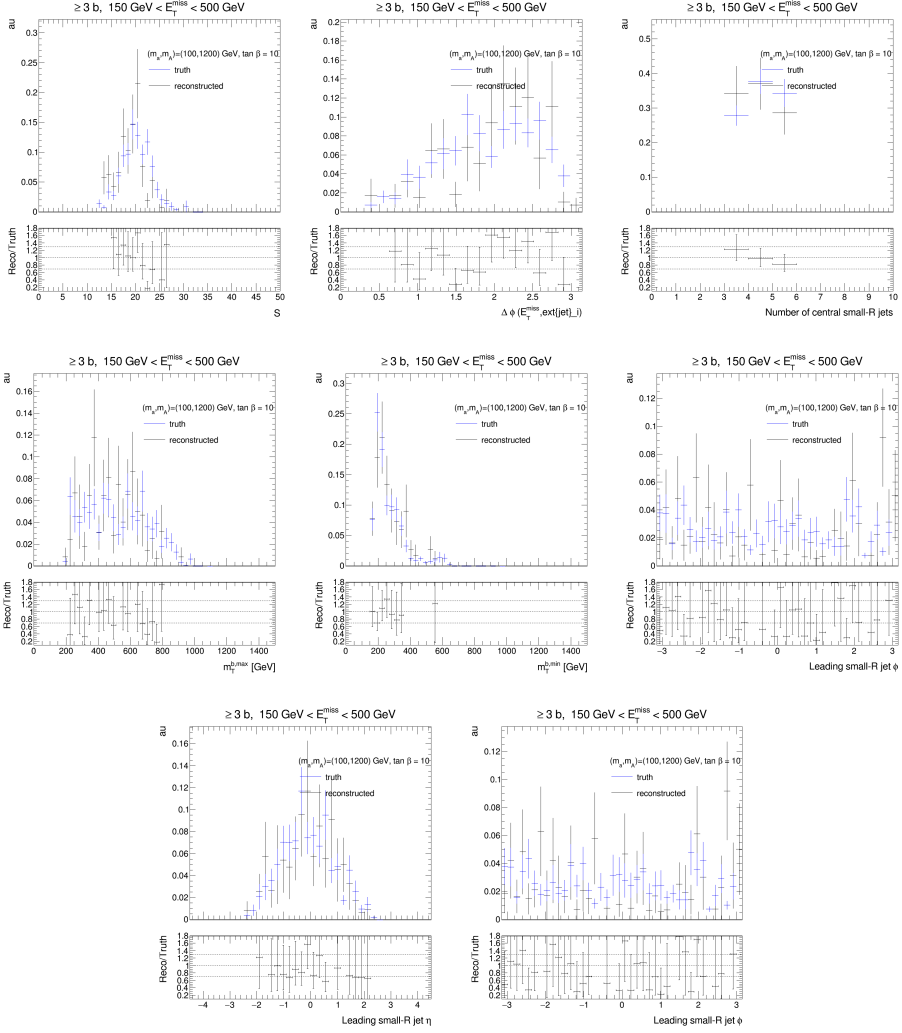


Figure B.2: Comparison plots for distributions in the resolved  $3b - tag$  signal region.

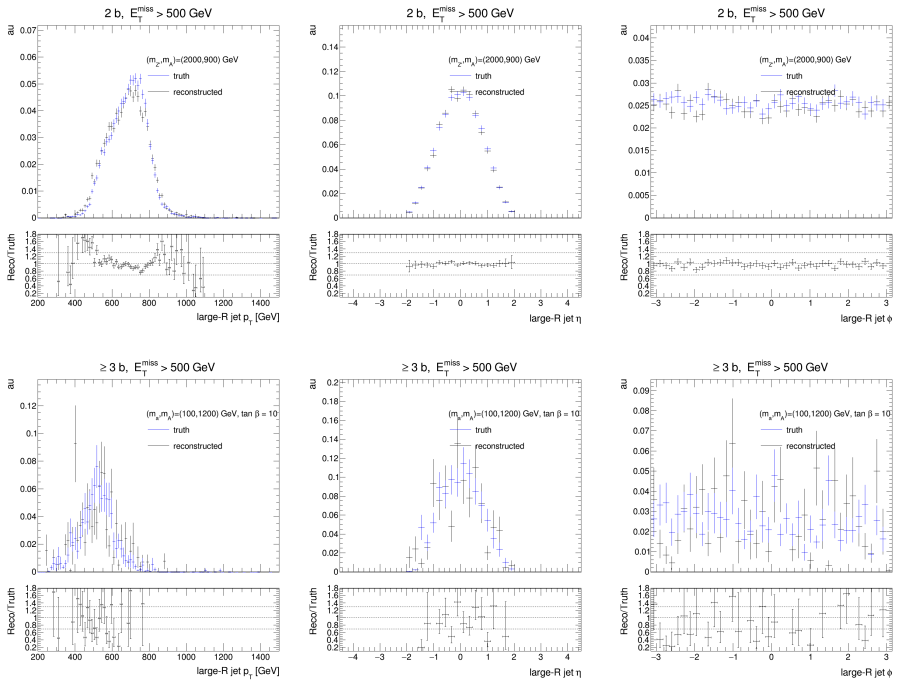


Figure B.3: Comparison plots for distributions in the merged signal region.

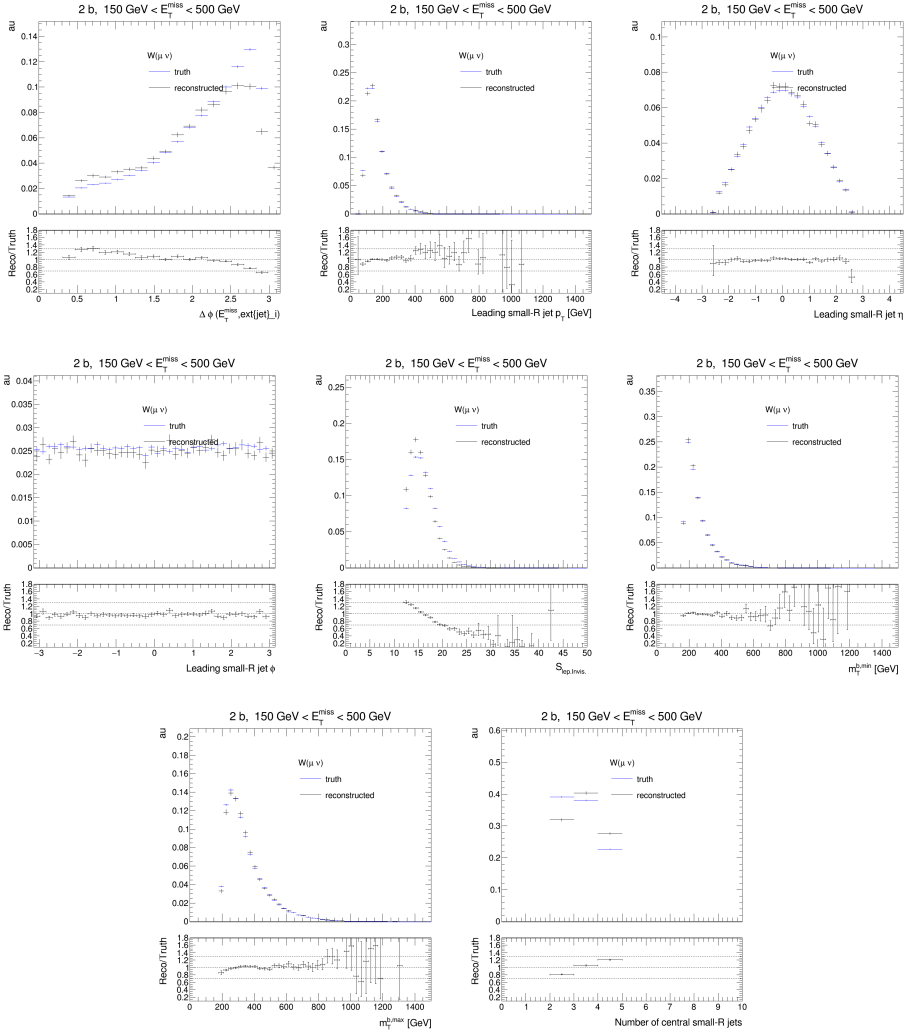


Figure B.4: Comparison plots in the resolved 2b one-muon control region.

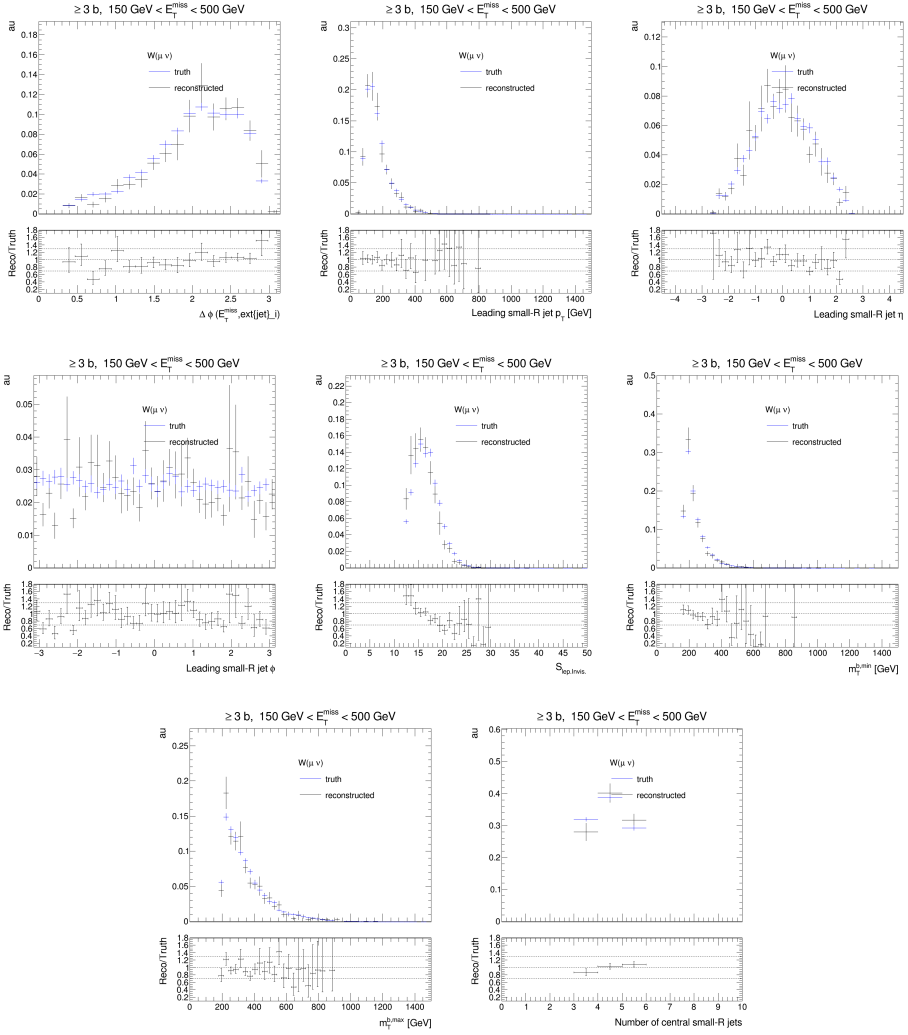


Figure B.5: Comparison plots in the resolved 3b one-muon control region.

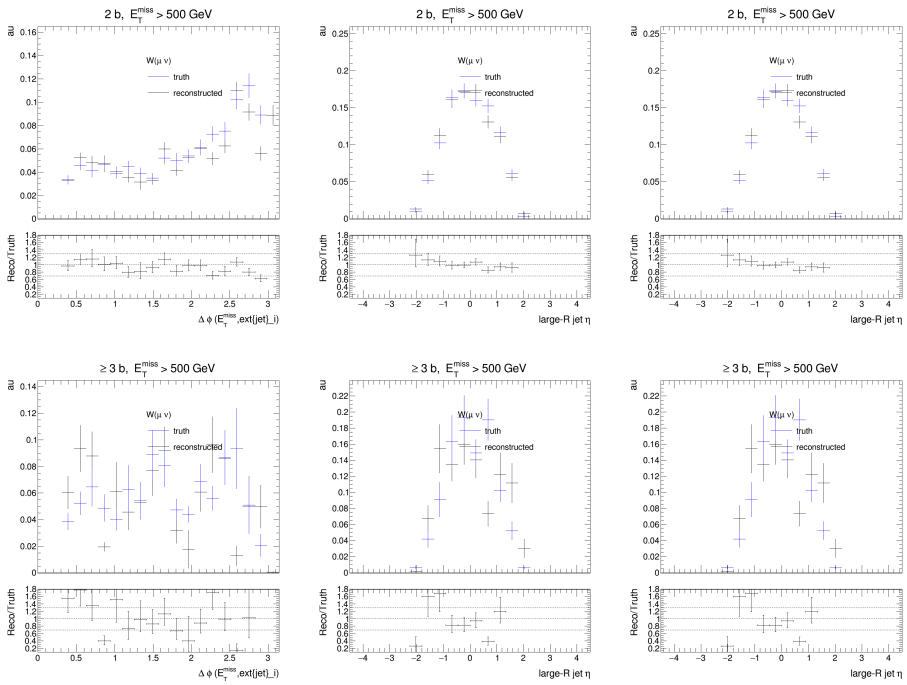


Figure B.6: Comparison plots in the Merged 2b and 3b one-muon control region.

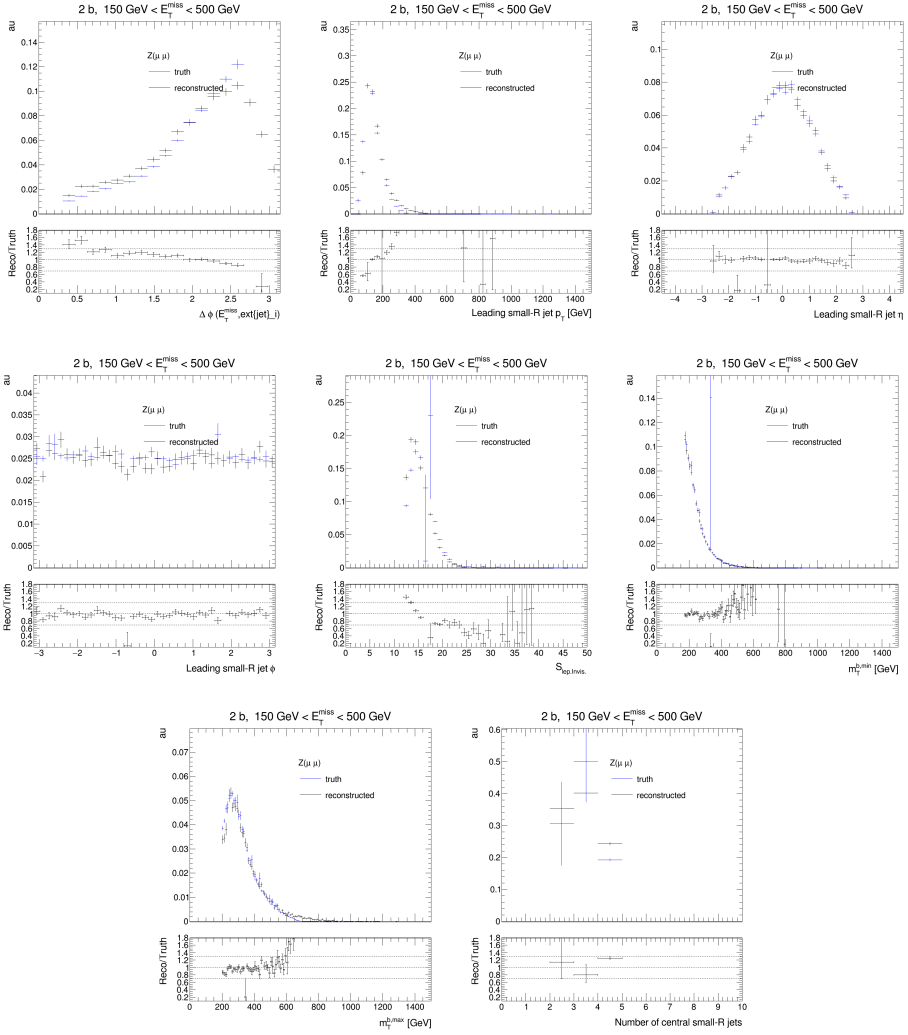


Figure B.7: Comparison plots in the resolved 2b two-lepton control region.

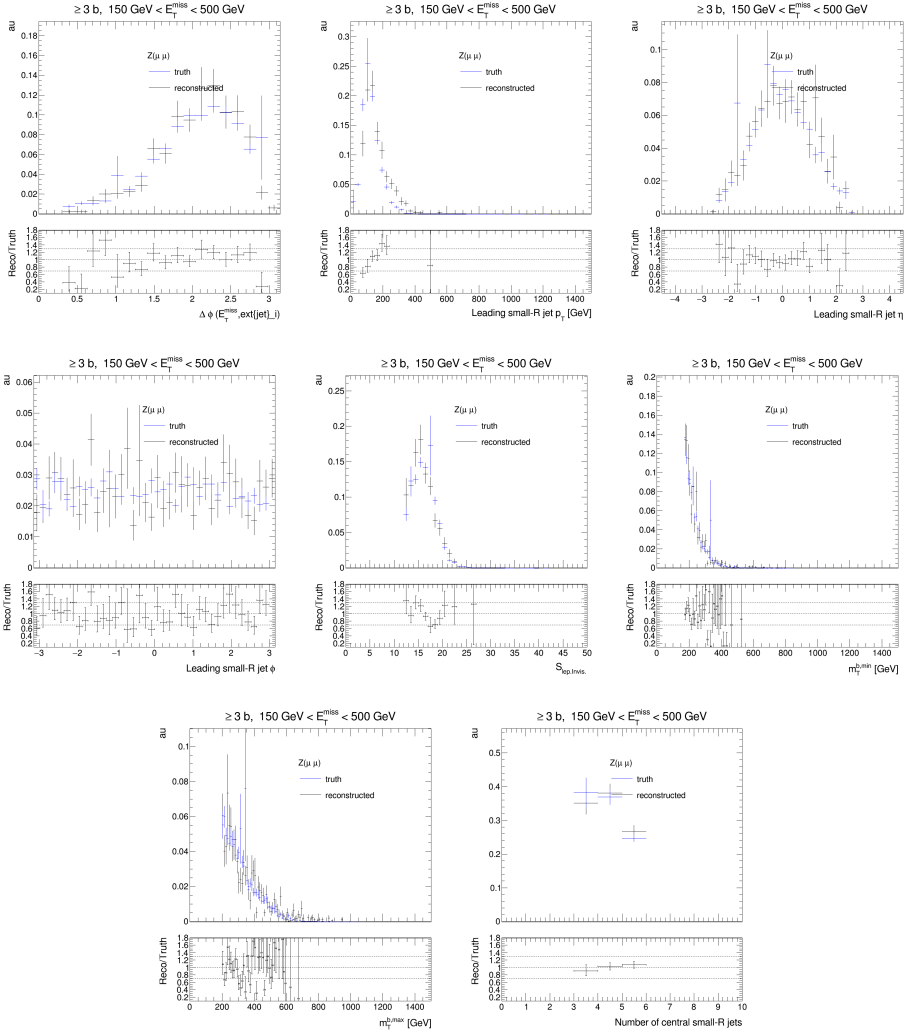


Figure B.8: Comparison plots in the resolved 3b two-lepton control region.

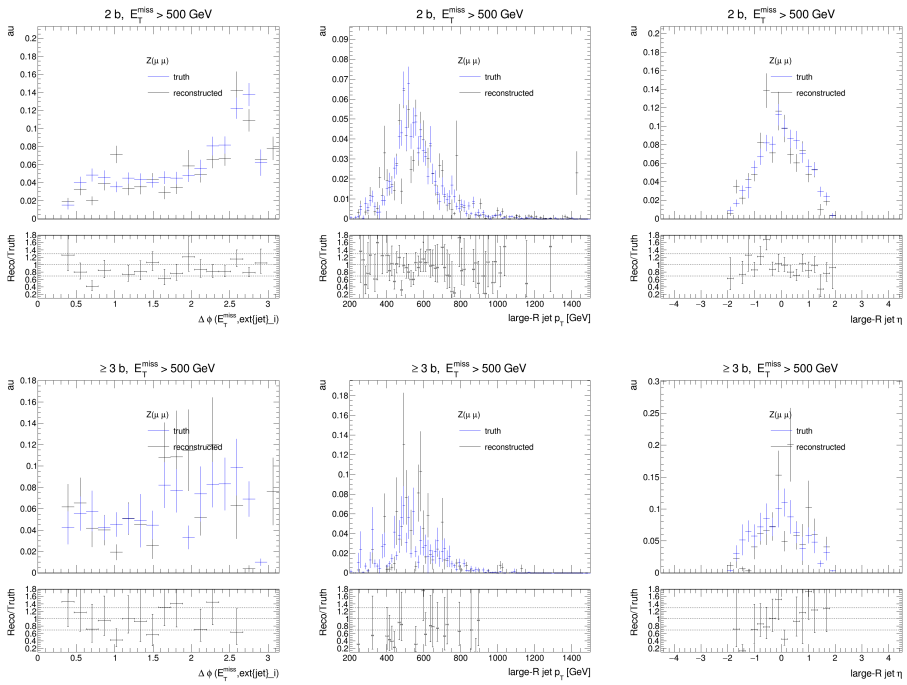


Figure B.9: Comparison plots in the Merged 2b and 3b two-lepton control region.

# Appendix C

## Comparison of Standard Model predictions to data

### C.1 Signal region pre-fit distributions

Figure C.1 shows the pre-fit distributions for the invariant mass of the Higgs-boson candidate in the resolved and merged regions for events in both b-tag categories. The same distributions for the three  $E_T^{\text{miss}}$  bins of the resolved  $2b$  and  $\geq 3b$ -tag region are shown in Figure C.3.

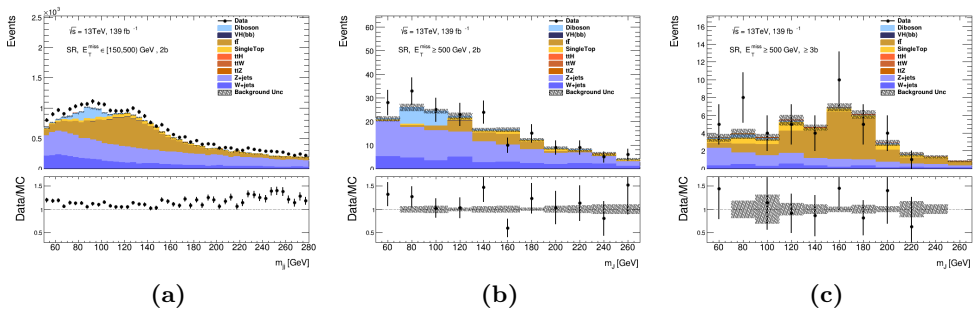


**Figure C.1:** Distributions of the invariant mass of the Higgs-boson candidate in different  $E_T^{\text{miss}}$  bins in the signal region for events in the 2-b tag category

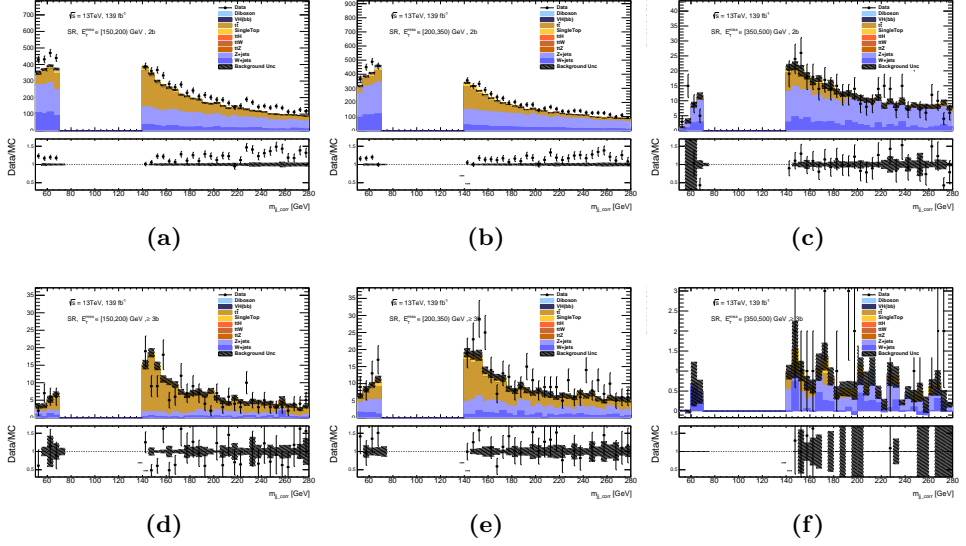


**Figure C.2:** The upper panel of each plot shows of  $m_{jj}$  in the signal region for events in the  $2b$ -tag (top) and three  $b$ -tag category in the three  $E_T^{\text{miss}}$  ranges of the resolved region. The bottom panel displays the ratio of data to the SM predictions. The experimental and statistical uncertainties for the SM expectations are indicated by the hatched band and do not consider any correlations between individual contributions.

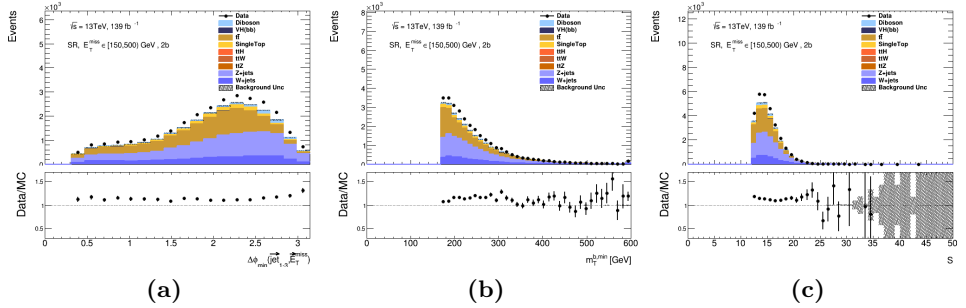


**Figure C.3:** The upper panel of each plot shows of  $m_{jj}$  in the signal region for events in the  $2b$ -tag (top) and three  $b$ -tag category in the three  $E_T^{\text{miss}}$  ranges of the resolved region. The bottom panel displays the ratio of data to the SM predictions. The experimental and statistical uncertainties for the SM expectations are indicated by the hatched band and do not consider any correlations between individual contributions.

## C.2 Selected pre-fit distributions in the one-muon control region

The muon charge distribution is shown in Figure C.4 in the resolved (top) and merged (bottom) CR1 before the fit for events with exactly two (left) and at least 3  $b$ -tagged jets (right). In fig. C.4a, the ratio is a little lower than one, indicating that the predicted event yields in both bins of the distribution overestimate the observed data. In fig. C.4b and C.4c the ratio is one, while in C.4d the second bin the ratio in the second bin is lower than one. Figure C.5 shows the distributions

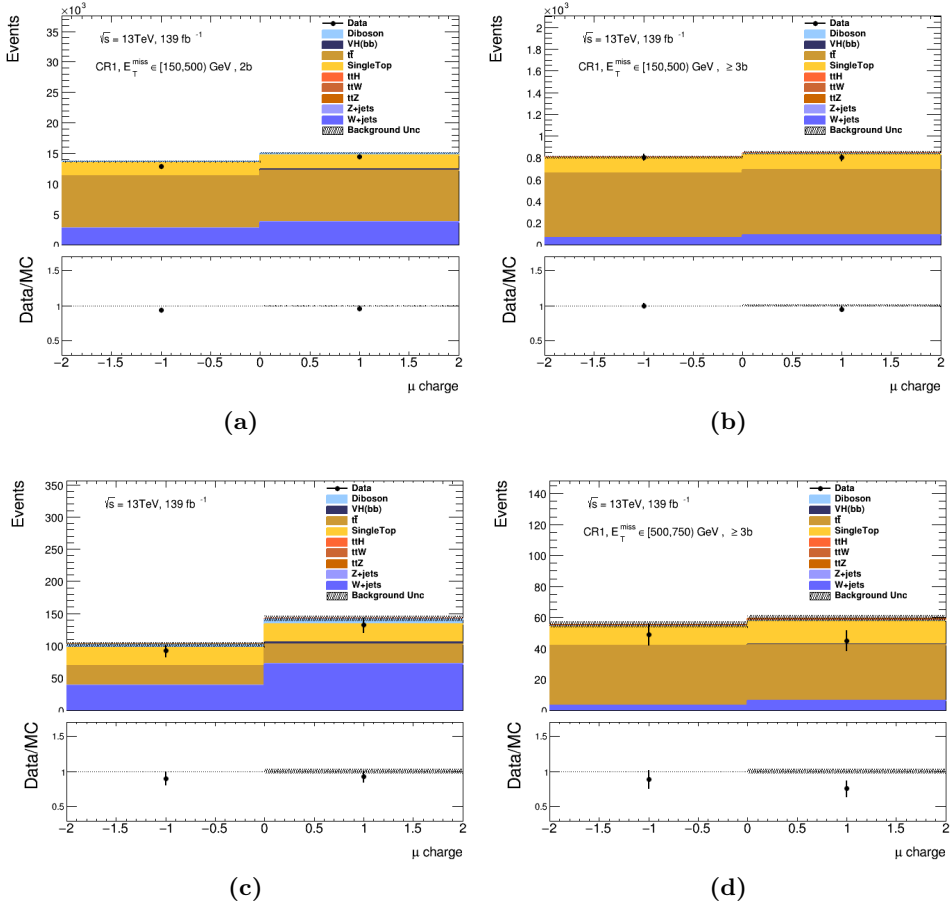


**Figure C.4:** Muon charge plots in the resolved (top) and merged (bottom) CR1 for events with exactly 2 (left) and at least 3  $b$ -tagged jets (right).

of the  $E_T^{\text{miss}}$  significance at the two lowest  $E_T^{\text{miss}}$  bins of the resolved region for both  $b$ -tag categories.

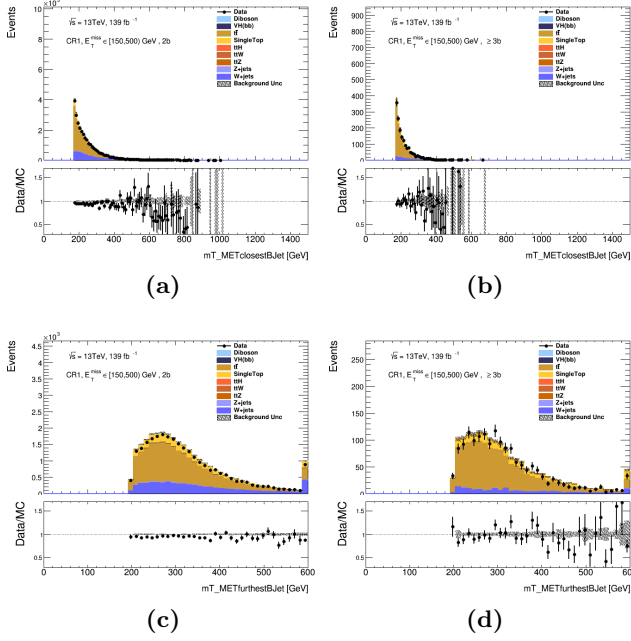


**Figure C.5:** Distributions of the in the resolved CR1 for events with exactly 2 (left) and at least 3  $b$ -tagged jets (right).

### C.3 Selected prefit distributions in the two-lepton signal region

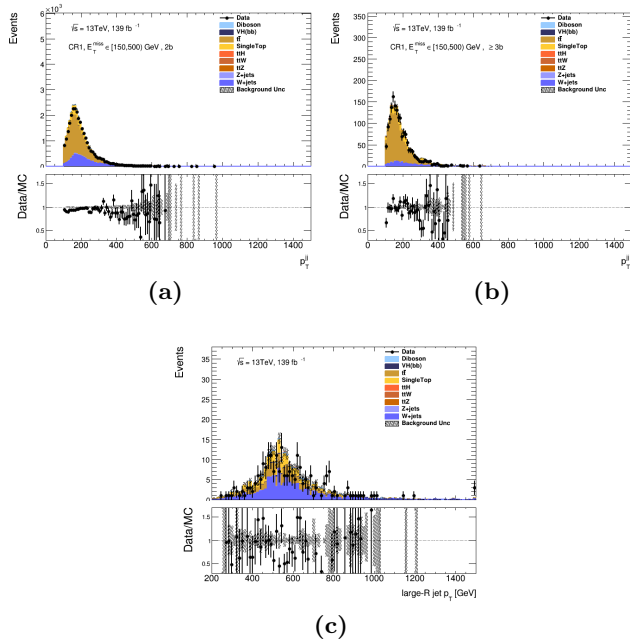
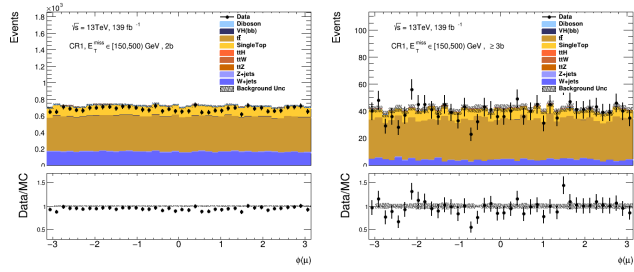
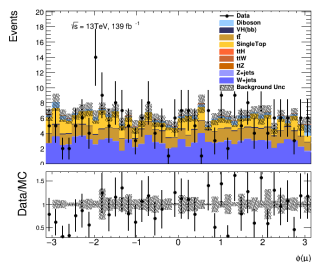


**Figure C.6:** Distributions of the  $p_T$  of the Higgs-boson candidate in the resolved (top) and merged (bottom) CR1 for events with exactly 2(left) and at least 3  $b$ -tagged jets(right).

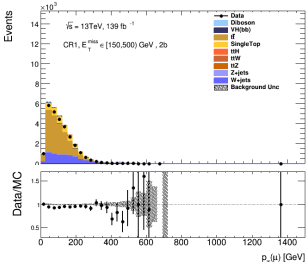


(a)

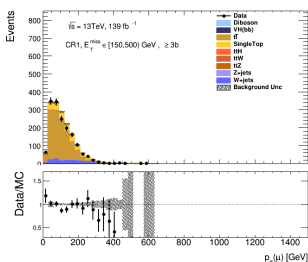
(b)



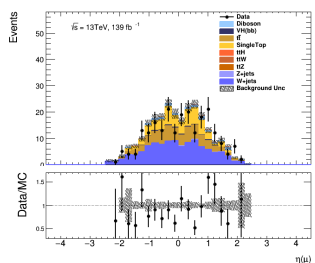
(c)



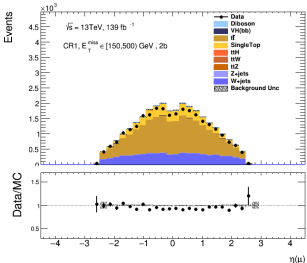
(d)



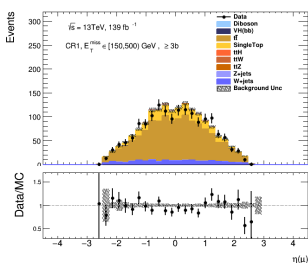
(e)



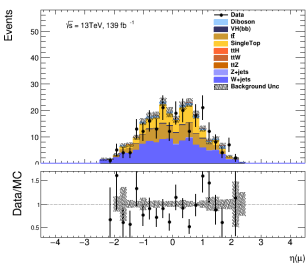
(f)



(g)

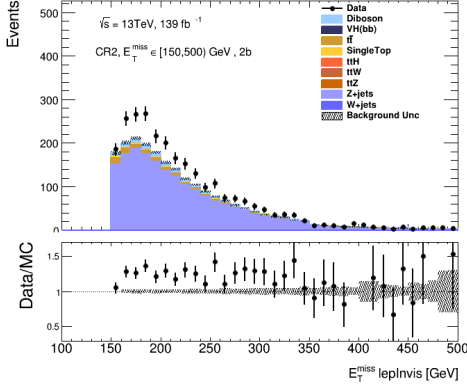


(h)

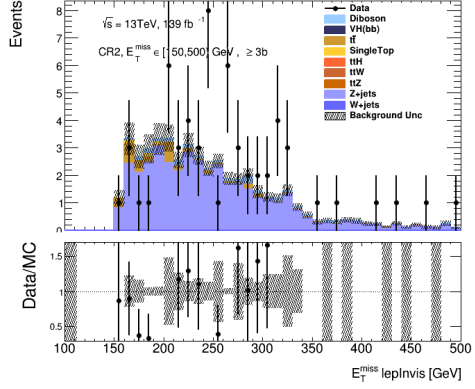


(i)

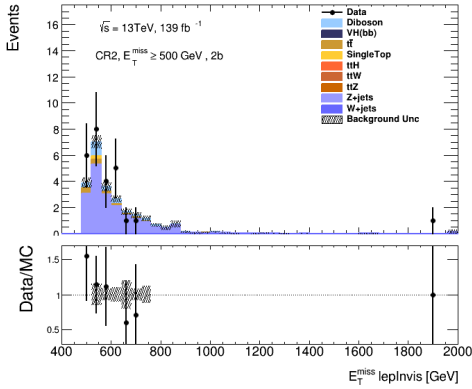
Figure C.7: Distributions of the  $\phi$ ,  $\eta$ , and  $p_T$  of the signal muon in the resolved and merged CR1.



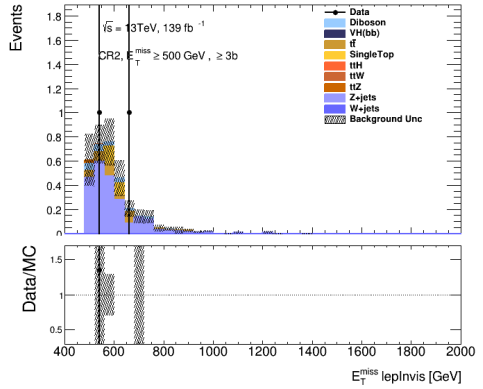
(a)



(b)

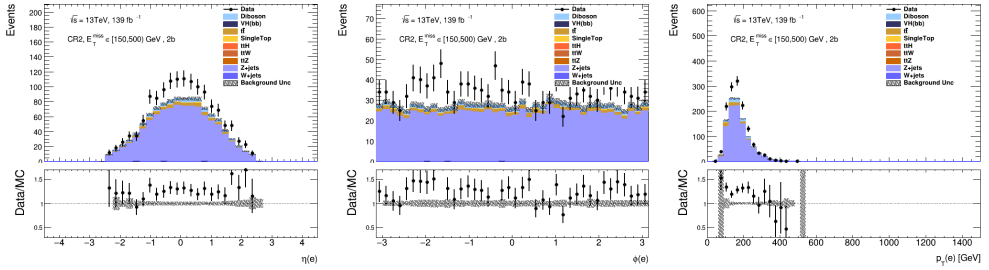


(c)



(d)

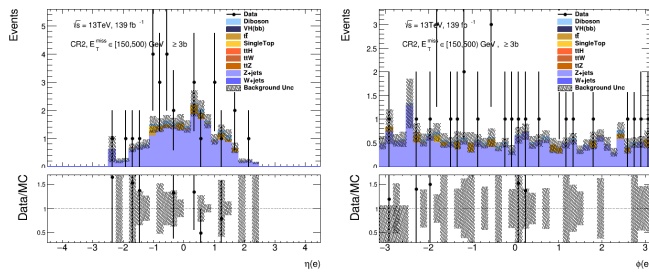
**Figure C.8:**  $E_{T, \text{lep, invis}}^{\text{miss}}$  spectra in the resolved (top) and merged (bottom) two-lepton control region, for events in the 2b-tag (left) and  $\geq 3b$ -tag (right) categories.



(a)

(b)

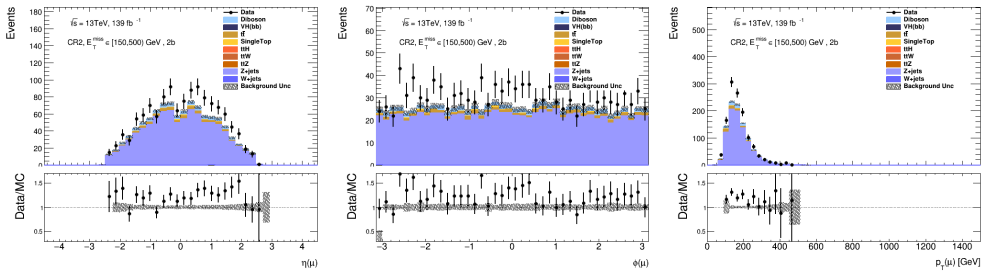
(c)



(d)

(e)

**Figure C.9:** Distribution of the invariant of the leading signal electron in resolved and merged regions for the  $2b$ -tag categories.



(a)

(b)

(c)

**Figure C.10:** Distribution of the invariant of the leading signal electron in resolved and merged regions for the  $2b$ -tag categories.

## Appendix D

# Mono-H analysis results-auxiliary material

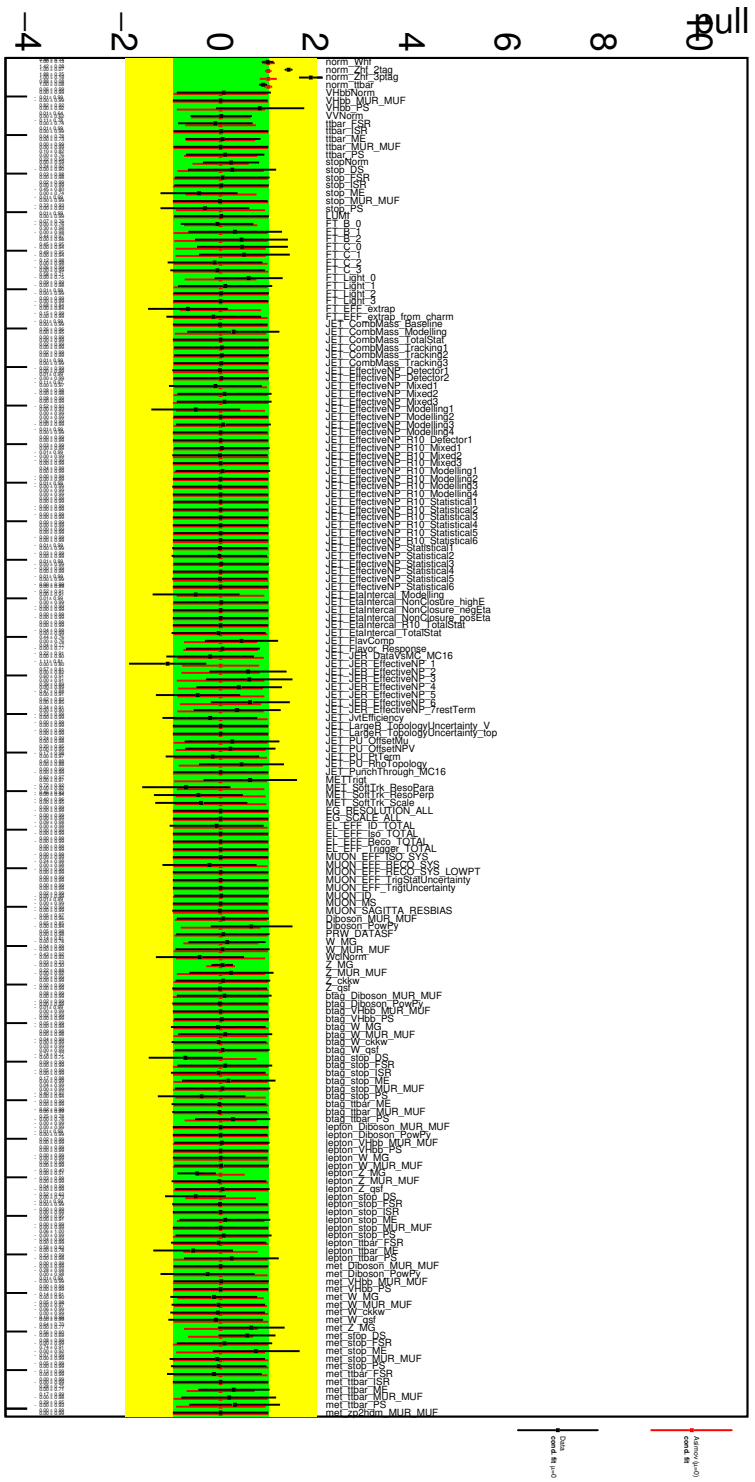


Figure D.1: Comparison of pulls for the NP in the combined signal and control region fit. The black points are calculated from a fit to data while the red correspond to an Asimov data set fit with  $\mu = 0$









Faculty of Science  
Department of Physics  
ISBN 978-91-8039-415-4

